CONFRONTING WARM-SEASON OZONE POLLUTION IN CHINA: INTEGRATING GLOBAL CHALLENGES, REGIONAL IMPACTS, AND LOCAL EMISSION CONSTRAINTS

BEINING ZHOU

PhD

The Hong Kong Polytechnic University

2026

The Hong Kong Polytechnic University

Department of Civil and Environmental Engineering

Confronting Warm-Season Ozone Pollution in China: Integrating Global Challenges, Regional Impacts, and Local Emission Constraints

Beining Zhou

A thesis submitted in partial fulfilment of the requirements for the degree of

Doctor of Philosophy

August 2025

CERTIFICATE OF ORIGINALITY

I hereby declare that this thesis is my own work and that, to the best of my knowledge and belief, it reproduces no material previously published or written, nor material that has been accepted for the award of any other degree or diploma, except where due acknowledgement has been made in the text.

_____ (Signed)

Beining Zhou (Name of student)

ABSTRACT

Surface ozone (O_3) pollution is a long-standing and intractable environmental problem that poses risks to human health and ecosystems, participates in atmospheric chemistry, and contributes to global warming. Despite ongoing efforts, widespread O_3 pollution during warm seasons remains a global challenge. In particular, China has experienced the most severe O_3 pollution with high and increasing O_3 levels over the past decade. However, this escalating O_3 pollution has not been fully addressed from a global perspective due to the delay in establishing a nationwide O_3 monitoring network in China. Therefore, the first aim of this thesis is to comprehensively assess the current status of warm-season O_3 pollution in China and worldwide, and to identify the current challenges of O_3 pollution control. Moreover, although China has been regarded as a large source of O_3 and its precursors, regional transport of air pollutants from upwind source regions with emerging emissions, such as Southeast Asia and marine shipping, could further exacerbate O_3 pollution in China. Hence, the second aim of this thesis zooms in on South China, where increasingly severe O_3 pollution has occurred in recent summers, to elucidate the transport impacts from Southeast Asia under the prevailing summer monsoon. In addition, as a secondary pollutant, surface O_3 is formed through complex reactions among its precursors, with volatile organic compounds (VOCs) playing a key role. Accurate quantification of VOC emissions is critical for O_3 pollution research, especially when using air quality models, yet current emission inventories are subject to significant biases. This gap motivates the third aim of this thesis to develop an observational constraint on VOC emissions to better represent local VOC emissions and improve O_3 modeling studies.

To understand the current O_3 pollution in China and worldwide, as well as its emerging challenges, ground-level O_3 measurements at over 4,300 monitoring stations across 48 countries

were compiled, showing significantly high O_3 concentrations with the fastest-ever increasing rate in China during warm seasons from 2014 to 2019. This unintentional rise in O_3 levels, primarily caused by emission reductions in nitrogen oxides (NO_x) and fine particulate matter ($PM_{2.5}$), underscores the necessity and urgency of coordinated emission controls for all O_3 precursors (both NO_x and VOCs) and $PM_{2.5}$. Meanwhile, increases in O_3 levels were also observed in developed regions, where emissions of O_3 precursors have already been substantially reduced, particularly in the western United States, southern and central Europe, and eastern Australian cities, indicating new challenges in O_3 air quality management. On the one hand, previously overlooked sources of O_3 precursors have emerged after traditional combustion-related sources were effectively reduced, such as the extensive use of volatile chemical products. On the other hand, the climate penalty on O_3 has intensified under a warming and drying climate, with more frequent and severe climate extremes amplifying high O_3 pollution episodes and O_3 exposures. As such, holistic management of multiple pollutants under a changing climate is urgently needed to confront this global threat.

To further understand the regional impacts on worsening summer O_3 pollution over South China in the recent decade, O_3 and its precursors from 2013 to 2022 were analyzed, revealing more frequent region-wide high O_3 episodes with elevated concentrations. Notably, 39 region-wide high O_3 episodes occurred under strong summer monsoon influences, which challenged the conventional view that clean air brought by the monsoon solely dilutes air pollution. Using a chemical transport model (WRF-CMAQ), the mechanisms building up these O_3 episodes were explored. While local emissions primarily drove daytime O_3 formation in South China, regional emissions from upwind mainland Southeast Asia and shipping activities in the South China Sea substantially contributed to O_3 pollution in South China by 4 ppbv. Unexpectedly, the Beibu Gulf acted as a critical O_3 reservoir, where O_3 and its precursors from upwind regions and ship

emissions underwent chemical processing and accumulated, sustaining high O_3 levels and supplying O_3 to South China through prevailing southwesterly winds. These findings redefine the dual role of the summer monsoon, demonstrating that it can both alleviate pollution and facilitate the transboundary transport of air pollutants. Moreover, the growing emissions in Southeast Asia and shipping activities introduce a new challenge to O_3 mitigation in South China, highlighting the need for international cooperation to manage transboundary pollution.

To constrain VOC emissions based on observations, concurrent VOC measurements were carried out across the Pearl River Delta (PRD) region, the most populous and developed city cluster in South China, during the summer of 2018. A mass-balance calculation, accounting for both physical and chemical processes, was developed to quantitatively estimate anthropogenic VOC emissions. After applying this observational constraint, the speciated emissions of VOCs exhibited clear diurnal variations and corrected the spatially concentrated priori emissions, reducing peak emissions in central PRD cities by 15% – 36% and elevating the sparse emissions in other cities. These observation-constrained VOC emissions improved the model simulations, better reproducing the spatiotemporal variations of VOCs and alleviating the biases from -55% – 85% to -13% – 13%. Moreover, simulations of peak O_3 concentrations were also amended to reduce the biases by 5% – 12% during high O_3 episodes. This observational constraint has effectively combined VOC field measurements with air quality modeling to achieve better simulations of VOCs and O_3, providing scientific support for further studies on the impacts of local and short-term emission changes on O_3 pollution, as well as its control strategies.

In summary, this thesis provides a multi-scale perspective for addressing the emerging O_3 pollution in China, encompassing a global overview of the status and current challenges of O_3 pollution control, a regional investigation of transboundary transport to South China, and a local

observational emission constraint on key O_3 precursors to advance O_3 pollution research and management. These findings serve as a scientific basis for formulating more effective O_3 air quality control policies in China to confront the persistent challenges of surface O_3 pollution in a changing climate.

THE NOVELTY OF THIS STUDY

Surface ozone (O_3) pollution remains a persistent global environmental challenge due to its complex chemistry, adverse effects, and intrinsic connection to the climate system. Driven by rapid industrialization and urbanization, China has faced a dilemma of worsening O_3 pollution for years, particularly during warm seasons. While extensive research has investigated O_3 pollution and its mitigation strategies from local to national scales, studies characterizing nationwide O_3 concentrations and variations have been limited, and O_3 pollution in China has not been comprehensively addressed within a global context. This study is **the first effort** to integrate recent O_3 measurements from China and 47 other countries, thoroughly examining warm-season O_3 levels, pollution episodes, and trends across China and worldwide over the past decade. Furthermore, the current and emerging challenges of O_3 pollution control in China and other countries under a changing climate are **innovatively** identified, supporting future O_3 air quality management strategies to confront this global threat.

The transport of O_3 and its precursors plays a critical role in regional O_3 pollution, especially over South China, where polluted air from central and northern China is frequently received under northerly winds, resulting in high O_3 levels typically in autumn. Although the formation mechanisms of autumn O_3 pollution in South China are well understood and the pollution has been partially alleviated, the causes of the increasingly severe O_3 pollution in summer when southerly winds prevail have rarely been explored. This study is **the first** to elucidate the physical and chemical processes driving summer O_3 buildup across South China. Moreover, the contributions of transboundary transport of both O_3 and its precursors from upwind Southeast Asia under the influence of the summer monsoon are quantified for **the first time**.

In addition, a clear understanding of the emission characteristics of O_3 precursors is crucial for O_3 pollution research and management. Despite numerous bottom-up and top-down efforts to create accurate VOC emission inventories, current anthropogenic VOC emission inventories are still subject to large uncertainties, owing to rapid spatiotemporal variations in human activities and the diversity of VOC species. This study developed an **innovative** observational constraint method to refine VOC emission estimates. It also represents **a new attempt** to incorporate concurrent VOC measurements with a chemical transport model, which significantly improves simulations of both VOCs and O_3. This advancement enables a more robust study of O_3 pollution under varying emission conditions and is adaptive for future studies.

PUBLICATIONS

1. **Zhou, B.**, Guo, H.*, Zeren, Y., Wang, Y., Lyu, X., Wang, B., & Wang, H. (2023). An Observational Constraint of VOC Emissions for Air Quality Modeling Study in the Pearl River Delta Region. *Journal of Geophysical Research: Atmospheres*, 128(11), e2022JD038122.

2. **Zhou, B.**, Zeren, Y., Guo, H.*, & Lyu, X.* (2025). Summer Ozone Pollution Episodes in South China and Transport Impacts from Southeast Asia. *Environmental Science & Technology*. (Accepted)

3. Xiong, E., Guo H.*, Fu T.*, Lyu X., Wang Y., **Zhou B.**, Xia M., Zou Z., Yuan Q., Yang J., Shek K., Chen J., Tao W., Zhang A., Lee S., & Wang, T. (2025). Complex impacts of oxygenated volatile organic compounds on radical photochemistry in the background air of Southern China. *Environmental Science and Ecotechnology*. (Accepted)

4. Li, H., Lyu, X.*, Xue, L.*, Huo, Y., Chen, T., Yao, D., Lu, H., **Zhou, B.**, & Guo, H.* (2025). Hydroxyl Dicarboxylic Acids at a Mountainous Site in Hong Kong: Formation Mechanisms and Implications for Particle Growth. *ACS Environmental Au*, 5(3), 277-286.

5. Yang, J., Zeren, Y., Guo, H.*, Wang, Y.*, Lyu, X., **Zhou, B.**, Gao, H., Yao, D., Wang, Z., Zhao, S., Li, J., & Zhang, G. (2024). Wintertime Ozone Surges: The Critical Role of Alkene Ozonolysis. *Environmental Science and Ecotechnology*, 22, 100477.

6. Huo, Y., Lyu, X.*, Yao, D., **Zhou, B.**, Yuan, Q., Lee, S. C., & Guo, H.* (2024). Exploring the Formation of High Levels of Hydroxyl Dicarboxylic Acids at an Urban Background Site in South China. *Journal of Geophysical Research: Atmospheres*, 129(6), e2023JD040096.

7. Lyu, X., Li, K., Guo, H.*, Morawska, L.*, **Zhou, B.**, Yangzong, Z., Jiang, F., Chen, C., Goldstein, A. H., Xu, X., Wang, T., Lu, X., Zhu, T., Querol, X., Chatani, S., Latif, M. T., Schuch, D., Sinha, V., Kumar, P., Mullins, B., Seguel, R., Shao, M., Xue, L., Wang, N., Chen, J., Gao, J., Chai, F., Simpson, I., Sinha, B., & Blake, D. R. (2023). A Synergistic Ozone-Climate Control to Address Emerging Ozone Pollution Challenges. *One Earth*, 6(8), 964-977.

8. Zeng, L., Li, K., Guo, H.*, **Zhou, B.**, Lyu, X., Huo, Y., Uhde, E., Yang, J., Zeren, Y., Lu, H., Yao, D., & Qian, Z. (2023). Contributions of Indoor Household Activities to Inhalation Health Risks Induced by Gaseous Air Pollutants in Hong Kong Home. *Aerosol and Air Quality Research*, 23(9), 230063.

9. Lyu, X., Guo, H.*, Zou, Q., Li, K., Xiong, E., **Zhou, B.**, Guo, P., Jiang, F., & Tian, X.* (2022). Evidence for Reducing Volatile Organic Compounds to Improve Air Quality from Concurrent Observations and In Situ Simulations at 10 Stations in Eastern China. *Environmental Science & Technology*, 56(22), 15356-15364.

10. Zeren, Y., **Zhou, B.**, Zheng, Y., Jiang, F., Lyu, X., Xue, L., Wang, H., Liu, X., & Guo, H.* (2022). Does Ozone Pollution Share the Same Formation Mechanisms in the Bay Areas of China? *Environmental Science & Technology*, 56(20), 14326-14337.

11. Zeren, Y., Guo, H.*, Lyu, X., **Zhou, B.**, Liu, X., Yang, L., Yuan, Z., & Wang, Y. (2022). Remarkable Spring Increase Overwhelmed Hard-earned Autumn Decrease in Ozone Pollution from 2005 to 2017 at a Suburban Site in Hong Kong, South China. *Science of The Total Environment*, 831, 154788.

12. Zeng, L., Guo, H.*, Lyu, X., **Zhou, B.**, Ling, Z., Simpson, I. J., Meinardi, S., Barletta, B., & Blake, D. R. (2021). Long-term Variations of C_1–C_5 Alkyl Nitrates and Their Sources in Hong Kong. *Environmental Pollution*, 270, 116285.

13. Lyu, X., Guo, H., Wang, Y., Zhang, F., Nie, K., Dang, J., Liang, Z., Dong, S., Zeren, Y., **Zhou, B.**, Gao, W., Zhao, S., & Zhang, G*. (2020). Hazardous Volatile Organic Compounds in Ambient Air of China. *Chemosphere*, 246, 125731.

ACKNOWLEDGEMENTS

The years of my PhD study have been filled with adventures and stories, making them some of the most memorable experiences of my life. Throughout this journey, I have been fortunate to receive guidance, support, and encouragement from many people, for which I am deeply grateful.

First and foremost, I would like to express my heartfelt appreciation to my supervisor, Prof. Hai Guo, for his invaluable guidance and constant support over the years. His patience in teaching, insightful advice, and selfless provision of resources have been instrumental in my research and personal growth. Prof. Guo's passion, wisdom, and rigorous approach to research have greatly inspired me and will continue to influence me in the future.

I am also sincerely grateful to all the teachers and collaborators who have taught and guided me along the way. Special thanks go to Prof. Boguang Wang, Prof. Jun Li, Prof. Hongli Wang, Prof. Fei Jiang, and Prof. Ke Li for providing valuable data, analytical methods, and suggestions for my research. I am thankful to Prof. Tao Wang, Prof. Xiangdong Li, Prof. Shun-Cheng Lee, and Prof. Ling Jin from our department for their advice and inspiration, as well as to all the supporting staff for their patient assistance. In memory of my undergraduate mentor, Prof. Jun Zhao, I am forever grateful for his guidance and encouragement, which set me on this path.

My sincere thanks also go to all members of our research group for their suggestions and help. Special appreciation goes to Dr. Xiaopu Lyu, who has motivated my scientific thinking and problem-solving skills, provided valuable suggestions, and offered great encouragement throughout my PhD journey. I am also grateful to Dr. Yu Wang, Dr. Lewei Zeng, Dr. Xufei Liu, Dr. Haoxian Lu, Dr. Yangzong Zeren, Dr. Dawen Yao, Dr. Jingcui Xu, Dr. Cunteng Wang, Dr.

Pei Zeng, Dr. Chenchao Zhan, Dr. Yunxi Huo, Ms Jin Yang, Mr Enyu Xiong, and Ms Luyao Zhang for their assistance in my research and support in daily life.

This work was supported by the National Key R&D Program of China (2017YFC0212001), the Research Grants Council of the Hong Kong Special Administrative Region via the General Research Fund (PolyU15212421 and HKBU15219621), the NSFC/RGC Joint Research Scheme (N_PolyU530/20), the Theme-based Research Scheme (T24-504/17-N), and the Research Support Scheme of The Research Institute for Land and Space at The Hong Kong Polytechnic University (1-CD79 and 1-CDLJ).

Friends are like stars; you don't always see them, but you know they are always there. I am deeply thankful to my dear friends for their steadfast support and love. Special thanks to Ms Xinyue Chen, Dr. Siyi Chen, Ms Yunhe Du, Ms Xiaoying Kuang, and Ms Yue Zhao, who stood by me through every high and low. I also wish to thank Ms Ziqi Xu, Ms Kexin Chen, Ms Yuying Zhong, Ms Chunyu Zhao, Ms Shengjun Xi, Ms Yongyi Zhou, and Dr. Zhancong Liang for their constant care and continuous encouragement. I also want to express my special appreciation to Mr Ziyi Ye and his family for their love and support.

Most importantly, I dedicate this thesis to my family. Especially to my parents, who have loved me unconditionally and always had faith in me. They are my role models, and I have learned so much from them. Thank you for everything. I am also grateful to my grandparents, aunties, uncles, and cousins for giving me endless confidence and courage to face the challenges of life. In memory of my beloved grandpas, I will always love you.

TABLE OF CONTENTS

Chapter 1 Introduction

1.1 Research background

Tropospheric ozone (O_3), a major secondary air pollutant, is formed through complex photochemical reactions among its precursors, including nitrogen oxides (NO_x), volatile organic compounds (VOCs), and carbon monoxide (CO), in the presence of sunlight (Atkinson, 2000). As these O_3 precursors are primarily emitted within the planetary boundary layer, O_3 pollution is principally observed at ground level, which not only has adverse impacts on human health (Lippmann, 1991; Brauer et al., 2016), ecosystems (Mills et al., 2018), and the climate (Shindell et al., 2006; Gaudel et al., 2018), but also plays a crucial role in atmospheric chemistry (Thompson, 1992; Seinfeld & Pandis, 2006). With rapid industrialization and urbanization, surface O_3 pollution has become an intricate and long-standing air quality problem, with the most severe pollution events typically occurring during warm seasons under high temperatures and intense solar radiation (Oltmans et al., 2004; Monks et al., 2015). In recent decades, surface O_3 pollution has worsened worldwide (Parrish et al., 2014; Gaudel et al., 2018; Tarasick et al., 2019). While developed countries, including the United States and those in Europe, have made significant progress in controlling O_3 levels through effective reductions in VOCs and NO_x emissions (Simon et al., 2015; Yan et al., 2018), many developing countries and regions, particularly China, continue to struggle with worsening O_3 pollution (Lu et al., 2025).

Due to the lack of ground-level observational data, studies on nationwide O_3 pollution in China were not available until the national air monitoring network was established in 2013. Since then, a handful of studies have examined the concentrations and variations of O_3 across China, reporting a significant upsurge of O_3 since 2013, primarily driven by decreasing levels of NO_x and fine

particulate matter ($PM_{2.5}$) (Li et al., 2017b; Lu et al., 2018b; Liu & Wang, 2020b; Lu et al., 2020). However, this increasing trend has not been analyzed within the same time frame and in a global context, despite preliminary efforts to compare it to trends in other countries. By addressing China's O_3 pollution from a global perspective, the experiences and lessons learned from past O_3 pollution control in other developed countries can inform current and future O_3 air quality management. Meanwhile, although staged successes in controlling O_3 pollution, with peak O_3 levels gradually decreasing since the late 1990s, have been achieved in developed regions, such as the United States (Simon et al., 2015) and Europe (Yan et al., 2018), recent elevations in background O_3 concentrations and urban exposures (Parrish & Ennis, 2019; Sicard et al., 2021a) underscore the urgency of identifying the emerging and global challenges to O_3 pollution control. Therefore, a comprehensive analysis of ground-level O_3 measurements worldwide is needed to examine the current status of O_3 pollution in China and worldwide, and to recognize the emerging challenges for O_3 air quality management globally.

In addition to the primary attribution from domestic emissions, transboundary transport of O_3 and its precursors from upwind source regions also contributes to the worsening O_3 pollution in China (Liu & Wang, 2020a). During warm seasons, the East Asian Summer Monsoon system dominates over China, bringing clean, moist marine air to South China and resulting in relatively low O_3 levels over this region (He et al., 2008; Zhao et al., 2010). However, recent studies have reported elevated summer and late-spring O_3 concentrations in South China, which are increasingly linked to the summer monsoon through changes in meteorological conditions and transboundary transport (Zhou et al., 2022; Zhang et al., 2024b). Wang et al. (2019b) further highlighted a concerning rise in O_3 within marine air masses transported to South China during summer, likely driven by enhanced anthropogenic emissions in upwind Southeast Asia. In fact,

rapidly growing emissions in Southeast Asia since the 2010s (Chen & Mauzerall, 2021; Cui et al., 2022) have led to a significant rise in local O_3 levels in these regions (Wang et al., 2022d), yet their regional impacts, especially on downwind South China, remain unclear. To address this knowledge gap, a detailed investigation of the physical and chemical processes contributing to summer O_3 buildup in South China is necessary to explore and quantify the contributions and transport pathways of O_3 and its precursors from Southeast Asia as influenced by the summer monsoon.

As O_3 is a secondary pollutant, a clear understanding of its precursors is critical for addressing O_3 pollution. VOCs, comprising hundreds of species, are key precursors to O_3. They are emitted from a wide variety of anthropogenic activities and natural sources, with distinctive local characteristics that vary among regions and cities (Guo et al., 2017), making emission quantification necessary yet challenging. Although VOC emission inventories have been established and widely applied in modeling studies of O_3 in China (Zheng et al., 2018; Geng et al., 2024), these bottom-up emission estimates were subject to large uncertainties due to limitations in measurements of emission factors, quantifications of activity levels, spatiotemporal allocations, and VOC speciation (Li et al., 2017b). Consequently, these uncertainties introduced biases when input to models, affecting not only the simulated VOCs (Chutia et al., 2019; Shen et al., 2019) but also their secondary products, particularly O_3 (Bouarar et al., 2019; Guo et al., 2019; Qu et al., 2020). To better simulate the spatiotemporal variations of both VOCs and O_3, top-down approaches using observed data have been developed to estimate VOC emissions (Li et al., 2021a). However, most top-down constraints relied on satellite observations, which are available for only two VOC species (Fu et al., 2007; Liu et al., 2012; Chaliyakunnel et al., 2019), while those using field measurement data have been limited by low spatial coverage (Chen et al., 2010; Kim et al.,

2011; Wang et al., 2020). Moreover, due to the lack of concurrent VOC measurements, observational constraints of VOC emissions using measured data have been scarce in China, even as local anthropogenic VOC emissions have changed rapidly under fast development and stringent control strategies. Therefore, an adaptive method and concurrently measured VOC data are indispensable for better representing local VOC emissions and improving O_3 pollution studies in China.

Overall, motivated by the knowledge gaps and limitations stated above, this thesis examines the current status and challenges of O_3 pollution in China from a global perspective, investigates the regional impacts of pollutants transported from upwind Southeast Asia on summer O_3 pollution in South China, and develops an observational constraint on local anthropogenic VOC emissions in the highly urbanized Pearl River Delta (PRD) region of South China. The global overview of O_3 levels and trends reveals the spatial disparity of O_3 pollution characteristics across different regions, with East and Southeast Asia exhibiting the highest levels. Thus, linking global O_3 characteristics to regional dynamics in South China and Southeast Asia provides essential context for understanding how transboundary transport exacerbates local pollution episodes. Furthermore, through the observational constraint on O_3 precursors' emissions at the city scale, the local contributions to O_3 pollution can be better quantified. Therefore, by a multi-scale perspective, this thesis highlights the need for differentiated yet coordinated actions across scales, advocating local anthropogenic emission controls to alleviate locally formed O_3, cross-regional efforts to mitigate transport effects, and integrated climate and air pollution policies for synergetic O_3 management worldwide.

1.2 Research objectives

This thesis aims to enhance our understanding of warm-season O_3 pollution in China from global, regional, and local perspectives. The objectives of this study are as follows:

1. To comprehensively evaluate the current status of O_3 pollution in China and worldwide, and to identify emerging challenges in global O_3 pollution control.
2. To elucidate the buildup mechanisms of summer O_3 pollution in South China, and to quantify the regional impacts of monsoon-driven transboundary transport of pollutants from upwind Southeast Asia.
3. To develop and apply an observational constraint on local VOC emissions in the PRD region, and to enhance the robustness of VOCs and O_3 model simulations.

This work addresses the emerging challenges hindering effective control of worsening O_3 pollution in China within a global context. It also deciphers the pathways and contributions of regionally transported pollutants to O_3 pollution in South China, demonstrating that international collaboration is essential for effective O_3 mitigation. In addition, this study develops a novel and adaptive approach to refine local and short-term VOC emission estimates, further strengthening O_3 modeling studies and policy assessment. The outcomes of this work provide feasible scientific support for further research into O_3 pollution at local, regional, and global scales, and guide policymakers in formulating effective O_3 air quality management strategies to confront this long-standing global challenge.

1.3 Thesis outline

This thesis consists of seven chapters: *Introduction*, *Literature Review*, *Methodology*, three chapters of results and discussion (*Chapters 4-6*), and a closing chapter of *Conclusions and Suggestions for Future Study*.

Chapter 1 (*Introduction*) introduces the research background of O_3 pollution in China and identifies the knowledge gaps in existing research. It highlights the motivations and objectives of this study.

Chapter 2 (*Literature Review*) reviews previous studies on surface O_3 pollution across global, national, and regional scales. The O_3-precursor relationship, the past and present-day emissions of O_3 precursors, and the development of emission inventories are also reviewed.

Chapter 3 (*Methodology*) describes the data sources, field measurements, and chemical analysis techniques used for observational data. It also summarizes the configurations, input data, and statistical evaluations of the chemical transport model (WRF-CMAQ). In addition, this chapter details the newly developed method for the observational constraint of VOC emissions.

Chapter 4 (*The Long-standing Global Threat of Surface Ozone*) examines warm-season O_3 pollution in China and worldwide, using extensive global measurement data. It further identifies the emerging challenges in global O_3 pollution control.

Chapter 5 (*Summer Ozone Pollution Episodes in South China and Transport Impacts from Southeast Asia*) investigates the driving factors behind the worsening summer O_3 pollution in South China and quantifies the contributions of transboundary transport from upwind Southeast Asia under the influence of the summer monsoon.

Chapter 6 (*An Observational Constraint of VOC Emissions for Air Quality Modeling Study in the Pearl River Delta Region*) develops and applies a novel approach to refine local VOC emissions based on concurrent field measurements in the PRD region. It further evaluates the model's performance in simulating both VOCs and O_3.

Chapter 7 (*Conclusions and Suggestions for Future Study*) summarizes the key findings and implications of this thesis. It also provides recommendations for future research.

Chapter 2 Literature Review

2.1 Surface O_3 pollution

Ozone (O_3) is a critical trace gas in the atmosphere. In the stratosphere, the ozone layer absorbs most of the ultraviolet radiation from the sun and protects the living beings on Earth. In contrast, O_3 in the troposphere directly contributes to global warming, which ranks as the third most significant greenhouse gas following carbon dioxide (CO_2) and methane (CH_4) (Myhre et al., 2013). It is also a key component of photochemical smog, posing detrimental effects on not only human and animal health (Lippmann, 1989; WHO, 2013), but also on vegetation and natural ecosystems (Fuhrer & Booker, 2003; Karnosky et al., 2007). More importantly, formed as a secondary air pollutant through photochemical reactions involving volatile organic compounds (VOCs) and nitrogen oxides (NO_x = nitric oxide [NO] + nitrogen dioxide [NO_2]) in the presence of sunlight (Haagen-Smit et al., 1953), surface O_3 acts as a chemically active oxidant with broad influences on atmospheric oxidative capacity, chemical lifetimes, and multiphase reactions (Thompson, 1992; Enami et al., 2008). Ever since the industrial revolution, the tropospheric O_3 burden has nearly doubled that in the pre-industrial era (Young et al., 2013), particularly in the mid-latitude regions of the Northern Hemisphere, driven by rapid increases of anthropogenic emissions of O_3 precursors (Parrish et al., 2014). Moreover, the climate penalty of increasing O_3 was predicted to intensify over polluted regions under future global warming (Zanis et al., 2022). Therefore, investigations on surface O_3 pollution and their underlying causes from global to regional scales have been conducted in the past decades. In this section, past and present-day studies on O_3 pollution and its long-term variations around the world and in China, especially in South China, will be reviewed.

2.1.1 Global O_3 pollution

The first photochemical smog was reported in Los Angeles in the 1940s (Haagen-Smit, 1952), which marked the beginning of O_3 pollution investigations. Since then, surface O_3 has been monitored and reported in fast-developing regions, such as North America and Europe (Stasiuk Jr & Coffey, 1974; Logan, 1985; Bojkov, 1986; Feister & Warmbt, 1987; Volz & Kley, 1988; Low et al., 1990). Meanwhile, research on the O_3 formation mechanism sprang up to combat the widespread O_3 increases resulting from the release of large quantities of NO_x and VOCs under rapid industrialization (Chameides & Walker, 1973; Fishman & Crutzen, 1978; Liu et al., 1987a). In response, the United States Environmental Protection Agency (US EPA) promulgated the National Ambient Air Quality Standards (NAAQS) for O_3 in 1979, followed by the enforcement of emission controls on major VOCs and NO_x sources in 1980 (Chock & Heuss, 1987). Likewise, the European Union initiated regulations on air pollutant emissions in the 1970s. Benefiting from these control measures, emissions of VOCs and NO_x have been effectively reduced across North America and Europe, thereby alleviating O_3 pollution. Specifically, since the 1990s, surface O_3 concentrations have significantly declined across the US, and the high O_3 pollution events in major cities have become less frequent (Lefohn et al., 2008; Lefohn et al., 2010; Simon et al., 2015). Similarly, the previously increasing O_3 levels in Europe (Staehelin et al., 1994) have leveled off in the 2000s (Logan et al., 2012) and even reversed to decrease in the early 2010s (Andersson et al., 2017; Yan et al., 2018). Nevertheless, recent studies revealed that repeated heatwaves in recent years have triggered regional-wide O_3 enhancements across Europe (Lin et al., 2020; Pope et al., 2023) and the western US (Chang et al., 2025). Moreover, emissions of VOCs from both biogenic and anthropogenic sources were found to be temperature-dependent, which could further exacerbate O_3 pollution under a warming climate (Pfannerstill et al., 2024; Qin et al., 2025). Thus,

the potential climate penalty may offset the hard-earned O_3 mitigation, underscoring coordinated efforts to control O_3 pollution and mitigate climate change.

Different from the substantially eased O_3 pollution in Europe and the US, this challenge remains severe in many other regions worldwide. Cooper et al. (2014) provided the first comprehensive overview of global tropospheric O_3, revealing a worldwide increase in tropospheric O_3 during the 20th century and a shift of heavily polluted regions to East Asia in the late 1990s. Indeed, surface O_3 levels have continued to rise in Japan and South Korea since the 1990s, despite the implementation of stringent measures to reduce VOCs and NO_x emissions (Akimoto et al., 2015; Vellingiri et al., 2015). Furthermore, the Tropospheric Ozone Assessment Report (TOAR), initiated in 2014 by the International Global Atmospheric Chemistry Project (IGAC), reported the highest O_3 levels and significant upward trends across South Korea, western Japan, northern India, Hong Kong, and China from 2000 to 2014 (Fleming et al., 2018; Gaudel et al., 2018; Mills et al., 2018). Meanwhile, although O_3 levels in the Southern Hemisphere were generally lower than those in the Northern Hemisphere, substantial O_3 increases were found over Australia, New Zealand, South Africa, and Antarctica during the same period (Gaudel et al., 2018). These observations underscore the clear regional patterns of surface O_3, with particularly concerning widespread high and increasing O_3 across East Asia since 2000.

However, a notable gap was left out in the full picture of global O_3 characteristics due to insufficient O_3 monitoring data in Asian countries, especially China. It was not until 2013 that China established nationwide O_3 monitoring. Years after that, Li et al. (2019a) first reported the high O_3 levels and rapid rises of O_3 in major city clusters in China during the summers of 2013 – 2017, while these O_3 increases further expanded to most parts of China and accelerated in 2013 – 2019 (Li et al., 2020; Lu et al., 2020). What is worse, recent research by Wang et al. (2024b)

revealed much faster O_3 increases in China with top O_3 levels than in other regions in the Northern Hemisphere from 2013 to 2022. It is noteworthy that these elevated O_3 levels in the East Asian continent can influence global O_3 concentrations through large-scale atmospheric circulations, making it an important contributor to tropospheric O_3 budgets (Lin et al., 2014; Lefohn et al., 2018). Hence, addressing O_3 pollution and its variations in a global context is imperative, with a special focus on China. Moreover, despite current emission control measures in East Asia, O_3 pollution is still worsening, urging more effective strategies that also account for climate factors in a changing climate.

2.1.2 Surface O_3 pollution in China

China has experienced severe O_3 pollution since its first report in 1979 (Chen et al., 1985), as a result of rapid urbanization and industrial development. Since then, O_3 pollution events have been frequently observed, causing deterioration of air quality across China in the 1990s (Luo et al., 2000; Cheung & Wang, 2001; Chan et al., 2003). In addition, limited long-term measurements of O_3 in China documented upward O_3 trends in the 2000s. For instance, Xu et al. (2008) found increases in daily maximum O_3 concentrations by 1.9%/yr – 2.7%/yr at a background station in eastern China (Lin'an) from 1991 to 2006, which was attributable to the increasing NO_x levels at 0.51 ppbv/yr during this period. Meanwhile, Wang et al. (2009) reported an overall O_3 rise of 0.58 ppbv/yr at a coastal background site (Hok Tsui) in southern China during 1994 – 2007 with an accelerated increasing rate of 0.87 ppbv/yr for the period of 2001 to 2007, strongly linked to the enhancement of anthropogenic emissions of O_3 precursors, especially NO_x, in the upwind mainland China. Later in 2003 – 2015, Ma et al. (2016) and Sun et al. (2016) revealed significant increases of O_3 at 1.13 ppbv/yr and 1.7 – 2.1 ppbv/yr in rural and mountainous areas of the North China Plain (NCP),

respectively, both of which suggested that the enhanced VOC emissions contributed to the observed O_3 increases.

In 2013, China promulgated the Action Plan on Prevention and Control of Air Pollution with a series of stringent emission reduction interventions (CSC, 2013). These efforts paid off as the concentrations of inhalable fine particulate matter ($PM_{2.5}$) declined rapidly from 2013 to 2017 across China (Zhang et al., 2019). However, nationwide O_3 concentrations were found to increase significantly in the meantime (Silver et al., 2018). Li et al. (2017a) reported widespread and persistent O_3 pollution across East China during the warm season of 2015, suggesting that emissions from industrial and transportation sources were the major contributors. Lu et al. (2018b) further uncovered that O_3 pollution was the most severe in China compared to that in the US, Europe, Japan, and South Korea, characterized by the much higher extreme O_3 levels, more frequent high O_3 episodes, and continuous rises in 2013 – 2017. While China's anthropogenic emissions decreased by 21% for NO_x and 33% for $PM_{2.5}$ from 2013 to 2017 under the Clean Air Actions, emissions of VOCs remained increasing by 11% from 2010 to 2017 (Zheng et al., 2018). Li et al. (2019a) then examined the anthropogenic drivers of this increasing O_3, especially in megacities like Beijing and Shanghai, which were mainly caused by the uncoordinated emission reductions of NO_x and VOCs, as NO_x emissions were considerably reduced in China, while VOC emissions changed little during this period. In addition, they pointed out that another important factor contributing to the elevated O_3 levels was the sharp decrease in $PM_{2.5}$ concentrations, which stimulated O_3 production by undermining the sink of hydroperoxyl (HO_2) radicals. Similarly, based on modeling studies, Liu and Wang (2020a & 2020b) gained a relatively comprehensive understanding of the complex drivers of worsening O_3 pollution in China that the implemented emission-control measures since 2013 have effectively mitigated O_3 pollution in rural areas,

whereas O_3 pollution aggravated over urban areas due to the nonlinear relationship between O_3 and its precursors as well as aerosol effects. Meanwhile, impacts of meteorological variations also played an important role in modulating O_3 levels across China. Later, Li et al. (2020) revealed that the serious O_3 pollution over China extended to 2019 with a more significant O_3 enhancement during 2018 – 2019 than in 2013 – 2017, resulting from not only the anthropogenic contributions of VOC emissions, but also meteorological variabilities.

In response to the severe O_3 pollution across China, the second phase of the Clean Air Actions was launched in 2018 with a specific emphasis on VOC emission reductions (CSC, 2018). During 2018 – 2020, the emissions of total VOCs in China were found to decrease by 2.6% per year, compared to a 1.1% per year increase during 2013 – 2017 (Geng et al., 2024). This coordinated control of NO_x and VOC emissions was partially effective, as the increasing rate of O_3 slowed down during 2017 – 2020, and the anthropogenic contributions to the rise of O_3 levels were reduced after 2017 (Liu et al., 2023). However, despite these efforts, O_3 concentrations continued to rise throughout these years, exhibiting distinct seasonal variations and spatial distributions. For example, although high O_3 pollution events generally occurred in warm seasons with favorable weather conditions, O_3 levels typically peaked during summer in North China and during autumn in South China (Wang et al., 2022c). More specifically, O_3 pollution hotspots lie in the densely populated city clusters, such as the Beijing-Tianjin-Hebei (BTH) region, the Yangtze River Delta (YRD) region, and the Pearl River Delta (PRD) region, where anthropogenic emissions are highly active (Xiao et al., 2022). Due to localized emission characteristics, distinct meteorological features, and unique geographical settings, the drivers of O_3 pollution vary across different regions, particularly under nationwide emission reductions. Therefore, it is necessary to elaborate on O_3 pollution at a regional scale.

2.1.3 Surface O_3 pollution in South China

As China grapples with O_3 pollution, one of the prominent O_3 hotspots is South China, where rapid urbanization has taken place since the late 1970s. This economic boost, accompanied by industrial growth, has led to substantial anthropogenic emissions of O_3 precursors, such as NO_x and VOCs. Meanwhile, the warm climate with intense sunlight provides favorable weather conditions for photochemical O_3 production, facilitating O_3 buildup in South China. The PRD region, a major economic hub in South China, has experienced particularly severe O_3 pollution over the past decades. Back in the 1990s, Kok et al. (1997) reported high O_3 levels in Hong Kong in 1994, attributing them to the mixed emissions from Hong Kong and upwind mainland China. Wang et al. (1998) also observed four high O_3 episodes at a coastal background site of South China with even higher O_3 levels than those in urban areas in 1994, which pointed out the significant impact of aged air masses transported from urban plumes on regional scales. Zhang et al. (1998) further recorded extremely high O_3 concentrations of 170 ppbv in Guangzhou during 1995. Unlike most parts of China, where O_3 peaks in summer, South China experiences its highest O_3 concentrations in autumn, while a notable trough of O_3 levels was found in summer associated with the Asian monsoon system (Chan et al., 1998). Thus, these severely high O_3 levels and their unique seasonal pattern in South China have drawn wide attention from researchers to investigate the underlying causes of this regional pollution challenge.

Previous studies have identified the key physical and chemical processes driving high O_3 concentrations in South China, particularly in autumn. Chan and Chan (2000) first uncovered that the winter monsoon and traveling cyclones were the most conducive to O_3 episodes in Hong Kong, due to the superimposed impacts of local emissions and O_3 formation, short-range transport of O_3 and other pollutants from the inland PRD region, and long-range transport of continental outflows.

Jiang et al. (2010) and Wu et al. (2013) examined the high O_3 episodes dominated by continental high-pressure systems in autumn, demonstrating that northerly synoptic winds transported O_3 and its precursors from upwind source regions, while persistently calm surface winds led to O_3 accumulation over South China. Meanwhile, the peripheral subsidence in the outskirts of typhoons also favored O_3 pollution by confining O_3 and its precursors within the shallow boundary layer above South China through vertical downdrafts and horizontal stagnation (Huang et al., 2005; Wei et al., 2016; Qu et al., 2021). Thus, continental anticyclones and tropical cyclones were the two major synoptic systems triggering high O_3 pollution events in South China, creating stable atmospheric conditions that restricted horizontal advection and vertical mixing of air pollutants, causing the accumulation of air pollutants in the region (Chen et al., 2022). Moreover, these synoptic systems often brought fine weather to South China with strong solar radiation, high temperatures, and low relative humidity, which stimulated intensive photochemical reactions and prompted local O_3 production (Wang et al., 2017a; Liu et al., 2021; Ouyang et al., 2022). In addition, outflows from the Asian continent were found to be another major contributor to high O_3 levels in South China, as they transported polluted and aged air masses, laden with O_3 and its precursors, from inland China to the southeastern coastal areas (Tang et al., 2007a; Ling et al., 2013; Wu et al., 2022). Beyond synoptic conditions and long-range transport, mesoscale circulations, including sea-land breezes, mountain-valley breezes, and urban heat island effects, also played crucial roles in modulating surface O_3 levels in South China. Ding et al. (2004) illustrated the evolution of O_3 in the PRD region under sea-land breeze circulations, revealing a secondary O_3 peak in the late afternoon caused by the recirculation of aged daytime O_3 plumes via onshore sea breezes. Later, Wang et al. (2018b) disclosed that sea breezes could exacerbate O_3 pollution in coastal cities of South China by recirculating high levels of O_3 formed over the sea as

a result of sufficient photochemical evolution and weak dry deposition on the water surface. Zeren et al. (2019) then concluded that the Pearl River estuary acted as an O_3 "pool" in South China, where O_3 and its precursors were trapped and underwent photochemical reactions over the estuary due to the interaction between synoptic wind fields and sea-land breeze circulations. This O_3 "pool" effect was also observed in other bay areas of China, leading to enhanced O_3 pollution in coastal regions (Zeren et al., 2022b). Li et al. (2016) further revealed that sea breezes were intensified by the convergence flow of urban heat island effects, which enhanced O_3 accumulation over the PRD region. Besides, Guo et al. (2013) demonstrated that with a unique landscape of mountainous and hilly terrain, mountain-valley breezes significantly redistributed air pollutants in Hong Kong, as valley breezes transport O_3 and its precursors from ground level to mountaintops, resulting in more severe O_3 pollution in mountainous regions than in urban areas.

While the buildup processes of high O_3 pollution in South China during autumn have been extensively examined, those in the other seasons remain relatively poorly understood. In fact, benefiting from stringent controls on anthropogenic emissions of O_3 precursors, the regional O_3 burden in autumn has been mitigated to some extent since 2013. Research has shown that the increasing O_3 trend of 0.11 ppbv/yr in the PRD region during autumn of 2006 – 2013 reversed to decline at -1.27 ppbv/yr in 2013 – 2017 (Liu et al., 2019). Similarly, Zeren et al. (2022a) revealed that the autumn O_3 variations leveled off, shifting from an increase of 0.67 ppbv/yr in 2005 – 2014 (Wang et al., 2017b) to a slight decrease of -0.21 ppbv/yr in 2005 – 2017, with a substantial drop at a rate of -2.0 ppbv/yr after 2013. Moreover, while long-term O_3 concentrations at a regional background site of South China have continued to rise since 1994, the rate of increase during autumn slowed from 0.68 ppbv/yr in 1994 – 2007 (Wang et al., 2009) to 0.40 ppbv/yr in 1994 – 2018 (Wang et al., 2019b). Strikingly, this background site recorded its highest-ever rise of

summer O_3 with a statistically significant growth rate of 0.50 ppbv/yr (Wang et al., 2019b). This summer O_3 increase has also been observed across the PRD region, as Li et al. (2020) and Lu et al. (2025) reported accelerated increasing rates of 1.10 ppbv/yr and 1.20 ppbv/yr during 2013 – 2019, compared to 0.60 ppbv/yr in 2013 – 2017 (Li et al., 2019a). This recent surge in summer O_3 pollution challenges the traditional view that summertime O_3 levels in South China were the lowest throughout the year due to the rainy season influenced by the East Asian Summer Monsoon (He et al., 2008; Zhao et al., 2010). Indeed, research has shown that the intensity and onset timing of the East Asian Summer Monsoon significantly affected O_3 concentrations in South China, with higher O_3 levels linked to stronger monsoon systems and earlier monsoon onset, which provided favorable weather conditions for O_3 formation and enhanced transboundary transport (Zhou et al., 2022; Zhang et al., 2024b). In addition, a few studies suggested that pollutants, including O_3 and its precursors, from upwind Southeast Asia, where emissions have grown in recent years, and marine shipping emissions could be transported alongside, contributing to the O_3 buildup over South China (Wang et al., 2019b; Xing et al., 2021; Qin et al., 2024). Furthermore, previous studies have identified the transport of springtime (March – April) biomass burning plumes from Southeast Asia to South China, which were uplifted and advected by the westerlies at high altitudes from 2 to 8 km, significantly elevating South China's O_3 levels in the free troposphere during pollution episodes (Fu et al., 2012). However, unlike the free tropospheric O_3 peak in spring, the summertime O_3 concentrations over South China were higher within the planetary boundary layer (Liao et al., 2021), indicating a distinct transport pattern in summer. Therefore, given the distinct dominant synoptic systems and O_3 characteristics in summer, these findings indicate that the physical and chemical drivers of summer O_3 pollution over South China differ from those in other seasons and are not fully understood. Further studies on the underlying causes of summertime O_3

pollution in South China, especially under the influence of the summer monsoon, and the potential contributions from Southeast Asian emissions are needed to effectively address the rising summer O_3 levels over South China.

2.2 O_3 precursors and their emission sources

Tropospheric O_3 is formed through complex photochemical reactions involving NO_x (NO + NO_2) and VOCs in the presence of sunlight (Haagen-Smit et al., 1953). The chemical mechanism of O_3 photochemistry is nonlinear, consisting of two major cycles, the "NO_x cycle" and the "RO_x cycle" (RO_x = hydroxyl radical [OH] + hydroperoxyl radical [HO_2] + organic peroxyl radical [RO_2]) (Figure 2.1). The "NO_x cycle" is a null cycle that produces O_3 without consuming NO_x, while the "RO_x cycle" generates peroxy radicals (HO_2 and RO_2), which prompt the "NO_x cycle" by oxidizing NO to NO_2 (Wang et al., 2017a).

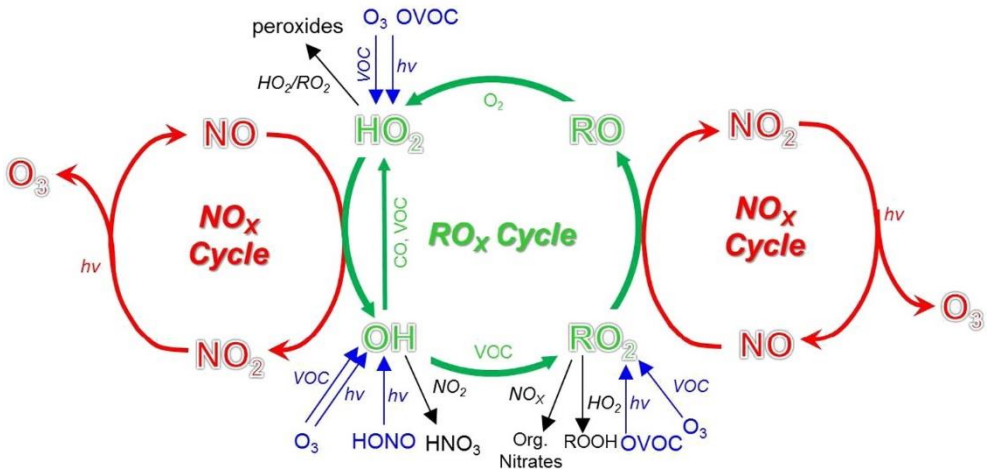

Figure 2.1. Sketch of the O_3 formation mechanism. "RO_x cycle" (photochemical radicals cycling, shown in green) and "NO_x cycle" (O_3 formation cycling, shown in red). The reaction pathways of radical initiation and termination processes are shown in blue and black (Wang et al., 2017a).

The principal reactions of O_3 formation can be summarized as the following reactions (R1-R8), where *hv* represents sunlight, and M is an energy-absorbing molecule (*e.g.*, N_2 or O_2) (Jacob, 1999; Wang et al., 2018c).

$$HO_2\cdot + NO \rightarrow NO_2 + OH\cdot \quad \text{(R1)}$$

$$O_3 + h\nu\ (\lambda < 320\ \text{nm}) \rightarrow O(^1D) + O_2 \quad \text{(R2)}$$

$$HONO + h\nu\ (\lambda < 320\ \text{nm}) \rightarrow OH\cdot + NO \quad \text{(R3)}$$

$$O_3 + \text{unsaturated VOCs} \rightarrow \text{carbonyls} + \text{Criegee intermediates} \quad \text{(R4)}$$

$$OH\cdot + O_3 \rightarrow HO_2\cdot + O_2 \quad \text{(R5)}$$

$$OH\cdot + VOCs + O_2 \rightarrow RO_2\cdot + H_2O \quad \text{(R6)}$$

$$OH\cdot + CO + O_2 + M \rightarrow HO_2\cdot + CO_2 + M \quad \text{(R7)}$$

$$OH\cdot + NO_2 + M \rightarrow HNO_3 + M \quad \text{(R8)}$$

$$OH\cdot + NO \rightarrow HONO \quad \text{(R9)}$$

$$RO_2\cdot + NO + H_2O \rightarrow HO_2\cdot + R'CHO + NO_2 \quad \text{(R10)}$$

$$HCHO + 2\ O_2 + h\nu\ (\lambda < 320\ \text{nm}) \rightarrow 2\ HO_2 + CO \quad \text{(R11)}$$

$$OH\cdot + HCHO + O_2 \rightarrow HO_2\cdot + H_2O + CO \quad \text{(R12)}$$

$$HO_2\cdot + O_3 \rightarrow OH\cdot + 2\ O_2 \quad \text{(R13)}$$

$$HO_2\cdot + HO_2\cdot \rightarrow HOOH + O_2 \quad \text{(R14)}$$

$$RO_2\cdot + HO_2\cdot \rightarrow ROOH + O_2 \quad \text{(R15)}$$

$$NO_2 + h\nu \rightarrow NO + O\ (^3P) \quad \text{(R16)}$$

$$O\ (^3P) + O_2 + M \rightarrow O_3 + M \quad \text{(R17)}$$

$$O_3 + NO \rightarrow NO_2 + O_2 \quad \text{(R18)}$$

These photochemical cycles are initiated by the degradation of VOCs and carbon monoxide (CO) through oxidation by the OH radical (R6 & R7) (Seinfeld & Pandis, 2006). The chain propagation reactions cycle the RO_x radicals (R1-R15), continuously supplying these radicals to stimulate photochemical reactions. The "RO_x cycle" oxidizes NO to NO_2 (R1 & R10), which then participates in the "NO_x cycle", where NO_2 is photolyzed to produce O_3 (R16-R17) and recycled through the titration of O_3 by NO (R18). During these chemical processes, primary air pollutants,

including NO_x, VOCs, and CO, serve as precursors of O_3, among which VOCs and NO_x are the key precursors, as CO is less reactive. As such, characterizing the sources of these key O_3 precursors and their contributions to O_3 production is crucial for managing O_3 pollution.

2.2.1 O_3-precursor relationship

A common feature of O_3 photochemistry is the nonlinear dependence of O_3 production on VOCs and NO_x. Depending on the relative levels of VOCs and NO_x, the NO_x/VOCs ratio typically indicates the dominance of either the "NO_x cycle" or the "RO_x cycle". These scenarios are primarily classified into three O_3 formation regimes: NO_x-limited, VOC-limited, and transitional regimes (Sillman, 1999; Jenkin & Clemitshaw, 2000). When the NO_x/VOC ratio is low, the "NO_x cycle" is less intense than the "RO_x cycle", making the "NO_x cycle" the limiting factor. Consequently, reducing NO_x concentrations can suppress O_3 production. On the other hand, in the VOC-limited regime, where the NO_x/VOCs ratio is high, O_3 formation is mainly limited by the intensity of the "RO_x cycle". Therefore, reducing VOC concentrations is more effective in limiting O_3 formation. The transitional regime is more complex because O_3 formation is sensitive to both NO_x and VOCs, meaning that a specific mix of NO_x and VOCs, along with meteorological factors, must be considered. Hence, it is necessary to identify O_3 formation regimes in different regions to formulate effective O_3 pollution control strategies, which target the critical precursor for emission reductions.

To determine O_3 formation regimes, a number of methods have been used to estimate the O_3-NO_x-VOC sensitivity, including the relative ratio of NO_x/VOC (Wolff & Korsog, 1992), observed indicators (such as O_3/NO_y, $HCHO/NO_y$, and H_2O_2/HNO_3) (Sillman, 1995), correlation analysis of O_3 with NO_x and VOCs (Martinez et al., 1983), and model analysis based on observations or emissions (Cardelino & Chameides, 1995). Based on these approaches, previous studies have

identified VOC-limited and NO_x-limited conditions in various regions with relative VOC-to-NO_x ratios. Typically, in urban areas, O_3 production is highly sensitive to VOCs, driven by intensive anthropogenic emissions, particularly from localized NO_x sources. This pattern has been demonstrated for major US cities (Sillman et al., 1997; Marr et al., 2002; Kleinman et al., 2005), Asian megacities (Guttikunda et al., 2005), and European urban agglomerations (Hammer et al., 2002; Spirig et al., 2002; Sillman et al., 2003). However, rural areas, characterized by relatively lower NO_x concentrations and elevated biogenic VOC emissions, are usually governed by the NO_x-limited regime (Liu et al., 1987b; Kleinman et al., 1994; Olszyna et al., 1994). Complementing these ground-based measurements and modeling studies, Martin et al. (2004) first applied the ratio of satellite-derived formaldehyde (HCHO) and tropospheric NO_2 columns to diagnose surface O_3 sensitivity across the Northern Hemisphere, revealing a predominant NO_x-sensitive regime throughout most continental regions, with exceptions in major urban centers such as Los Angeles and industrial areas of Germany.

While O_3 formation regimes have been broadly delineated in many regions, the sensitivity of O_3 to VOCs and NO_x is influenced by variations in meteorological conditions, biogenic emissions, anthropogenic activities, and other factors. For instance, a seasonal transition in O_3 photochemistry from NO_x-limited during warm seasons to VOC-limited in winter was observed across most parts of the US except for megacities, as a result of reduced solar radiation and biogenic emissions of VOCs, notably isoprene (Jacob et al., 1995; Zhang et al., 2009b). Similar seasonal dynamics were found in China, where the O_3 formation regime shifted from NO_x-limited in summer to VOC-limited in winter, though major city clusters maintained VOC-limited conditions throughout the entire year (Liu et al., 2010; Jin & Holloway, 2015; Sun et al., 2018b). Furthermore, O_3 production in urban areas is closely tied to anthropogenic emissions of its precursors. In particular, daily

variations in NO_x emissions, primarily from vehicle exhausts, have led to elevated O_3 levels on weekends in VOC-sensitive urban areas due to significantly reduced NO_x emissions (Jenkin et al., 2002; Heuss et al., 2003; Tang et al., 2008). Studies also indicated that diurnal fluctuations in VOCs and NO_x emissions, along with photochemical consumption of precursors, could cause a shift from VOC-limited to NO_x-limited regimes between morning and afternoon in certain cities (Zou et al., 2015; Wang et al., 2016; Xie et al., 2023). Additionally, nighttime O_3 concentrations in both urban and rural environments are determined by NO_x levels, as NO titrates O_3 (R18) in the absence of NO_2 photolysis that regenerates O_3 (R16-R17), and NO_2 consumes O_3 to form nitrate radical (NO_3) (Brown & Stutz, 2012). More importantly, the implementation of extensive emission reduction policies across countries over recent decades has modulated the relative abundances of VOCs and NO_x, thereby reshaping O_3 formation regimes over time. Recent studies have revealed that the NO_x-limited regime has expanded among US cities from the 1990s to 2016, primarily due to substantial reductions in NO_x emissions during this period (He et al., 2020; Jin et al., 2020; Koplitz et al., 2022). Similarly, transitions have been reported in China, where the O_3 formation regime has shifted from VOC-limited to transitional in major city clusters (Jin & Holloway, 2015), and have even led to NO_x-limited regime under uncoordinated NO_x and VOCs emission reductions since 2013 (Li et al., 2021b; Ren et al., 2022; Zhu et al., 2023). Long-term satellite observations further confirmed a continuing trend towards NO_x-sensitive conditions around cities throughout the Northern Hemisphere from 2005 to 2021 (Johnson et al., 2024).

Overall, the nonlinear and ever-changing O_3-percursor relationship underscores its regional variability. Therefore, precise regulations on NO_x and VOCs emissions that account for local O_3 formation regimes are essential for effective O_3 pollution control (Lu et al., 2019a).

2.2.2 Sources of O_3 precursors

Ambient NO_x and VOCs are emitted from a wide variety of sources. In nature, surface NO_x is mainly emitted from lightning (Tie et al., 2002; Nault et al., 2017) and fertilized soils (Oikawa et al., 2015; Lu et al., 2021). Wildfires are a significant source of NO_x and VOCs (Urbanski et al., 2008; Simpson et al., 2011; Permar et al., 2021; Gkatzelis et al., 2024), contributing to O_3 production not only within fire plumes but also in downwind urban regions (Jaffe & Wigder, 2012; Xu et al., 2021; Jin et al., 2023). Additionally, biogenic VOCs, primarily emitted from vegetation, play a critical role in O_3 chemistry due to their large quantity (Guenther et al., 1995; Guenther et al., 2006; Wang et al., 2024a) and high reactivity (Atkinson & Arey, 2003; Di Carlo et al., 2004). Nevertheless, in populated urban areas, anthropogenic emissions remain the dominant contributors to both NO_x and VOCs.

Fossil fuel combustion, particularly in power plants, on-road vehicles, and industrial processes, is the primary anthropogenic source of NO_x and VOCs (Friedrich & Obermeier, 1999). As illustrated in Figure 2.2 and Figure 2.3, road transport is the largest contributor to NO_x emissions, accounting for 35% and 25% of the total emissions in Europe (2022) and the US (2024), respectively, despite considerable reductions of 51% in Europe and 82% in the US of their emissions in 1990. Energy production, another major source sector, has substantially reduced its NO_x emissions by 78% in Europe and 89% in the US since 1990, contributing only 14% and 11% to total NO_x emissions in Europe (2022) and the US (2024), respectively (Henneman et al., 2021; EEA, 2024a). These significant emission reductions in the energy sector benefited from the implementation of advanced techniques, such as low-NO_x burners, NO_x scrubbers, and catalytic reduction systems, as well as improvements in energy efficiency and the adoption of clean energy (EEA, 2024b; USEPA, 2024b). For VOCs, although road transport was previously the dominant

source, its emissions have substantially declined by approximately 90% compared with 1990, contributing only 7% to current VOC emissions in both Europe and the US, thanks to stringent emission standards and advances in vehicle technologies (EEA, 2024c; Ferrarese et al., 2024; USEPA, 2025b). In contrast, industrial processes and solvent use remain the leading sources of VOCs over the past decades, with their relative contribution increasing to 41% in Europe (2022) and 54% in the US (2024) and continuing to rise (McDonald et al., 2018; Lewis et al., 2020; Gkatzelis et al., 2021). Additionally, emissions from other sources, such as residential heating, agriculture (mainly livestock waste and agricultural field burning), and marine vessels, also contribute to NO_x and VOCs in these countries, with their relative importance growing as vehicular and power plant emissions were effectively reduced (EEA, 2024b; USEPA, 2025a).

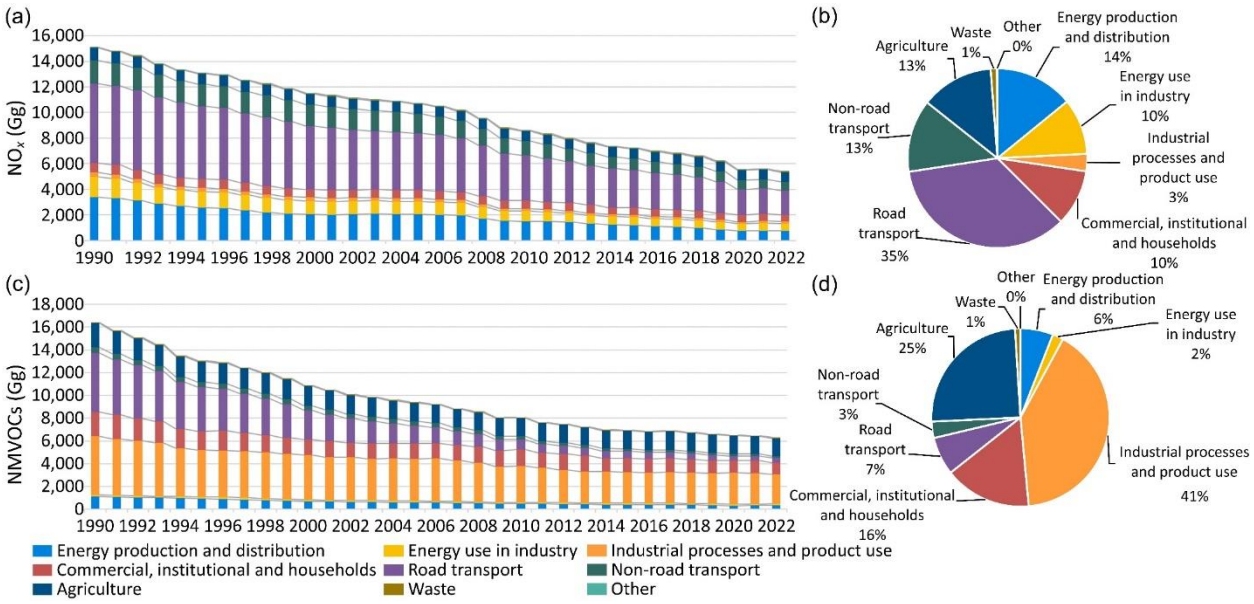

Figure 2.2. Sectoral emissions of NO_x (a-b) and VOCs (c-d) in the European Union. (a, c) Trends of emissions from 1990 to 2022. (b, d) Share of emissions by sector groups in 2022. Data obtained from the European Environment Agency (EEA, 2024b).

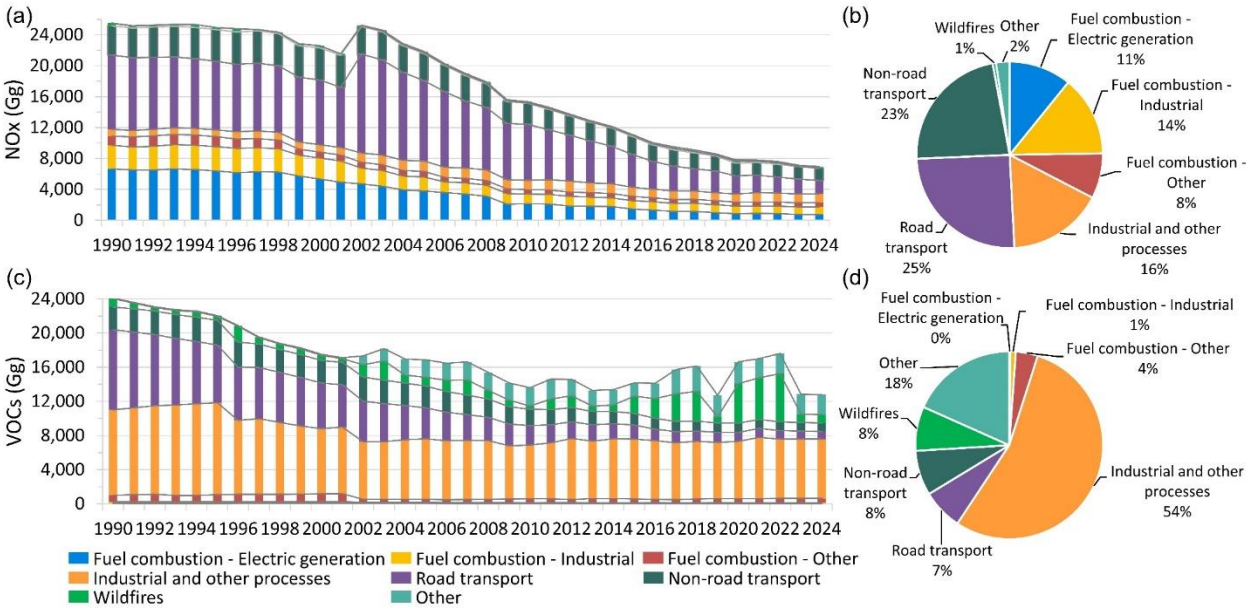

Figure 2.3. Sectoral emissions of NO_x (a-b) and VOCs (c-d) in the US. (a, c) Trends of emissions from 1990 to 2024. (b, d) Share of emissions by sector groups in 2024. Data obtained from the US Environmental Protection Agency (USEPA, 2025a).

In contrast to the substantial reductions in total anthropogenic NO_x and VOC emissions in Europe and the US since the 1990s, anthropogenic emissions in China increased markedly until 2013 (Figure 2.4), when the national Clean Air Action Plan was implemented (CSC, 2013). Sun et al. (2018a) reviewed the historical trends of anthropogenic NO_x and VOCs emissions, which grew rapidly since the 1980s, driven by the economic reform of China. NO_x emissions, primarily from fossil fuel combustion in power generation, industry, and residential sectors, increased consistently due to elevated energy consumption and were exacerbated by the delayed adoption of effective end-of-pipe control technologies across the country until 2010 (Zhao et al., 2013; Liu et al., 2015; Tong et al., 2018). Meanwhile, the expanding vehicle population resulted in a significant rise in on-road transport emissions, which accounted for 31% of the total NO_x emissions in 2013, despite early efforts to regulate vehicular emissions (Wu et al., 2016b; Zheng et al., 2018). Vehicular emissions of VOCs also increased from the 1990s onward, becoming the largest

contributor to VOC emissions by 2005 (Lang et al., 2014; Guo et al., 2017; Sun et al., 2018a). Moreover, emissions from industrial processes and solvent use grew sharply after 2000, making them the predominant sources of VOC emissions thereafter, contributing 25.6% and 24.9% of the total VOC emissions by 2012, respectively (Wu et al., 2016a; Li et al., 2021a). This surge in emissions led to severe air pollution across China in the early 2010s, urging systematic and nationwide emission reduction interventions.

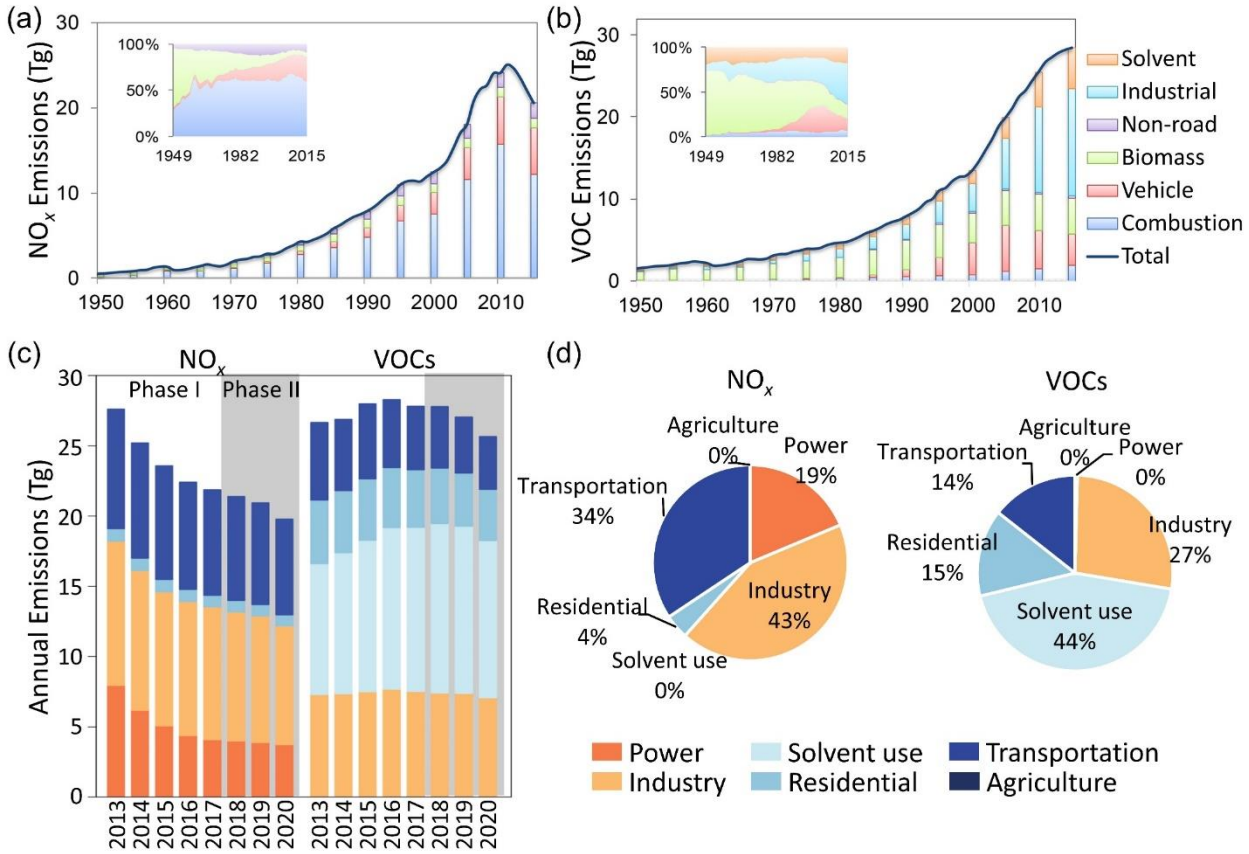

Figure 2.4. Sectoral emissions of NO_x and VOCs in China. (a-b) Historical trends of emissions from 1950 to 2015 (Sun et al., 2018a). (c) Emissions from 2013 – 2020 and share of sector groups in 2020. (d) Share of emissions by sector groups in 2020 (Geng et al., 2024).

In the past decade, China has committed to alleviating air pollution through the first nationwide Clean Air Action (Phase I: 2013 – 2017) (CSC, 2013), which successfully reduced NO_x emissions

by 21%, with emissions from power plants declining the most (by 47%) due to extensive installations of de-NO_x devices (Zheng et al., 2018). These significant NO_x reductions were further confirmed by satellite observations and ground-level measurements (Liu et al., 2016a; Liu et al., 2017a; Wang et al., 2019a; Jiang et al., 2022). However, VOC emissions increased by 4% during this period, with contributions from solvent use and industry rising by 26% and 3%, respectively, while emissions from transportation and residential sectors decreased by 18% and 9%, respectively (Li et al., 2019c; Li et al., 2021a; Geng et al., 2024). Subsequently, the second phase of the Clean Air Action was implemented in 2018, emphasizing VOC emission control. As a result, VOC emissions decreased gradually by 8% from 2018 to 2020, with solvent use being the dominant source (44%) (Geng et al., 2024). Meanwhile, NO_x emissions continued to decline until 2022, while industrial combustion and on-road transport remained their major contributors (Li et al., 2024).

Furthermore, as these traditional anthropogenic emission sources have been effectively controlled, other sources of NO_x and VOCs have emerged in recent years. For instance, biogenic VOC emissions from not only rural forests but also urban greening have gained prominence in O_3 formation in major cities, particularly under high temperature conditions (Gu et al., 2021; Wang et al., 2022b; Maison et al., 2024; Pfannerstill et al., 2024). Moreover, volatile chemical products, including paints, coatings, personal care products, and cleaning agents, have become significant sources of VOCs in urban environments, contributing to elevated O_3 levels and exhibiting a positive correlation with temperature (McDonald et al., 2018; Coggon et al., 2021; Qin et al., 2021; Seltzer et al., 2022; Askari & Chan, 2024; Wang et al., 2024c; Qin et al., 2025). Enhanced emissions of NO_x and VOCs from shipping activities have also been reported following the transition from high- to low-sulfur fuels, with VOC emissions increasing by 90% in 2020

compared to 2016, thereby exacerbating O_3 pollution in coastal regions (Wu et al., 2020; Luo et al., 2024; Zheng et al., 2024). Therefore, in the context of the persistent global challenge of O_3 pollution, these emerging sources of NO_x and VOCs should be carefully considered in air quality management strategies.

2.2.3 Emission inventories of O_3 precursors

Emission inventories, which comprehensively catalog the quantities of various air pollutants emitted by specific sources over a defined period, are essential tools for identifying and quantifying major emission sources in different areas, thereby aiding in air pollution control and management. These inventories are also fundamental inputs for atmospheric and climate models used to research the physical and chemical evolution of air pollutants. For natural sources, emission inventories are primarily established based on regularly updated observations with high spatial coverage. For example, biogenic emission inventories for vegetation and soils are generated using satellite-derived land cover and vegetation data, alongside meteorological parameters and carbon dioxide concentrations from weather models driven by assimilated observational data (Guenther et al., 2012; Bash et al., 2016; USEPA, 2023). Similarly, fire emissions are estimated from satellite-based observations that not only detect active fire locations, timing, and burned areas, but also characterize fuel loadings based on land cover and vegetation density (Wiedinmyer et al., 2011; van der Werf et al., 2017; Wiedinmyer et al., 2023). In contrast, anthropogenic emissions are impractical to observe or measure comprehensively and continuously due to their complexity and dynamic nature. Therefore, these emissions are commonly estimated using the bottom-up approach, which combines the intensity of activities (activity rates) with coefficients of the quantities of pollutants emitted per unit of activity (emission factors) (EEA, 2023; USEPA, 2024a).

Activity rates are typically obtained from statistical data recorded in yearbooks and surveys, including energy consumption in power plants and residential sectors (Zhang et al., 2009a; Zheng et al., 2009b; Liu et al., 2015), industrial product yields (Wei et al., 2008; Mo et al., 2021), and traffic flow density and vehicle population (Liu et al., 2011; Zheng et al., 2014; Wu et al., 2017). However, significant discrepancies have been identified when the emissions are estimated using different national statistical datasets in China (Guan et al., 2012). Hong et al. (2017) further reported uncertainties of 16% for NO_x emissions and 7.7% for VOC emissions when calculations were based on provincial and national statistics. Despite recent efforts to enhance the representativeness of activity data through field surveys and data mining, these studies are often limited to specific regions and sources, such as power plants (Tang et al., 2020; Gu et al., 2022), large industrial factories (Liu et al., 2020; Cheng et al., 2024), and vehicles (Liu et al., 2017b; Liu et al., 2018; Jiang et al., 2021). In addition, although large numbers of real-world emission factors for local sources have been measured in China over the past decade (Yang et al., 2021a; Wang et al., 2022a; Bai et al., 2023; Wang et al., 2023), most emission factors used in estimations are still sourced from international databases (EEA, 2023; USEPA, 2025c), national guidelines (MEE, 2024), and previous literature, particularly for comprehensive regional or national-scale emission inventories (Simayi et al., 2019; Liang et al., 2020; An et al., 2021; Huang et al., 2021; Li et al., 2023). These non-local and generic emission factors are insufficient to capture the actual emission characteristics of various sources under rapidly changing conditions, thereby introducing significant uncertainties into emission inventories (Li et al., 2017b).

Furthermore, for applications in air quality modeling, emission inventories must be spatially gridded and temporally resolved to an hourly resolution. These spatiotemporal allocations are primarily based on linear proxies derived from sectoral information, such as the locations of point

sources (Liu et al., 2015; Zhou et al., 2017), trajectories of mobile sources (Zheng et al., 2014), population density (Zhang et al., 2009a; Kurokawa et al., 2013), and economic data (Zhong et al., 2018; Mo et al., 2021), which are shared within the same source categories and among species. Previous studies have revealed that these empirical proxies tend to overestimate urban emissions (Geng et al., 2017; Wu et al., 2021a; Zheng et al., 2021a; Wu et al., 2024), introducing biases of 3% – 13% in simulated concentrations. These biases are further exacerbated as the grid spacing is reduced, with additional biases of 8% – 73% due to the decoupling of emission facilities in suburban areas (Zheng et al., 2017). Moreover, the speciation of VOCs into model-configured species represents another source of uncertainty in emission inventories, with underestimations of up to 30% due to missing species-specific source profiles, especially for oxygenated VOCs (Li et al., 2014; Mo et al., 2016). Thus, despite numerous efforts to refine emission inventories, biases persist, which can propagate into model simulations.

To enhance air quality model simulations, top-down approaches using observational data have been developed to constrain model emission inputs. Leue et al. (2001) first derived global NO_x emissions from satellite-observed NO_2 columns, while Fu et al. (2007) estimated regional total VOC emissions from satellite measurements of formaldehyde columns. With advances in satellite observation products, studies have shown that such satellite constraints improve model simulations of not only the constrained NO_x but also its secondary product, O_3, capturing previously missed hotspots and peak concentrations for both species (Ghude et al., 2013; Visser et al., 2019; Yang et al., 2021b). Although many inversions used simplified methods with arbitrary indicator ratios between observed and prior simulated levels, these satellite-based methods provided a convenient and effective way to refine NO_x emission estimates and model performance. However, they offered only coarse constraints on total VOC emissions (Zhang et al., 2017; Chaliyakunnel et al., 2019)

because spaceborne observations were limited to two VOC species, *i.e.*, formaldehyde (HCHO) and glyoxal (CHOCHO). Consequently, satellite-based top-down VOC emission estimates remain uncertain owing to the diversity of VOC speciation and the complex atmospheric processes they undergo. To overcome these limitations, a few pioneering studies have used in-situ measurements to constrain VOC emissions, but these efforts have been limited by sparse spatial coverage and a narrow range of measured species (Chen et al., 2010; Hsu et al., 2010; Kim et al., 2011; Fang et al., 2016; Wang et al., 2020). Accurate quantification of VOC emissions, therefore, remains a significant gap and is often considered a major cause of model biases. Currently, top-down constraints based on concurrent measurements at multiple sites with high temporal resolution and covering a broader range of VOC species are needed to complement VOC emission estimates and improve model simulations of VOCs and their secondary products.

Chapter 3 Methodology

3.1 Observational data collection

3.1.1 Global and regional O_3 data

Hourly O_3 concentrations were commonly measured by ultraviolet photometric techniques, and the data quality control procedures primarily adhered to standards directed by the United States Environmental Protection Agency (US EPA) (USEPA, 2017). To ensure data completeness, stringent screening criteria, based on the US EPA guidelines (USEPA, 1998b), were applied in this study. Specifically, a valid daily dataset for each station required at least 75% of hourly data within any 8 consecutive hours (referred to as 8-hour data), and no fewer than 12 valid 8-hour data points per day. Monthly data were included only if there were more than 20 valid daily data points in that month. Stations were deemed valid if their monthly data completeness exceeded 85%. In the global study (Chapter 4), O_3 data were collected from over 8,000 air quality monitoring stations across 48 countries. After this screening process, 4,308 stations in 37 countries met the criteria and were used for analysis. Short-term data mainly covered the period of 2014 – 2019, with exceptions for Japan (2013 – 2017), Malaysia (2014 – 2018), and 4 stations in Victoria, Australia (2014 – 2018) due to data availability. Long-term O_3 data for the US, Europe, South Korea, Mexico, Malaysia, Japan, and Australia from 2000 to 2019 were also obtained to compare with the short-term O_3 trend. Moreover, historical O_3 measurements for the US from 1980 onward and for Europe from 1990 onward were further compiled to assess the impact of emission reduction policies on O_3 changes. Data sources for each country or region are provided in Table 3.1, while station locations and other relevant information are available at https://doi.org/10.6084/m9.figshare.23292365.v1.

Table 3.1. Global O_3 monitoring data sources for each country and region.

Country/Region (No. of stations used in this study)	**Data Source**
Australia (45)	Department of Water and Environmental Regulation, Government of Western Australia (https://www.dwer.wa.gov.au/); North Territory Environment Protection Authority (https://ntepa.nt.gov.au/); Open Data Portal of Queensland government (https://www.data.qld.gov.au/dataset); Data SA of South Australia government (https://data.sa.gov.au/data/dataset); Planning, Industry & Environment website of the New South Wales government (https://www.dpie.nsw.gov.au/air-quality/search-for-and-download-air-quality-data); Data Vic of Victoria government (https://discover.data.vic.gov.au/dataset/epa-air-watch-all-sites-air-quality-hourly-averages-yearly/historical).
Brazil (11)	São Paulo State Environmental Agency (CETESB). Data was compiled and provided by Dr. Daniel Schuch from Northeastern University.
Chile (24)	Ministry of the Environment, Chile (https://sinca.mma.gob.cl/).
China (765)	China National Environmental Monitoring Centre (http://www.cnemc.cn/).
Europe (1317)	European Environment Agency (https://discomap.eea.europa.eu/map/fme/AirQualityExport.htm); Tropospheric Ozone Assessment Report (https://doi.org/10.1594/PANGAEA.876110).
India (1)	Data was compiled and provided by Prof. Vinayak Sinha from the Indian Institute of Science Education and Research, Mohali.
Japan (1085)	National Institute for Environmental Studies, Japan (http://www.nies.go.jp/index-e.html).
Malaysia (33)	Department of Environment (DOE), Malaysia. Data were compiled and provided by Prof. Mohd Talib Latif from Universiti Kebangsaan Malaysia.
Mexico (15)	Mexico Automated Atmospheric Monitoring Network (http://www.aire.cdmx.gob.mx).
South Korea (305)	Korea Environment Corporation (https://www.airkorea.or.kr/web).
Thailand (3)	Acid Deposition Monitoring Network in East Asia (https://monitoring.eanet.asia/document/menu/index).
United States (704)	United States Environmental Protection Agency (https://www.epa.gov/outdoor-air-quality-data).

In addition, South China, comprising the three southernmost provinces of Guangdong, Guangxi, and Hainan, was the focus of Chapter 5. Hourly O_3 concentrations from May to August for each year from 2013 to 2022 were sourced from the China National Environmental Monitoring Center (CNEMC), with data collection and quality control procedures strictly following the China National Environmental Protection Standard (CNEMC, 2013). Initially, 218 monitoring stations across South China were considered, but this number was reduced to 147 stations after the data screening process. This valid dataset was then used to analyze summertime O_3 levels and trends across South China in this study. Moreover, additional O_3 data at 18 stations in Hong Kong (2013 – 2022), 10 in Taiwan (2016 – 2021), 4 in Thailand (2013 – 2022), and 18 in Malaysia (2013 – 2018), were sourced from the Hong Kong Environmental Protection Department (HKEPD), the Tropospheric Ozone Assessment Report (TOAR) database, the Acid Deposition Monitoring Network in East Asia (EANET), and the Department of Environment Malaysia (Table 3.1), respectively. These observed O_3 data were also employed in this study for the statistical evaluation of model simulation results. The locations of all O_3 monitoring stations used in Chapter 5 are presented in Figure 3.1.

Furthermore, the Pearl River Delta (PRD) region in South China comprises nine mainland cities, *i.e.*, Dongguan (DG), Foshan (FS), Guangzhou (GZ), Huizhou (HZ), Jiangmen (JM), Shenzhen (SZ), Zhuhai (ZH), Zhaoqing (ZQ), and Zhongshan (ZS). Hourly O_3 and NO_2 concentrations at 56 national monitoring stations were collected from CNEMC for use in the observational constraint of VOC emissions in Chapter 6 (Table 3.2).

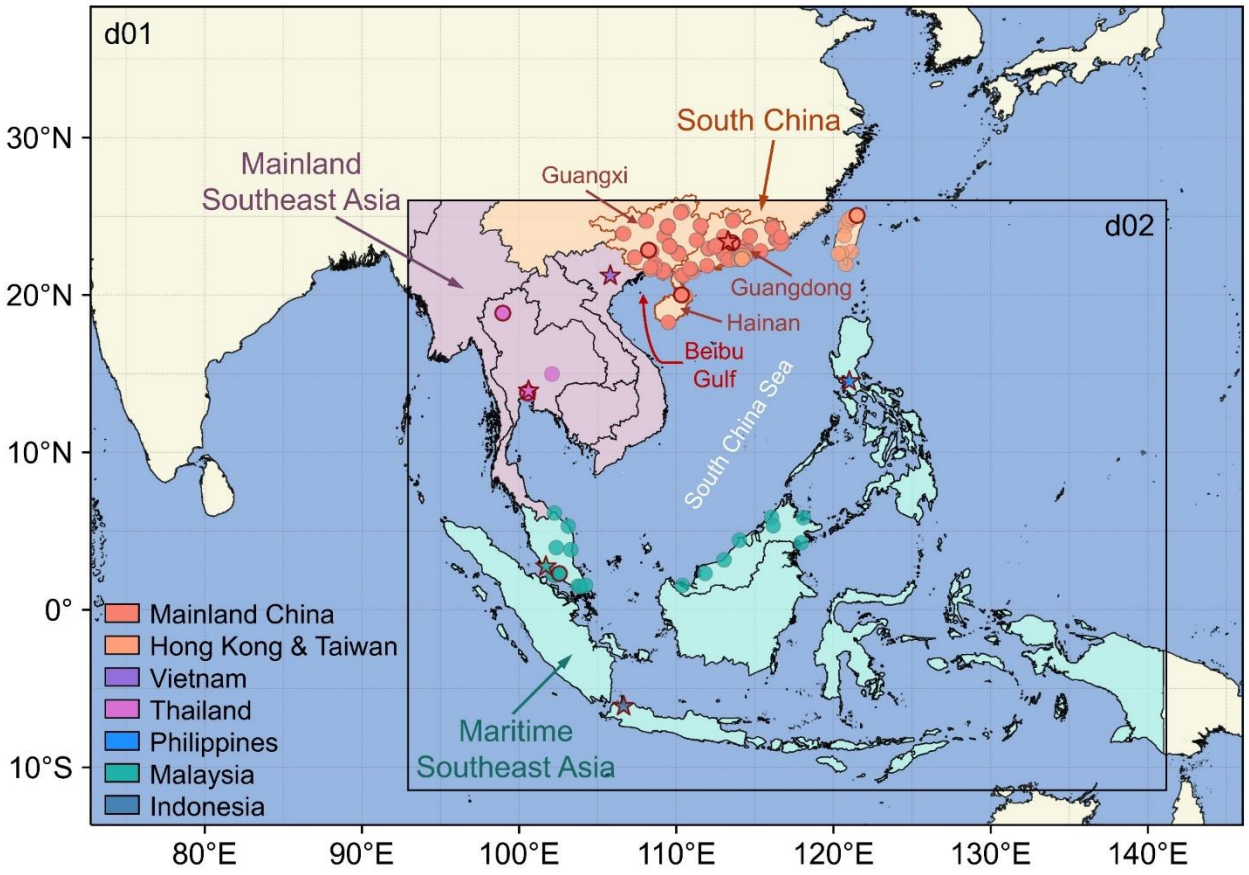

Figure 3.1. Nested domains used in the WRF-CMAQ simulations. The three tagged regions, *i.e.*, South China, Mainland Southeast Asia, and Maritime Southeast Asia, are shaded in different colors. Scatter circles are the locations of all 197 O_3 monitoring stations, while stars represent the locations of six meteorological observation stations. Circles with dark red edges highlight representative O_3 monitoring stations in seven major cities, which were selected to evaluate the time series performance of the chemical transport model.

Table 3.2. Information on the national environmental monitoring stations in the PRD region.

City	Site	Lon[1]	Lat[2]	City	Site	Lon	Lat	City	Site	Lon	Lat
DG	1387A*	113.78	23.05	HZ	1392A*	114.42	23.05	SZ	1356A	114.11	22.55
	1388A	113.75	23.03		1393A	114.41	23.08		1357A	114.12	22.56
	1389A	113.75	23.06		1394A	114.41	23.11		1358A*	113.99	22.54
	1390A	113.79	23.01		1395A	114.32	22.82		1359A	113.92	22.52
	1391A	113.74	22.97		1396A	114.53	22.74		1360A	114.26	22.59
FS	1371A	113.13	23.01	JM	1383A	113.1	22.61		1361A	114.24	22.73
	1372A*	113.11	23.04		1384A*	113.07	22.58		1362A	113.89	22.58
	1373A	113.14	23.05		1385A	113.02	22.53		1363A	114.49	22.54
	1374A	113.29	22.81		1386A	113.08	22.59		1364A	114.41	22.63
	1375A	113.26	22.76	ZQ	1397A	112.43	23.07		1365A	114.3	22.6
	1376A	112.84	22.87		1398A*	112.47	23.05		1366A	114.09	22.75
	1377A	112.89	23.16		1399A	112.57	23.16	ZS	1379A	113.38	22.52
	1378A	112.86	23.19		1400A	112.47	23.08		1380A	113.39	22.55
GZ	1345A	113.24	23.14	GZ	1352A	113.26	23.13		1381A*	113.41	22.51
	1346A	113.26	23.11		1353A	113.57	23.28		1382A	113.44	22.49
	1348A	113.35	23.09		1354A	113.28	23.16	ZH	1367A	113.57	22.26
	1349A	113.43	23.11		1355A*	113.59	23.55		1368A*	113.5	22.23
	1350A	113.35	22.95		2846A*	113.32	23.13		1369A	113.63	22.43
	1351A	113.22	23.39						1370A	113.3	22.23

[1]Lon: longitude; [2]Lat: latitude; *Stations that are close to the VOC sampling sites in each city.

3.1.2 Field measurements and chemical analyses of VOCs

In this study, concurrent field measurements were carried out in the PRD region during the summer of 2018 for VOC samplings. The sampling sites covered nine cities, with one typical urban site in each city being selected. These urban sites were located in the residential and commercial areas within the central circles of each city (within a radius of 5 – 10 km from the city center). There were no industrial factories or highways nearby, and the sites were far from boulevards. As a result, instantaneous emissions from industries and vehicles were rare. In addition, one suburban site, Conghua (GZ-CH), was also chosen in a suburban town in the northern PRD region. Figure 3.2 and Table 3.3 show the geographical locations of these sampling sites. The samplings were set up in open and high locations (the rooftops of buildings, about 20 m above the ground) without tall buildings and/or trees blocking the air exchanges. Therefore, the samples collected were relatively well-mixed air masses representative of urban and suburban environments.

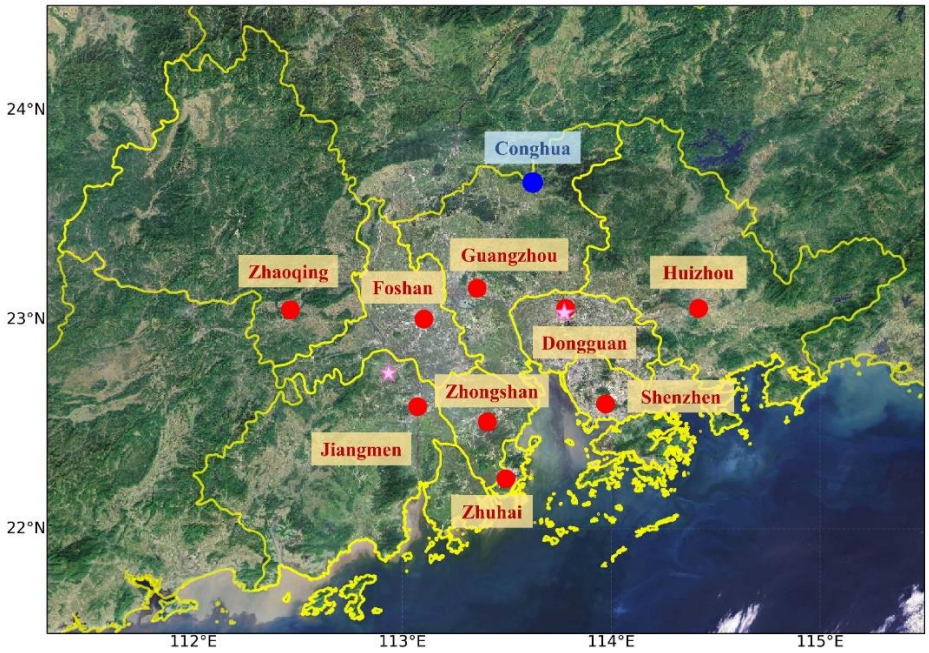

Figure 3.2. Location of the VOC sampling sites. The circles denote offline measurement sites, and the pink stars refer to the online measurement sites.

Table 3.3. Description of the sites and dates for VOC samplings.

City	Site	Location	Lon/Lat	Dates	No. of VOC samples
Dongguan	DG	Dongguan Experimental High School	113.78°E 23.05°N	6 June, 9-13 June	18
Foshan	FS	Foshan Environmental Monitoring Center Station	113.10°E 23.00°N	6 June, 9-13 June	18
Guangzhou	GZ-U	Guangzhou Institute of Geochemistry	113.36°E 23.15°N	29 June to 4 July	17
Huizhou	HZ	Huizhou Environmental Monitoring Station	114.42°E 23.05°N	6 June, 9-10 June, 12-14 June	16
Jiangmen	JM	Jiangmen Environmental Protection Bureau	113.07°E 22.58°N	7 June, 9-13 June	18
Shenzhen	SZ	Peking University Shenzhen Research Institute	113.97°E 22.60°N	6 June, 9-13 June	17
Zhuhai	ZH	Zhuhai Environmental Monitoring Center Station	113.50°E 22.24°N	6 June, 9-13 June	17
Zhaoqing	ZQ	Zhaoqing Jinjiang Hotel	112.46°E 23.05°N	6 June, 9-13 June	18
Zhongshan	ZS	Zhongshan Zimaling Park	113.41°E 22.51°N	6 June, 9-13 June	18
Guangzhou	GZ-CH	Guangzhou Conghua Tianhu Environmental Monitoring Station	113.62°E 23.65°N	29 June to 4 July	17
Dongguan	online-U	Dongguan Dongcheng Qifenghui	113.78°E 23.02°N	June 2018	Online measurement
Jiangmen	online-B	Jiangmen Heshan Taoyuan Town	112.93°E 22.72°N	July 2019	Online measurement

Offline VOC samples were collected at these ten sampling sites. The 1-hour whole air samples were collected using electro-polished stainless-steel SUMMA canisters with valves to ensure that the canisters were filled gradually within one hour. The samples were collected at 08:00, 12:00, and 16:00 local time (the China Standard Time [CST], UTC+8), and the sampling days were selected based on weather forecasts and analyses of synoptic systems so that days with heavy rain were avoided. Details of the sampling dates and the number of valid samples collected are listed in Table 3.3. The VOC species were identified and quantified by gas chromatography (GC) coupled with a mass spectrometer detector (MSD), an electron capture detector (ECD), and a flame ionization detector (FID). Two sets of GC units were connected to MSD/ECD and FID, respectively. In the GC-MSD/ECD system, 250 mL of air from the canister sample was injected

into a pre-concentrator and separated into two pathways to enter MSD and ECD, respectively. In the GC-FID system, the 250 mL air sample was concentrated and injected into the FID for chemical analysis of C_2-C_3 NMHCs. The determination of VOCs followed the US EPA TO-15 method (USEPA, 1999), and Table 3.4 lists the limit of detection, precision, and accuracy of each NMHC species. In total, 60 VOCs were quantified, including 27 alkanes, 18 alkenes, 1 alkyne, and 14 aromatics. Moreover, regular inter-laboratory comparisons of NMHCs analysis were performed with the Rowland-Blake group at the University of California, Irvine (Blake et al., 2003; Simpson et al., 2010). Reasonably good agreements were achieved for the analysis results between the two laboratories, with the goodness of fit (R^2) between 0.85 – 0.97 and slopes close to 1.0 (*i.e.*, 0.85 – 1.24) for different species, indicating good reliability and quality of the data.

In addition to the offline VOC measurements, hourly VOC concentrations were continuously measured at an urban site in DG (online-U) and a suburban site in JM (online-B) (Table 3.3) by the online gas chromatograph-mass spectrometer (GC-MS/866, Chromatotec). This instrument quantified 56 VOC species and was calibrated weekly during the sampling periods. The R^2 values were greater than 0.98 for the calibration curves between the standard gas concentrations and the instrumental response signal, and the limits of detection ranged from 0.02 to 0.35 ppbv for the VOC species. Details about the online GC-MS measurements can be found in Qi et al. (2021). From the online VOC measurements, the monthly average diurnal variations of VOC species were obtained at both urban and suburban sites during summer, which were used for model evaluation and the calculation of the VOC emission constraint in Chapter 6. Note that 51 out of the 56 VOCs measured online were included in the 60 VOCs measured offline. Hence, 50 of them were selected and used in the observational constraint of anthropogenic VOC emissions (Table 3.4), according to their abundance, reactivity, and sources. The 50 VOC species were then mapped to eight VOC

groups in the Carbon Bond chemical mechanism (CB05), listed in Table 3.5 for further calculations and model evaluations by the chemical transport model.

Table 3.4. Limit of detection (LoD), precision, and accuracy of offline chemical analyses for 60 VOC species (C_2-C_3 VOCs analyzed by GC-FID; other species by GC-MSD/ECD).

Species	LoD (pptv)	Precision (%)	Accuracy (%)	Constraint
Alkanes (27)				
ethane	31.11	2.74	0.71	√
propane	23.18	2.32	-3.26	√
n-butane	55.77	4.57	5.85	√
i-butane	28.46	7.16	2.69	√
2,2-dimethylbutane	18.88	6.32	-2.34	√
2,3-dimethylbutane	15.69	6.33	-8.29	√
n-pentane	10.54	5.58	-4.62	√
i-pentane	18.02	7.21	-10.36	√
2-methylpentane	16.04	8.04	-8.68	√
3-methylpentane	16.84	5.64	-5.92	√
cyclopentane	18.95	9.22	0.79	√
methylcyclopentane	6.30	3.94	8.71	√
2,3-dimethylpentane	7.05	5.37	-6.49	√
2,4-dimethylpentane	10.75	7.65	-4.99	√
2,2,4-trimethylpentane	7.80	8.25	-5.61	√
2,3,4-trimethylpentane	7.77	8.24	-8.88	√
n-hexane	8.52	4.40	-8.12	√
cyclohexane	8.31	5.30	-4.10	√
2-methylhexane	9.46	5.78	-3.03	√
3-methylhexane	16.21	5.49	-5.79	√
methylcyclohexane	9.17	6.54	-11.47	√
n-heptane	10.71	5.99	-5.58	√
2-methylheptane	5.24	8.9	-8.78	√
3-methylheptane	6.58	7.38	-4.02	√
n-octane	10.81	8.55	-2.72	√
n-nonane	10.19	5.45	-0.74	√
n-decane	18.33	4.43	-7.12	√
Alkyne (1)				
ethyne	34.12	2.41	3.11	√

Species	LoD (pptv)	Precision (%)	Accuracy (%)	Constraint
Alkenes (18)				
ethene	30.02	0.86	-3.11	√
propene	53.78	7.93	2.70	√
1-/*i*-butene	36.39	5.71	4.53	√
2-methyl-1-butene	22.91	9.76	-1.45	
1,3-butadiene	18.97	6.41	-7.47	
trans-2-butene	55.84	5.79	2.87	√
cis-2-butene	15.02	10.36	0.16	√
3-methyl-1-butene	21.21	8.13	1.93	
2-methyl-2-butene	8.89	6.87	-1.96	
1-pentene	35.49	7.75	-8.04	√
trans-2-pentene	9.40	5.48	-7.59	√
cis-2-pentene	15.59	8.78	-3.99	√
cyclopentene	20.44	7.51	-6.47	
4-methyl-1-pentene	15.14	9.50	2.10	
2-methyl-1-pentene	13.14	7.07	-7.65	
Isoprene	21.00	25.89*	-22.58	
α-pinene	13.16	6.17	-3.47	
β-pinene	13.07	7.11	-5.13	
Aromatics (14)				
benzene	18.14	9.24	-8.46	√
toluene	10.53	9.16	-6.58	√
ethylbenzene	12.66	5.86	-3.85	√
m/*p*-xylene	17.79	6.54	-6.32	√
o-xylene	10.80	7.49	-4.16	√
styrene	4.97	8.36	-2.15	√
i-propylbenzene	12.20	7.66	-0.87	√
n-propylbenzene	16.96	6.02	-5.86	√
2-ethyltoluene	15.19	8.64	-7.21	√
3-ethyltoluene	12.76	6.66	-8.91	√
4-ethyltoluene	8.95	6.92	-7.98	√
1,2,3-trimethylbenzene	19.99	7.77	-14.5	√
1,2,4-trimethylbenzene	15.12	5.80	-12.22	√
1,3,5-trimethylbenzene	14.42	6.51	-9.31	√

*Note that the relatively poor precision for isoprene likely results from its low mixing ratio in the standard gas mixture, which yields a weak analytical signal relative to the instrument background noise.

Table 3.5. CB05 VOC species in the observation-constrained emission profiles.

CB05 species	Description	No. of carbons	Explicit/Lumped
PAR	Paraffinic carbon bond (C-C)	1	Lumped
ETHA	Ethane	2	Explicit
ETH	Ethene	2	Explicit
OLE	Terminal olefinic carbon bond (R-C=C)	2	Lumped
IOLE	Internal olefinic carbon bond (R-C=C-R)	4	Lumped
BENZENE	Benzene	6	Explicit
TOL	Toluene and other monoalkyl aromatics	7	Lumped
XYL	Xylene and other polyalkyl aromatics	8	Lumped

3.1.3 Meteorological data

Ground-level meteorological parameters, including temperature, relative humidity, wind speed and direction, and pressure, were obtained from the Integrated Surface Database (Smith et al., 2011). Meteorological data for the study period (2013 – 2022) were collected from one international airport station in each of the following countries: China, Vietnam, Thailand, the Philippines, Malaysia, and Indonesia (Figure 3.1), thereby covering the study area of South China and Southeast Asia. These meteorological datasets were employed for the statistical evaluation of model simulation results in Section 3.2 because the weather conditions at open areas of the airports were not affected by buildings and other local infrastructure. Hourly meteorological parameters from district monitoring stations near the VOC sampling sites in the PRD region were also acquired from the Guangdong Meteorological Bureau. These observed meteorological data were used to validate the model simulation results and to calculate observation-constrained VOC emission profiles in Chapter 6.

Besides, gridded global weather conditions, including temperature, wind fields, and pressure fields, were sourced from the fifth-generation European Centre for Medium-Range Weather Forecasts (ECMWF) reanalysis dataset (ERA5) (Hersbach et al., 2023).

3.2 Chemical transport model configuration

3.2.1 Model description and numerical settings

In this study, the Weather Research and Forecast (WRF v4.0) model and the Community Multiscale Air Quality Modeling System (CMAQ v5.0.2) were applied to simulate the meteorological conditions and atmospheric chemistry. The WRF model, developed by the National Center for Atmospheric Research (NCAR) along with other collaborators, can produce simulations based on actual atmospheric conditions (Skamarock et al., 2019). The CMAQ model established by the US EPA is compatible with the WRF model and provides fast and technically sound simulations of airborne gases and particles (Binkowski & Roselle, 2003). The WRF-CMAQ model has been widely used to study regional-scale air quality and is confirmed to be robust in modeling O_3 pollution in previous studies (Wang et al., 2015b; Wang et al., 2018b; Wang et al., 2022b).

As shown in Figure 3.1, two domains were adopted in the simulations of summer O_3 pollution episodes in South China (Chapter 5), with spatial resolutions of 36 km and 12 km, respectively. The inner domain covered South China, mainland Southeast Asia, maritime Southeast Asia, and the South China Sea. Additionally, Figure 3.3 illustrates the three-nested domain employed for simulating the observation-constrained VOC emissions in the PRD region (Chapter 6), with a spatial resolution of 3 km for the innermost domain. To ensure compatibility between the WRF and CMAQ models, one grid cell was removed from each WRF lateral boundary in the CMAQ domains. Despite this adjustment, the innermost domain still fully encompasses the targeted regions of this study. Vertically, the WRF model was configured with 51 terrain-following sigma levels extending up to 50 hPa, while these layers were compressed to 15 layers in the CMAQ model, with approximately 7 layers within the boundary layer. The specific physical and chemical

mechanisms used in the WRF-CMAQ simulations are detailed in Table 3.6. These model configurations have been successfully applied in previous studies of O_3 pollution in South China (Zheng et al., 2021b; Zeren et al., 2022b; Zheng et al., 2024). Simulations were performed individually for each high O_3 pollution day (Chapter 5) and for the entire month of June 2018 (Chapter 6). A 24-hour spin-up run was conducted prior to each simulation.

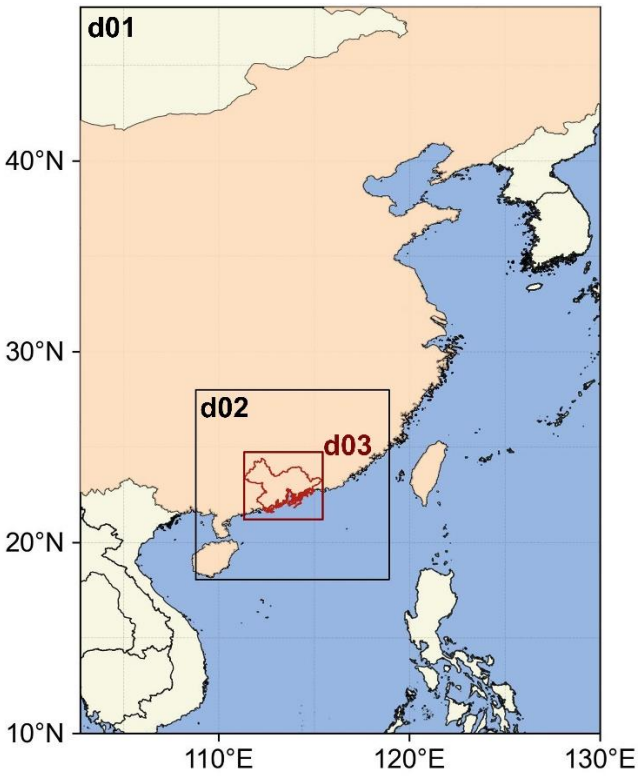

Figure 3.3. Nested domains for WRF-CMAQ simulations in the PRD region. The outermost domain (d01, 27 km resolution) covered the majority of East Asia, including China, the Korean Peninsula, and parts of Southeast Asia. The second domain (d02, 9 km resolution) covered South China. The innermost domain (d03) focuses on the PRD region and has a grid spacing of 3 km.

Table 3.6. Physical and chemical schemes employed in the WRF-CMAQ model.

WRF model	
Microphysics	WRF Single-Moment 3-class scheme (Hong et al., 2004)
Longwave/Shortwave radiation	Rapid Radiative Transfer Model (Mlawer et al., 1997)
Surface layer	Revised MM5 Monin-Obukhov scheme (Jiménez et al., 2012)
Land surface model	Unified Noah land surface model (Tewari et al., 2004)
Planetary boundary layer	Yonsei University scheme (Hong et al., 2006)
Cumulus parameterization	Kain-Fritsch (new Eta) scheme (Kain, 2004)
CMAQ model	
Gas-phase chemistry	CB05 (Yarwood et al., 2005) with updated toluene (Whitten et al., 2010) and chlorine (Tanaka et al., 2003) chemistry
Aerosol module	AERO6 (Carlton et al., 2010)

In the CMAQ simulations, the Integrated Process Rate (IPR) module within Process Analysis was applied to quantify the contributions of various processes to O_3 concentrations. The Integrated Source Apportionment Method (ISAM) in the CMAQ model was also used in the innermost domain to determine the source contributions of O_3 and its precursors from various emission sectors. ISAM addresses the challenges posed by the highly nonlinear nature of O_3 photochemistry and enhances computational efficiency (Kwok et al., 2015; Zhu et al., 2023). To analyze the transport impacts from Southeast Asia on summer O_3 pollution episodes in South China (Chapter 5), nine tags were established to track the contributions from anthropogenic, biogenic, and biomass burning emissions in South China, mainland Southeast Asia, and maritime Southeast Asia. An additional tag was assigned to shipping emissions. Untagged emissions, as well as concentrations from initial and boundary conditions, were also evaluated with ISAM.

3.2.2 Model input data and sources

The WRF model was driven by the Final Operational Global Analysis data (FNL) (NCEP, 2000), which had a spatial resolution of 1° × 1° and a temporal resolution of 6 hours. The outdated default land cover in WRF was updated using the annual Moderate Resolution Imaging Spectroradiometer (MODIS) Land Cover Climate Modeling Grid (MCD12C1) Version 6 and Version 6.1 at a spatial resolution of 5.6 km (Friedl & Sulla-Menashe, 2015 & 2022).

For the CMAQ model, several anthropogenic emission inventories were used in the simulations of summer O_3 pollution episodes in South China (Chapter 5). The 2017-based high-resolution gridded emissions with spatial resolutions of 3 km and 1 km, respectively, were applied for Guangdong province and Hong Kong (Huang et al., 2021). The Multi-resolution Emission Inventory for China (MEICv1.4) for 2013 – 2020 (Li et al., 2014; Geng et al., 2024) was applied for mainland China, except for Guangdong province. The Hemispheric Transport of Air Pollution (HTAPv3) mosaic for Asia for 2013 – 2018 (Crippa et al., 2023) was applied for the rest of the model domains. These anthropogenic emission inventories were spatially allocated to the model grids, and the inventory for each respective years were used where available. Note that, due to delays in updating inventories, emissions for later years were held constant using the most recent available data. In addition, daily biomass burning emissions were obtained from the Global Fire Emission Database (GFED v4.1s) (van der Werf et al., 2017), and the 2017-based global Shipping Emission Inventory Model (SEIM) database (Liu et al., 2016b) was also incorporated into the model. Biogenic emissions were estimated using the Model of Emissions of Gases and Aerosols from Nature (MEGAN2.1) (Guenther et al., 2012), based on meteorological parameters from the WRF simulations. These global emissions were also spatially regridded to the model domains and combined with the anthropogenic emissions as the final emission input for the CMAQ model.

Moreover, in the study of the observational constraint of VOC emissions (Chapter 6), the priori anthropogenic emissions were based on the MEIC emission inventory in 2017 (Zheng et al., 2018) and the 2010-based Asian emission inventory (MIX) (Li et al., 2017c) within and outside China, respectively. These priori anthropogenic emission inventories (with grid resolution at 0.25° × 0.25°) were applied to the base model simulation, while in the constrained model simulation, the anthropogenic VOC emissions in the PRD region were updated by the observation-constrained emissions (posteriori emissions) calculated in Section 3.3. In addition to the anthropogenic emissions, the MEGAN model version 2.04 (Guenther et al., 2006) was also used to derive the biogenic emissions in this study.

3.2.3 Model performance

The WRF-CMAQ model simulations were validated against observational data. Statistical metrics, including the mean bias (MB), root mean square error (RMSE), correlation coefficient (COE), and index of agreement (IOA), were used to assess the model performance based on observations at meteorological stations. These metrics are calculated via Equations (1-4) as follows:

$$\mathrm{MB} = \frac{1}{n}\sum_{i=1}^{n}(\mathrm{Sim}_i - \mathrm{Obs}_i) \qquad \text{Equation (1)}$$

$$\mathrm{RMSE} = \sqrt{\frac{1}{n}\sum_{i=1}^{n}(\mathrm{Sim}_i - \mathrm{Obs}_i)^2} \qquad \text{Equation (2)}$$

$$\mathrm{COE} = \frac{\sum_{i=1}^{n}(\mathrm{Sim}_i - \overline{\mathrm{Sim}})(\mathrm{Obs}_i - \overline{\mathrm{Obs}})}{\sqrt{\sum_{i=1}^{n}(\mathrm{Sim}_i - \overline{\mathrm{Sim}})^2 \sum_{i=1}^{n}(\mathrm{Obs}_i - \overline{\mathrm{Obs}})^2}} \qquad \text{Equation (3)}$$

$$\mathrm{IOA} = 1 - \frac{\sum_{i=1}^{n}(\mathrm{Sim}_i - \mathrm{Obs}_i)^2}{\sum_{i=1}^{n}(|\mathrm{Sim}_i - \overline{\mathrm{Obs}}| + |\mathrm{Obs}_i - \overline{\mathrm{Obs}}|)^2} \qquad \text{Equation (4)}$$

where *n* is the total number of samples, and *i* is the parameter or species. Sim represents simulated values, and Obs represents observed values. $\overline{\mathrm{Sim}}$ and $\overline{\mathrm{Obs}}$ are the mean values of the simulation and observation for all samples, respectively.

For the simulations of summer O_3 pollution episodes in South China (Chapter 5), simulated meteorological fields were further evaluated using observed temperature, relative humidity, sea level pressure, and wind fields from six international airport stations. Figure 3.4 and Table 3.7 present the modeled and observed values for these parameters, along with their corresponding statistical metrics. Despite a slight overestimation of temperature (MB: 0.84 °C) and an underestimation of relative humidity (MB: –9.03%), the simulations demonstrated strong reliability, with COE values of 0.80 and 0.71, and high IOA values of 0.87 and 0.76, respectively. Accurate simulation of sea level pressure further confirms that the model successfully reproduced the prevailing weather processes during the simulation periods. Although the model showed relatively weaker performance in simulating wind speed, this remains a common challenge for the WRF model, often attributed to imprecise land-use data or the limitations of coarse spatial resolution in representing complex terrains (Carvalho et al., 2012; Sicard et al., 2021b). Nevertheless, the simulated surface wind speeds and their eastward and northward components remained comparable to observations. The RMSE value for wind speed was 1.54 m/s, and the IOA was 0.69, both within accepted statistical benchmarks of 2 m/s and 0.6, respectively (Emery et al., 2001). Figure 3.5 further demonstrates that the WRF model has effectively captured the spatial distributions and magnitudes of surface temperature and wind fields over the study area. Overall, these validation results indicate that the WRF model reliably simulated meteorological fields during the study periods, providing a robust foundation for the subsequent CMAQ simulations.

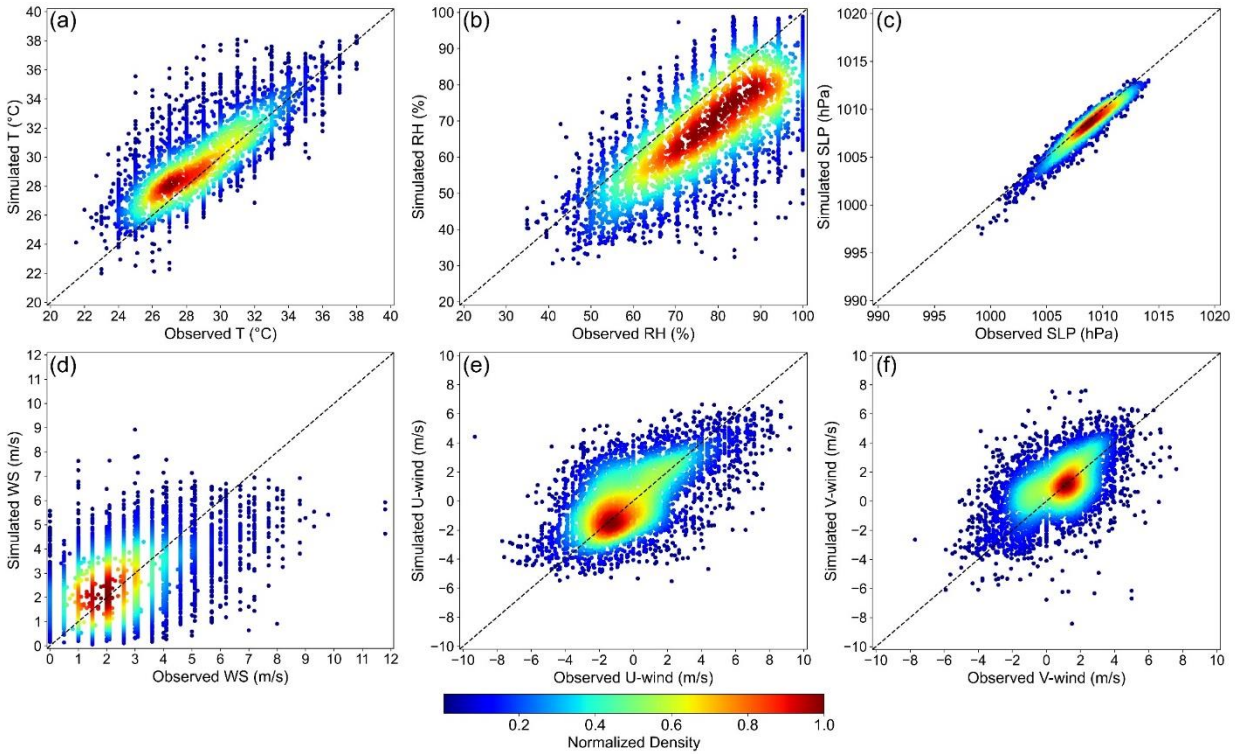

Figure 3.4. Scatter plots comparing observed (horizontal axis) and WRF-simulated (vertical axis) meteorological parameters at six international airport stations (see Figure 3.1) during simulated O_3 episodes in Chapter 5. (a) 2 m temperature (T), (b) 2 m relative humidity (RH), (c) sea level pressure (SLP), (d) 10 m wind speed (WS), (e) 10 m zonal wind component (U-wind), and (f) 10 m meridional wind component (V-wind). Note: SLP data are available at 3-hour intervals with missing values for Hanoi, while all other parameters have hourly data at all stations.

Table 3.7. Statistical evaluation of simulated hourly meteorological parameters, *i.e.*, 2 m temperature, 2 m relative humidity, sea level pressure, 10 m wind speed, 10 m zonal wind component (U-wind), and 10 m meridional wind component (V-wind), at each station and for the combined statistics of six stations during simulated O_3 episodes.

Variables	Parameters		China Guangzhou	Vietnam Hanoi	Thailand Bangkok	Philippines Manila	Malaysia Kuala Lumpur	Indonesia Jakarta	Overall
2 m T (°C)	Mean[1]	Obs	29.82	29.78	29.78	29.00	28.02	28.01	29.07
		Sim	30.39	30.58	31.16	29.81	28.66	28.88	29.91
	MB[2]		0.57	0.80	1.37	0.81	0.64	0.86	0.84
	RMSE[3]		2.06	2.15	2.29	1.78	1.65	1.60	1.94
	COE[4]		0.79	0.78	0.76	0.74	0.79	0.85	0.80
	IOA[5]		0.88	0.86	0.82	0.81	0.86	0.89	0.87
2 m RH (%)	Mean	Obs	73.59	78.62	74.92	80.38	81.05	73.42	76.96
		Sim	66.84	74.41	60.53	71.64	72.52	61.89	67.97
	MB		-6.75	-4.20	-14.36	-8.73	-8.53	-11.54	-9.03
	RMSE		12.22	11.98	17.75	12.65	12.12	13.46	13.53
	COE		0.74	0.69	0.68	0.63	0.67	0.84	0.71
	IOA		0.81	0.81	0.66	0.68	0.71	0.75	0.76
SLP (hPa)	Mean	Obs	1006.28	–	1007.17	1008.80	1009.42	1010.48	1008.41
		Sim	1005.53	1003.44	1006.59	1008.08	1009.21	1009.96	1007.13
	MB		-0.76	–	-0.58	-0.75	-0.22	-0.52	-0.56
	RMSE		1.14	–	0.91	1.16	0.72	0.86	0.97
	COE		0.95	–	0.94	0.91	0.92	0.91	0.95
	IOA		0.95	–	0.95	0.92	0.95	0.93	0.96
10 m WS (m/s)	Mean	Obs	2.11	2.84	3.12	2.83	1.83	2.93	2.61
		Sim	2.48	2.73	3.60	2.99	2.42	2.15	2.73
	MB		0.37	-0.11	0.48	0.19	0.59	-0.79	0.12
	RMSE		1.39	1.58	1.72	1.72	1.24	1.53	1.54
	IOA		0.55	0.52	0.67	0.75	0.68	0.71	0.69
10 m U-wind (m/s)	RMSE		2.11	2.94	2.19	2.38	1.44	1.91	2.22
	IOA		0.58	0.45	0.68	0.77	0.70	0.78	0.78
10 m V-wind (m/s)	RMSE		2.07	2.06	1.92	1.88	1.63	1.61	1.88
	IOA		0.63	0.70	0.68	0.57	0.75	0.79	0.73

Note: SLP data are available at 3-hour intervals with missing values for Hanoi.

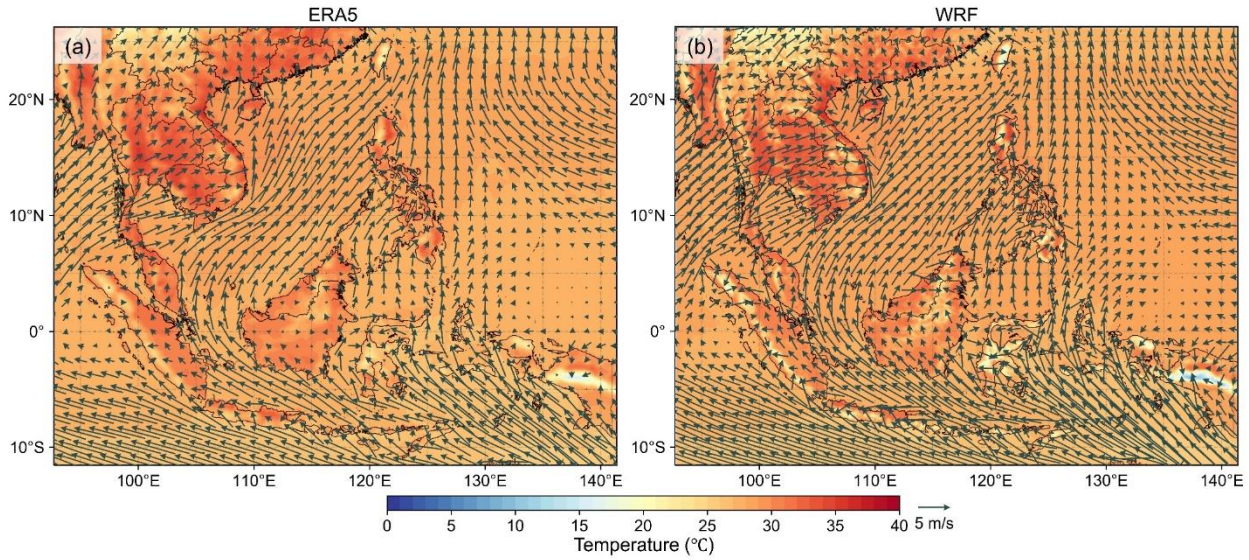

Figure 3.5. Comparison of mean (a) observed and (b) simulated temperature (2 m above ground level, a.g.l.) and wind fields (10 m a.g.l.) over the simulation domain at 14:00 China Standard Time (CST, UTC+8) during simulated O_3 episodes. Observational data are the ERA5 reanalysis.

For the simulations of the observation-constrained VOC emissions in the PRD region (Chapter 6), the WRF model captured the dominant weather systems over East Asia (d01) during the simulation period (Figure 3.6), and the meteorological fields in the PRD region were reproduced. Table 3.8 lists the values of the evaluation statistics for meteorological parameters at nine district monitoring stations in the PRD cities. The surface temperature and relative humidity were well simulated in all cities, indicated by good correlations (COE ranged from 0.73 – 0.89 and 0.76 – 0.85, respectively) and good agreements (IOA ranged from 0.78 – 0.92 and 0.79 – 0.90, respectively). The positive biases (MB ranged from 0.65 – 1.65 m/s) reflected that the surface wind speeds were slightly overestimated. Such biases in the simulated wind speed using the WRF model have been commonly reported in previous studies (Matsui et al., 2009; Li et al., 2016), which can be attributed to the deficiency in the rough terrains adopted in the model. Despite that, the agreements between the simulated and observed wind speeds were within a reliable range (0.56 –

0.80), and the RMSE values were within the benchmark of 2 m/s (Emery et al., 2001). In addition, the time series of the simulated and observed meteorological parameters at Guangzhou airport station presented in Figure 3.7 further demonstrates that the simulations matched the observations. Discrepancies were mainly found on days influenced by tropical cyclones (5-9 June) and the outskirts of the Western Pacific Subtropical High-Pressure system (20-26 June), which had unstable atmospheric conditions with precipitation and strong surface winds. The complexity of the unstable atmosphere has made it difficult to achieve accurate simulations with WRF (Kumar et al., 2012). Nonetheless, the simulated wind directions were consistent with those observed, indicating that the simulations of surface wind fields were reliable. Furthermore, the model captured the temperature gradients and the strongly mixed vertical wind profiles in the planetary boundary layer (Figure 3.8), enhancing the credibility of the simulation of boundary layer dynamics.

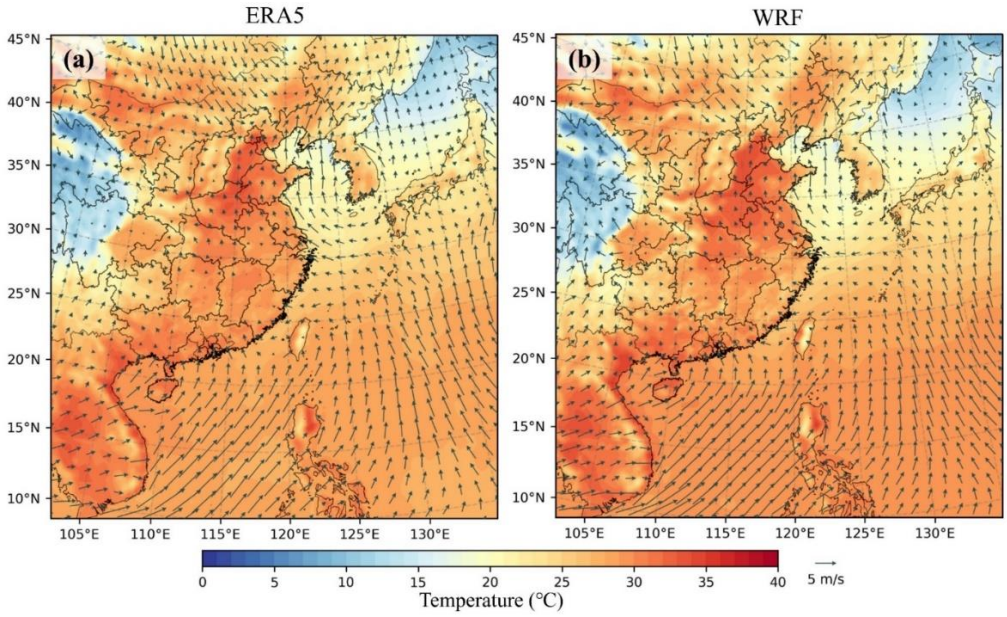

Figure 3.6. Comparison between the monthly mean (a) observed and (b) simulated temperature (2m a.g.l) and wind fields (10 m a.g.l.) at 14:00 CST during June 2018. The observation data is the ERA5 reanalysis for the global climate and weather.

Table 3.8. Statistical assessments of simulated meteorological parameters, *i.e.*, 2 m temperature, 2 m relative humidity, and 10 m wind speed, in each city.

Variables	Parameters		DG	FS	GZ	HZ	JM	SZ	ZH	ZQ	ZS
2 m T (°C)	Mean	Obs	27.87	28.44	28.22	27.31	28.52	28.15	28.21	27.84	28.34
		Sim	28.35	29.01	28.85	27.44	28.15	28.22	28.04	27.46	28.41
	MB		0.47	0.58	0.63	0.12	-0.37	0.06	-0.24	-0.37	0.07
	RMSE		1.37	1.41	1.77	1.71	1.55	1.46	1.34	1.44	1.36
	COE		0.81	0.84	0.83	0.82	0.77	0.80	0.73	0.89	0.81
	IOA		0.89	0.91	0.89	0.88	0.85	0.86	0.78	0.92	0.89
2 m RH (%)	Mean	Obs	82.15	79.56	82.19	83.37	82.13	82.52	82.04	86.20	82.43
		Sim	80.83	76.91	79.33	83.47	83.59	83.06	85.59	83.06	81.24
	MB		-1.32	-2.52	-5.90	0.10	1.47	0.53	4.86	-2.70	-1.19
	RMSE		7.90	8.35	10.91	8.76	8.29	7.77	8.54	8.14	8.49
	COE		0.80	0.83	0.76	0.78	0.81	0.82	0.78	0.85	0.81
	IOA		0.89	0.90	0.83	0.87	0.88	0.87	0.79	0.91	0.88
10 m WS (m/s)	Mean	Obs	3.12	2.95	2.57	2.74	3.14	2.93	4.12	2.90	2.65
		Sim	3.92	3.50	3.55	3.71	4.12	4.57	5.18	3.28	4.18
	MB		0.89	0.65	1.06	0.98	1.10	1.65	1.06	0.83	1.54
	RMSE		1.66	1.64	1.79	1.82	2.05	2.40	2.22	1.57	2.17
	IOA		0.65	0.66	0.57	0.64	0.57	0.56	0.62	0.80	0.55

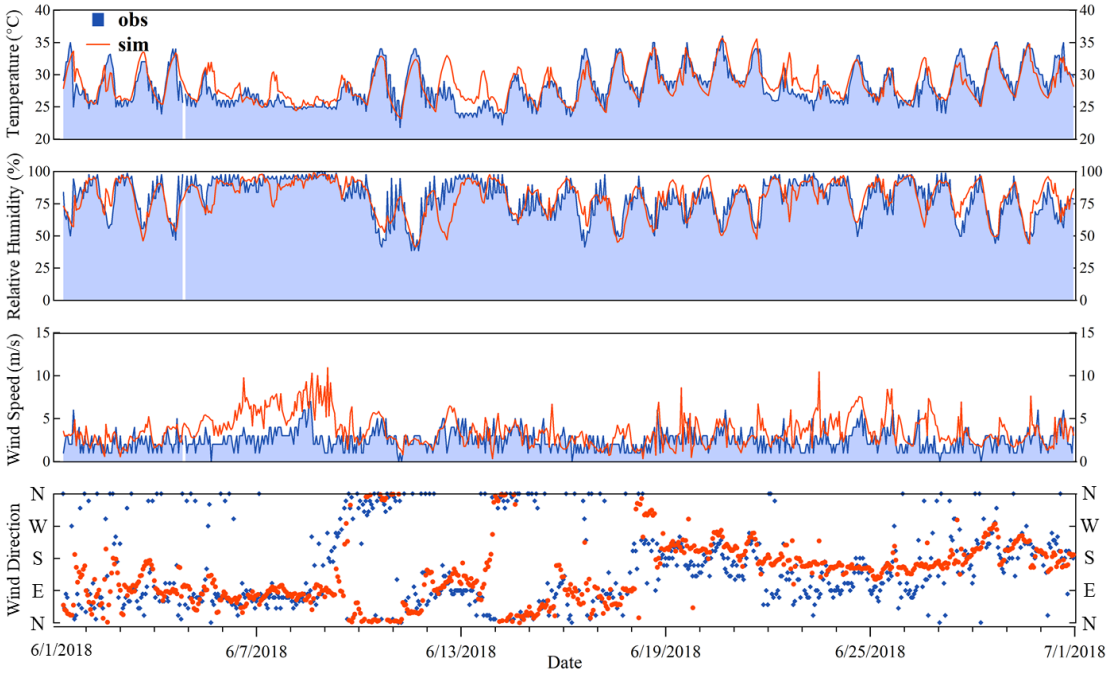

Figure 3.7. Time series of simulated and observed meteorological parameters at Guangzhou Baiyun International Airport station, including 2 m temperature, 2 m relative humidity, and 10 m wind speed and wind direction.

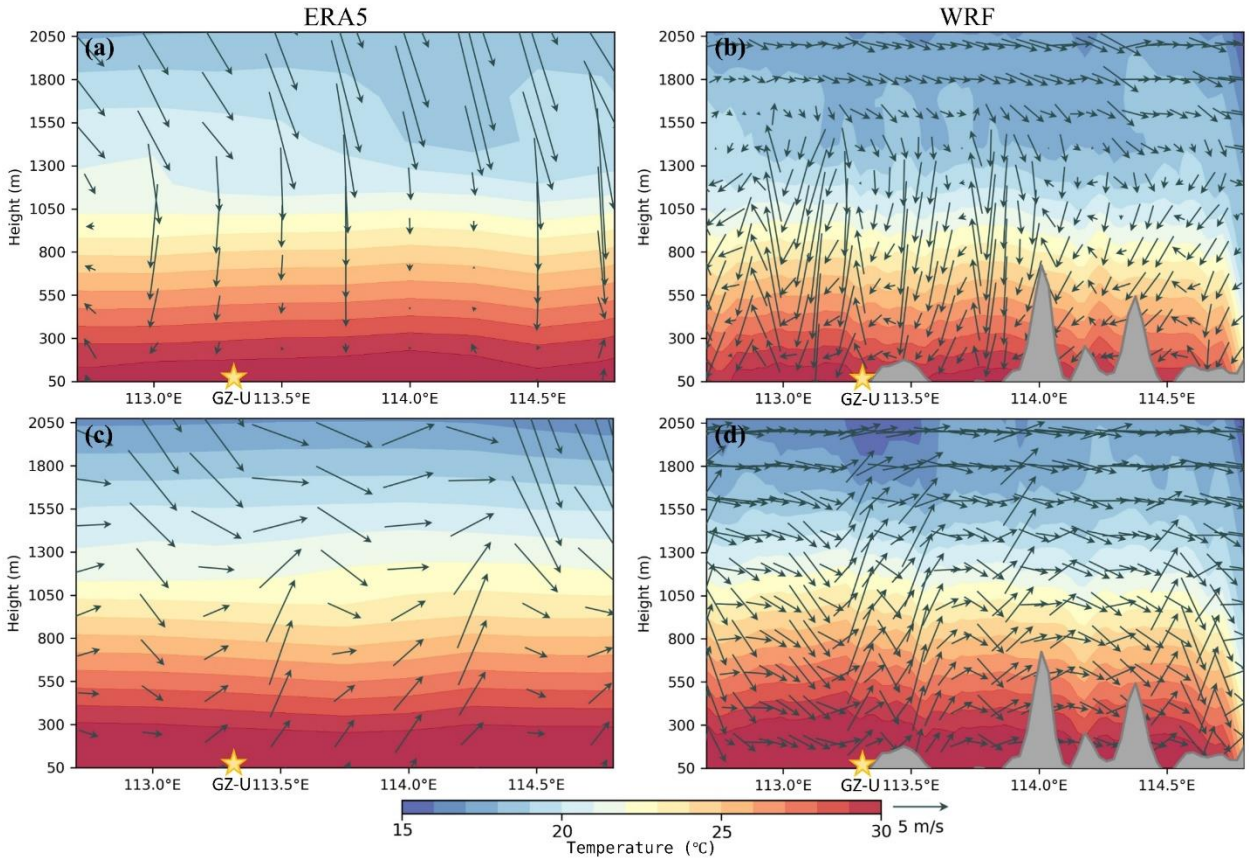

Figure 3.8. Vertical profiles of winds (m/s) and temperatures (°C) along the latitude (23.15°N) across the PRD region at 14:00 CST on (a-b) 11 June 2018 and (c-d) 29 June 2018. (a, c) Observations (ERA5 reanalysis data); (b, d) WRF model simulations.

The overall good performance of the WRF model in simulating the meteorological fields has provided confidence in the simulations of chemical fields by the CMAQ model. Figures 3.9 and 3.10, along with Table 3.9, compare the simulated and observed concentrations of hourly O_3 across all monitoring stations and at representative stations in seven major cities for the simulated O_3 episodes in Chapter 5. While some biases were observed in modeling low O_3 levels at night and high O_3 peaks in some instances, the RMSE for simulated O_3 was 18.62 ppbv (11.24 – 19.82 ppbv for the 7 representative stations), aligning with the range of 19.2 – 22.6 ppbv reported in previous studies in South China (Wang et al., 2019a; Zeren et al., 2022b; Huang et al., 2023). Such

discrepancies are common in chemical transport model simulations and are often attributed to uncertainties and time lags in emission inventories (Saikawa et al., 2017; Qu et al., 2020; Wang et al., 2020), difficulties in resolving complex urban dynamics at coarse spatial resolution (Cuchiara et al., 2014), and simplifications in chemical mechanisms (Mar et al., 2016). Importantly, the simulated and observed O_3 concentrations exhibited good correlation and agreement, with a COE of 0.57 (0.56 – 0.80 for the 7 representative stations) and an IOA of 0.73 (0.68 – 0.87 for the 7 representative stations), meeting the benchmark criteria of 0.5 (Emery et al., 2017) and 0.7 (Huang et al., 2025), respectively. Overall, the model has reasonably reproduced hourly O_3 concentrations, providing confidence in the subsequent analysis of the driving factors for high O_3 episodes over South China in Chapter 5.

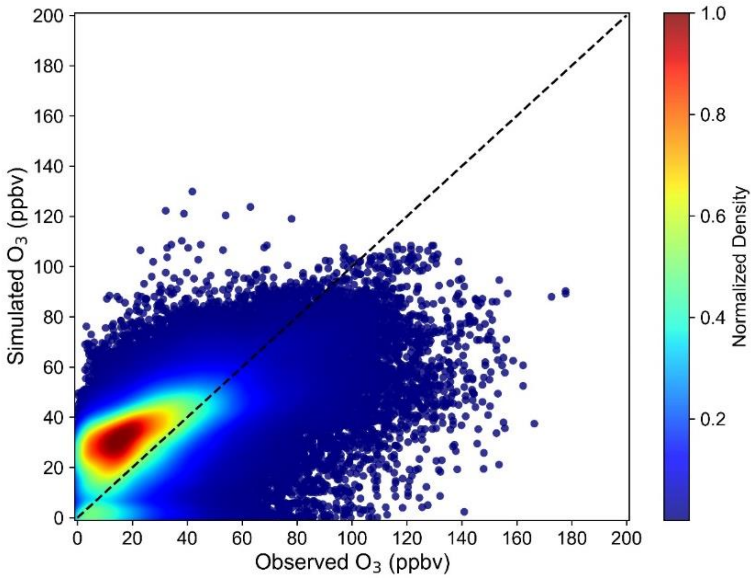

Figure 3.9. Scatter plots comparing observed (horizontal axis) and CMAQ simulated (vertical axis) hourly O_3 concentrations at 197 monitoring stations (see Figure 3.1) during simulated O_3 episodes.

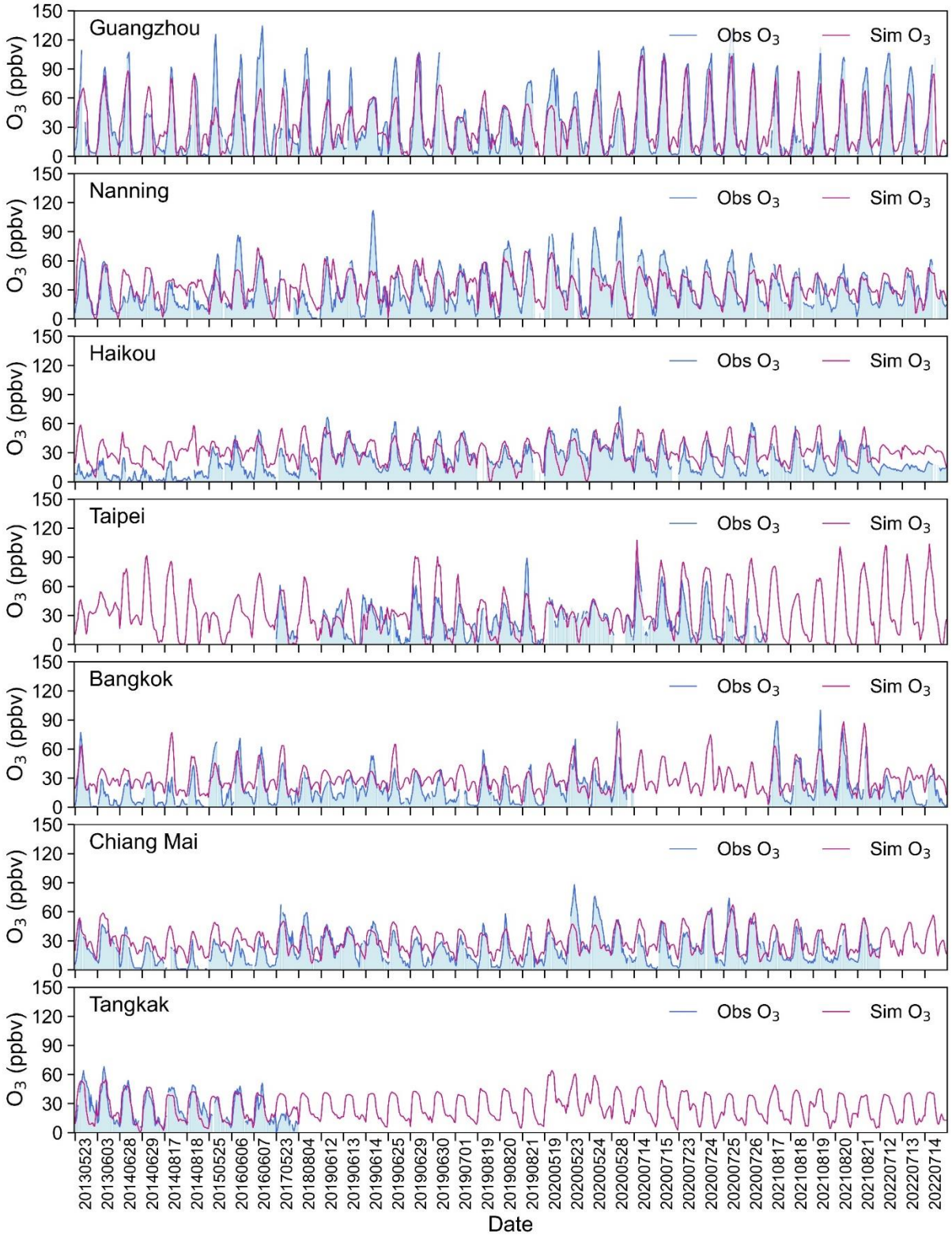

Figure 3.10. Time series of observed and CMAQ-simulated O_3 concentrations at representative stations in seven major cities (highlighted in Figure 3.1) during simulated O_3 episodes.

Table 3.9. Statistical evaluation of CMAQ simulated hourly O_3 concentrations at 197 monitoring stations (overall) and representative stations in seven major cities (highlighted in Figure 3.1) during simulated O_3 episodes.

O_3 (ppbv)	Mean		MB	RMSE	COE	IOA
	Obs	Sim				
Overall Hourly O_3	28.07	31.71	3.79	18.62	0.57	0.73
Guangzhou	33.71	30.07	-2.99	19.82	0.80	0.87
Nanning	30.15	33.88	3.88	15.91	0.66	0.78
Haikou	21.52	30.89	9.46	15.71	0.56	0.68
Taipei	22.90	33.01	7.95	18.96	0.66	0.76
Bangkok	19.28	29.71	10.29	16.30	0.66	0.73
Chiang Mai	22.15	29.30	6.97	13.48	0.69	0.77
Tangkak	25.06	26.49	0.80	11.24	0.72	0.85

The simulations of O_3 concentrations in the PRD region also agreed well with the observations in the study of the observational constraint (Chapter 6). As shown in Figure 3.11 and Table 3.10, the COE values ranged from 0.56 to 0.82, above the accepted benchmark of 0.5 (Emery et al., 2017), and the IOA values were between 0.74 and 0.86. Moreover, the statistics of simulated oxidant (O_x = O_3 + NO_2), which eliminates the effects of the conversion between O_3 and NO_x, were better than those of O_3 (Table 3.11), indicating reasonable simulations of the chemical fields. However, discrepancies between simulated and observed O_3 concentrations remain, related to uncertainties in emission inputs of O_3 precursors, biases in rough urban terrain (Jiménez et al., 2010), and limitations in the model presentation of complex urban dynamics (Zhang et al., 2013; Cuchiara et al., 2014) and photochemical reactions (Tuccella et al., 2012; Mar et al., 2016). Even though the modeled O_3 concentrations in the constrained model simulation were generally

comparable with those in the base model simulation (Figure 3.11), the O_3 levels on high O_3 days were better represented. The improvements in simulated O_3 using observation-constrained anthropogenic VOC emissions will be further discussed in Chapter 6.

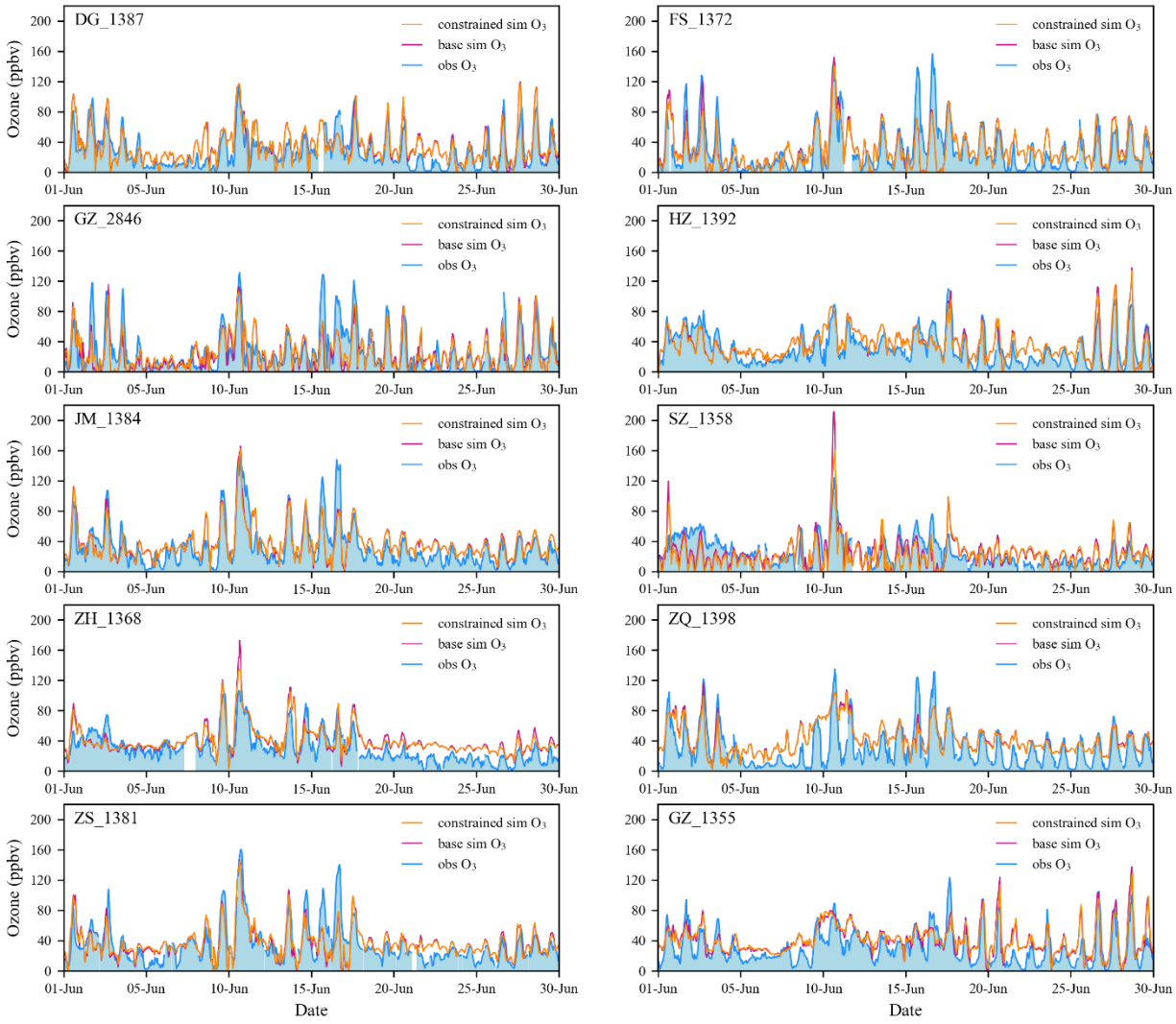

Figure 3.11. Time series of simulated and observed O_3 concentrations at 10 environmental monitoring stations listed in Table 3.2 during June 2018.

Table 3.10. Statistical assessments of simulated hourly O_3 concentrations at each site during June 2018 (from the base and constrained model simulations).

O_3 (ppbv)	Obs	Base model simulation					Constrained model simulation				
	Mean	Mean	MB	RMSE	COE	IOA	Mean	MB	RMSE	COE	IOA
DG	27.28	30.95	4.69	17.70	0.74	0.84	30.84	3.27	16.80	0.73	0.84
FS	28.36	29.26	0.34	21.12	0.71	0.82	28.74	0.17	21.18	0.70	0.81
GZ	26.77	24.59	-4.11	19.44	0.71	0.83	26.38	-0.56	19.37	0.70	0.82
HZ	31.02	35.98	4.20	16.18	0.75	0.85	35.48	4.06	16.08	0.73	0.83
JM	32.89	37.16	3.38	18.29	0.82	0.86	36.74	2.94	18.08	0.81	0.85
SZ	25.06	25.10	0.50	19.73	0.56	0.74	24.56	-0.05	18.98	0.53	0.75
ZH	30.51	40.00	9.52	17.57	0.74	0.80	40.24	9.42	16.83	0.74	0.81
ZQ	30.63	41.40	10.74	22.59	0.68	0.75	40.52	10.03	22.43	0.69	0.75
ZS	34.48	36.17	1.89	18.14	0.74	0.84	36.18	1.49	17.79	0.75	0.84
GZ-CH	30.79	40.87	9.82	18.74	0.74	0.80	40.18	9.21	18.28	0.74	0.79

Table 3.11. Statistical assessments of simulated hourly O_x concentrations at each site during June 2018 (from the base and constrained model simulations).

O_x (ppbv)	Obs	Base model simulation					Constrained model simulation				
	Mean	Mean	MB	RMSE	COE	IOA	Mean	MB	RMSE	COE	IOA
DG	40.92	51.06	9.66	16.67	0.80	0.84	50.35	8.30	15.53	0.81	0.85
FS	44.68	53.37	7.68	20.13	0.78	0.83	51.56	5.03	19.23	0.78	0.83
GZ	45.80	53.93	7.96	18.87	0.78	0.85	51.78	5.80	17.70	0.79	0.86
HZ	41.16	46.13	4.85	14.05	0.80	0.87	45.97	4.68	13.97	0.81	0.87
JM	45.72	49.39	3.48	15.94	0.84	0.90	48.73	3.06	15.36	0.84	0.90
SZ	40.69	47.11	7.02	16.37	0.74	0.83	45.65	5.68	15.11	0.76	0.84
ZH	41.75	45.23	3.48	14.58	0.76	0.86	44.28	2.76	13.87	0.77	0.86
ZQ	45.60	48.17	3.05	16.98	0.77	0.85	47.19	2.98	16.07	0.77	0.86
ZS	41.00	47.50	6.90	17.54	0.81	0.86	46.83	6.28	17.28	0.80	0.86
GZ-CH	41.23	47.46	6.09	15.86	0.75	0.83	47.90	6.19	15.85	0.74	0.82

3.3 Calculation of the Observational Constraint

The calculation of observational constraint was based on the Eulerian Box Model according to the mass conservation of a species inside a fixed box (Seinfeld & Pandis, 2006). In the Eulerian box, the atmosphere in the area of interest is assumed to be well-mixed, and the concentration of a species is determined by its emission, chemical reactions, removal (dry and wet depositions), horizontal transport, and vertical dilution. Each PRD city, except for GZ, where GZ-U and GZ-CH were treated separately, was regarded as a three-dimensional box. Thereby, the mass-balanced rate of change with time (t) for the concentration of species (i) within the box of volume ($L \cdot W \cdot H(t)$) can be calculated via Equations (5a) and (5b) as follows:

$$\frac{dc_i}{dt} = \frac{q_i}{H(t)} - R_i - \frac{s_i}{H(t)} + \frac{c_i^0 - c_i}{\tau_r} \quad \text{for } \frac{dH(t)}{dt} \leq 0 \qquad \text{Equation (5a)}$$

$$\frac{dc_i}{dt} = \frac{q_i}{H(t)} - R_i - \frac{s_i}{H(t)} + \frac{c_i^0 - c_i}{\tau_r} + \frac{(c_i^a - c_i)}{H(t)}\frac{dH(t)}{dt} \quad \text{for } \frac{dH(t)}{dt} > 0 \qquad \text{Equation (5b)}$$

where i represents CB05 VOCs; c_i (molecules·cm^{-3}) is the concentration of VOC_i; q_i (molecules·cm^{-2}·s^{-1}) is the mass emission rate of VOC_i, H(t) (cm) is the planetary boundary layer height (PBLH); R_i (molecules·m^{-3}·s^{-1}) is the chemical loss rate of VOC_i; s_i (molecules·cm^{-3}·s^{-1}) is the removal rate of VOC_i; c_i^0 (molecules·m^{-3}) is the background concentration of VOC_i; τ_r (s) is the residence time of air in the box; c_i^a (molecules·cm^{-3}) is the concentration of VOC_i above the planetary boundary layer.

Furthermore, Equations (5a) and (5b) can be rearranged to solve for the VOC emission rate (q_i), yielding Equations (6a) and (6b):

$$q_i = \frac{dc_i}{dt}H(t) + R_i H(t) + s_i - \frac{c_i^0 - c_i}{\tau_r}H(t) \quad \text{for } \frac{dH(t)}{dt} \leq 0 \qquad \text{Equation (6a)}$$

$$q_i = \frac{dc_i}{dt}H(t) + R_i H(t) + s_i - \frac{c_i^0 - c_i}{\tau_r}H(t) - (c_i^a - c_i)\frac{dH(t)}{dt} \quad \text{for } \frac{dH(t)}{dt} > 0 \qquad \text{Equation (6b)}$$

The constraint calculation employed both field measurements and base model simulation. The offline measured VOC concentrations at each site and the online measured diurnal variations of VOCs were used, along with the measured O_3 concentrations and meteorological parameters. In addition, the WRF-CMAQ simulations of the hydroxyl (OH) radical and nitrate (NO_3) radical concentrations, as well as the PBLH, were applied in the calculation. Details for estimating each term in Equations (6a) and (6b) are discussed in the following sections. After the constraint calculation, daily emission profiles of CB05 VOC species in each city, including GZ-U and GZ-CH, were obtained. The gridded emissions in the priori emission inventory at each city point were then replaced by the observation-constrained emissions. Thereby, spatially distributed diurnal VOC emissions for the PRD region, which are ready for input into the chemical transport models, are achieved. Finally, the observation-constrained VOC emission profile was input into the CMAQ model for the constrained simulation, and the outputs were evaluated.

3.3.1 VOC concentrations in the city "box" (c_i)

The measured VOCs at each site were assumed to be representative of each city (including GZ-U and GZ-CH), according to the sampling site selection (Table 3.3). Therefore, the averaged VOC concentrations at each site were used in the calculation of each city and district. Meanwhile, the change rate of VOC concentrations ($\frac{dc_i}{dt}$) was derived from the measured diurnal variations of each VOC. The derivative was calculated by numerical differentiation, *i.e.*, the central difference. As shown in Equation (7), the VOC concentration at time t ($c_{i,t}$) was determined by that at the former ($c_{i,t-1}$) and later ($c_{i,t+1}$) time points, where the time interval (Δt) was one hour.

$$\frac{dc_{i,t}}{dt} = \frac{c_{i,t-1} - c_{i,t+1}}{2\Delta t} \qquad \text{Equation (7)}$$

3.3.2 Chemical loss of VOCs (R_i)

Ambient VOCs are actively involved in photochemical reactions, where the VOCs are oxidized by OH radical, O_3, and NO_3 radical (Wang et al., 2017a). During the daytime, OH radical initiates the oxidation of VOCs, promoting O_3 formation (Atkinson & Arey, 2003; Taccone et al., 2016), while nighttime oxidation by either O_3 or NO_3 removes VOCs, especially alkenes (Warneke et al., 2004; Brown et al., 2011; Wang et al., 2018a). Therefore, the chemical loss of VOCs (R_i) via reactions with OH radical, O_3, and NO_3 radical were estimated in Equation (8):

$$R_i = k_{OH,i}\, c_{OH}\, c_i + k_{O_3,i}\, c_{O_3}\, c_i + k_{NO_3,i}\, c_{NO_3}\, c_i \qquad \text{Equation (8)}$$

where k is the reaction rate constant of oxidants with individual VOC ($cm^3 \cdot molecules^{-1} \cdot s^{-1}$); c is the concentration of oxidants and VOCs ($molecules \cdot cm^{-3}$).

The reaction rate constants (k_{OH}, k_{O_3}, and k_{NO_3}) for each VOC were obtained from the CB05 mechanism (Yarwood et al., 2005) and calculated according to the observed temperature in each city. Meanwhile, observed O_3 concentrations at each site, as well as the model-derived OH and NO_3 concentrations, were adopted in the calculation due to the lack of direct measurements of the radical concentrations (Lu et al., 2018a). As shown in Figure 3.12a, the simulated OH concentrations exhibited a distinct diurnal pattern with a peak around noon, following the diurnal variations of solar radiation intensity. Meanwhile, the modeled average daily maximum OH concentrations ranged from 5.63×10^6 to 9.63×10^6 molecules/cm^3 in the PRD cities, with the daily peak values reaching 17.75×10^6 molecules/cm^3. Previous field campaigns observed that daily maximum OH concentrations varied from 15×10^6 to 26×10^6 molecules/cm^3 at a suburban site in downwind PRD cities during the summer of 2006 (Hofzumahaus et al., 2009; Lu et al., 2012). More recent measurements conducted in the PRD region during autumn reported that the

average daily maximum OH concentrations in suburban area Heshan, Jiangmen was 4.5× 10^6 molecules/cm^3 (Tan et al., 2019), while the peak OH values in urban Shenzhen (SZ) were between 2 × 10^6 and 9 × 10^6 molecules/cm^3 (Yang et al., 2022). Although there were discrepancies between observed and simulated OH concentrations, the modeled peak OH values were comparable with those measured, and the diurnal patterns of OH were reasonably reproduced. Hence, the model-derived OH concentrations were used in the calculations. In addition, the model represented the diurnal variations of NO_3 radical (Figure 3.12b), in which high concentrations were only shown at nighttime due to rapid photo-dissociation and the reaction with NO during daytime (Wayne et al., 1991; Wang et al., 2015a). In terms of the NO_3 levels, the simulated daily nighttime (19:00 – 06:00 CST) average NO_3 concentrations in the PRD cities were 1.53 – 35.94 pptv, which were comparable with the observed mean nighttime NO_3 concentrations of 21.8 ± 1.8 pptv and 7 ± 12 pptv at two downwind sites of the PRD region, respectively (Li et al., 2012; Yan et al., 2019). Thus, the reasonably simulated NO_3 concentrations were also used in the calculation.

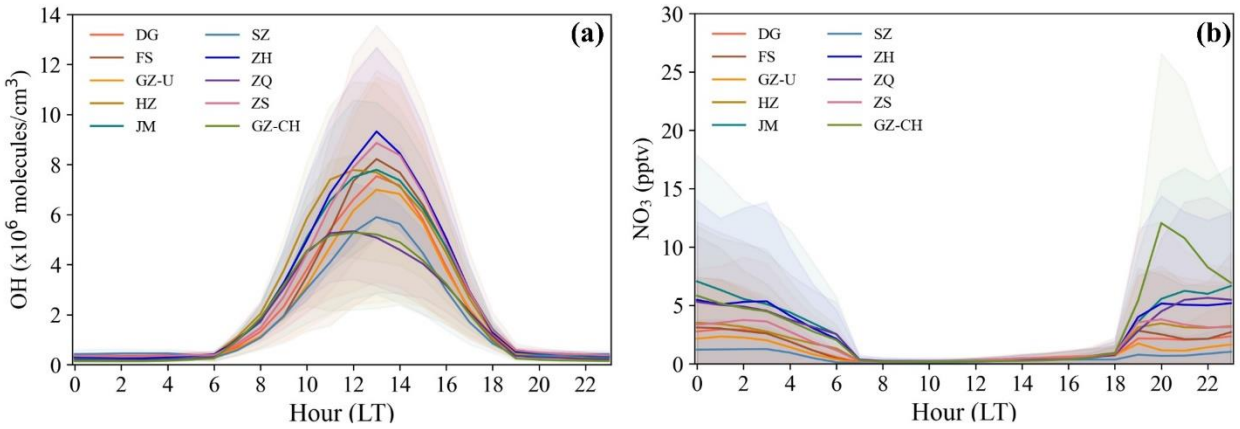

Figure 3.12. Monthly average diurnal variations of simulated OH radical (× 10^6 molecules/cm^3) and NO_3 radical (pptv) in each city and district. The shaded areas represent standard deviations. Note that LT refers to local time, which is the China Standard Time (CST, UTC+8) in this study.

3.3.3 Removal of VOCs (s_i)

Dry deposition is important in removing gaseous pollutants (Seinfeld & Pandis, 2006). The dry deposition flux is usually calculated by Equation (9), where the dry deposition velocity ($v_{d,i}$, cm·s^{-1}) was determined by the nature of the depositing surface and the chemical properties of the depositing species (Wesely, 1989). Existing gaseous dry deposition schemes considered inorganic gases, including sulfur dioxide, O_3, and a small number of organic compounds (Zhang et al., 2023). Most of these organic species are oxygenated VOCs (OVOCs) such as carbonyls, acids, and peroxides, which were efficiently deposited by vegetation stomatal uptake or by the effective Henry's law partitioning onto moist surfaces (Karl et al., 2010; Nguyen et al., 2015; Wu et al., 2021b). However, the OVOC species were not measured in this study, while little information is available on the dry deposition of VOC species other than OVOCs (Goldstein & Galbally, 2007), especially in the urban environment, where the dry deposition loss is very weak due to the large resistance in barren and urban land use (Zhang et al., 2002; Zhang et al., 2003). Thus, the dry deposition of VOCs was not considered in estimating the observation-constrained VOC emissions.

$$s_i = v_{d,i}\, c_i \qquad \text{Equation (9)}$$

3.3.4 Horizontal transport of VOCs out of the city "box" (T)

The contributions of horizontal transport to VOC concentrations within the box (T) are determined by the residence time (τ_r, s) and the background VOC concentrations (c_i^0, molecules·cm^{-3}), as presented in Equation (10a), where positive and negative values represent the horizontal transport of VOCs out of and into the box, respectively.

$$T = -\frac{c_i^0 - c_i}{\tau_r} H(t) \qquad \text{Equation (10a)}$$

$$\tau_r = \frac{L}{u} \qquad \text{Equation (10b)}$$

As presented in Equation (10b), the residence time (τ_r) of air in the area was expected to be the ratio of the length of each city box in the prevailing wind direction (L, cm) to the average observed wind speed (u, cm/s). According to Figure 3.13, southerly and easterly winds prevailed in most PRD cities during the study period (June 2018), except for GZ-U, where north winds accounted for relatively high percentages. Hence, the box length (L) for each city is estimated based on the south-north and west-east length of the minimum envelope for the administrative area of each city. The calculated residence time ranged from 4 hours to 12 hours. Besides, the minimum VOC concentrations measured at the suburban site (GZ-CH) were used as the background concentrations in the calculation.

3.3.5 Vertical dilution of VOCs in the city "Box" (E)

The planetary boundary layer evolves with time as a result of the heat transfer between the surface and atmosphere, which leads to vigorous vertical mixing of the air (Holzworth, 1967). Generally, the PBLH varies diurnally, with low values during the nighttime and higher values during the daytime. The developments of PBLH have a great impact on the concentrations of air pollutants by modulating the box volume and entraining the air above the boundary layer. Physically, when the PBLH decreases ($\frac{dH(t)}{dt} \leq 0$), there is no direct change in the concentration inside the box, as the air originally inside the box is left aloft above the box (Seinfeld & Pandis, 2006). However, when the PBLH increases ($\frac{dH(t)}{dt} > 0$), the box entrains air from the layer above, the free troposphere, where the concentrations of most air pollutants were considerably lower than those in the boundary layer. Subsequently, this entrainment will dilute the emitted pollutants inside the box. Thus, the entrainment of the air above the boundary layer was also considered when the PBLH increases ($\frac{dH(t)}{dt} > 0$).

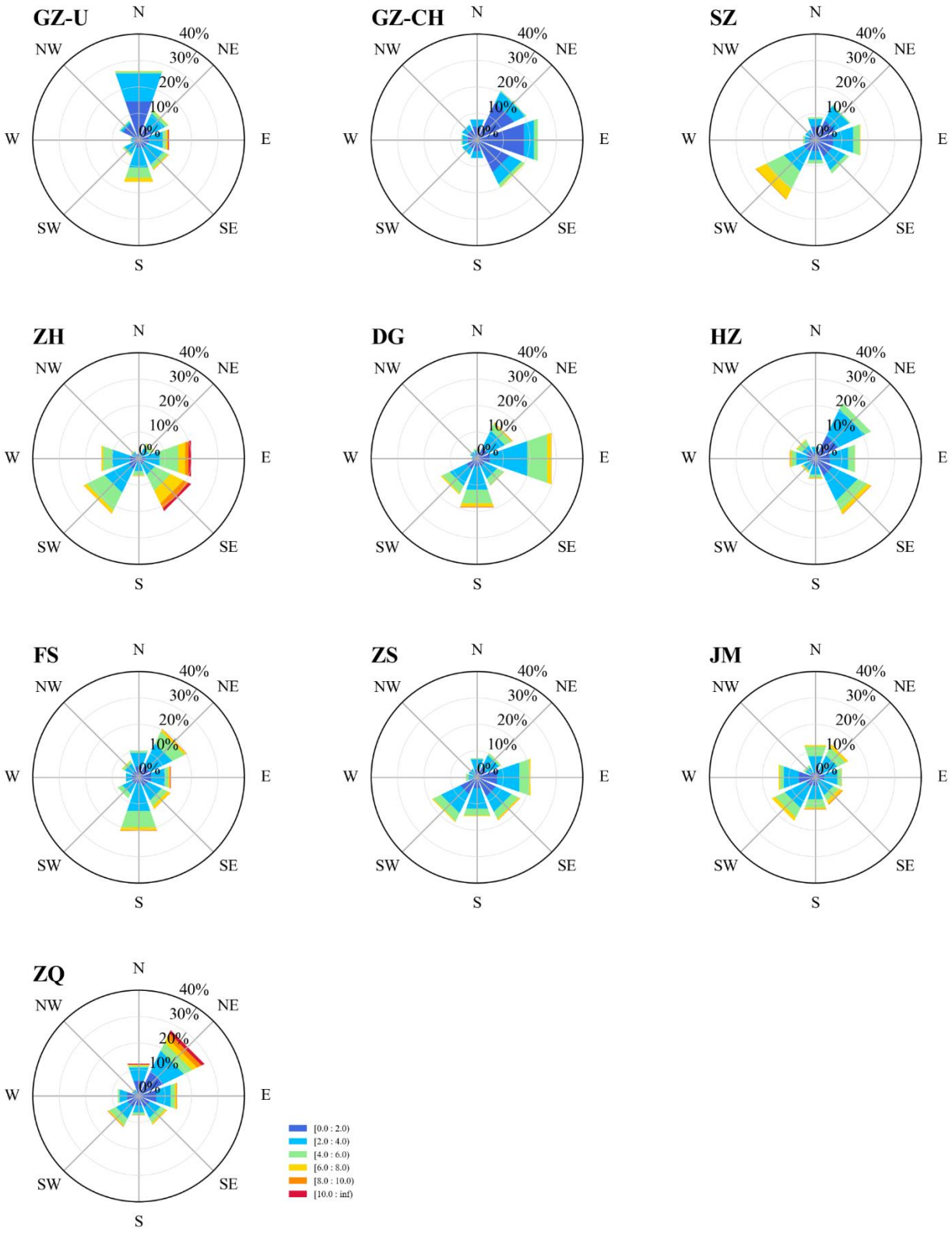

Figure 3.13. Observed surface winds (2 m a.g.l.) in each city and district during June 2018. The wind speeds are presented by colors (unit: m/s).

The vertical dilution rate of the entrainment (E) was calculated by Equation (11a), considering the differences between the VOC concentrations aloft (c_i^a) and inside (c_i) the box, as well as the change rate of PBLH ($\frac{dH(t)}{dt}$). As VOCs were primarily emitted from sources inside the boundary layer, the concentrations of VOCs above the boundary layer (c_i^a) were thereby assumed to be zero for all VOC species.

$$E = -(c_i^a - c_i)\frac{dH(t)}{dt} \qquad \text{Equation (11a)}$$

$$\frac{dH(t)}{dt} = \frac{H_{t-1} - H_{t+1}}{2\Delta t} \qquad \text{Equation (11b)}$$

The mean PBLH in each city and district was extracted from the WRF simulations, as there were no available measurements during the sampling campaign. The PBLH were generally well-simulated with clear diurnal patterns (Figure 3.14), and the daily maximum heights were in line with the recorded seasonal average of 800 – 1000 m during summertime (Guo et al., 2016). Besides, the change rate of the PBLH ($\frac{dH(t)}{dt}$) was calculated by the numerical differentiation of the PBLH at former and later time points (Equation 11b).

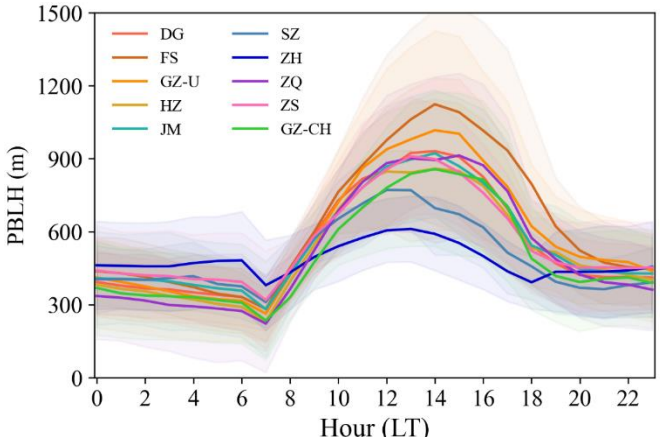

Figure 3.14. Monthly average diurnal variations of simulated PBLH (m) in each city and district during June 2018. The shaded areas represent standard deviations.

3.3.6 Monte Carlo method

The Monte Carlo method, a random sampling experiment, is widely applied to assess the reliability and robustness of systems in a variety of fields (Helton, 1994; Fishman, 2013). It consists of performing a large number of successive simulations with the same model system using a particular set of random variables at each time. By repeating the process, a set of simulation results, each corresponding to a different set of input variables, is obtained (Ang & Tang, 1984), which allows useful quantification of uncertainties in the model outputs based on statistical tests. Benefiting from the common principle, this approach has been progressively used for estimating the uncertainties of bottom-up emission inventories (Kumar et al., 2004; Zhao et al., 2011). Therefore, the uncertainties in the observation-constrained VOC emissions brought by the input parameters were also estimated by the Monte Carlo analysis. Specifically, the targeted input parameter was randomly sampled from the pre-defined ranges. For each random set of inputs, the observation-constrained emission was calculated. This process was repeated 10,000 times to obtain relatively stable results, and the output emissions were expressed as a cumulative distribution function. Finally, the uncertainties associated with the input parameter were quantified according to the statistical values (*e.g.*, mean and percentiles) of the probability distributions of emissions. The propagation of uncertainties in the observation-constrained emissions was quantified and discussed in Section 6.6.

Chapter 4 The Long-standing Global Threat of Surface Ozone

4.1 Introduction

Surface ozone (O_3) poses significant threats to human health (Lippmann, 1991; Fleming et al., 2018; HEI, 2020) and ecosystems (Mills et al., 2018; Emberson, 2020; Unger et al., 2020), and plays a crucial role in climate change (Shindell et al., 2006; IPCC, 2021). It forms through the photochemical reactions of nitrogen oxides (NO_x), volatile organic compounds (VOCs), methane (CH_4), and carbon monoxide (CO) under sunlight (Atkinson, 2000). The O_3 formation chemistry is highly nonlinear and can also be affected by fine particulate matter ($PM_{2.5}$) (Li et al., 2019a). Anthropogenic emissions of O_3 precursors, atmospheric chemistry, and meteorology are the primary drivers shaping the levels and spatiotemporal patterns of ground-level O_3. In addition, stratosphere–troposphere exchange also contributes to tropospheric O_3 levels, particularly in alpine areas and during the winter-spring season (Stohl et al., 2003; Lin et al., 2015). The present-day surface O_3 level has nearly doubled since the preindustrial era (Young et al., 2013; Tarasick et al., 2019), with the highest concentrations and the most pronounced increases observed in rapidly industrializing and urbanizing mid-latitude regions of the Northern Hemisphere (Cooper et al., 2014; Gaudel et al., 2018; Cooper et al., 2020). Currently, ambient O_3 exposure was responsible for a total of 365,000 premature deaths (175,000 – 564,000) globally in 2019 according to the Global Burden of Disease (Murray et al., 2020).

As a global threat, the rise in ground-level O_3 across many regions of the world has been extensively studied (Oltmans et al., 2013; Cooper et al., 2014; Parrish et al., 2014; Cooper et al., 2020). In particular, the framework of the Tropospheric Ozone Assessment Report (TOAR) has provided a comprehensive evaluation of the historical and present-day situations of global O_3

pollution (Tarasick et al., 2019) and its impacts on human health (Fleming et al., 2018), ecosystems (Mills et al., 2018), and climate (Gaudel et al., 2018). However, changes in O_3 levels have not been temporally consistent nor spatially homogeneous, due to different emission patterns and meteorological variabilities. The first phase of the TOAR project included O_3 records up to 2014, but more recent global O_3 observations have not been assessed. Moreover, ground-level O_3 observation data in many developing and underdeveloped regions are scarce or unavailable, making current global O_3 studies incomplete. For example, in China, the world's most populous country, a nationwide O_3 monitoring network was not established until 2013. Although the recent upsurge of O_3 in China has garnered growing attention (Lu et al., 2018b; Li et al., 2019a; Liu & Wang, 2020b), this increasing trend has not been analyzed within the same time frame and from a global perspective.

In addition to recognizing the current status of global O_3 pollution, understanding past O_3 pollution control strategies and the climatic impacts is crucial for effectively combating global O_3 pollution. Decades of relentless efforts have been undertaken by developed countries and regions to mitigate O_3 pollution. In the United States (US) and Europe, anthropogenic emissions of VOCs and NO_x have been substantially reduced, followed by significant declines in O_3 levels in the early 2010s (Simon et al., 2015; Xing et al., 2015; Lin et al., 2017; Yan et al., 2018). Nevertheless, O_3 pollution persists in these regions. The effectiveness of traditional emission reduction strategies in decreasing O_3 concentrations is diminishing (Sicard et al., 2021a), while this problem is further exacerbated by the climate penalty due to the intrinsic link between O_3 and climate (Rasmussen et al., 2013; Colette et al., 2015; Lin et al., 2020; Laughner et al., 2021; Crooks et al., 2022). High O_3 episodes are also increasingly related to more frequent extreme events under climate change, such as heatwaves (Lin et al., 2020) and wildfires (McClure & Jaffe, 2018). More notably, many

parts of the world, particularly in East and Southeast Asia, are still grappling with worsening O_3 pollution in the early stages of establishing air quality control regulations (Anenberg et al., 2018; Gaudel et al., 2020; Liu & Wang, 2020b). Therefore, it is imperative to integrate anthropogenic emission reductions with climate change coordinately for more efficient O_3 pollution control.

In this chapter, a comprehensive analysis of ground-level O_3 measurements from 2013-2014 onward was conducted with the recently available O_3 datasets in China and some developing countries, enriching the global O_3 database. Global O_3 distributions and variations in warm seasons throughout the past two decades were systematically examined in the same temporal context. Impacts of air pollution control policies and climate variables on O_3 abatement were further evaluated. Finally, a feasible strategy that synergizes ozone pollution control with multi-pollutant joint control and climate change mitigation is suggested to address this long-standing global threat.

4.2 Global O_3 distributions

By compiling ground-level O_3 measurements from 4,308 monitoring stations worldwide during warm seasons (April-September in the Northern Hemisphere and October-March in the Southern Hemisphere) from 2014 to 2019 (Section 3.1.1 and Table 3.1), evidence confirms that surface O_3 pollution is emerging globally. Figure 4.1 illustrates the global distribution of the mean monthly 95th percentile daily maximum 8-hour average (DMA8) O_3 during the study period. This 95th percentile represents high O_3 values of regulatory concern (Simon et al., 2015; Yan et al., 2018), and was calculated monthly using the nearest rank method with linear interpolation. High levels of DMA8 O_3 were observed in the mid-latitude band of the Northern Hemisphere (30°-50° N), consistent with previous observations and model simulations (Gaudel et al., 2018; Cooper et al., 2020). This global distribution is in line with the intensity of anthropogenic activities, as indicated

by tropospheric NO_2 column densities (Figure 4.3). Notably, East Asian countries, including China, South Korea, and Japan, experienced the most severe O_3 pollution during this period. High DMA8 O_3 levels were also observed in north India and Mexico City, reaching over 90 ppbv and 80 ppbv, respectively (Table 4.1), despite the limited availability of observational data. Meanwhile, although O_3 levels were generally lower in most parts of the US and Europe, elevated DMA8 O_3 were still recorded in the western US and central Europe, underscoring the ongoing need for O_3 pollution control.

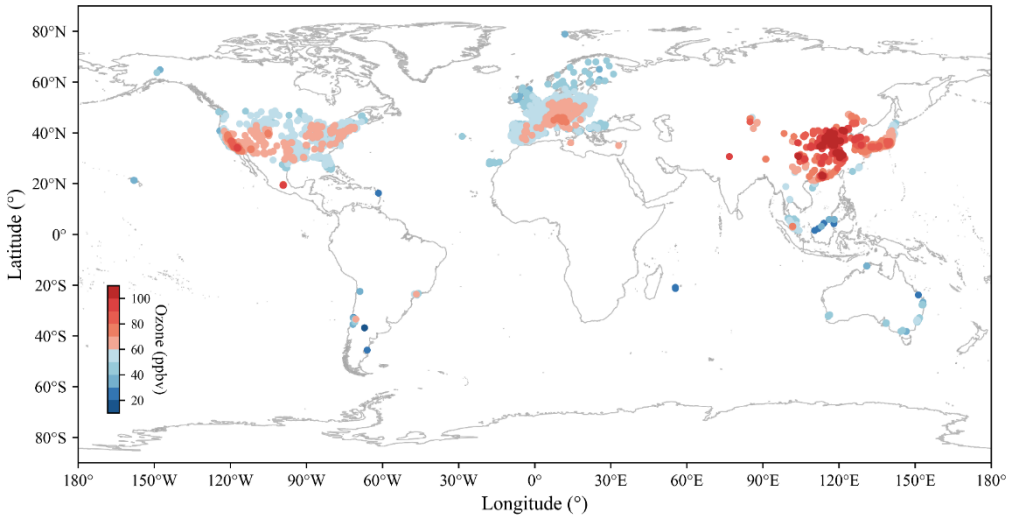

Figure 4.1. Global distribution of average monthly 95th percentile DMA8 O_3 in warm seasons of 2014 – 2019. Note that time frames are different for Japan (2013 – 2017), Malaysia (2014 – 2018), and 4 stations in Victoria, Australia (2014 – 2018) due to data availability (see Section 3.1.1).

Furthermore, the number of days when DMA8 O_3 levels exceeding the World Health Organization (WHO) guideline value of 47 ppbv (NDGT47) and the benchmark of 60 ppbv (NDGT60) per year during warm seasons of 2014 – 2019 are depicted in Figure 4.2. The spatial distribution of the number of O_3 exceedance days closely mirrors that of the average DMA8 O_3. In East Asia, India, and Mexico, O_3 levels exceeded the WHO guideline on over half of the days during warm seasons (> 90 days), while frequent exceedances also occurred in the western US and

southern Europe. Even with a more lenient standard (NDGT60), which aligns with the median of global O_3 air quality standards (Figure 4.4), the number of non-attainment days in these regions remained significant, with an annual average of 90 days in north India, 77 days in Mexico City, 64 days across China, 51 days in South Korea, and 42 days in Japan. These frequent high O_3 days highlighted the severity of O_3 exposure in densely populated regions. In addition, although O_3 levels and high O_3 exceedances in Australia were relatively lower than those in the Northern Hemisphere, severe wildfires beginning in November 2019 resulted in 11 days of NDGT47 across the country during November-December alone, comparable to the annual average of 12 days in warm seasons. Thus, climate extremes also have an undeniable impact on regional O_3 air quality.

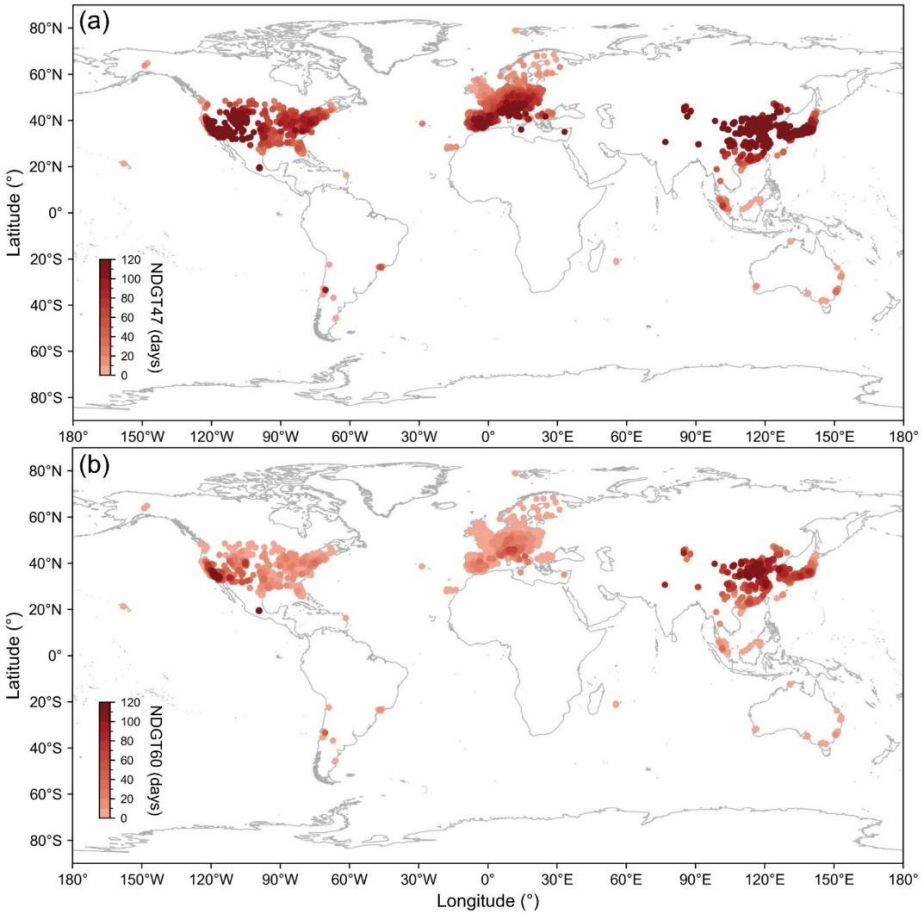

Figure 4.2. Average number of days with DMA8 O_3 concentrations greater than (a) 47 ppbv (NDGT47) and (b) 60 ppbv (NDGT60) per year in warm seasons of 2014 – 2019.

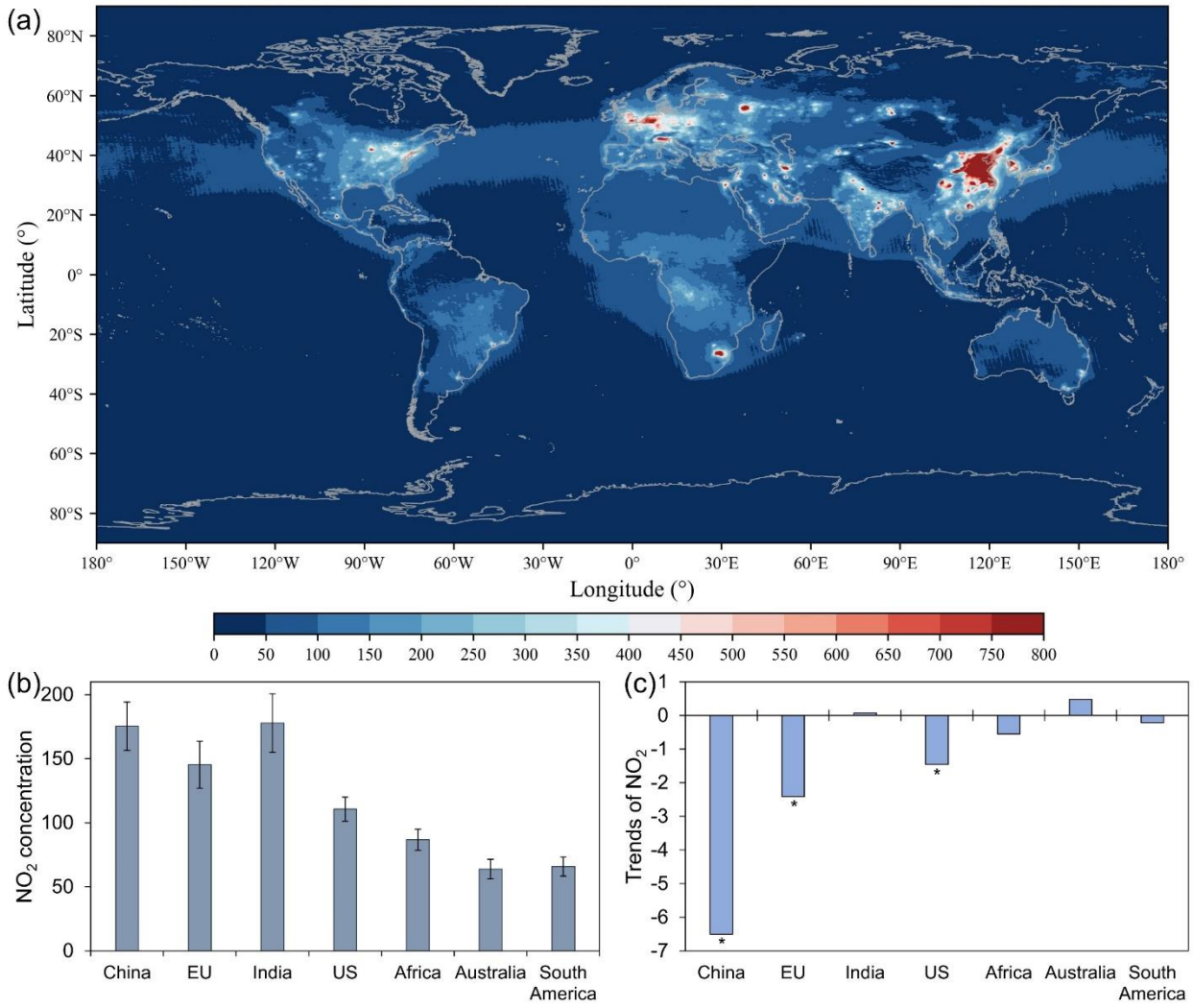

Figure 4.3. Tropospheric NO_2 column concentrations during 2014 – 2019. (a) Global distribution of monthly average concentrations (unit: 10^{13} molecules/cm^2). (b) Average concentrations in different countries/regions (unit: 10^{15} molecules/cm^2). (c) Trends in different countries/regions with asterisks indicating statistically significant trends ($p < 0.05$) (unit: 10^{15} molecules/cm^2/year).

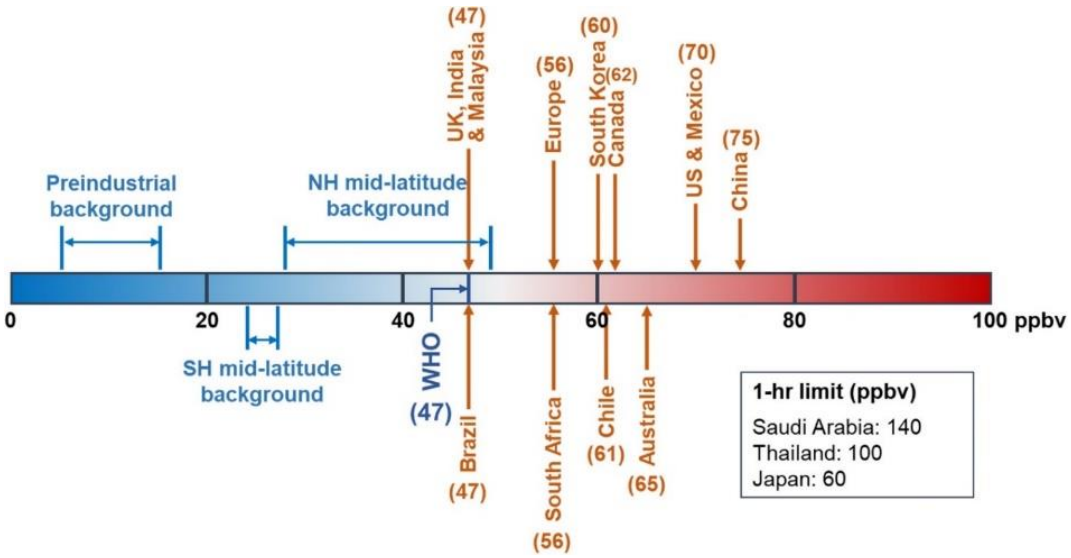

Figure 4.4. Current O_3 air quality standards for selected countries and the WHO guideline. Numbers in parentheses are DMA8 O_3 limits (ppbv); the inserted box lists 1-hour limits for countries without DMA8 limits. Mass-based standards ($\mu g/m^3$) were converted to ppbv under standard conditions (1,013 hPa, 273 K). NH: Northern Hemisphere; SH: Southern Hemisphere.

4.3 Trends of global O_3

Trends in O_3 variations were estimated using ordinary linear regression applied to the monthly anomalies of the 95th percentile DMA8 O_3 concentrations in warm seasons during 2014 – 2019 and 2000 – 2019, following the method proposed by Cooper et al. (2020). The use of anomalies eliminates the masking effect of seasonality, thereby isolating the forced component from the natural seasonal cycle. This enables robust spatial and temporal comparisons across regions worldwide and reduces the influence of systematic measurement error. Moreover, by standardizing data to a baseline, trends derived from anomalies are less sensitive to biases introduced by missing data. Figure 4.5 illustrates the global distribution of O_3 trends from 2014 – 2019, providing the first comparison of recent O_3 trends in China within the same time frame. Widespread increases in 95th percentile DMA8 O_3 were observed in China during this period, with almost half of the

stations recording significant upward trends and a nationwide increasing rate of 2.88 ± 0.14 ppbv/year (p<0.05) (Table 4.1). This national growth rate was much higher than those in other countries and regions (Table 4.1) and even surpassed previous reports of 2.4 ppbv/year across 243 stations in China during warm seasons from 2013 – 2019 (Lu et al., 2020), indicating increasingly severe O_3 pollution in China primarily driven by anthropogenic factors (Li et al., 2019a). In Japan and South Korea, although the national O_3 growth rates were much lower than those in China, 0.09 ± 0.21 ppbv/year (p = 0.87) in Japan and 0.73 ± 0.17 ppbv/year (p = 0.16) in South Korea, significant increases also occurred at 12% and 24% of the stations, respectively. Conversely, an overall decline in O_3 was observed in Malaysia (-0.80 ± 0.18 ppbv/year, p = 0.13) during this short-term period, whereas Figure 4.6 depicts a significant rise in O_3 at 41% of stations in Peninsular Malaysia over a longer period (2000 – 2018). Rapidly changing anthropogenic emissions over Southeast Asia have resulted in enhanced O_3 burdens in these regions (Wang et al., 2022d), while inter-annual variations of meteorological conditions have also contributed to slight recent decreases. Besides, limited observation records have made it difficult to obtain a complete understanding of O_3 trends in Thailand and India, despite a significant increase of 1.95 ± 0.23 ppbv/year (p < 0.05) and a decreasing trend of -0.67 ± 0.37 ppbv/year (p = 0.51), respectively.

Benefiting from effective reductions of anthropogenic emissions, the 95th percentile DMA8 O_3 has been reported to decrease by -2 – -1 ppbv/year in the US (Simon et al., 2015) and -0.42 ppbv/year in Europe (Yan et al., 2018) during 1998 – 2013. However, these effects diminished in 2000 – 2019, with decreasing rates of -0.35 ± 0.01 ppbv/year (p < 0.05) in the US and -0.05 ± 0.01 ppbv/year (p = 0.26) in Europe (Figure 4.6). Notably, elevated O_3 levels have emerged in recent years, as O_3 increases were recorded at 6% and 25% of the stations during 2014 – 2019, mostly in the western US and central Europe (Figure 4.5). Similar trends were also observed in Mexico City,

where O_3 decreased at -0.62 ± 0.02 ppbv/year ($p < 0.05$) during 2000 – 2019 and at a slower rate of -0.08 ± 0.15 ppbv/year ($p = 0.87$) in 2014 – 2019. These recent rises of DMA8 O_3 were likely attributed to the slowdown of emission reductions (Jiang et al., 2018) and meteorological variations (Lin et al., 2020). Moreover, although O_3 levels were generally lower in the Southern Hemisphere (Figure 4.1), significant increases were recorded in Australia during 2014 – 2019 (1.02 ± 0.14 ppbv/year, $p < 0.05$) compared to a gradual decrease of -0.05 ± 0.01 ppbv/year ($p < 0.26$) in 2000 – 2013. In particular, the megafire in November-December 2019 elevated O_3 levels in Australia by over 30% above the decadal average (2000 – 2019), causing significant air quality deterioration in eastern Australian cities (Ryan et al., 2021). Furthermore, a long-term study has indicated that global warming is partially responsible for the continuous increase in tropospheric O_3 in the Southern Hemisphere since 1990 (Lu et al., 2019b). Therefore, these findings highlight the impacts of meteorological variabilities and climate extremes on O_3 pollution, which may become more pronounced under climate change, making O_3 pollution mitigation more challenging.

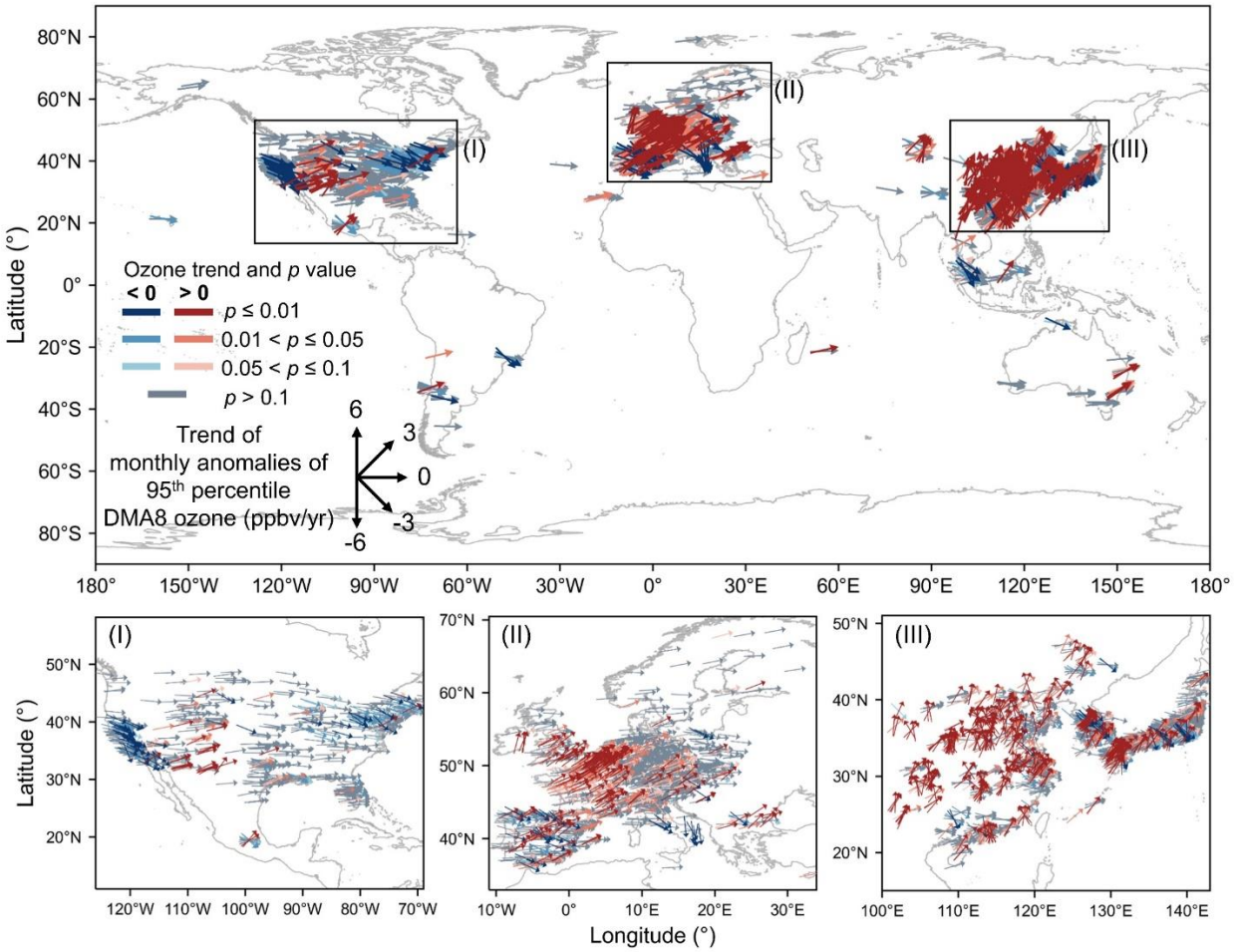

Figure 4.5. Trends in monthly 95th percentile DMA8 O_3 anomalies in warm seasons during 2014 – 2019. Insets zoom into regions with arrow overlap: (I) the US, (II) Europe, and (III) East Asia. Arrow color denotes trend direction (positive/negative) and statistical significance (*p*-value).

Table 4.1. Mean value of monthly 95th percentile DMA8 O_3, annual average NDGT60, and trends of monthly 95th percentile DMA8 O_3 in each country/region in warm seasons during 2014 – 2019.

Country/Region (time frame)	**Mean ± 95% C.I.**[a] (ppbv)	**NDGT 60** (days)	**NDGT 47** (days)	**National average rate ± 95% C.I.**[b] (ppbv/yr)	**Change rate ± 95% C.I.**[c] (ppbv/yr)	**Range of change rates**[d] (ppbv/yr)	**Number of sites with positive trends** ($p < 0.05$)	**Number of sites with negative trends** ($p < 0.05$)
Australia (2014 – 2019)[#]	45.5 ± 2.1 (45)[e]	3	12	1.02 ± 0.14 ($p < 0.05$)	1.85 ± 0.54 (14)[f]	-1.63 – 2.53	13	1
Brazil (2014 – 2019)	54.0 ± 3.8 (11)	7	27	-1.36 ± 0.18 ($p < 0.05$)	-2.16 ± 0.60 (4)	-3.07 – -1.72	0	4
Chile (2014 – 2019)	34.8 ± 5.8 (24)	3	13	0.14 ± 0.07 ($p = 0.54$)	0.32 ± 1.03 (6)	-1.68 – 1.39	4	2
China (2014 – 2019)	84.6 ± 1.0 (765)	64	101	2.88 ± 0.14 ($p < 0.05$)	4.87 ± 0.33 (391)	-6.34 – 17.03	372	19
Europe (2014 – 2019)	55.3 ± 0.4 (1,317)	11	53	0.68 ± 0.12 ($p = 0.07$)	1.38 ± 0.16 (373)	-6.58 – 5.72	326	47
India (2014 – 2019)	91.3[†] (1)	90	115	-0.67 ± 0.37 ($p = 0.51$)	-0.67[†] (0)	-0.67[†]	0	0
Japan (2013 – 2017)	70.5 ± 0.4 (1,085)	42	98	0.09 ± 0.21 ($p = 0.87$)	1.10 ± 0.43 (191)	-5.82 – 6.52	125	66
South Korea (2014 – 2019)	76.2 ± 1.0 (305)	51	98	0.73 ± 0.17 ($p = 0.16$)	1.55 ± 0.55 (100)	-6.79 – 7.59	73	27
Malaysia (2014 – 2018)	49.3 ± 4.2 (33)	7	27	-0.80 ± 0.18 ($p = 0.13$)	-2.10 ± 1.71 (8)	-4.34 – 3.61	1	7
Mexico (2014 – 2019)	81.8 ± 4.0 (15)	77	122	-0.08 ± 0.15 ($p = 0.87$)	0.48 ± 2.63 (5)	-2.93 – 3.38	3	2
Thailand (2014 – 2019)	52.7 ± 4.9 (3)	15	33	1.95 ± 0.23 ($p < 0.05$)	3.45 ± 2.78 (2)	2.03 – 4.87	2	0
United States (2014 – 2019)	60.1 ± 0.6 (704)	23	82	-0.16 ± 0.06 ($p = 0.43$)	-0.67 ± 0.24 (144)	-5.01 – 3.65	45	99

[a] Mean value of monthly 95th percentile DMA8 O_3 across all eligible stations (see Section 3.1.1). 95% C.I. = two-tailed 95% confidence interval.

[b] National average trend calculated using the single time series of monthly anomalies of 95th percentile DMA8 O_3 averaged across all eligible stations.

[c] Average of the significant ($p < 0.05$) trends of monthly 95th percentile DMA8 O_3.

[d] Range of the significant ($p < 0.05$) trends of monthly 95th percentile DMA8 O_3.

[e] Number of eligible stations meeting the data capture criteria described in Section 3.1.1.

[f] Number of stations with significant ($p < 0.05$) trends of monthly 95th percentile DMA8 ozone.

[#] Time frame is 2014 – 2018 for four stations in Victoria, Australia.

[†] Not available (NA) because there is only one station

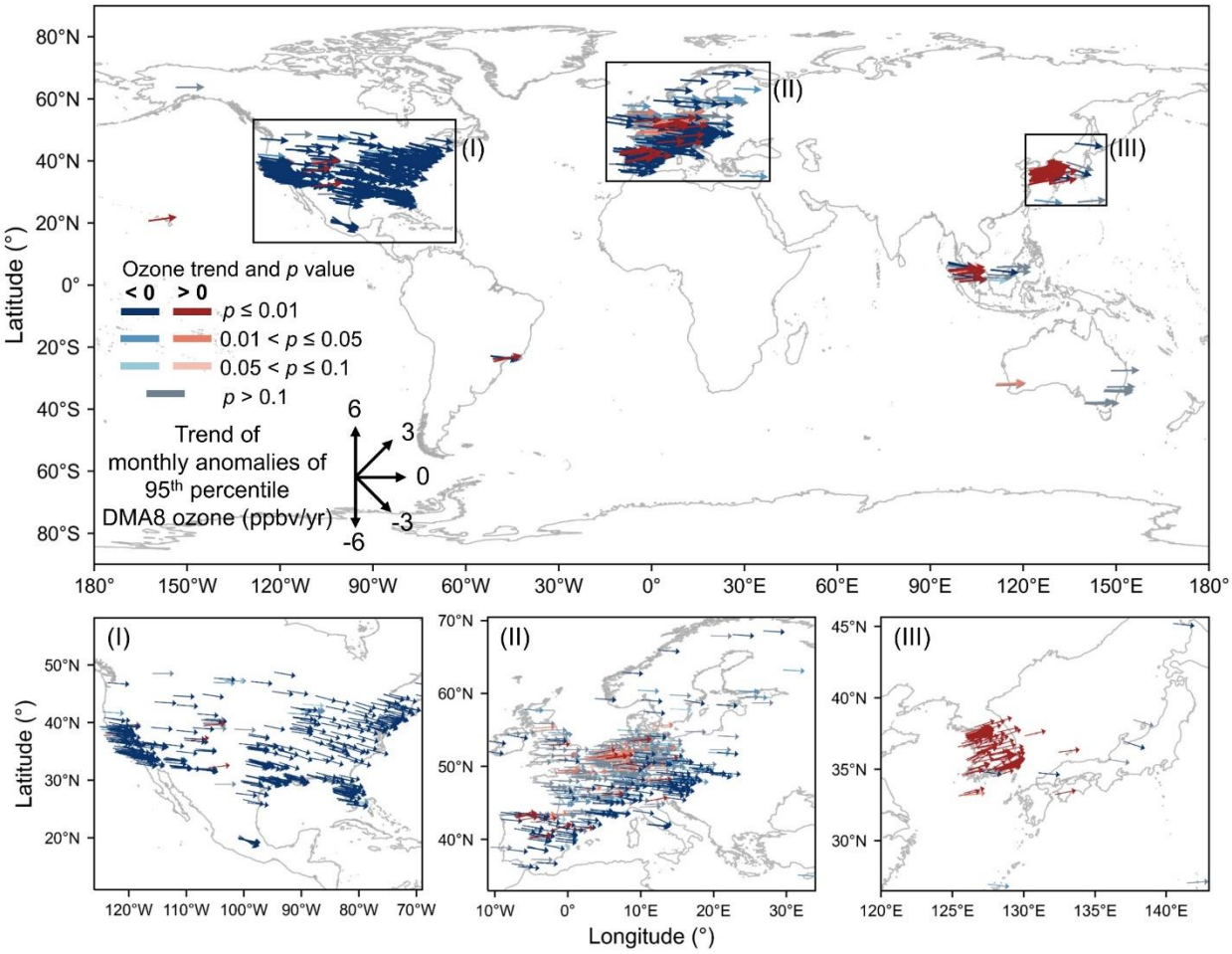

Figure 4.6. Trends in monthly 95th percentile DMA8 O_3 anomalies in warm seasons during 2000 – 2019. Insets zoom into regions with arrow overlap: (I) the US, (II) Europe, and (III) East Asia. Arrow color denotes trend direction (positive/negative) and statistical significance (*p*-value). Note that time frames are different for Japan (2000 – 2017), South Korea (2001 – 2019), Malaysia (2000 – 2018), and 4 stations in Victoria, Australia (2000 – 2018) due to data availability.

4.4 Impacts of anthropogenic emission control strategies on O_3 pollution

O_3 pollution is primarily driven by anthropogenic emissions of its precursors through photochemical production. Figure 4.7 compares historical O_3 concentrations in the US, Europe, and China, showing remarkable declines in DMA8 O_3 in the US over the past four decades and a

notable increase in China in recent years. Decadal efforts have been undertaken to reduce peak O_3 levels in the US throughout past decades, achieving staged successes in the 2000s. Since the 1980s, the US EPA has implemented VOC emission reductions as O_3 production in US cities was thought to be VOC-limited. During this period, significant decreases in O_3 concentrations mainly occurred in the western US, with the peak O_3 level in Los Angeles declining by over 50% at a rate of -3.66 ± 0.49 ppbv/year ($p < 0.05$) from 1980 to 2000. However, it was not until 1998 when strict NO_x-targeted emission reductions (Figure 2.3), the NO_x State Implementation Plan Call Regulations, were enacted (USEPA, 1998a), that O_3 pollution was effectively controlled across the US. In contrast, although European countries introduced back-to-back emission control policies targeting NO_x and VOCs around 1990 (UNECE, 1988 & 1991) with substantial reductions thereafter (Figure 2.2), peak O_3 levels were not consequently mitigated across Europe and even slightly increased after 2014 (Figure 4.5 and Table 4.1). This dilemma could be largely attributed to variations in climatic factors. Moreover, despite continuous interventions on VOC emissions in the US, recent increases in VOC emissions (Figure 2.3), due mainly to the extensive use of volatile chemical products (McDonald et al., 2018; Coggon et al., 2021) and enhanced wildfires (Wentworth et al., 2018), have partially hindered the national O_3 reductions (Table 4.1). Thus, updates in targeted emission reduction plans are still needed for further improving O_3 air quality.

In China, emissions of NO_x and VOCs continued to increase over the past decades (Figure 2.4) until 2013 and 2018, respectively, when two phases of Clean Air Action plans were promulgated (CSC, 2013 & 2018). The first nationwide air pollution control strategy primarily focused on $PM_{2.5}$, along with effective regulations on NO_x emissions. However, unexpected and extensive O_3 surges occurred at the fastest increasing rate in the world during the same period (Figure 4.5 and Table 4.1). This worsening O_3 pollution has posed a new challenge to China's air quality management.

On the one hand, although NO_x concentrations significantly declined in China from 2014 to 2019, their levels remained high, particularly over the North China Plain (Figure 4.3). Instead of shifting the O_3 formation regime toward NO_x-limited, as in the US and Europe (Jin et al., 2017), these decreases in NO_x accelerated O_3 production in urban China, where O_3 chemistry is VOC-sensitive. On the other hand, substantial reductions in $PM_{2.5}$ have not only enhanced solar radiation but also reduced the aerosol uptake of hydroperoxyl (HO_2) radicals, thereby prompting O_3 photochemistry in China, as indicated by recent studies (Li et al., 2019a; Shao et al., 2021). Additionally, meteorological variabilities also contributed to these short-term O_3 increases (Li et al., 2020; Liu & Wang, 2020a). Therefore, the unintentional rise of O_3 in China has alarmed us that coordinated air pollution control strategies, considering multiple pollutants and their formation mechanisms (including both chemical and physical processes), are urgently needed.

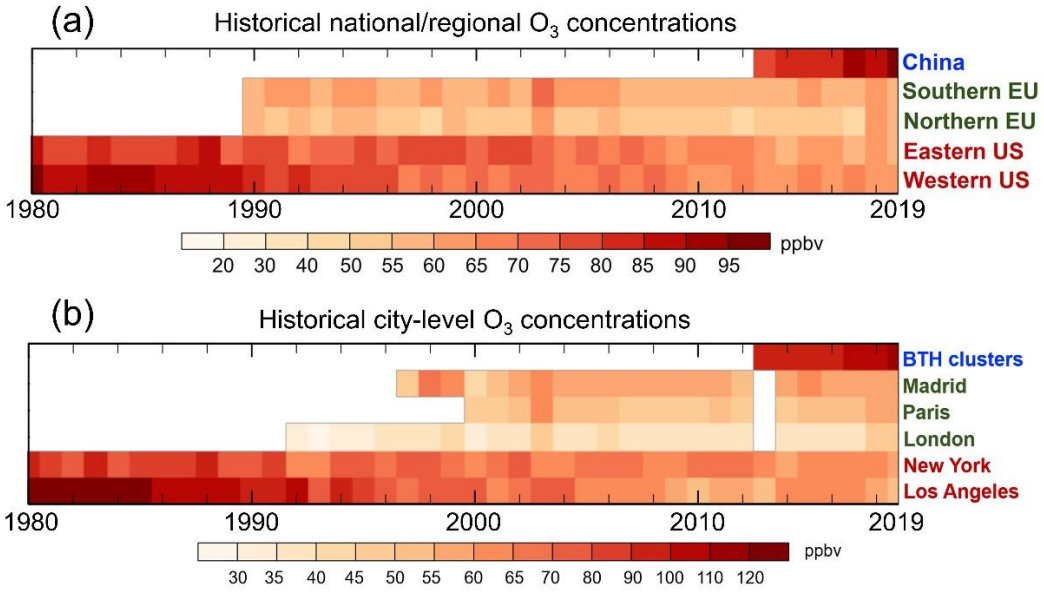

Figure 4.7. O_3 concentrations over time in (a) different countries and regions and (b) representative cities. The monthly 95th percentile DMA8 O_3 in warm seasons is averaged over China, the southern EU (south of 50°N), northern EU (north of 50°N), eastern US (east of 100°W), and western US (west of 100°W). BTH: the Beijing-Tianjin-Hebei city cluster in China.

4.5 Influences of climate extremes on O_3 pollution

In addition to anthropogenic drivers, O_3 pollution is also modulated by a changing climate through variations in natural emissions, chemical composition and processes, large-scale circulation and transport patterns, and climate extremes, such as intensified heatwaves, droughts, wildfires, and heavy precipitation. High O_3 pollution episodes have commonly been observed to co-occur with heatwaves, amplifying the adverse effects on human health and ecosystems (Gao et al., 2023). Recently, during the summer of 2022, widespread heatwaves occurred in the Northern Hemisphere mid-latitude band. Figure 4.8 illustrates marked O_3 enhancements of 4 – 16 ppbv across the eastern US, western and central Europe, and eastern China in June-July 2022 compared to the same period in 2021, corresponding to regions experiencing elevated temperatures. This spatial alignment between summertime O_3 anomalies and high temperatures provides a clear demonstration of the close relationship between O_3 pollution and heat events. Moreover, droughts further exacerbate the frequency of O_3 pollution episodes through not only meteorological processes but also vegetation feedbacks, especially the reduced stomatal uptake of O_3 (Lin et al., 2020), which has become increasingly severe under a warming and drying climate (Zhang & Wang, 2016; Lei et al., 2022). In addition, as discussed in previous Sections 4.2 and 4.3, wildfires have significantly elevated regional O_3 concentrations in Australia. Studies have also revealed that recent frequent wildfires across western US forests, with increasing burned areas and smoke days (NIFC, 2024), greatly enhanced O_3 production in downwind urban areas (McClure & Jaffe, 2018; Xu et al., 2021). Among the numerous factors contributing to the recent rise in fire activity, anthropogenic forcing on increasingly warm, dry conditions has created a more favorable fire environment that significantly enhanced fuel aridity over the past two decades and is projected to continue (Abatzoglou & Williams, 2016; Higuera et al., 2021; Zhuang et al., 2021). Overall, these

climate-driven O_3 episodes are becoming increasingly severe due to more frequent climate extremes, while the escalating climate penalty has emerged as a key contributor to O_3 pollution, particularly in developed regions where the potential for further reductions in anthropogenic emissions is lessening, such as in Europe (Colette et al., 2015; Schnell et al., 2016). Therefore, it is essential to integrate climate change mitigation in O_3 pollution control strategies, as climate variability exerts significant impacts.

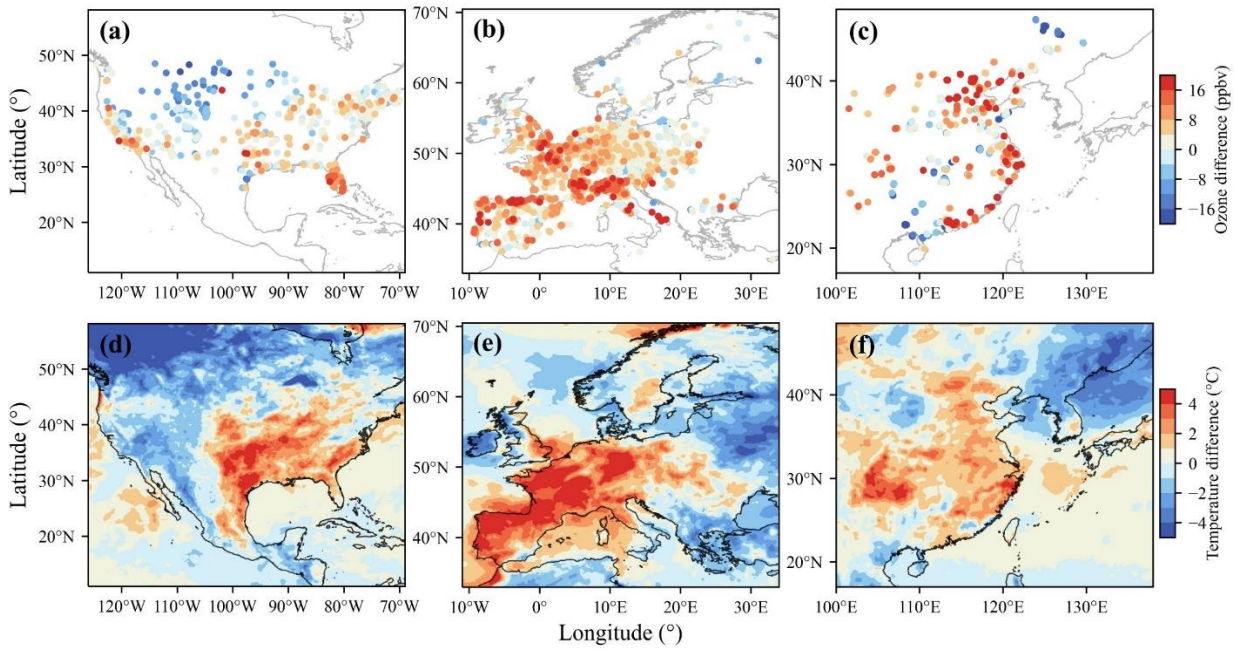

Figure 4.8. Spatial distribution of O_3 and temperature anomalies in June-July 2022 relative to 2021. (a-c) The 95th percentile DMA8 O_3 concentration anomalies (ppbv). (d-f) The anomalies of daily maximum surface temperature (°C). (a, d) North America, (b, e) Europe, and (c, f) East Asia.

4.6 Implications

Surface O_3 pollution is a long-standing global concern with intricate challenges to alleviate. By compiling ground-level measurements from air-quality monitoring stations across 48 countries, this chapter presents an emerging challenge of O_3 pollution worldwide. High levels of daily peak

O_3 were observed primarily in the mid-latitude band of the Northern Hemisphere, and the O_3 air quality standard was frequently exceeded in many parts of the world, indicating widespread and severe O_3 exposure. More importantly, significant increases in surface O_3 concentrations from 2013/2014 onwards have been evident in many countries, demonstrating this emerging air quality problem. Past O_3 pollution control strategies in some developed countries and regions have showcased the effectiveness of emission reductions targeting key O_3 precursors, *i.e.*, NO_x and VOCs. However, the unintended yet rapid rise of O_3 in China since 2013, driven by declining NO_x and $PM_{2.5}$ concentrations, emphasizes the necessity of coordinated control policies for multiple pollutants. Furthermore, a changing climate characterized by warmer and drier conditions not only modulates short-term O_3 variations but also enhances the severity and frequency of climate extremes, which facilitate high O_3 pollution episodes. This climate penalty on O_3 is intensifying under global warming, highlighting another challenge to O_3 pollution mitigation. To address this complex issue, a synergistic O_3-climate control strategy incorporating joint O_3-$PM_{2.5}$ control is essential. First, O_3 precursors, $PM_{2.5}$, and greenhouse gases share common emission sources, enabling their joint regulation. Second, the underlying physical and chemical processes of O_3, $PM_{2.5}$, and climate change are interconnected, so that merely controlling one factor may inadvertently exacerbate others. Third and most critically, both air pollution and climate change exert harmful effects on human health and ecosystems, building up the foundation for integrated control policies. Therefore, by strategically leveraging the shared emission sources, interacting mechanisms, and common health and environmental risks associated with O_3 pollution and climate change, holistic management offers a viable pathway to effectively address the current challenges of global O_3 pollution.

Chapter 5 Summer Ozone Pollution Episodes in South China and Transport Impacts from Southeast Asia

5.1 Introduction

Surface ozone (O_3) pollution remains a persistent global challenge due to its detrimental effects on public health (Fleming et al., 2018), ecosystems (Unger et al., 2020), and the climate system (Shindell et al., 2006). Tropospheric O_3 is a secondary air pollutant formed through complex photochemical reactions involving precursors such as nitrogen oxides (NO_x) and volatile organic compounds (VOCs) under sunlight (Atkinson, 2000). In recent decades, surface O_3 pollution has exacerbated worldwide (Parrish et al., 2014; Gaudel et al., 2018; Tarasick et al., 2019), particularly in China and Southeast Asia (Lyu et al., 2023; Lu et al., 2025). Since the implementation of China's nationwide Clean Air Action Plan in 2013, fine particulate matter ($PM_{2.5}$) pollution has been successfully mitigated, yet O_3 pollution has unexpectedly emerged (Lu et al., 2020). Alarmingly, high O_3 episodes—where daily maximum concentrations exceed ambient air quality standards—are frequently observed in key regions such as the North China Plain, the Yangtze River Delta, and the Pearl River Delta (PRD) (Wang et al., 2017a). This surge in O_3 pollution is driven by multiple factors, including uncoordinated controls of VOCs and NO_x emissions (Liu & Wang, 2020b), reduced aerosol uptake of reactive gases (Li et al., 2019a), changing meteorological conditions, and increasing transboundary transport of pollutants (Liu & Wang, 2020a).

South China has unique O_3 pollution characteristics, with peak O_3 levels in autumn and the lowest levels in summer (Zheng et al., 2010). Extensive research has explored the drivers behind this autumnal O_3 pollution. Favorable weather conditions, including continental anticyclones, downdrafts around tropical cyclones, stagnant wind fields, and sea-land breeze circulations,

prompt local photochemical O_3 production, transport polluted air masses from inland China, and facilitate the accumulation of O_3 and its precursors (Ding et al., 2004; Huang et al., 2006; Jiang et al., 2015; Xue et al., 2016; Wang et al., 2018b; Wang et al., 2019c; Zeren et al., 2019; Liu et al., 2021). These insights have informed targeted O_3 control strategies, which have partially alleviated autumn O_3 levels in South China. For instance, Liu et al. (2019) reported a decline in autumn O_3 concentrations in the PRD region at -1.27 ppbv/yr from 2013 to 2017, while Zeren et al. (2022a) observed a similar decrease of -2.04 ppbv/yr in Hong Kong during the same period. Additionally, long-term measurements at a regional background station in South China also documented a slowing autumn O_3 increase, from 0.68 ppbv/yr (1994 – 2007) to 0.40 ppbv/yr (1994 – 2018). However, it is noteworthy that summer O_3 at this background station increased at the fastest rate among all seasons, reaching 0.50 ppbv/yr and surpassing the autumn trend (Wang et al., 2009; Wang et al., 2019b). Moreover, Li et al. (2020) reported an acceleration in the upward trend of summer O_3 across the PRD, with rates increasing from 0.60 ppbv/yr (2013 – 2017) to 1.1 ppbv/yr (2013 – 2019).

In contrast to the well-studied autumnal O_3 pollution, summer has traditionally been regarded as the cleanest season in South China, benefiting from the influx of clean, humid marine air masses with weak photochemical activity brought by the East Asian Summer Monsoon—the dominant large-scale weather system during this period (He et al., 2008; Zhao et al., 2010). However, recent studies revealed that elevated O_3 levels in summer and late spring over South China are increasingly linked to the summer monsoon, influenced by changes in meteorological conditions and transboundary transport (Zhou et al., 2022; Zhang et al., 2024b). Wang et al. (2019b) further highlighted a concerning rise in O_3 within marine air masses transported to South China during summer, likely driven by enhanced anthropogenic emissions in upwind Southeast Asia. Indeed,

rapidly growing emissions in Southeast Asia since the 2010s (Chen & Mauzerall, 2021; Cui et al., 2022) have led to a significant rise in O_3 levels over these regions (Wang et al., 2022d). Unlike the free tropospheric O_3 peak at 2 – 6 km in spring resulting from the transport of uplifted biomass burning plumes from Southeast Asia to South China via westerlies (Fu et al., 2012), the summertime O_3 concentrations over South China were higher within the planetary boundary layer (Liao et al., 2021), indicating a distinct transport pattern in summer. Therefore, the mechanisms underlying the enhanced summer O_3 pollution over South China, particularly regarding the influence of upwind Southeast Asia under the summer monsoon, remain unclear. To address this knowledge gap, the summertime (May-August) O_3 pollution across South China over the past decade (2013 – 2022) was examined, and monsoon-induced regional O_3 pollution episodes were identified in this chapter. Then, the physical and chemical processes contributing to these O_3 episodes and the transport pathways of O_3 and its precursors influenced by the summer monsoon were comprehensively investigated. Furthermore, the contributions of emissions from upwind Southeast Asia and local sources were also quantified. This chapter aims to elucidate the mechanisms driving the monsoon-induced summer O_3 episodes in South China and the role of transboundary transport, thereby informing more effective O_3 pollution control strategies for the region.

5.2 Worsening summer O_3 pollution in South China

From 2013 to 2022, regional high O_3 pollution events were frequently observed across South China during summertime (May-August). In this chapter, regional high O_3 episodes are defined as days when at least 10 of the 147 valid monitoring stations in South China (See Section 3.1.1 and Figure 3.1) record daily maximum hourly O_3 concentrations exceeding 100 ppbv (the Grade II standard of China's national ambient air quality). Figure 5.1a summarizes the frequency of these

summertime O_3 episodes, revealing an average of 27.6 episodes per year and a modest upward trend of 0.73 days per year (p = 0.3) from 2013 to 2022. Moreover, peak O_3 levels of these regional episodes have elevated in recent years, marked by the mode (the most frequently occurring value) of daily maximum O_3 concentrations among all stations rising from 55.6 ppbv (2013 – 2017) to 60.5 ppbv (2018 – 2022) (Figure 5.1b). Hence, regional O_3 pollution in summer has been exacerbated over South China throughout the past decade.

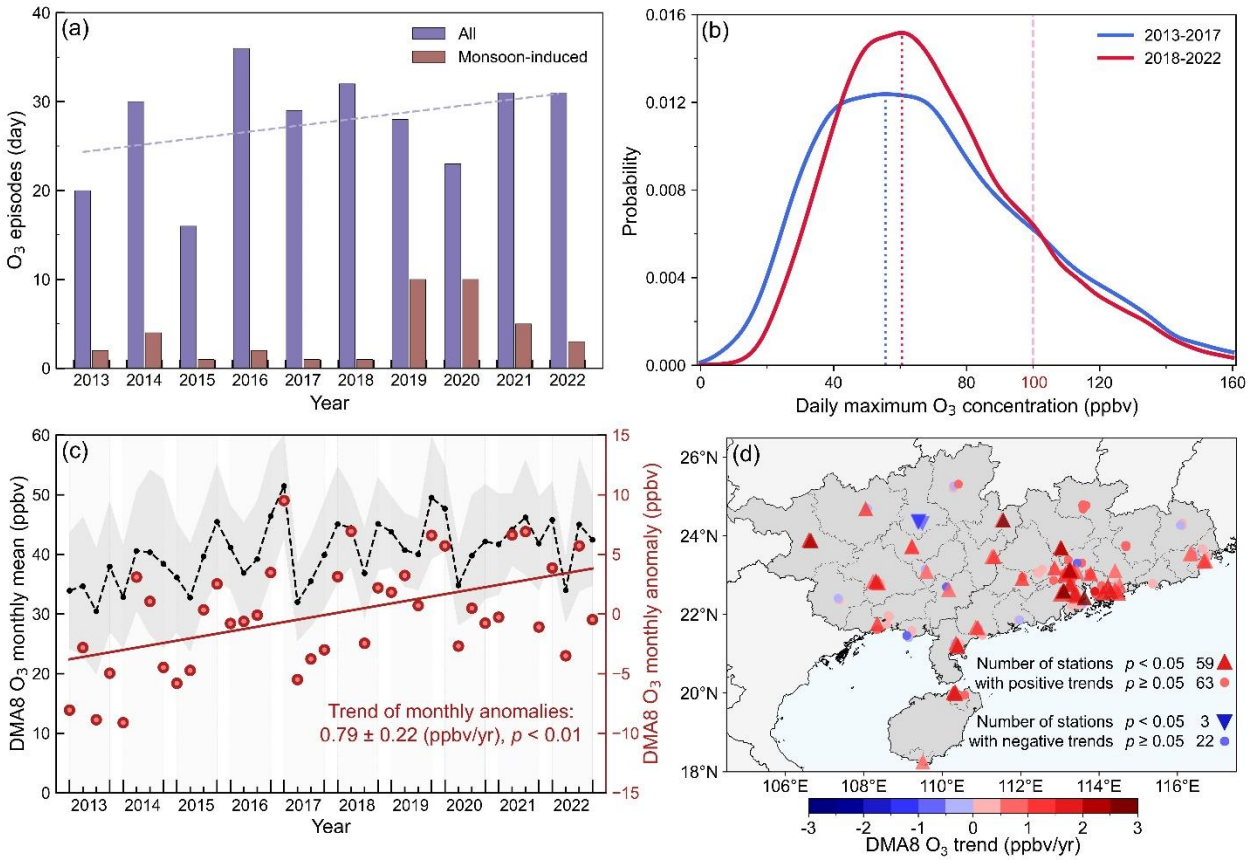

Figure 5.1. (a) Number of regional high-O_3 episodes and monsoon-induced episodes in South China during summertime from 2013 to 2022. (b) Probability density functions of daily maximum O_3 concentrations during these O_3 episodes. The thick blue and red lines illustrate 2013 – 2017 and 2018 – 2022, respectively. The dotted lines represent the peak values, *i.e.*, the mode of the probability distribution functions. (c) Regional trend of O_3 during the study period. Time series

showing the average (black dots with dashed line, left axis) and anomaly (dark red dots, right axis) of monthly mean DMA8 O_3. The gray shading represents the standard deviation of mean values across stations. The solid red line is the linear fit to the monthly anomalies, representing the overall trend based on the method proposed by Cooper et al. (2020). (d) Spatial distribution of summertime O_3 trends. Upward and downward triangles represent statistically significant increasing and decreasing trends ($p < 0.05$), respectively, while circles represent insignificant trends ($p \geq 0.05$). Colors indicate the magnitude of the trend.

Meanwhile, the daily maximum 8-hour average (DMA8) O_3 levels continued to increase during the summertime of 2013 – 2022, with a regional mean increasing rate of 0.79 ± 0.22 ppbv/yr ($p < 0.01$) (Figure 5.1c). This pattern corroborates and extends beyond previous findings of summer DMA8 O_3 increases in the PRD region at rates of 1.1 ppbv/yr (Li et al., 2020) and 1.2 ppbv/yr (Lu et al., 2025) during 2013 – 2019. More specifically, 83% of the stations in South China recorded rises in summertime DMA8 O_3, with approximately half of these stations exhibiting statistically significant upward trends ranging from 0.70 – 2.71 ppbv/yr (Figure 5.1d). In contrast, only 3 stations in Guangxi province recorded significant declines, with rates between -1.07 ppbv/yr and -0.78 ppbv/yr. These pronounced increases in DMA8 O_3 highlighted the dilemma posed by significant reductions in NO_x emissions since 2013 (Liu & Wang, 2020b). However, despite a sharp decrease in nitrogen dioxide (NO_2) concentrations, the observed oxidant ($O_x = O_3 + NO_2$) concentrations continued to increase during the study period (Figure 5.2), indicating that NO_x reductions did not fully explain the significant increases in O_3. For instance, interannual meteorological variations were reported to contribute 73% to summer O_3 increases over the PRD region from 2013 to 2019 (Li et al., 2020). Wang et al. (2019b) showed that the rising emissions from Southeast Asia and the South China Sea would have led to a faster O_3 increase (0.59 ppbv/yr),

without the offsetting effect of meteorological variations on O_3 (-0.23 ppbv/yr). This highlighted the potential importance of transboundary transport in elevating summer O_3 levels in South China.

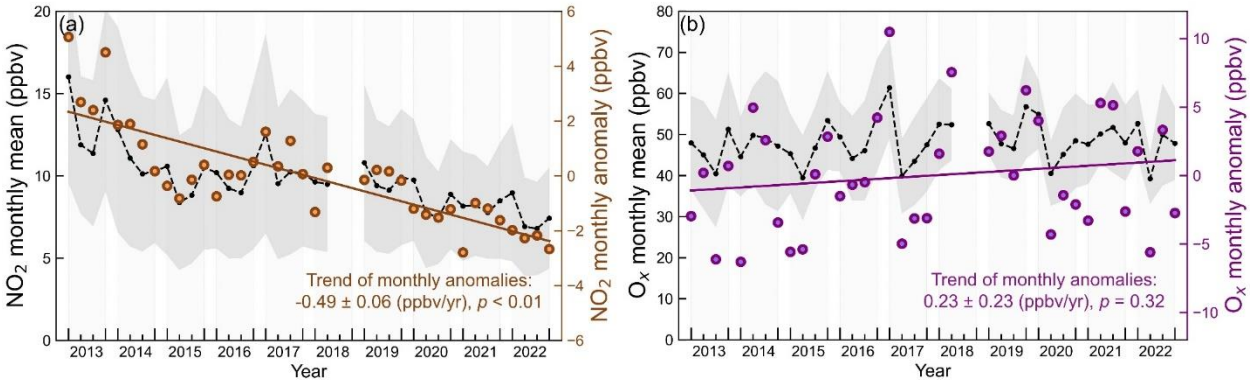

Figure 5.2. Trends of (a) NO_2 and (b) O_x across South China during the summertime of 2013 – 2022. Time series of the average (black dots with dashed line, left axis) and anomaly (right axis) of monthly mean daily mean NO_2 (brown dots) and monthly mean DMA8 O_x (purple dots). The gray shading represents the standard deviation of mean values across all stations. Solid lines are linear fits to the monthly anomalies, illustrating trends over the study period.

Additionally, the regional mean nighttime O_3 (19:00 – 06:00 China standard time [CST], UTC+8) in South China increased at a rate of 0.65 ± 0.14 ppbv/yr ($p < 0.01$) during the study period (Figure 5.3a). Although this rise was largely driven by reductions in NO_x (Figure 5.3b), other factors, such as meteorological variations and transport, might have also played a role, given the slight increase in O_x (Figure 5.3c). Unlike daytime photochemical O_3 production, the shallow nocturnal boundary layer with suppressed turbulent mixing at night could allow low-level jets to transport pollutants from upwind regions to South China (Kong et al., 2020). The distinct summer circulations, particularly the East Asia summer monsoon, could further modulate these processes, complicating the dynamics and formation mechanisms of summertime O_3 buildup. Therefore, it is crucial to

unravel the causes of the summertime O_3 pollution episodes across South China and the impact of transboundary transport under the influence of monsoonal airflows.

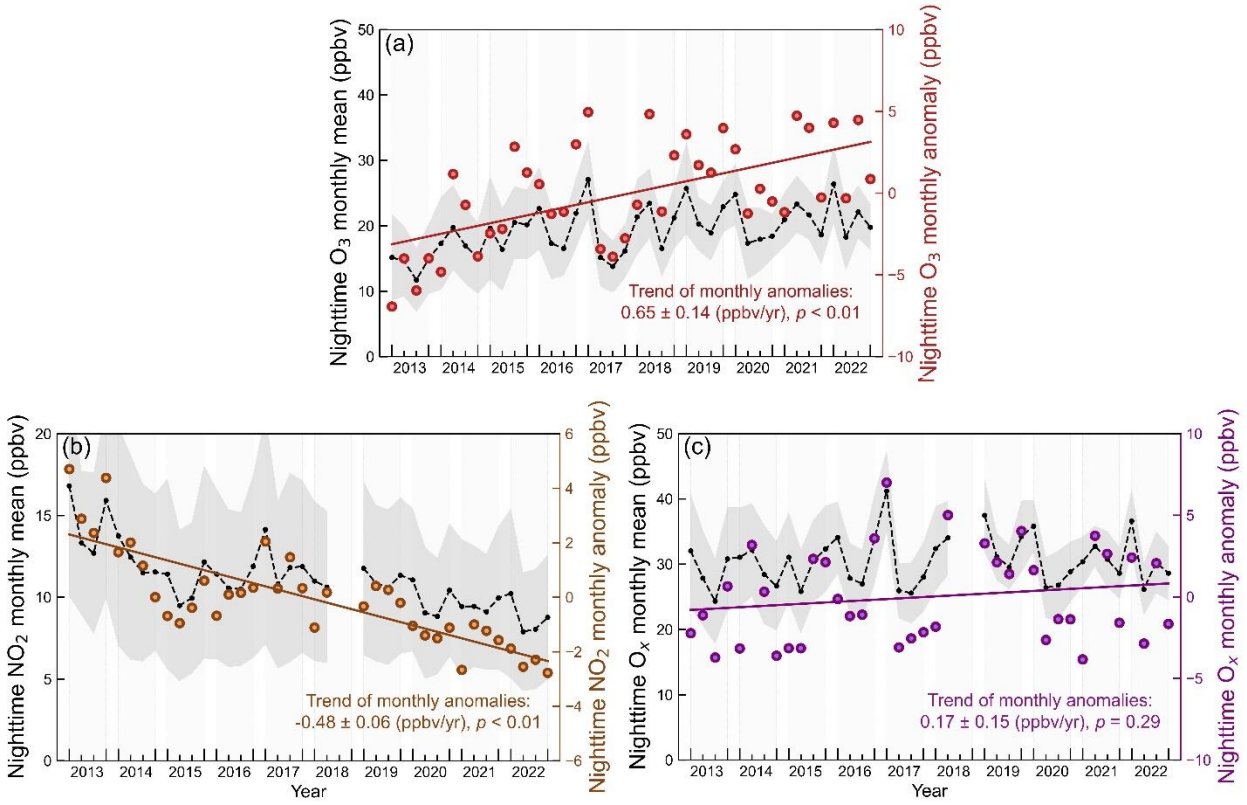

Figure 5.3. Time series of the monthly mean and anomaly of nighttime (a) O_3, (b) NO_2, and (c) O_x across 147 monitoring stations in South China during 2013 – 2022. Black dots with dashed lines and gray shading represent the mean values and standard deviations across stations. The colored dots and solid lines show the monthly anomalies and their linear fit, illustrating the trend over the study period.

To this end, through analysis of surface pressure and wind fields to exclude other synoptic influences (*e.g.*, tropical cyclones or high-pressure systems), along with 72-hr backward trajectories of air masses, 39 monsoon-induced O_3 episodes over South China during the summer months of 2013 – 2022 were identified (Table 5.1). These episodes are characterized by prevailing southerly or southwesterly winds and air masses originating from the South China Sea and

Southeast Asia, representing a strong monsoon influence. In contrast to the traditional view that the summer monsoon primarily dilutes air pollutants in South China by bringing clean marine air and precipitation, this region experienced O_3 pollution during these episodes, which underscores the complexity of summertime O_3 dynamics in South China. To decipher the mechanisms driving these monsoon-induced O_3 episodes, the following section provides a detailed analysis of the relevant physical and chemical processes based on WRF-CMAQ simulations.

Table 5.1. Date information of monsoon-induced high O_3 episodes in South China during summertime (May-August) of 2013 – 2022.

Year	Date
2013	23 May, 3 Jun.
2014	28 Jun., 29 Jun., 17 Aug., 18 Aug.
2015	25 May
2016	6 Jun., 7 Jun.
2017	23 May
2018	4 Aug.
2019	12 Jun., 13 Jun., 14 Jun., 25 Jun., 29 Jun., 30 Jun., 1 Jul., 19 Aug., 20 Aug., 21 Aug.
2020	19 May, 23 May, 24 May, 28 May, 14 Jul., 15 Jul., 23 Jul., 24 Jul., 25 Jul., 26 Jul.
2021	17 Aug., 18 Aug., 19 Aug., 20 Aug., 21 Aug.
2022	12 Jul., 13 Jul., 14 Jul.

5.3 Atmospheric dynamics and chemistry during monsoon-induced O_3 episodes

5.3.1 Spatial Distributions of O_3 over South China

Figure 5.4 presents the horizontal and vertical distributions of simulated O_3 and winds over South China and Southeast Asia during monsoon-induced O_3 episodes. In daytime (14:00 CST), high O_3 concentrations were simulated across South China and Southeast Asia, particularly in urban areas, such as the PRD region, Bangkok, Kuala Lumpur, and Jakarta. These O_3 hotspots

were primarily attributed to intense photochemical formation, as these densely populated regions are associated with high anthropogenic emissions of O_3 precursors (Figure 5.5). Interestingly, high O_3 levels were also simulated over the Beibu Gulf, a marine environment. This phenomenon could be associated with the combined effects of coastal and marine vessel emissions that facilitate local O_3 production and the sea breeze circulation that generates downdrafts and traps air pollutants near the water surface, which has been reported in other bay areas (Zeren et al., 2019; Zeren et al., 2022b). O_3 distributions on vertical cross-sections further indicate that the elevated O_3 extended from Thailand into South China (Figure 5.4b), while the high-O_3 zone between Peninsular Malaysia and South China was geographically discontinuous (Figure 5.4c). This suggests potential transboundary transport along the prevailing monsoonal airflow, with the Beibu Gulf being a key stop on the transport path.

During nighttime (20:00 CST), surface O_3 was depleted over most land areas due to efficient titration by nitric oxide (NO) at ground level, while the residual layer (500 m – 1500 m) above urban areas, particularly in the PRD region, retained elevated O_3 levels left over from the daytime. In contrast, over the Beibu Gulf, surface O_3 concentrations remained high near the water surface (below ~300m), comparable to daytime values and exceeding those observed over the land areas of South China. This persistence was attributed to a weaker NO titration effect and a lower dry deposition rate of O_3 on water surfaces. After sunset, suppressed turbulence in the boundary layer intensified onshore southwesterly winds, which enabled the transport of aged, O_3-rich air masses from the gulf toward South China. This marine air mass mixed with the residual layer under the influence of topographic lifting and was subsequently carried inland. As a result, it was likely that O_3 transport from the Beibu Gulf sustained high nighttime O_3 concentrations in the residual layer over South China, thereby influencing the regional background O_3 levels.

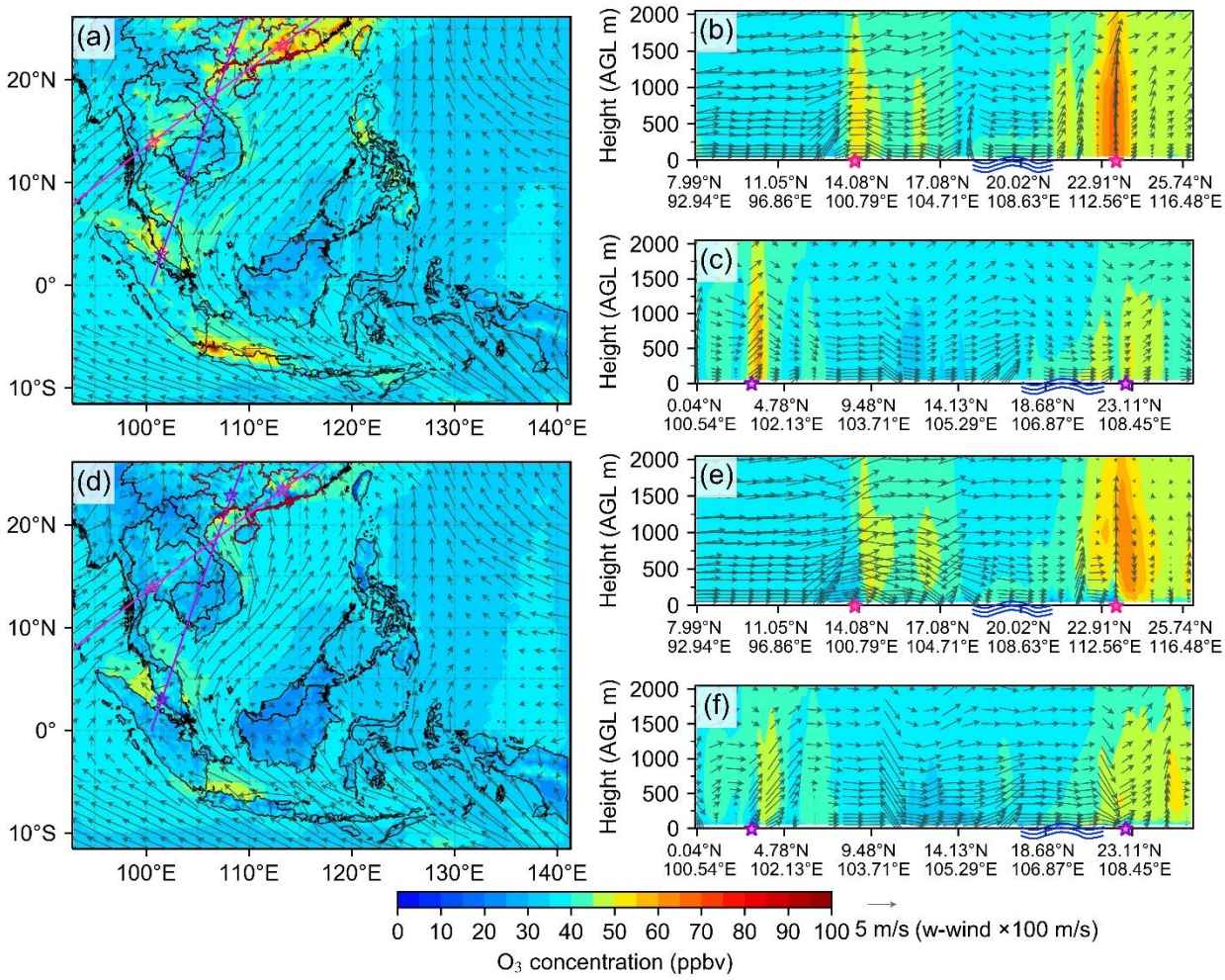

Figure 5.4. Average spatial patterns of (a, d) simulated surface O_3 concentrations and wind fields, along with (b-c, e-f) vertical cross-sections during monsoon-induced high O_3 episodes at (a-c) 14:00 CST and (d-f) 20:00 CST. Stars indicate the representative stations used for the cross-section lines: (b, e) Bangkok to Guangzhou and (c, f) Kuala Lumpur to Nanning. Blue lines denote the Beibu Gulf region.

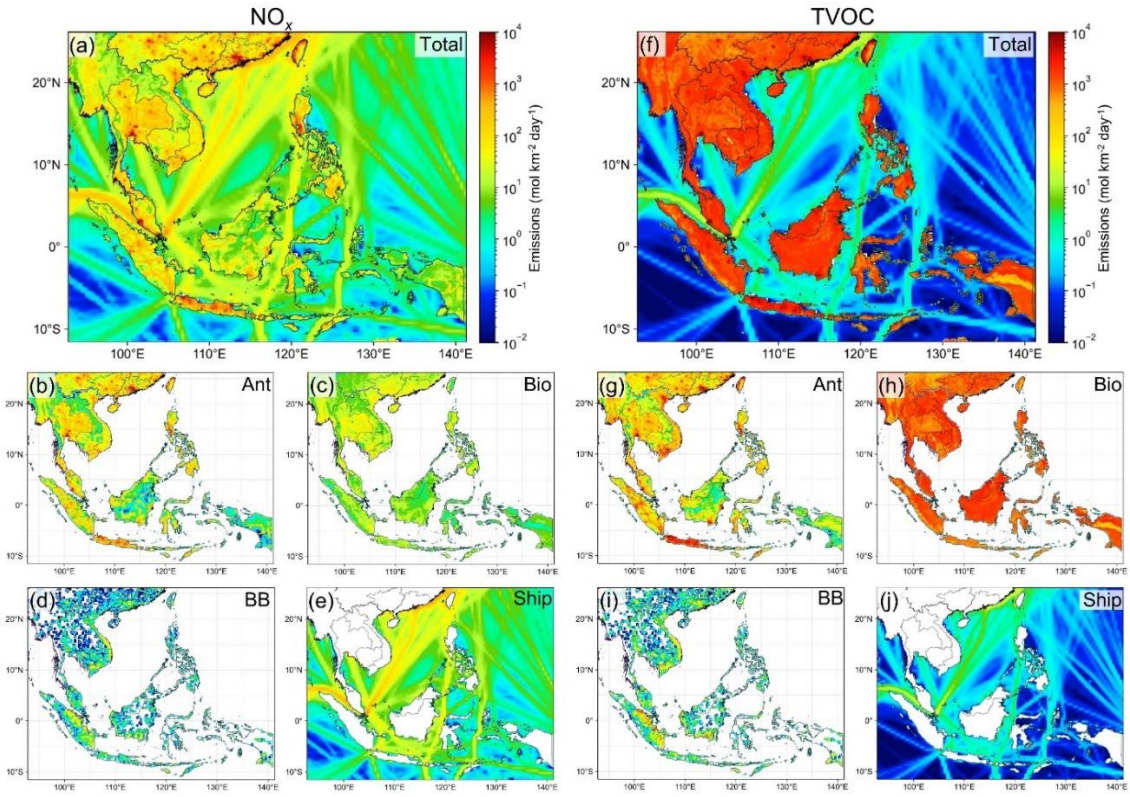

Figure 5.5. Average emissions of total volatile organic compounds (TVOC; panels a-e) and nitrogen oxides (NO_x; panels f-j) from (a, f) all sectors, (b, g) anthropogenic sources, (c, h) biogenic sources, (d, i) biomass burning, and (e, j) shipping. Emission data are extracted from emission inventories used in this study (see Section 3.2.2 for details).

5.3.2 Atmospheric processes of O_3 pollution in South China

To further elucidate the evolution of O_3 pollution in South China, we employed the IPR module in CMAQ to analyze the key processes: advection, diffusion, dry deposition (DDEP), cloud processes (CLDS), and the overall effects of chemical reactions (CHEM). For clarity, horizontal advection and diffusion were combined as horizontal transport (HTRAN), while vertical advection and diffusion were grouped as vertical transport (VTRAN). The sum of HTRAN and VTRAN represented total transport. Figures 5.6 and 5.7 illustrate the average process contributions to surface O_3 change rates during monsoon-induced O_3 episodes.

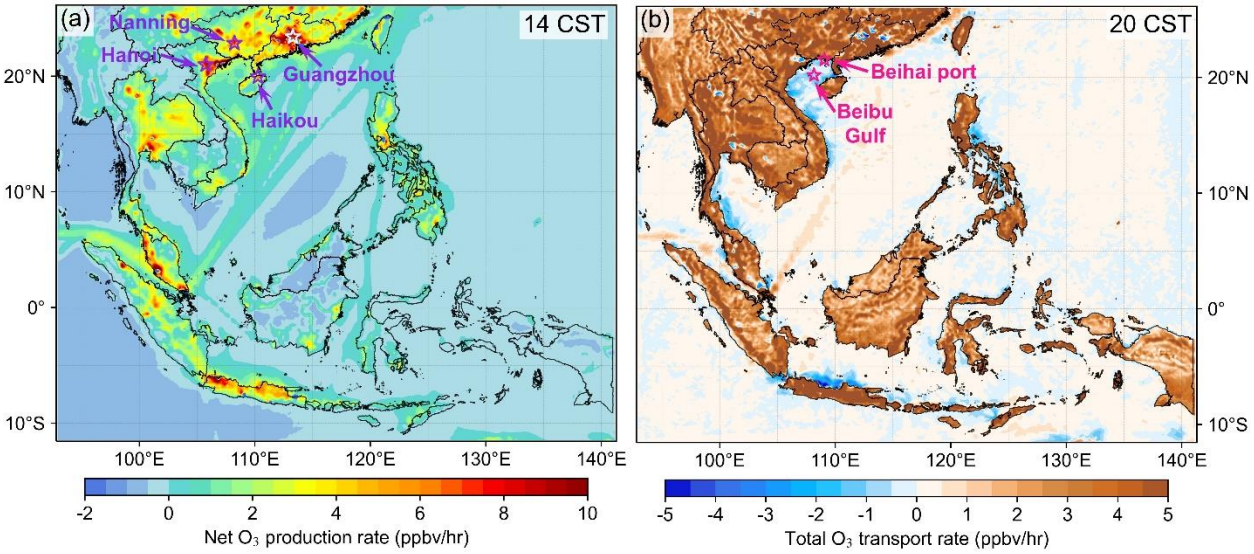

Figure 5.6. Average spatial distribution of surface net O_3 production rates at 14:00 CST (a) and total O_3 transport rates at 20:00 CST (b) during monsoon-induced high O_3 episodes. Stars indicate the key cities/locations.

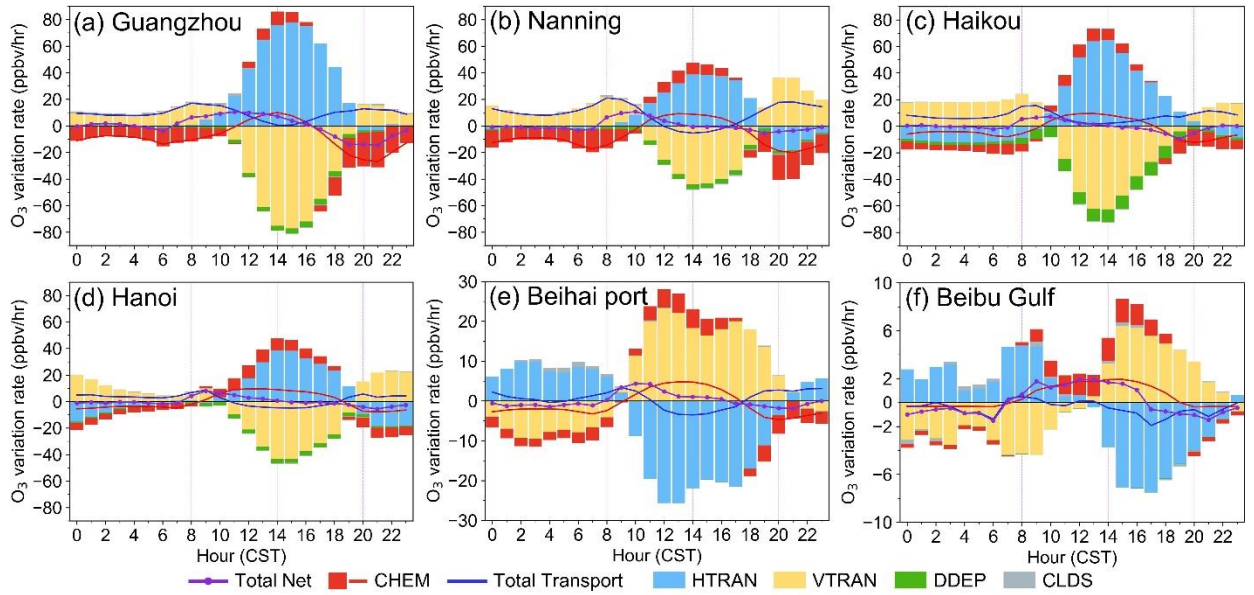

Figure 5.7. Average diurnal contributions of different processes to surface O3 variations in (a) Guangzhou, (b) Nanning, (c) Haikou, (d) Hanoi, (e) Beihai port, and (f) the Beibu Gulf. The locations are indicated by stars in Figure 5.6.

During the day, strong solar radiation, combined with high emissions of NO_x and VOCs (Figure 5.5), led to pronounced chemical production of O_3 over South China, peaking in major cities like Guangzhou (10.04 ppbv/hr), Nanning (9.30 ppbv/hr), and Haikou (9.55 ppbv/hr) around noon (12:00 – 14:00 CST). Meanwhile, intensive local O_3 production was also found in Hanoi (9.62 ppbv/hr), but the net O_3 concentration increased by only 2.08 ppbv/hr. The difference might be explained by O_3 transport to the surrounding areas, including the Beibu Gulf. Notably, chemical buildup of O_3 was also evident over the South China Sea, especially the Beibu Gulf, driven by shipping emissions and continental outflow from Vietnam. The maximum O_3 production rate was 4.82 ppbv/hr at Beihai port, located in the northern Beibu Gulf, and 1.94 ppbv/hr over the Beibu Gulf. The intensive daytime photochemical reactions were further evidenced by abundant hydrogen oxide radicals (HO_x = OH + HO_2) across both land areas and the South China Sea, particularly in the Beibu Gulf (Figure 5.8). These highly reactive HO_x radicals, primarily produced through photochemical reaction cycles, serve as key indicators of atmospheric oxidation capacity due to their short atmospheric lifetimes and strong dependence on local chemical conditions (Seinfeld & Pandis, 2006). As such, photochemical O_3 production was the dominant driver of the daytime O_3 buildup over South China and the Beibu Gulf during these O_3 episodes. It is worth noting that relatively low HO_x concentrations in the PRD region and along the eastern coast of China were attributed to high NO_x emissions from shipping in these areas (Figure 5.5e), as HO_x radicals could be consumed by reactions such as OH + NO, OH + NO_2, and HO_2 + NO (Wang et al., 2018c).

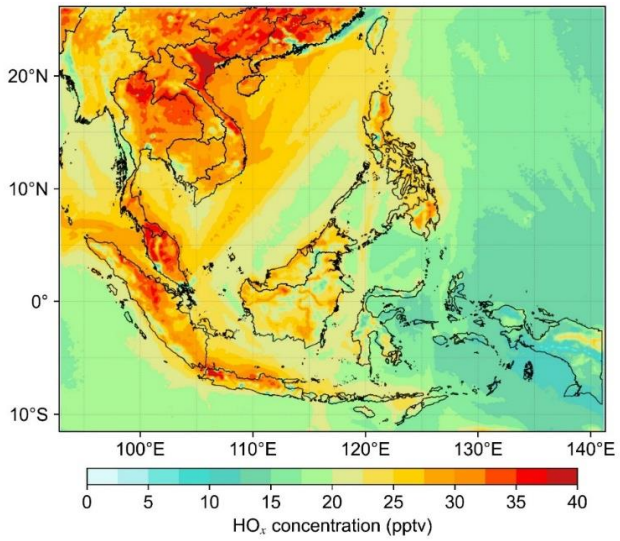

Figure 5.8. Average spatial distribution of hydrogen oxide radicals (HO_x) during monsoon-induced high O_3 episodes at 14:00 CST.

In addition to the critical role of chemical production, transport processes also contributed in part to elevate O_3 levels across South China. Daytime horizontal transport (10:00 – 18:00 CST) imported O_3 into downwind South China, leading to O_3 increases at average rates of 52.74 ppbv/hr in Guangzhou, 28.11 ppbv/hr in Nanning, and 41.50 ppbv/hr in Haikou. The horizontal advections were simultaneously offset by strong vertical mixing within the boundary layer, which diluted surface O_3 at average rates of -46.08 ppbv/hr, -26.69 ppbv/hr, and -36.64 ppbv/hr in Guangzhou, Nanning, and Haikou. Overall, the net contributions of total transport, though weaker than chemical production, still increased daytime O_3 by 6.66 ppbv/hr in Guangzhou, 1.42 ppbv/hr in Nanning, and 4.58 ppbv/hr in Haikou. Over the Beibu Gulf, however, vertical transport enhanced surface O_3 in the afternoon (14:00 – 18:00 CST) at an average rate of 5.28 ppbv/hr, while horizontal transport exported O_3 to coastal areas at -6.33 ppbv/hr. This pattern was driven by land-sea temperature differences, which caused pollutant-laden air over land areas, particularly along the coast of Vietnam, to rise, subside over the gulf, and then diverge outward. Prevailing southwesterly winds further amplified this divergence, enhancing horizontal O_3 transport toward

South China. At night (19:00 – 06:00 CST), while the individual impacts of horizontal and vertical transport on O_3 concentrations in South China diminished, their combined effect remained significant (Figure 5.6b), positively contributing to O_3 levels in Guangzhou (9.75 ppbv/hr), Nanning (12.48 ppbv/hr), and Haikou (7.81 ppbv/hr). In contrast, negative contributions of total transport over the Beibu Gulf suggested that O_3 was exported to South China at an average rate of -0.51 ppbv/hr under southwesterly winds.

Previous studies have suggested potential contributions of O_3 and its precursors transported from upwind Southeast Asia and the South China Sea to summer O_3 in South China, as indicated by ground-level observations (Wang et al., 2019b; Lu et al., 2025). Here, these results reveal that while chemical production predominantly generated O_3 in South China during the day, transport processes played a pivotal role in redistributing O_3 regionally. More importantly, the Beibu Gulf received O_3 and its precursors transported from upwind Southeast Asian regions, accumulated locally formed O_3, and subsequently supplied O_3 to South China during both day and night. The findings illustrate a key pathway for potential transboundary transport of O_3 and its precursors, with the Beibu Gulf acting as an O_3 reservoir. The contributions of emissions from different source regions to O_3 in South China are elucidated below.

5.4 Contributions of emissions to O_3 pollution in South China

Given the significant impact of regional transport on O_3 pollution over South China under prevailing southwesterly winds during monsoon-induced O_3 episodes, the contributions of different regions and sectors to O_3 were quantified using the ISAM module in CMAQ. Specifically, O_3 precursors emitted from three source regions (Figure 3.1), *i.e.*, South China (CHN), mainland Southeast Asia (LSA), and maritime Southeast Asia (MSA), were examined. For each region,

emissions from anthropogenic (ant), biogenic (bio), and biomass burning (bb) were evaluated, together with shipping emissions (Ship) across the domain. Contributions from other emission sources (Other) and background concentrations (BG) were also assessed. The BG concentrations comprised the carryover initial field (ICON) from the prior day's simulation and lateral boundary conditions (BCON) from the outer domain. Figure 5.9 illustrates the average contributions from major sources to O_3 concentrations over the study region during these episodes, while their diurnal contributions to O_3 in South China and the Beibu Gulf are depicted in Figure 5.10.

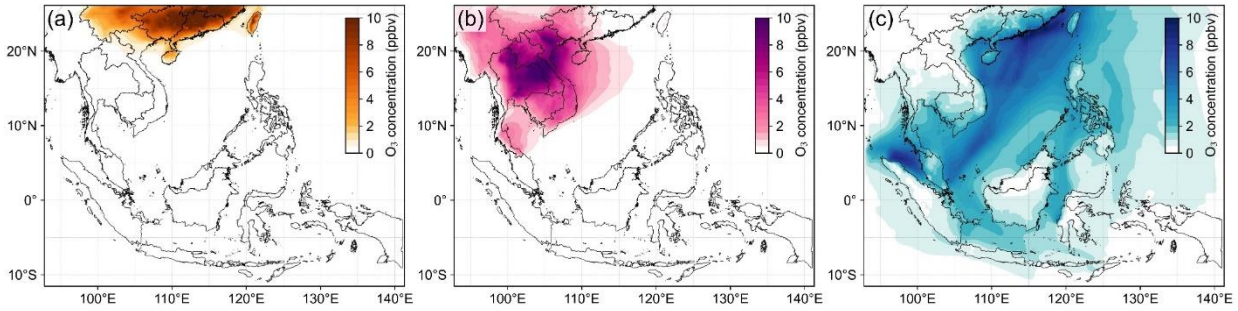

Figure 5.9. Average contributions of emissions from (a) South China (CHN), (b) mainland Southeast Asia (LSA), and (c) shipping to surface O_3 concentrations over the study region.

Overall, despite the dominant influence of background O_3 (23.3 ppbv, 64.8%), local emissions from CHN primarily contributed to O_3 concentrations in South China by 7.22 ppbv (20.1%, with 14.4% from CHNant and 5.3% from CHNbio). Emissions from LSA and shipping further elevated O_3 levels over South China by 1.54 ppbv (4.3%) and 2.13 ppbv (5.9%), respectively. Due to the considerable distance between MSA and South China, emissions and O_3 formed in MSA had minimal direct impact on South China, accounting for only 0.7%. In addition, although intensive biomass burning occurred in MSA during these periods, agricultural residue burning in LSA and CHN was reduced during this rainy season under the summer monsoon (Lan et al., 2022; Marvin et al., 2024), resulting in a contribution of only 0.9% from biomass burning to O_3 in South China.

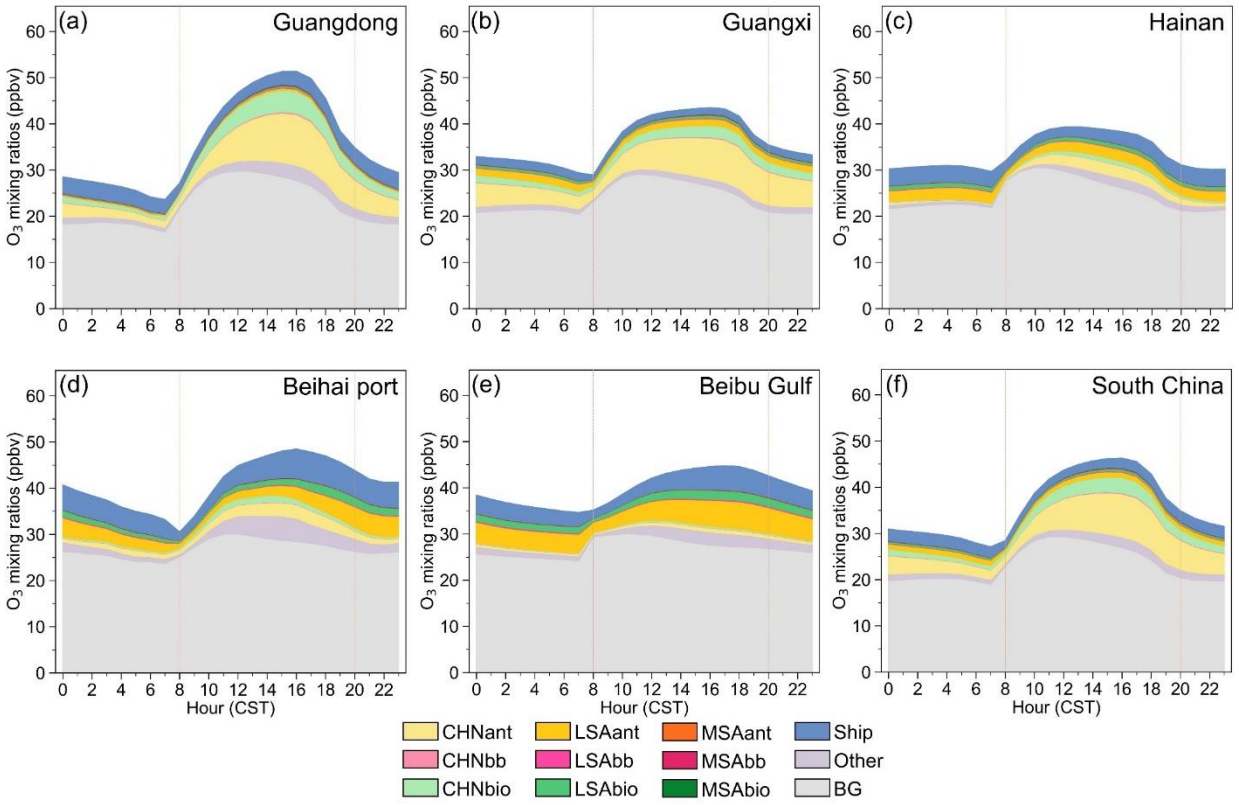

Figure 5.10. Average diurnal contributions of different sources to surface O_3 concentrations in (a-c) South China provinces, (d-e) the Beibu Gulf, and (f) the overall contributions to South China. Here, South China refers specifically to Guangdong, Guangxi, and Hainan provinces.

The contributions of different sources varied across South China provinces. In Guangdong and Guangxi provinces, CHNant emissions accounted for 5.21 ppbv (14.5%) and 5.62 ppbv (15.5%) of the daily mean O_3 concentrations with maximum hourly enhancements of 11.01 ppbv and 9.18 ppbv during the day, while CHNbio emissions added an average of 2.41 ppbv (6.7%) and 1.73 ppbv (4.8%) to O_3 concentrations in Guangdong and Guangxi, respectively. In addition, shipping emissions contributed an average of 2.97 ppbv (8.2%) to O_3 in Guangdong and 1.43 ppbv (4.0%) in Guangxi, and had a stronger impact on Hainan's O_3 (2.99 ppbv, 8.9%), where local anthropogenic emissions are relatively weak (contribution to O_3: 1.21 ppbv, 3.6%). Furthermore, LSA emissions had a notable influence on Hainan and Guangxi, increasing hourly average O_3 by

3.11 ppbv (9.2%) and 2.02 (5.6%) ppbv, respectively. The transboundary impact of LSA emissions was more pronounced at night, with maximum hourly O_3 enhancements of 3.59 ppbv in Hainan and 2.33 ppbv in Guangxi. This highlights the efficient nighttime transport of O_3 from Southeast Asia to South China, due to the enhanced onshore winds.

Over the Beibu Gulf, continental outflows from LSA were the largest contributors to hourly O_3 concentrations, accounting for an average of 6.19 ppbv (4.46 ppbv from LSAant and 1.49 ppbv from LSAbio). In contrast, CHN made a much lower contribution of 0.87 ppbv, as inhibited by the prevailing southerly winds. Even at the Beihai port, the CHN's contribution to O_3 (2.44 ppbv) was surpassed by that of LSA (4.16 ppbv). Prevailing southerly winds advected O_3 from LSA into the Beibu Gulf, and the downdrafts over the gulf confined O_3 within a shallow marine boundary layer (Figure 5.4e). Notably, the influence of LSA on the gulf was strongest in late afternoon and early evening (Figure 5.10e). In addition to the transboundary transport, shipping emissions from marine vessels, both offshore and at ports, also made a substantial contribution of 3.71 ppbv to O_3 in the Beibu Gulf on average. The combined contribution of LSA and shipping emissions reached up to 13.29 ppbv (29.8%) over the Beibu Gulf at 18:00 CST, followed by transport to South China via horizontal advection (Figure 5.7c).

As shown in Figures 5.11 and 5.12, although local CHN emissions were the primary sources of O_3 precursors (81.2% of NO_x and 65.5% of VOCs), shipping emissions also contributed 2.7% to NO_x concentrations over South China, mostly along the coast of Guangdong. Besides, LSA emissions accounted for 5.1% of VOCs in South China, with stronger influences in Hainan (14.4%) and Guangxi (6.7%). This indicates that not only can O_3 be transported from LSA to South China, but its precursors can also reach the region and participate in local O_3 photochemistry. Additionally, the concentrations of O_3 precursors were comparatively low over the Beibu Gulf due to sparse

direct emissions. Shipping was the dominant NO_x source (31.0%) in the gulf, while VOCs were mainly transported from LSA (46.6%). These O_3 precursors underwent photochemical reactions within the gulf during the day, forming O_3 that was subsequently transported to South China via prevailing southwesterly winds, especially at night.

In summary, shipping emissions substantially increased O_3 and NO_x levels in both South China and the Beibu Gulf, while regional transport of O_3 and its precursors, especially VOCs, from upwind LSA also had a considerable impact. Notably, O_3 and its precursors tended to accumulate in the Beibu Gulf, effectively making it an O_3 reservoir that supplied additional O_3 to South China via southwesterly winds. These findings indicate that regional influences from Southeast Asia were partly responsible for the monsoon-induced O_3 pollution observed in South China.

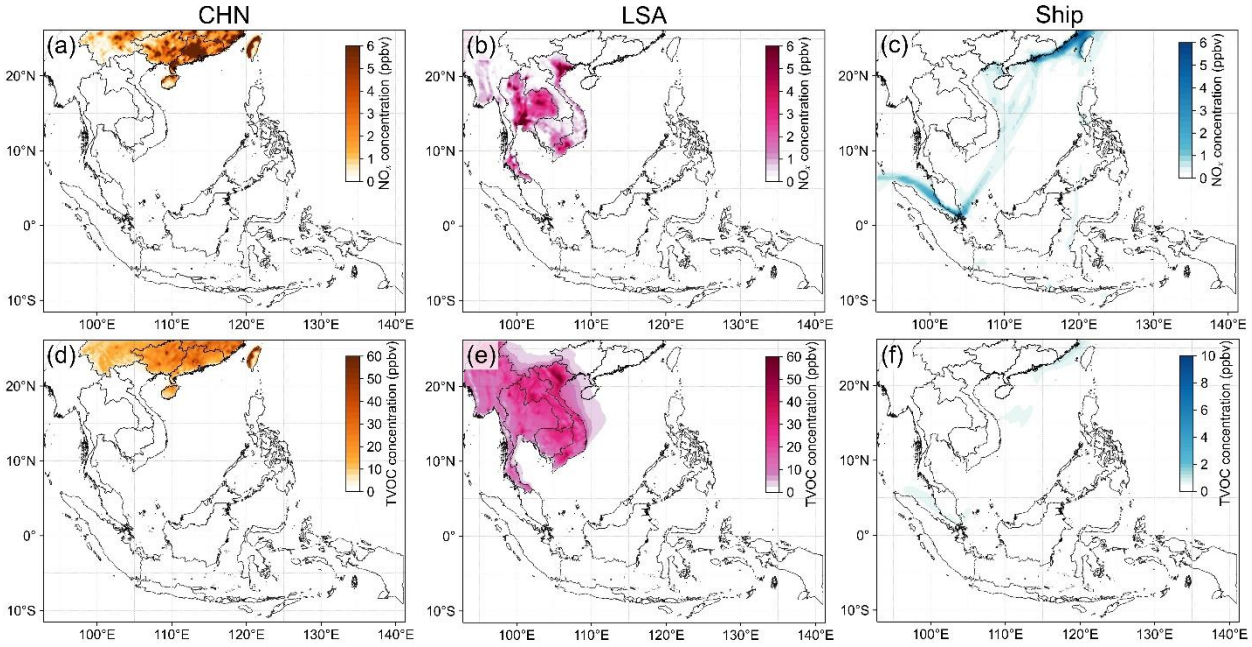

Figure 5.11. Average contributions of emissions from South China (CHN), mainland Southeast Asia (LSA), and shipping (Ship) to NO_x concentrations (a-c) and TVOC concentrations (d-f) over the study region.

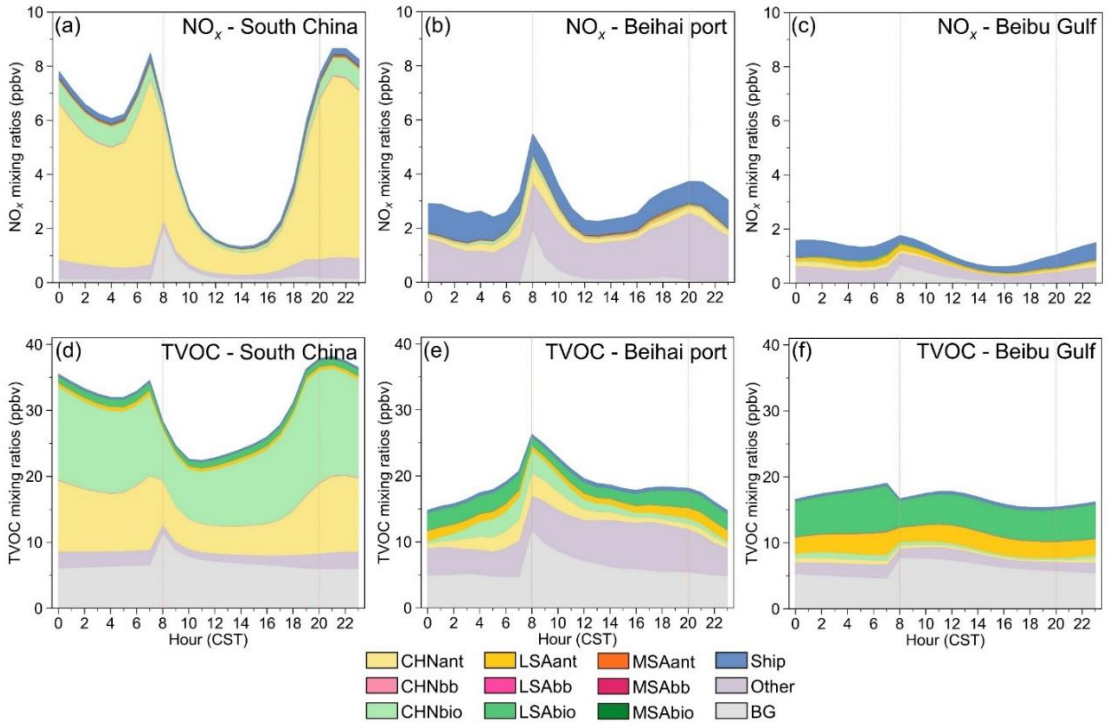

Figure 5.12. Average diurnal contributions of different sources to (a-c) NO_x and (d-f) TVOC concentrations in (a, d) South China, (b, e) Beihai port, and (c, f) the Beibu Gulf.

5.5 Discussion on limitations

Despite the insights into transboundary impacts on summertime O_3 pollution in South China, several limitations remain. First, there are unavoidable uncertainties in emission inventories, including variability in activity data, local emission factors, spatiotemporal allocation, and speciation (Hong et al., 2017; Li et al., 2017b; Wang et al., 2021), which are often considered a major cause of model bias (Hu et al., 2016; Saikawa et al., 2017; Qu et al., 2020). In addition, because up-to-date emission inventories were not available for the entire simulation period (2013 – 2022), anthropogenic emissions for later years were fixed at levels from the most recent inventories, which cannot reflect year-to-year variations, especially those driven by emission control measures and the COVID-19 lockdowns. In fact, sensitivity tests indicate that simulations with fixed emissions performed comparably to those based on year-specific emissions, suggesting

that this uncertainty did not substantially bias the simulations or the key findings. Second, the model overestimated O_3 with a mean bias of 3.97 ppbv, likely related to imperfections of physical parameterizations and chemical mechanisms, in addition to uncertainties in emission inventories (Sarwar et al., 2008; Carvalho et al., 2012; Hu et al., 2013; Sicard et al., 2021b). Besides, due to the large spatial coverage of our study area, the inner domain has a relatively coarse spatial resolution of 9 × 9 km and could not resolve subgrid processes, which also contributed to model bias (Liu et al., 2010; Torres-Vazquez et al., 2022). Third, the ISAM cannot distinguish between the direct O_3 transport from upwind Southeast Asia and O_3 formed through transported precursors, leaving gaps in understanding O_3 transport mechanisms. Further studies are suggested to conduct observations and modeling along the transport path, particularly over the Beibu Gulf. Fourth, this study focuses on monsoon-induced O_3 episodes, leaving investigations of long-term O_3 variations and their causes, including meteorological and emission impacts, for future research. Simulations with updated emission inventories would better quantify the trends of transboundary transport of O_3 from Southeast Asia and benefit joint O_3 control strategies across regions.

5.6 Summary

Surface O_3 pollution in South China has become increasingly severe during the summertime (May-August) over the past decade (2013 – 2022), when high O_3 episodes with elevated peak O_3 levels have been frequently observed. In summer, the weather patterns in South China are largely shaped by the East Asia Summer Monsoon, featuring southerly winds that are typically associated with clean, moist marine air. However, 39 regional O_3 pollution events were identified under monsoon conditions during the study period. To investigate the physical and chemical drivers of these monsoon-induced O_3 episodes and to assess the role of upwind Southeast Asia in O_3 pollution in South China, the WRF-CMAQ model was applied.

Simulation results revealed pronounced O_3 hotspots over urban areas with intensive anthropogenic emissions, especially in the PRD region of South China, primarily driven by daytime photochemical processes. Meanwhile, regional sources from upwind mainland Southeast Asia and shipping emissions further elevated concentrations of O_3 (by 1.54 ppbv and 2.13 ppbv, respectively) and its precursors across South China, particularly in Hainan island, where these regional sources accounted for 18.1% of its O_3 concentrations (6.1 ppbv). Unexpectedly, O_3 levels over the Beibu Gulf were considerably high not only during the day but also at night. This was attributable to the transport of O_3 and its precursors from upwind mainland Southeast Asia and marine shipping emissions, which increased O_3 in the gulf by 6.2 ppbv and 3.7 ppbv, respectively. As a result, the Beibu Gulf acted as an O_3 reservoir, where O_3 formed and accumulated, continuously supplying O_3-rich air to South China under prevailing southwesterly winds. These findings challenge the conventional view that the East Asia Summer Monsoon solely brings clean air to South China and dilutes air pollution. Instead, the interplay between local emissions and transboundary contributions facilitated by the monsoon, along with the unique dynamics over the Beibu Gulf, underscores the complexity of summer O_3 pollution across South China. Therefore, effective management of the deteriorating summertime O_3 air quality in South China requires comprehensive mitigation strategies that integrate local emission controls and regional cooperation. To reduce transboundary O_3 pollution, intergovernmental collaboration, sharing of best practices, and participation in international air quality scientific and policy forums should be enhanced, together with global regulation of shipping emissions. In addition, timely updates to emission inventories are also urgently needed, and studies on long-term summer O_3 variations and their causes should be conducted to fully understand the characteristics of summer O_3 in South China.

Chapter 6 An Observational Constraint of VOC Emissions for Air Quality Modeling Study in the Pearl River Delta Region

6.1 Introduction

Volatile organic compounds (VOCs) play essential roles in atmospheric chemistry as they are the key precursors of secondary air pollutants such as ozone (O_3) and secondary organic aerosol (SOA). Ambient VOCs are composed of hundreds of species that are emitted from a wide variety of anthropogenic activities and natural sources, and the contributions of different emission sources vary among regions and cities, corresponding to the distinctive city structures (Guo et al., 2017). Therefore, estimations of the VOC emissions are important for investigating air pollution and atmospheric chemistry.

The VOC emission inventories with gridded emissions are necessary inputs for the chemical transport models (CTMs) to study regional air pollution. Current emissions inventories of anthropogenic VOC emissions are generated by bottom-up approaches, according to the emission estimations by the annual statistical yearbook on energy consumption and product yields (Zheng et al., 2009b; Liu et al., 2015; Zheng et al., 2018; Huang et al., 2021). However, the limited local measurements of emission factors and the high spatiotemporal variability of the sources have led to difficulties in estimating emissions accurately and timely (Liu et al., 2012; Hong et al., 2017; Li et al., 2017b). In addition, the spatial and temporal allocations of VOC emissions from different source sectors (Wang et al., 2011; Chen et al., 2016; Geng et al., 2017; Zheng et al., 2017), along with the speciation of total VOCs into the lumped groups chemical mechanisms (Li et al., 2014; Mo et al., 2016), have introduced biases into the model-ready VOC emissions. Consequently,

potential errors exist in the emission inventories and could further affect the simulations of VOCs and atmospheric photochemistry in the CTMs.

Discrepancies can be found when applying top-down validations to the model outputs. Recent studies reported that the deviations of simulated and observed VOC concentrations remain even with the latest emission inventories. Shen et al. (2019) reported that the high and increasing anthropogenic VOC emissions dampened the decrease of open fire emissions in parts of China. As a result, the model failed to reproduce the decreasing trend of formaldehyde in these regions. Previous studies also revealed that though the simulated total VOC levels were comparable with those of the observations, biases existed for individual VOC species, such as propane, ethene, toluene, and formaldehyde (Jiang et al., 2010; Chutia et al., 2019; Zeren et al., 2019). In addition, Wang et al. (2020) found large differences in the monthly variations of the simulated and observed aromatics in Shanghai, which was caused by the misrepresentation of the monthly emissions. Besides, the discrepancies in the simulated spatiotemporal variations of O_3 concentrations were partially attributable to the biases in emission inventories (Wang et al., 2010; Saikawa et al., 2017; Bouarar et al., 2019), especially for the peak values on O_3 pollution days (Chen et al., 2013; Guo et al., 2019), as well as their spatial distributions (Qu et al., 2020).

In order to better simulate the spatiotemporal variations of VOCs and secondary pollutants, top-down approaches using observed data have been developed to estimate the VOC emissions (Li et al., 2021a). For example, based on inversion models, satellite observations of formaldehyde and glyoxal have been used to estimate the total VOC emissions, representing the spatiotemporal variabilities of the emissions (Fu et al., 2007; Liu et al., 2012; Chaliyakunnel et al., 2019). Although better simulations of secondary pollutants were achieved using satellite-inversed emissions, the constrained species were limited, and the retrievals for the same species from

different satellite instruments have discrepancies (Stavrakou et al., 2015; Zhang et al., 2017; Cao et al., 2018). In addition to the satellite observations, field-measured VOCs were applied to constrain the emissions by using the emission ratios of VOCs relative to an inert tracer (e.g., carbon monoxide and acetylene) (Hsu et al., 2010; Borbon et al., 2013). Meanwhile, the source-receptor relationships, the mixed layer mass balance techniques, as well as the eddy covariance flux measurements were also reliable and complementary for estimating the VOC emissions (Karl et al., 2007; Yuan et al., 2015; Fang et al., 2016; Mo et al., 2020). Studies revealed that after constraining the VOC emissions by measured VOCs, the CTM simulated VOCs and O_3 had better agreement with the observations, particularly for their temporal variations, compared with the simulations without constraining (Chen et al., 2010; Kim et al., 2011; Wang et al., 2020). In spite that frameworks for top-down constraints of VOC emissions with measured data have been established, they suffered from low spatial coverage, and a limited number of them were applicable to input into CTMs. Moreover, due to the lack of concurrent VOC measurements, the use of observational constraints to estimate VOC emissions was scarce in China, whereas the VOC emissions changed rapidly under fast developments and strengthened control strategies. Therefore, top-down VOC emission constraints in China are necessary for complementing VOC emission assessments and enhancing the CTM simulations of VOCs and secondary pollutants.

The Pearl River Delta (PRD) region is one of the most prosperous city clusters in China. The rapid developments were accompanied by unprecedented VOC emissions, leading to severe air pollution in this region. Since the early 2000s, studies based on field measurements and bottom-up emission inventories have been conducted to characterize the VOC emission sources and O_3 formation chemistry in the PRD region (Guo et al., 2006; Liu et al., 2008; Zheng et al., 2009a; Lu et al., 2013; Huang et al., 2021; Liu et al., 2021). However, no observational constraints of VOC

emissions with measured data have been applied to air quality modeling studies to date. This chapter establishes an updated approach for constraining the anthropogenic VOC emissions by combining concurrent VOC measurements in nine PRD cities and CMAQ simulations. Then, the CMAQ simulations using both priori and posteriori emissions were assessed. This is a new attempt to employ the field measurements of VOCs in CTM simulations in the PRD region to improve simulations of VOCs and secondary pollutants for further studying atmospheric chemistry. In addition, the proposed observational constraint is applicable to future studies on short-term emission changes.

6.2 Overview of the Field Measurements

During the study period, *i.e.*, June 2018, the PRD region (Figure 3.2 and Table 3.3) was under the impact of the summer monsoon and tropical cyclones, which were representative of typical summertime weather conditions in South China. The measured total VOC concentrations varied among different areas, as shown in Figure 6.1a. In urban areas, ZQ and FS had the highest total VOC concentrations (31.16 ± 6.51 ppbv and 30.46 ± 6.07 ppbv, respectively), followed by SZ (29.14 ± 5.32 ppbv) and DG (28.05 ± 8.78 ppbv). The total VOC concentrations in the other urban areas were around 23 – 26 ppbv, nearly double that in the suburban site GZ-CH (13.27 ± 3.82 ppbv). The higher VOC concentrations in urban areas than those in the suburban areas were mainly due to the more intensive anthropogenic VOC emissions, such as vehicular emissions, which were found to be the major VOC sources in the PRD region (Guo et al., 2011; Guo et al., 2017). In addition to the spatial distributions of total VOC concentrations, the compositions of VOC groups in different areas were also different. Among the three VOC groups, alkanes accounted for the largest percentage of total VOC concentrations at all sites (41.94% – 57.46%), consistent with previous studies in the PRD region (Zou et al., 2015; He et al., 2019; Meng et al., 2022).

Meanwhile, the proportions of alkenes and alkyne (24.70% – 40.85%) were higher than those of aromatics (12.30% – 25.90%). The higher contribution of alkenes and alkyne to the total VOC concentrations in GZ-CH (40.85%) than in the urban areas (24.70% – 33.38%) was attributable to the weaker anthropogenic emissions of alkanes and alkenes and relatively stronger biogenic emissions of isoprene in the suburban areas (Tang et al., 2007b). Besides, aromatics, mainly evaporated from volatile solvents (Guo et al., 2007), had different contributions to the total VOC concentrations among cities, with higher proportions in JM (25.90%), HZ (22.87%), and ZQ (21.45%). The spatial variations of VOC compositions in the PRD region were related to the different emission sources among cities (Yuan et al., 2012; Louie et al., 2013).

Furthermore, online VOCs observations were carried out at urban and suburban sites (online-U and online-B) (Table 3.3), and the concentrations of VOCs were consistent with those at the 10 offline sampling sites (Figure 6.1a). Figures 6.1b-e illustrate the monthly averaged diurnal variations of VOC concentrations at online-U and online-B. The VOC concentrations were found to have similar daily patterns in both urban and suburban areas, with slight increases in the early morning and significant decreases from noon to afternoon, under the influences of emissions, photochemical reactions, and vertical mixing. During the daytime, both anthropogenic activities and biogenic emissions were enhanced, while the photochemical reactions were boosted, and the vertical mixing of air was facilitated by the evolution of the planetary boundary layer, leading to decreases in VOC concentrations in the afternoon (An et al., 2014; Zou et al., 2015; Wei et al., 2018; Li et al., 2019b).

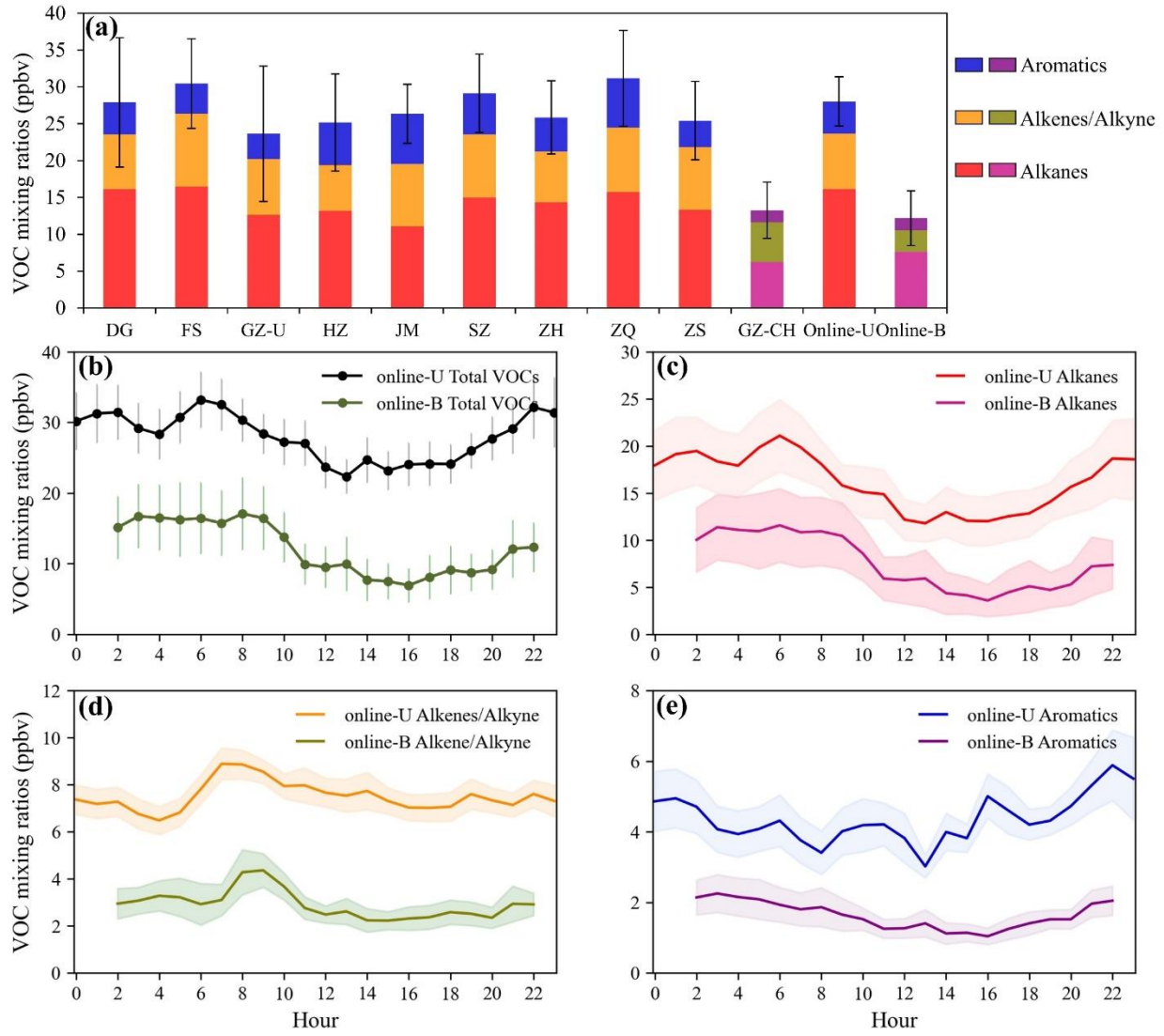

Figure 6.1. (a) Average VOC concentrations (ppbv) at 10 sampling sites measured offline and 2 sites measured online (online-U and online-B) (Table 3.3). (b-e) Monthly average diurnal variations of total VOC concentrations and VOC groups (ppbv) measured online. The total VOCs and VOC groups refer to the 50 constrained VOC species listed in Table 3.4 and 3 biogenic VOCs (isoprene, α-pinene, and β-pinene). The error bars and the shaded areas present the standard deviations of the total VOC concentrations and the concentrations of VOC groups, respectively. Note that time is in local time, which is the China Standard Time (CST, UTC+8) in this study.

The field measurements showed that the total VOC concentrations and VOC compositions in the PRD region had noticeable spatiotemporal variations, corresponding to the different VOC emissions characteristics among cities and areas. Given the intensive anthropogenic activities in this region, VOCs were mainly emitted from anthropogenic sources (Barletta et al., 2005; Liu et al., 2008; Bian et al., 2019). Therefore, this study only focused on anthropogenic VOCs.

6.3 Base model simulation

Before constraining the anthropogenic VOC emissions, the priori emission inventory was used as input for the base model simulation. Figure 6.2a illustrates the spatial distributions of the total CB05 VOC concentrations (*i.e.*, the sum of eight CB05 VOC species listed in Table 3.5) in the PRD region from field measurements and base model simulation. The measured total CB05 VOC concentrations were in the range of 60 – 80 ppbv in urban areas and around 30 ppbv in suburban areas. Although the base model simulation has generally reproduced the higher VOC concentrations in the central PRD region than in the suburban and rural areas around, the simulated VOC concentrations were overestimated at SZ (113.11 ± 37.61 ppbv), GZ-U (110.77 ± 26.50 ppbv), and FS (104.96 ± 28.06 ppbv) by 39% – 85%. Meanwhile, the simulated VOC concentrations in western PRD cities, *i.e.*, ZQ (44.22 ± 24.21 ppbv), JM (42.57 ± 15.76 ppbv), and ZH (36.19 ± 15.46 ppbv), were underestimated by -32% – -55%. As shown in Figure 6.2c, high anthropogenic VOC emissions were allocated to SZ, FS, and GZ-U in the priori emission inventory, whereas ZQ, JM, and ZH had rather low VOC emissions. It was found that the simulated VOC concentrations were highly related to the input anthropogenic VOC emissions in the CMAQ model. Hence, constraining the anthropogenic VOC emissions based on field measurements in each city would be beneficial for better simulating the VOC concentrations.

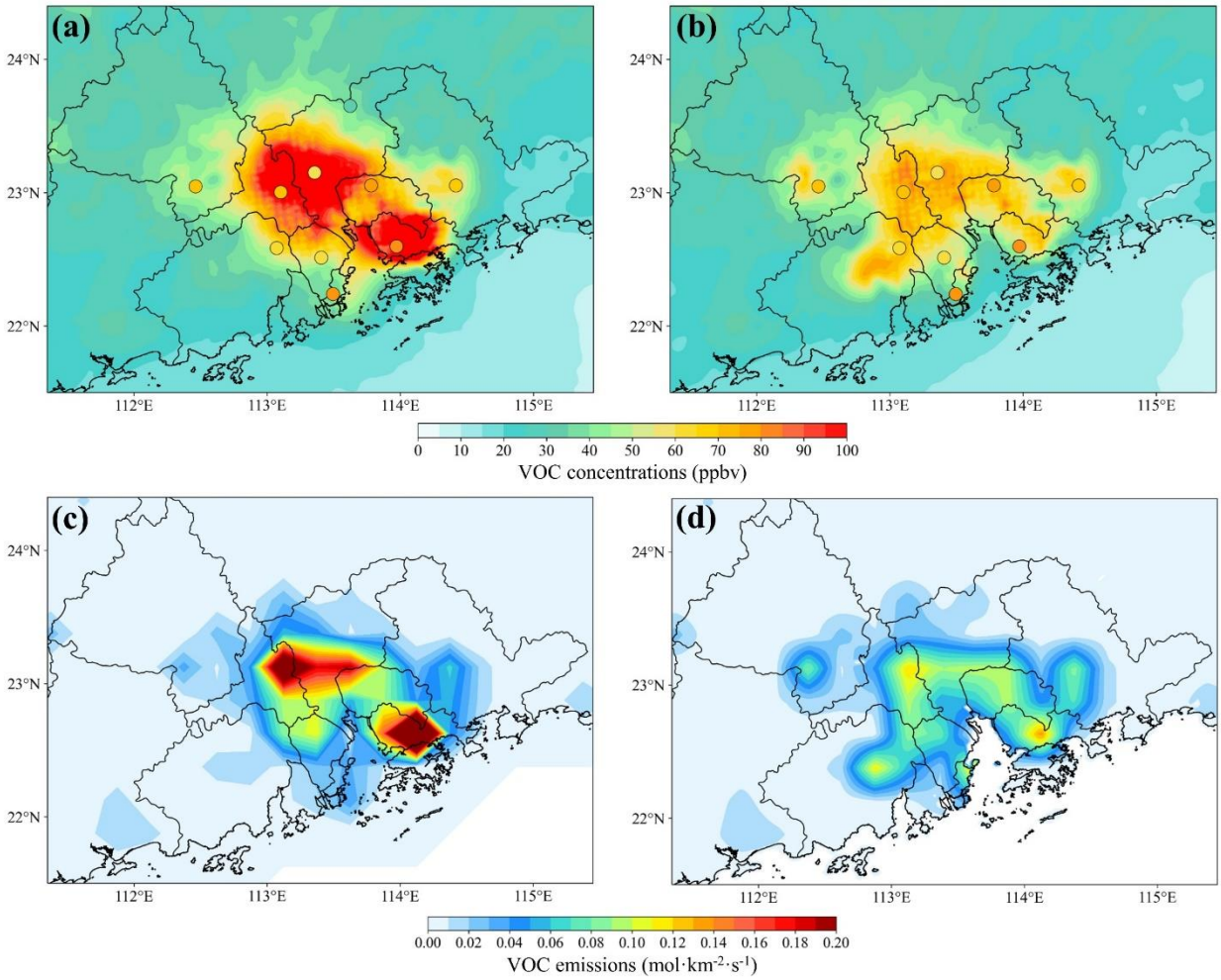

Figure 6.2. (a-b) Average total CB05 VOC concentrations (sum of eight CB05 VOC species listed in Table 3.5) throughout the study period (ppbv). (a) Base model simulation; (b) constrained model simulation. The contour colors represent the CMAQ simulations; scatter points are the field measurements. (c-d) Monthly average total CB05 VOC emissions ($mol \cdot km^{-2} \cdot s^{-1}$). (c) VOC emissions in the priori emission inventory. (d) Observation-constrained VOC emissions.

In addition to the total CB05 VOC concentrations, the VOC compositions had essential influences on atmospheric photochemistry, as the reactivity of VOCs with oxidants varied among species. For instance, alkenes with olefinic carbon bonds (ETH, OLE, and IOLE) are more reactive than alkanes with only paraffinic carbon bonds (ETHA and PAR) (Atkinson, 1997), while the

concentration of PAR is proportionally greater than that of other groups because it lumps more VOC species. Aromatics (BENZENE, TOL, and XYL) are grouped according to the number of alkyls, with XYL having polyalkyl, such as xylenes, being more reactive than other aromatics (Atkinson, 1986). Due to the different emission characteristics of VOC sources, the composition of VOCs was inconsistent among the PRD cities. Thus, the reactivity of CB05 VOC species with the OH radical, which initiates the oxidation of VOCs, from field measurements and the base model simulation, was compared in Figure 6.3. In line with the spatial distributions of total CB05 VOC concentrations, the simulated total OH reactivity from the base model was much higher in SZ (9.85 ± 2.87 s^{-1}), GZ-U (8.86 ± 2.64 s^{-1}), and FS (8.69 ± 2.31 s^{-1}) and much lower in ZQ (2.79 ± 0.59 s^{-1}), JM (2.83 ± 0.58 s^{-1}) and ZH (2.76 ± 0.57 s^{-1}), compared with the measured OH reactivity in the PRD cities, which was within the range of 4.78 – 6.45 s^{-1}. Though the simulated total CB05 VOC concentrations in DG (72.81 ± 39.85 ppbv) and HZ (59.16 ± 26.32 ppbv) were close to the observations (78.60 ± 39.25 ppbv and 69.11 ± 33.01 ppbv, respectively), discrepancies were still found in the simulations of OH reactivity, with higher total OH reactivity in DG (base simulation: 6.64 ± 1.96 s^{-1}; measurement: 4.97 ± 0.60 s^{-1}) and lower in HZ (base simulation: 3.34 ± 0.86 s^{-1}; measurement: 5.65 ± 0.71 s^{-1}). Apart from that, differences were also found in the contributions of individual VOC species to the total OH reactivity, especially for the species that have rather low concentrations but high reactivity. The model has overestimated the proportion of IOLE (base simulation: 9.41% – 21.71%; measurement: 4.15% – 9.24%) while the contributions of XYL (base simulation: 14.03% – 17.62%; measurement: 17.74% – 38.11%) were underestimated. These discrepancies further indicated that there were large biases in the simulations of VOC compositions. Therefore, it is necessary to constrain the emissions of individual VOCs separately in order to better reproduce the VOC compositions in each city.

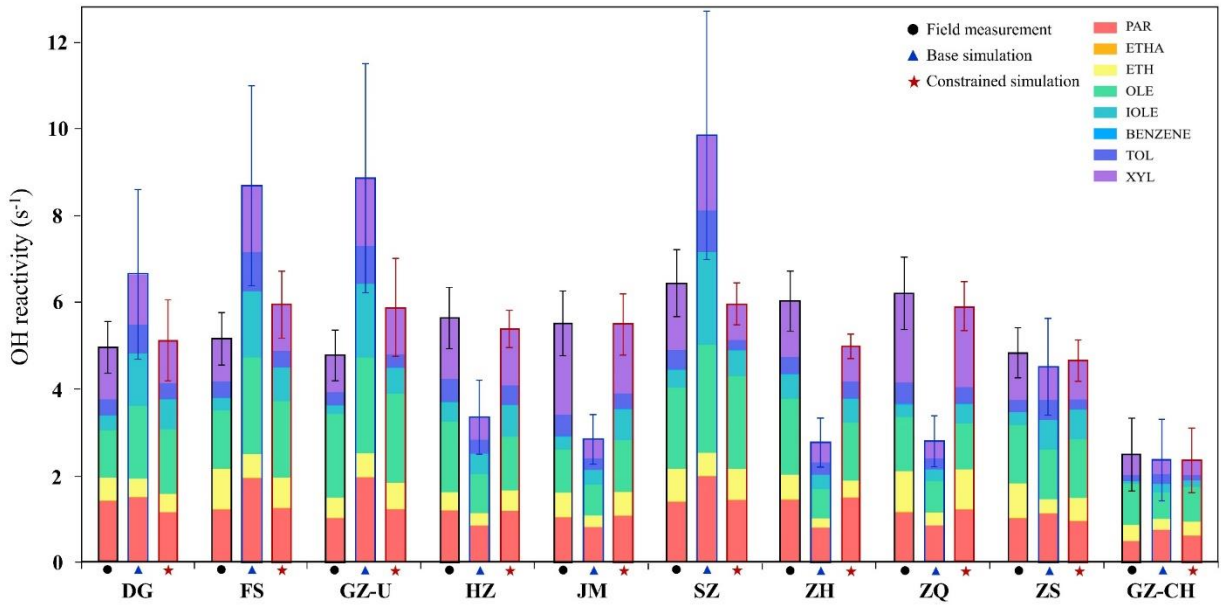

Figure 6.3. Average OH reactivity (s^{-1}) of CB05 VOC species at 10 sampling sites. The black circle, blue triangle, and red star denote the field measurements, base model simulation, and constrained model simulation, respectively. The error bars represent the standard deviations. OH reactivity = $k_i \times [VOC]_i$, where k_i represents the reaction rate constant of each CB05 VOC species with the OH radical; $[VOC]_i$ represents the concentration of each CB05 VOC species.

As for the temporal variations of VOC concentrations, Figure 6.4a presents the monthly average diurnal patterns of total CB05 VOC concentrations from the base model simulation at each city and the observations at online-U and online-B. It was clear that the base model simulation reproduced the general decrease of VOC concentrations around noon, relating to the boosted photochemical reactions and the increased boundary layer height. However, the prominent peaks in the early morning and the evening were unrealistic compared to the relatively gentle changes in the field measurements. More specifically, the diurnal variations of measured VOCs varied among species in different areas (Figure 6.5). Slight increases in the early morning and decreases during daytime were observed at both urban and suburban sites for PAR, ETHA, ETH, and OLE, while

the aromatic species showed different patterns in urban and suburban areas. For example, the concentrations of BENZENE increased during the daytime, and the levels of TOL and XYL varied throughout the day in urban areas. However, the simulated VOCs had similar diurnal patterns for all CB05 VOC species in each city. Hence, discrepancies between the simulated and observed VOCs were mainly found during the daytime. Given the biases in both spatial distributions and diurnal variations of simulated VOCs, the observational constraint of VOC emissions was applied in this chapter to improve the simulations of VOCs by the CMAQ model.

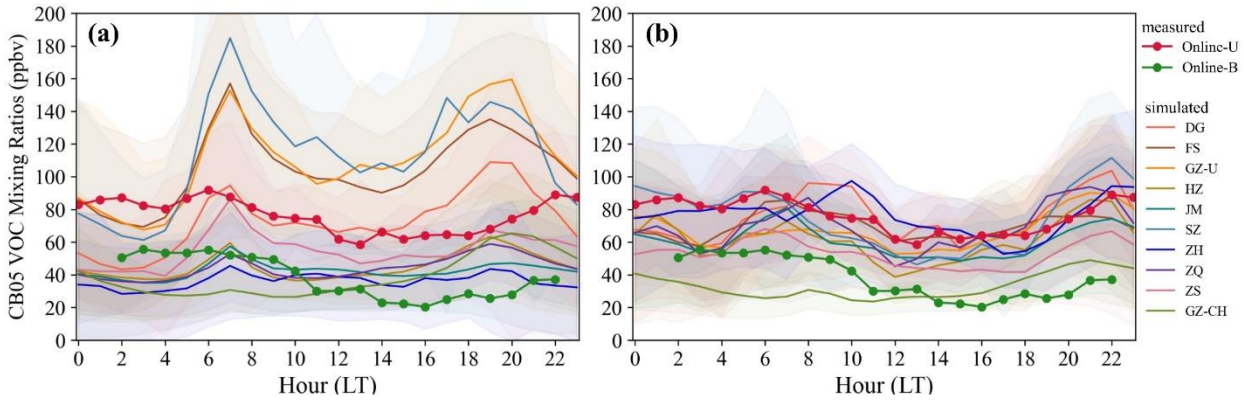

Figure 6.4. Monthly average diurnal variations of total CB05 VOC concentrations at each site (ppbv). (a) The base model simulation; (b) The constrained model simulation. The red and green curves are the measured data at online-U and online-B, respectively; the other lines are the model simulations with standard deviations shown in shaded areas. Note that LT refers to local time, which is the China Standard Time (CST, UTC+8) in this study.

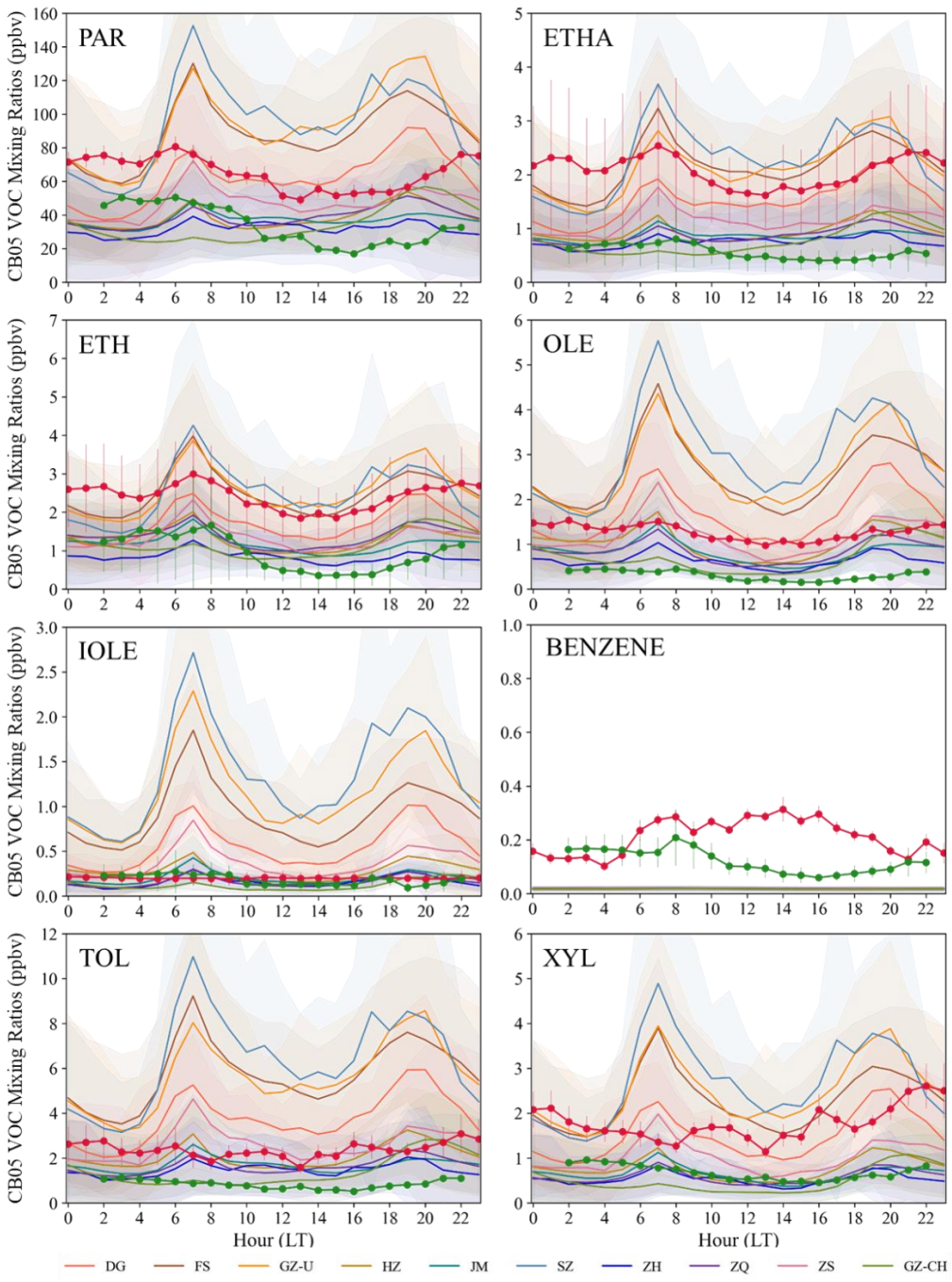

Figure 6.5. Monthly average diurnal variations of CB05 VOC concentrations at each site in the base model simulation (ppbv). The red and green curves are the measured data at online-U and online-B, respectively; the other lines are simulated concentrations with the standard deviations shown in shaded areas. Note that BENZENE was not input in the base model simulation as it was not speciated in the emission inventory.

6.4 Observation-constrained VOC emissions

By applying the observational constraint in Section 3.3, diurnal emission profiles of each anthropogenic VOC species in different cities can be obtained. As shown in Figure 6.6, the VOC emissions had clear diurnal patterns in the urban areas with more intensive emissions in the daytime, whereas the emissions in suburban areas were relatively low with insignificant diurnal variations. In order to estimate the VOC emissions in each city, the locally emitted VOCs removed by chemical consumption, horizontal transport, and vertical dilution were calculated according to Equations (8-11).

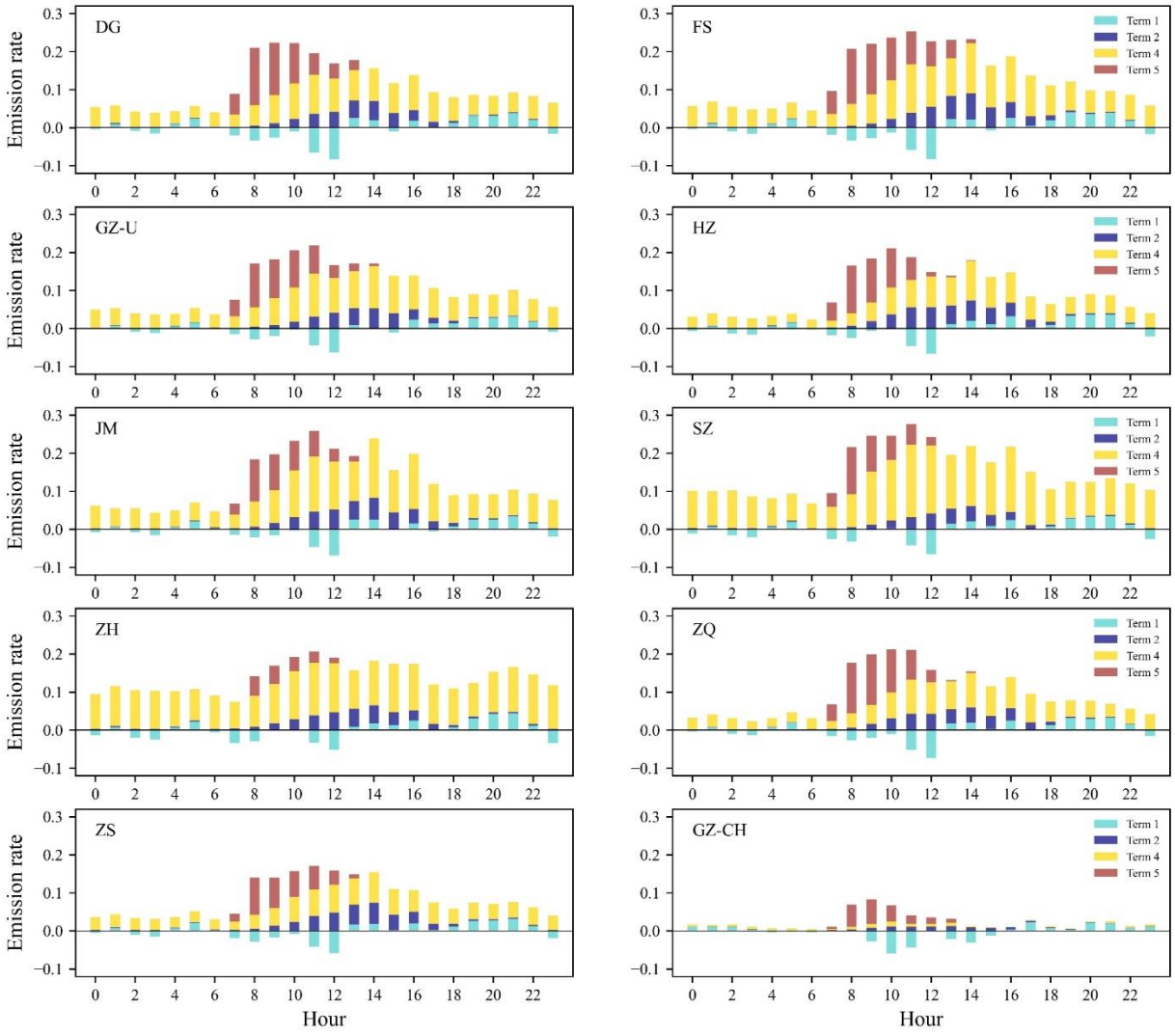

Figure 6.6. Observation-constrained total CB05 VOC emission profiles in each city and district. The colors represent different terms in the calculation (Equations 6a-b), where Term 1 is the change rate of VOC concentrations; Term 2 is the chemical loss rate; Term 3 is the removal rate, which was not considered in the calculation in Section 3.3.3; Term 4 is the horizontal transport rate; Term 5 is the vertical dilution rate. Unit: $mol \cdot km^{-2} \cdot s^{-1}$.

Specifically, horizontal transport out of the city had the highest contributions to the total VOC emissions, accounting for 73.36% – 89.71% in urban areas and 57.95% in suburban areas. The contributions of horizontal transports were associated with the wind speeds in different cities, which were higher in ZH (4.04 ± 2.19 m/s) and lower in GZ-CH (1.69 ± 1.03 m/s). In comparison, vertical dilution and chemical consumption mainly contributed during the daytime. The vertical dilution was strong in the morning (8:00 – 10:00 CST) when the boundary layer rose (Figure 3.14), and gradually weakened until early afternoon (13:00 – 14:00 CST) when the planetary boundary layer height (PBLH) reached its daily maximum. The PBLH in each city also affects the intensity of vertical dilution, and as the PBLH values were derived from WRF simulation, the accompanying uncertainty was analyzed in the following Section 6.6. Similarly, the chemical reactions of VOCs were boosted during noon-time (11:00 – 14:00 CST), corresponding to the enhancement of solar radiation and OH radical concentrations (Figure 3.12). The calculated chemical loss of VOCs was dominated by OH-initiated oxidations, accounting for 86.67% – 90.95% of the total chemical loss in all cities and districts on average. Meanwhile, the chemical loss of alkenes via reactions with O_3 and NO_3 was found to be significant at night, with the mean contributions of 8.44% – 12.12% and 0.21% – 1.21%, respectively. The significant oxidation reaction with the OH radical was, therefore, a dominant loss mechanism of VOCs (Parrish et al., 2007; de Gouw et al., 2017). Given that the model-simulated OH concentrations were employed

in the calculations, the biases of the simulations could result in uncertainties, which were further estimated in Section 6.6. Besides, the VOC change rates (Equation 7) were used to offset the VOC emissions related to processes that were not considered in the calculation. The impacts of the VOC change rates on the total VOC emissions were considerably smaller than the abovementioned three terms (*i.e.*, horizontal transport rate, vertical dilution rate, and chemical loss rate), with negative contributions around noon (11:00 – 12:00 CST), which led to slight decreases in VOC emissions. Overall, the diurnal variations of anthropogenic VOC emissions were associated with human activities when emissions from vehicles, industries, etc., were mainly recorded during the daytime.

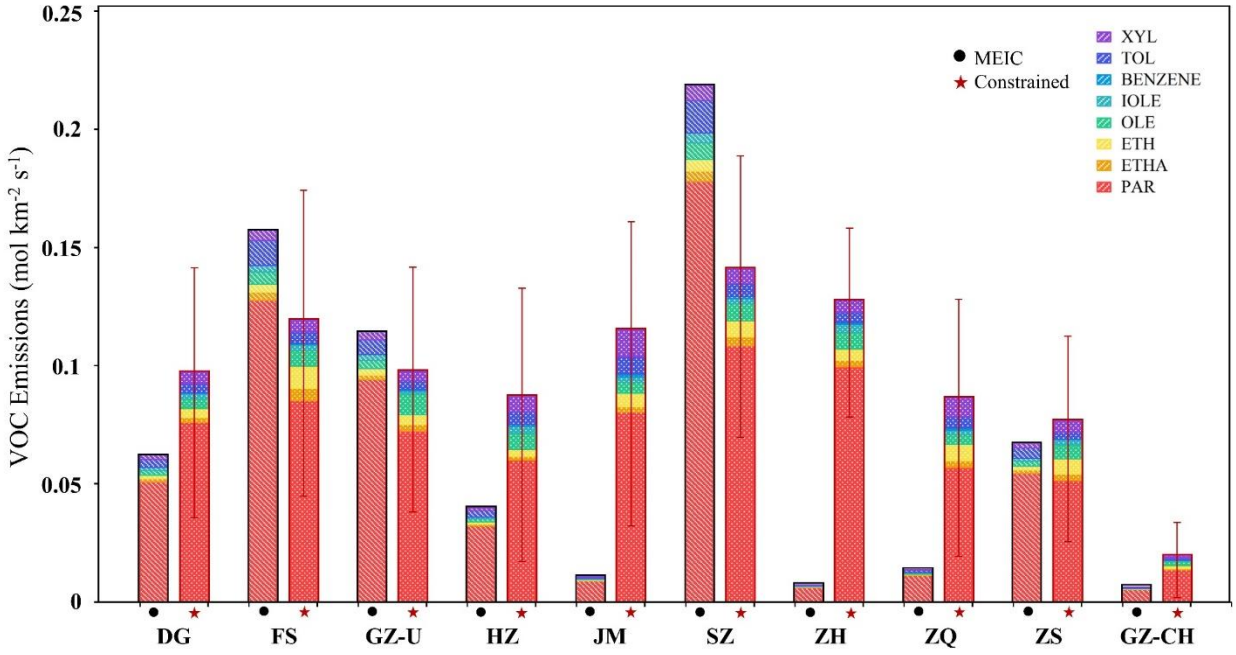

Figure 6.7. Daily average CB05 VOC emissions (mol·km^{-2}·s^{-1}) in each city and district. The black circle and red star denote the 2017-based MEIC emission and the observation-constrained emissions, respectively. The error bars represent the standard deviations.

The daily average VOC emission rates from the priori emission inventory and the observational constraint are presented in Figure 6.7. In the priori emission inventory, the total anthropogenic VOC emissions were mainly concentrated in SZ (0.22 mol·km^{-2}·s^{-1}), FS (0.16 mol·km^{-2}·s^{-1}), and

GZ (0.12 mol·km^{-2}·s^{-1}). In contrast, the emissions in ZQ, JM, and ZH were noticeably low, less than 0.02 mol·km^{-2}·s^{-1}. In comparison, the observation-constrained emissions in SZ, FS, and GZ-U were reduced by 15% – 36% to 0.14 ± 0.05 mol·km^{-2}·s^{-1}, 0.12 ± 0.06 mol·km^{-2}·s^{-1}, and 0.10 ± 0.05 mol·km^{-2}·s^{-1}, respectively, while the anthropogenic VOC emissions in other cities were enhanced after the observational constraint. In particular, the total VOC emissions in JM, ZH, and ZQ were substantially elevated from 0.012 mol·km^{-2}·s^{-1}, 0.007 mol·km^{-2}·s^{-1}, and 0.014 mol·km^{-2}·s^{-1} to 0.12 ± 0.06 mol·km^{-2}·s^{-1}, 0.13 ± 0.04 mol·km^{-2}·s^{-1}, and 0.09 ± 0.05 mol·km^{-2}·s^{-1}, respectively.

Table 6.1 further compares the emissions of each VOC species in priori and posteriori emission profiles, showing that the magnitudes of the emission correction varied for each city due to different emission characteristics of VOC species across cities. It is worth noting that, in addition to incorporating BENZENE emissions into the constrained profiles, the emission intensities of VOC species did not necessarily increase or decrease with the increase or decrease of total VOC emissions. Specifically, the reductions in the total VOC emissions in FS and GZ-U mainly resulted from the reduced emissions of PAR, TOL, and IOLE, while the emissions of ethane (ETHA), ethene (ETH), OLE, and XYL rose after the constraints. Moreover, although the total VOC emissions in ZS showed the smallest increase among cities (by 14%), the compositions of VOC emissions changed with the decreases of PAR and TOL and the increases of other species, especially alkenes (ETH, OLE, and IOLE). The above results suggest that observation-constrained emissions not only corrected the levels of total VOC emissions in the priori emission inventory but also modulated the proportions of VOC species in the emission profiles, which would affect the simulations of VOC compositions and O_3 photochemistry in the CMAQ model. The observation-constrained VOC emission profiles for the different VOC species in each city and

district were then interpolated into the model grids using the spatial distribution factors within each city. Accordingly, the spatially-distributed posteriori anthropogenic VOC emissions in the PRD region were obtained (Figure 6.2d) with more accordant emissions distributed in the urban areas of each city than the priori emissions (Figure 6.2c).

Table 6.1. Daily average CB05 VOC emissions ($\times 10^2$ mol·km^{-2}·s^{-1}) in each city and district from the 2017-based MEIC emission and the observation-constrained emissions. (Mean ± standard deviation over time)

VOCs	Emission	DG	FS	GZ-U	HZ	JM	SZ	ZH	ZQ	ZS	GZ-CH
PAR	MEIC	5.09	12.77	9.41	3.21	0.89	17.80	0.62	1.11	5.45	0.52
	Constrained	7.60±4.09	8.51±4.24	7.24±3.63	6.00±3.90	8.04±4.03	10.85±4.29	9.96±2.92	5.70±3.46	5.14±2.69	1.36±1.32
ETHA	MEIC	0.12	0.33	0.20	0.09	0.02	0.43	0.01	0.03	0.14	0.01
	Constrained	0.19±0.09	0.51±0.25	0.26±0.12	0.17±0.10	0.23±0.10	0.37±0.12	0.27±0.05	0.28±0.16	0.29±0.13	0.05±0.05
ETH	MEIC	0.15	0.34	0.26	0.09	0.03	0.48	0.02	0.03	0.15	0.02
	Constrained	0.39±0.24	0.96±0.61	0.42±0.25	0.29±0.20	0.57±0.33	0.69±0.29	0.47±0.15	0.68±0.45	0.64±0.41	0.14±0.10
OLE	MEIC	0.20	0.52	0.35	0.13	0.03	0.71	0.02	0.05	0.22	0.02
	Constrained	0.41±0.38	0.66±0.63	0.88±0.78	0.68±0.63	0.46±0.40	0.71±0.52	0.71±0.50	0.42±0.37	0.58±0.55	0.20±0.13
IOLE	MEIC	0.14	0.26	0.25	0.06	0.02	0.41	0.02	0.02	0.12	0.01
	Constrained	0.21±0.20	0.25±0.24	0.14±0.13	0.31±0.27	0.23±0.20	0.21±0.15	0.34±0.21	0.19±0.16	0.22±0.19	0.03±0.01
BENZENE	MEIC	-	-	-	-	-	-	-	-	-	-
	Constrained	0.04±0.02	0.05±0.03	0.06±0.05	0.06±0.04	0.13±0.11	0.10±0.07	0.08±0.05	0.10±0.08	0.03±0.02	0.01±0.00
TOL	MEIC	0.34	1.07	0.62	0.28	0.06	1.38	0.02	0.10	0.43	0.04
	Constrained	0.38±0.28	0.49±0.39	0.36±0.28	0.55±0.46	0.72±0.53	0.55±0.33	0.44±0.23	0.47±0.38	0.29±0.22	0.07±0.05
XYL	MEIC	0.19	0.45	0.34	0.11	0.03	0.64	0.02	0.04	0.19	0.02
	Constrained	0.51±0.47	0.51±0.50	0.40±0.37	0.64±0.61	1.15±1.03	0.62±0.46	0.53±0.39	0.80±0.75	0.50±0.48	0.11±0.09
Total VOCs	MEIC	6.22	15.74	11.44	3.98	1.09	21.86	0.74	1.38	6.71	0.64
	Constrained	9.70±5.29	11.93±6.46	9.74±5.17	8.63±5.77	11.51±6.43	14.10±5.95	12.79±4.00	8.57±5.44	7.64±4.34	1.73±1.59

Overall, the updates in the diurnal variations and spatial allocations of anthropogenic VOC emissions after the observational constraint have better represented the VOC emission characteristics in the urban areas of the PRD region. Thereby, with the observation-constrained VOC emissions, the performance of the CMAQ model simulation for the VOCs in the PRD cities would be further enhanced compared with that of the base model simulation.

6.5 Constrained model simulation

The observation-constrained anthropogenic VOC emissions herein were used to drive the CMAQ model again for the constrained model simulation. Figure 6.2b shows that the total VOC concentrations from the constrained model simulation were in agreement with the field measurements, as the normalized biases between simulated and observed average total VOC concentrations across cities dropped from -55% – 85% to -13% – 13% in the simulation period. The modeled VOC levels were higher in urban areas (53.29 – 76.57 ppbv) and lower in the suburban area GZ-CH (33.19 ± 17.33 ppbv). Compared with the base model simulation (Figure 6.2a), the unexpectedly high VOC concentrations in SZ, GZ-U, and FS decreased substantially by 33% – 39% in the constrained simulation, while the relatively high VOCs observed in urban ZQ and JM were reproduced. In terms of the VOC compositions, the model better simulated the OH reactivity of VOCs after the observational constraint (Figure 6.3). The modeled monthly average OH reactivity in urban areas varied from 4.66 s^{-1} to 5.98 s^{-1}, within the measured range of 4.78 – 6.45 s^{-1}. Besides, the modeled reactive VOC species in the constrained simulation were more comparable with the field measurements. In particular, the contributions of ETH and XYL to the total OH reactivity were enhanced to 7.58% – 15.54% and 14.05% – 31.60%, respectively, in the constrained simulation. Similar levels were found in observed ETH and XYL, with contributions of 7.30% – 17.93% and 17.74% – 38.11%, respectively. The proportions of IOLE with constraint were reduced to 7.48% – 14.71%, comparable to the measurement (4.15% – 9.24%). As a result, the CMAQ simulations better represented the spatial distributions of the VOC concentrations and compositions in the PRD region after applying the observation-constrained VOC emissions.

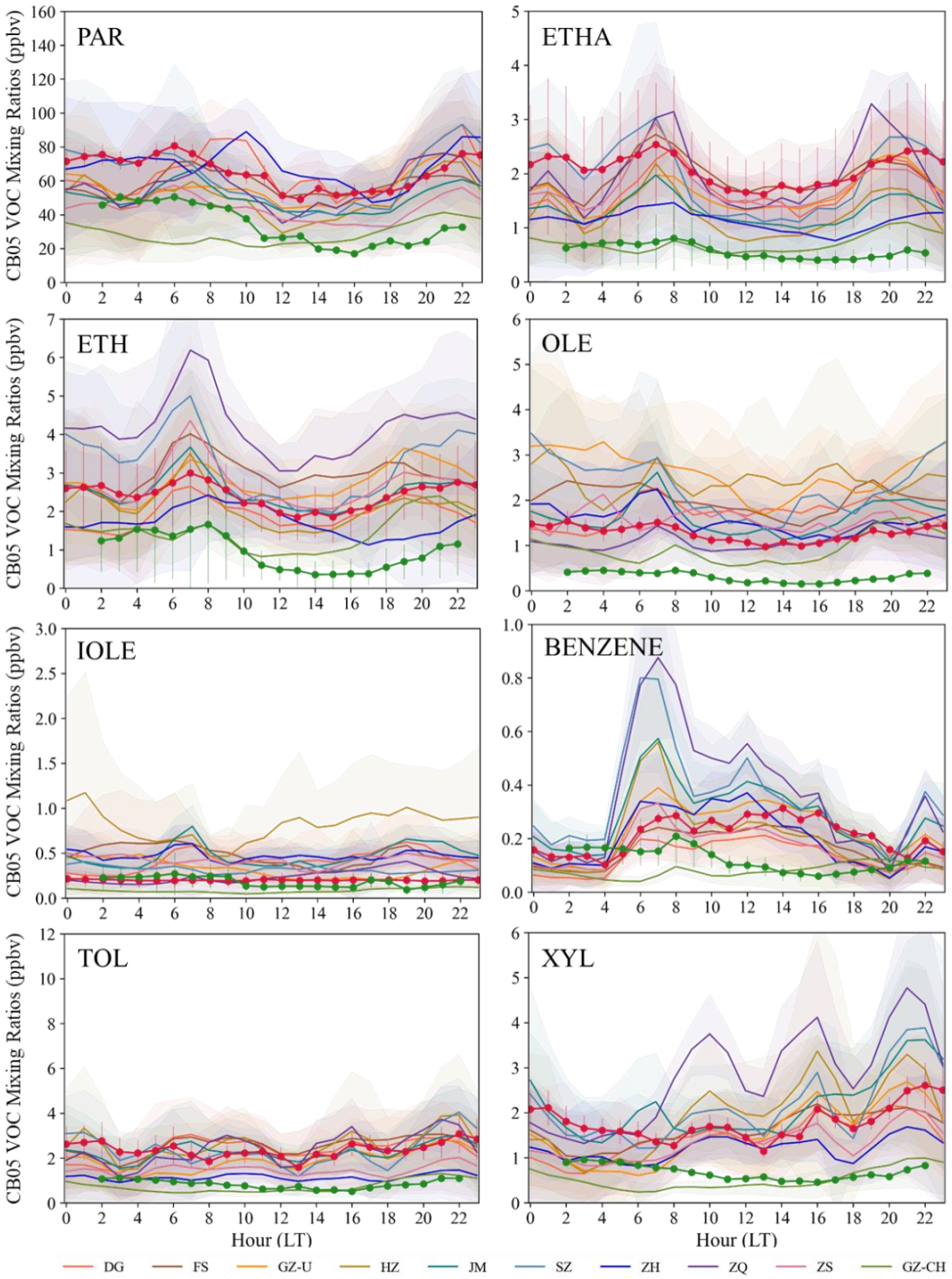

Figure 6.8. Monthly average diurnal variations of CB05 VOC concentrations at each site in the constrained model simulation (ppbv). The red and green curves are the measured data at online-U and online-B, respectively; the other lines are simulated concentrations with the standard deviations shown in shaded areas.

The diurnal variations of simulated VOCs were more consistent with those measured after observational constraint (Figure 6.4b), which had small peaks in the morning and evening, accompanied by considerable troughs in early afternoon. Moreover, the simulated VOCs presented different diurnal patterns among species, as shown in Figure 6.8. For PAR, ETHA, ETH, and OLE, the increases in the morning and decreases around noon were well-reproduced by the constrained model simulation in different cities. The model also captured the different patterns for aromatic species (*i.e.*, BENZENE, TOL, and XYL) in urban and suburban areas. Hence, benefiting from the diurnal emission profiles after observational constraint, the CMAQ model could better reveal the temporal variations of VOCs in the PRD region.

Furthermore, the modeled O_3 concentrations were well-improved on O_3 pollution days (Figure 3.11), especially on 11 June, when 40 out of 56 environmental monitoring stations recorded daily maximum O_3 concentrations over 100 ppbv, the Grade II standard of China's national air quality. The high-pressure system on 11 June (Figure 6.9) provided favorable weather conditions for photochemical reactions with intense solar radiation and high temperature, prompting the O_3 formation. Figure 6.10 shows the spatial distribution of simulated and observed O_3 concentrations during this O_3 pollution event. The base model simulation overestimated the O_3 levels, with the mean normalized bias (MNB) of 17% between observed and simulated O_3. Meanwhile, the 95th percentile of modeled O_3 concentrations across the innermost domain (d03) reached 147.98 ppbv in FS and offshore areas. The overestimation was in accordance with the high chemical production rates of O_3 in these areas. As key O_3 precursors, the abundance and composition of VOCs modulate the O_3 production. Therefore, with the improved simulations of VOCs using observation-constrained VOC emissions (Figure 6.2d), the CMAQ model was able to simulate the O_3 photochemistry better. In the constrained simulation, the modeled O_3 chemical production rates

were alleviated in FS and the offshore areas, while slightly enhanced in JM. Consequently, the modeled O_3 concentrations were amended, as the MNB value decreased to 12%, and the 95th percentile of O_3 concentrations in d03 also reduced by 10% to 133.46 ppbv. Thereafter, the pivot area of high O_3 levels moved to the western PRD region and the estuary. Similar improvements were found on 29 June, when O_3 concentrations in the eastern PRD region were relatively high (Figure 6.11). By using observation-constrained VOC emissions, the simulation of O_3 was greatly improved, reducing the MNB value from 30% to 18% and the 95th percentile by 8%. In addition, the O_3 hotspot in GZ and HZ was mitigated as a result of the eased O_3 chemical production. The reduced biases between simulation and observation after constraining the VOC emissions reflect that the CMAQ model performed better in simulating the spatial distributions of O_3 concentrations on high O_3 days.

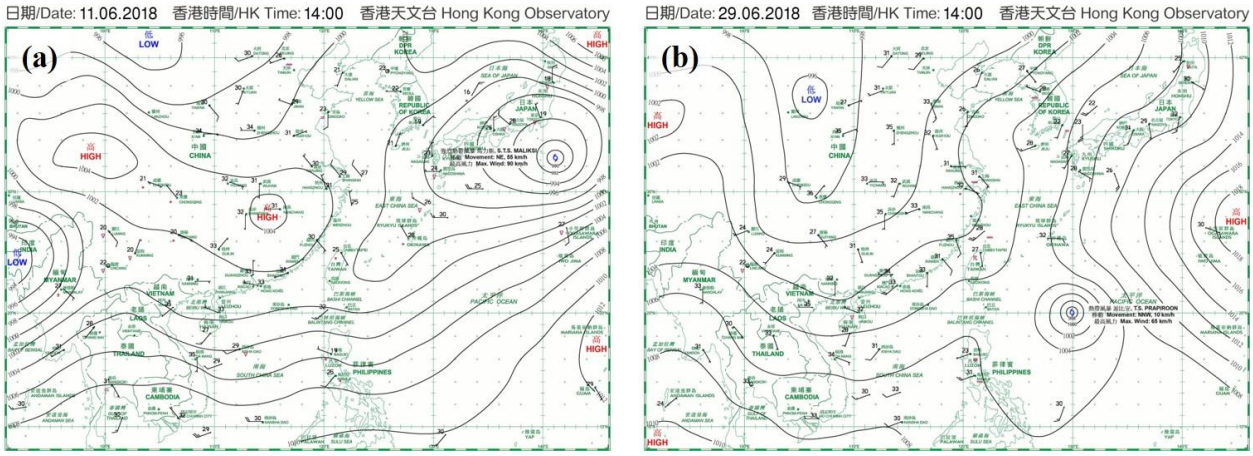

Figure 6.9. Surface weather charts at 14:00 CST on (a) 11 June 2018 and (b) 29 June 2018. The weather charts are available from: https://www.hko.gov.hk/.

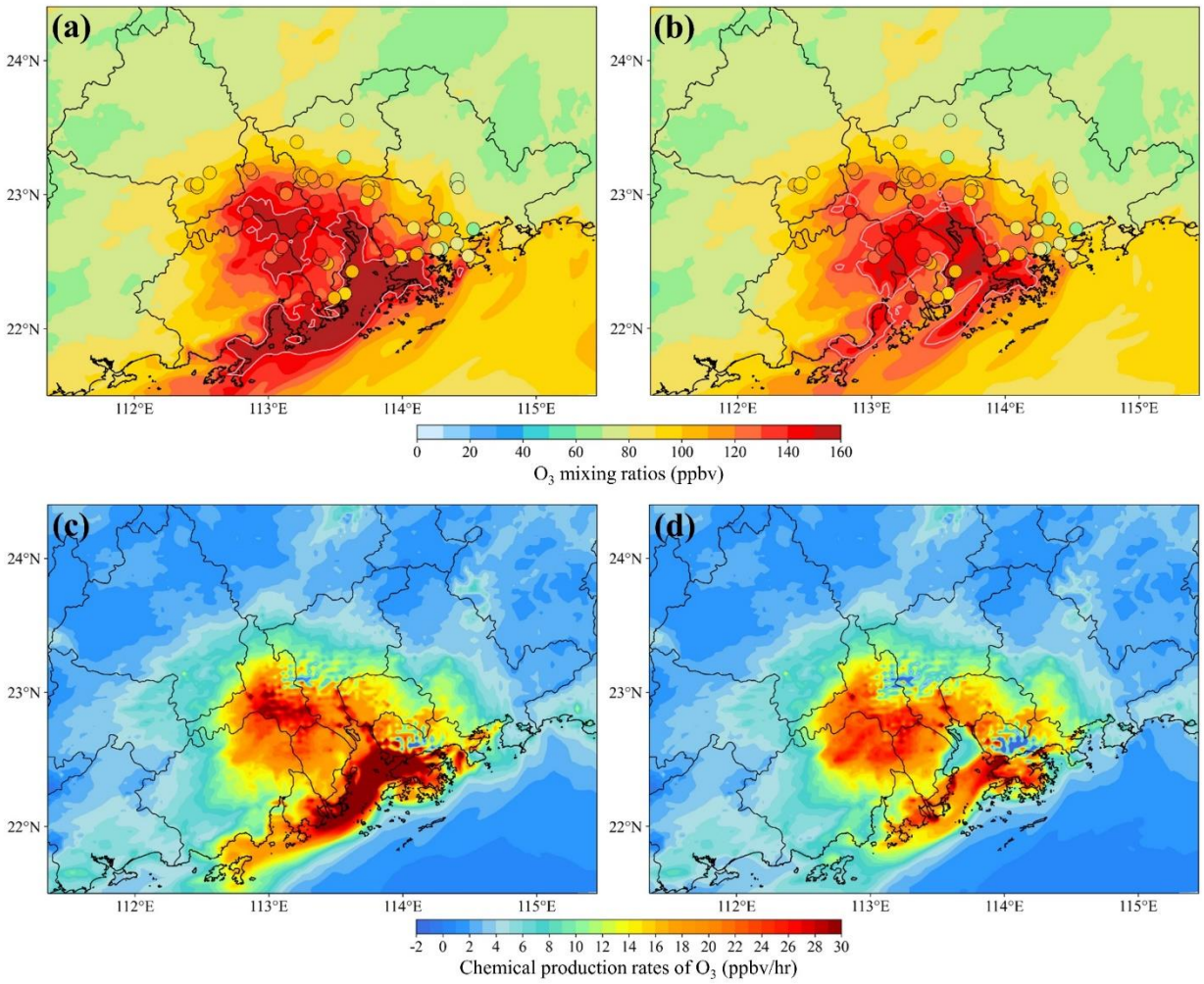

Figure 6.10. (a) Ground-level O_3 concentrations (ppbv) on 11 June 2018 at 14:00 CST from the base model simulation (background color) and observations (colored circles). (b) Same as (a) but for modeled O_3 concentrations (ppbv) from constrained model simulation. The pink contour line refers to the 95th percentile of O_3 concentrations in the study domain (d03), which was 147.98 ppbv in (a) the base model simulation and 133.46 ppbv in (b) the constrained model simulation. The O_3 monitoring stations are listed in Table 3.2. (c-d) Modeled chemical production rates of O_3 (ppbv/hr) on 11 June 2018 at 14:00 CST from (c) the base model simulation and (d) the constrained model simulation.

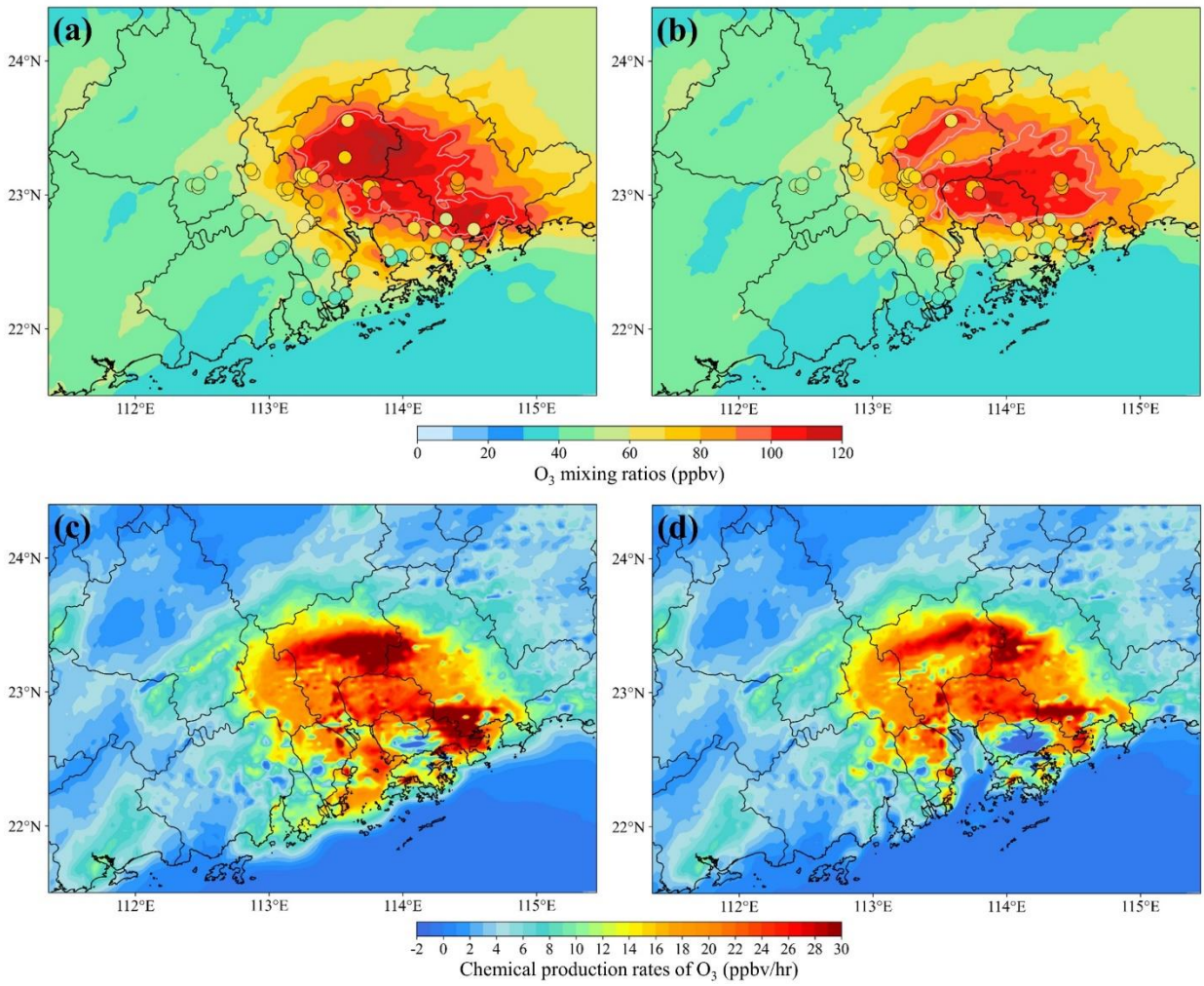

Figure 6.11. (a) Ground-level O_3 concentrations (ppbv) at 14:00 CST on 29 June 2018 from the base model simulation (background color) and observations (colored circles). (b) Same as (a) but for modeled O_3 concentrations (ppbv) from constrained model simulation. The pink contour line refers to the 95th percentile of O_3 concentrations in the study domain (d03), which was 103.39 ppbv in (a) the base model simulation and 95.11 ppbv in (b) the constrained model simulation. The O_3 monitoring stations are listed in Table 3.2. (c-d) Modeled chemical production rates of O_3 (ppbv/hr) at 14:00 CST on 29 June 2018 from (c) the base model simulation and (d) the constrained model simulation.

In spite of the improvements in high-level O_3 concentrations during O_3 pollution events, the modeled O_3 concentrations on days without extreme O_3 pollution were comparable between constrained and base model simulations (Figure 3.11) because the concentrations of O_3 were influenced by meteorological conditions and photochemical reactions (Liu & Wang, 2020a). Moreover, due to the non-linearity of O_3-persour relationships, both VOCs and NO_x levels impact regional O_3 pollution (Lu et al., 2019a). Although improved VOC simulations can indirectly enhance the representation of secondary oxygenated VOCs (OVOCs), primary OVOC emissions were not constrained in this study. Given that OVOCs also play significant roles in atmospheric radical cycling through photolysis and affect O_3 formation (Lary & Shallcross, 2000), unconstrained OVOC emissions may also limit improvements in O_3 simulations, especially outside peak hours. Consequently, insignificant differences in simulated O_3 concentrations between the constrained and base model simulations were found in lower-level O_3 concentrations. The remaining discrepancies in simulations and observations were the combined results of complex urban dynamics and O_3 photochemistry, which might not be fully captured by WRF and CMAQ models.

6.6 Uncertainty analysis

In the calculation of observational constraints, model-derived radical concentrations and PBLH in the PRD cities were applied due to the lack of direct measurements. Although the modeled OH concentrations and PBLH were within reasonable ranges compared with previous field measurements, as discussed in Section 3.3, the biases of simulated values would introduce uncertainties into the calculated emission profiles. Therefore, the Monte Carlo framework (see Section 3.3.6 for details) was applied to quantify the propagation of uncertainties in the observation-constrained emissions. In addition, the box length was determined by the size of the

minimum envelope covering the administrative area of each city and might vary when using different measurement methods. Hence, the sensitivity of the calculated emissions to different box lengths was also estimated using a Monte Carlo framework. Given that SZ has the highest VOC emission rates among the PRD cities in both the priori emission inventory and observation-constrained emissions, the uncertainty analysis for SZ was selected as a representative of the observation-constrained emissions in the PRD region. The daily maximum OH concentrations observed in urban SZ, ranging from $2 – 9 \times 10^6$ molecules/cm^3 (Yang et al., 2022), were employed in the Monte Carlo runs. The noon-time PBLH was set to the range of 600 – 1200 m, according to the measured PBLH in Guangdong province during summer (Guo et al., 2016). As for the city's box length, it ranged from half to twice the original city length. The input parameters, *i.e.*, OH concentrations, PBLH, and box lengths, were randomly sampled from the pre-defined ranges, and then the Monte Carlo simulations were repeated 10000 times.

The Monte Carlo runs yielded the probability distributions of estimated emissions, which statistically assessed the uncertainties corresponding to each input parameter. In the simulations for OH concentrations (Figure 6.12a), the total CB05 VOC emissions had an average of 0.140 mol·km^{-2}·s^{-1} under the 5th – 95th percentiles of 0.135 – 0.146 mol·km^{-2}·s^{-1}. Accordingly, the estimated uncertainties in the total VOC emissions based on the mean value were between -3.97% and 3.80%. Meanwhile, due to the more significant contributions of the chemical reaction term to the emissions of reactive VOC species, the uncertainties for OLE, IOLE, and XYL were relatively larger, reaching ±18% – ±23%. In terms of the PBLH simulations, the 5th – 95th percentiles of the total VOC emissions were 0.117 – 0.188 mol·km^{-2}·s^{-1}, with the mean value at 0.149 mol·km^{-2}·s^{-1}. Hence, the uncertainties related to the PBLH were between -21.93% and 26.20% (Figure 6.12b), which were more influential compared with those caused by the OH concentrations. Moreover,

Figure 6.12c shows that the sensitivity of the total VOC emissions to the city's box length was relatively high, and the deviations from the average emissions (0.145 mol·km^{-2}·s^{-1}) were -25% – 37%. Nonetheless, the levels of the uncertainties herein were much less than those estimated for VOC emission inventories in China, which were over 50% (Li et al., 2017b; Liu et al., 2017b; Huang et al., 2021). Therefore, the uncertainty analysis indicated that the uncertainties brought by the use of model-derived values and the estimations of the city's box length do not substantially impact the validity of the observation-constrained VOC emissions.

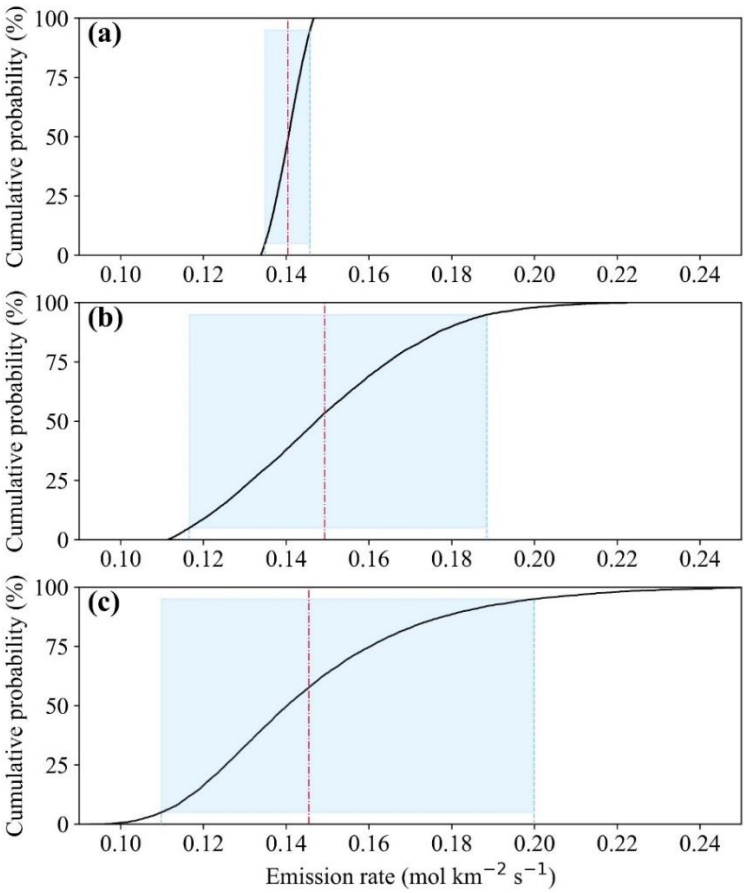

Figure 6.12. Cumulative probability distributions of the total CB05 VOC emission rate from 10,000 times Monte Carlo simulations for (a) OH radical concentrations, (b) PBLH, and (c) box lengths. The red dashed line represents the mean values, and the blue-colored area indicates the 5th – 95th percentiles.

6.7 Summary

Estimates of the VOC emissions are important for studying the formation of secondary air pollutants, especially for their applications in air quality models. Although efforts have been made to create accurate VOC emission inventories, biases still exist, which further influence the model simulations of VOCs and secondary pollutants. Hence, in this chapter, an observational constraint of the anthropogenic VOC emissions based on concurrent field measurements and WRF-CMAQ simulations was employed in the PRD region. The VOC characteristics of diurnal variations and species compositions in nine PRD cities were investigated through concurrent field measurements in the summer of 2018. Large discrepancies were found between the simulated and observed VOCs regarding the spatial distributions and temporal variations of the VOCs and their compositions when using the a priori emission inventory. The normalized biases of the average total VOC concentrations across the PRD cities ranged from -55% to 85% during the study period. By applying the observational constraint, diurnal VOC emission profiles in each city were assigned, corresponding to the removal of VOCs by chemical compositions, horizontal transport, and vertical dilution. Instead of concentrating the total anthropogenic VOC emissions in SZ, GZ, and FS in the priori emission inventory, the observation-constrained emissions corrected the spatial allocations of VOC emissions in the urban PRD region. The total VOC emissions in SZ, FS, and GZ-U were reduced by 36%, 24%, and 15%, respectively, while substantially higher emissions were apportioned to ZH, JM, ZQ, DG, and HZ. Therefore, after using the posteriori emissions in the CMAQ model, the normalized biases of the average total VOC concentrations dropped to -13% – 13%. The simulated VOC levels were comparable to observations, with overestimated VOC levels decreased by 33% – 39% in SZ, GZ-U, and FS, while underestimated VOC concentrations increased in ZH, JM, and ZQ. The diurnal VOC emissions also facilitated better simulations of the

temporal variations of different VOC species. Furthermore, as VOCs are key precursors to O_3, the simulations of O_3 photochemistry were amended so that the high-level O_3 concentrations on O_3 pollution days were better reproduced. The mean normalized biases between observed and simulated O_3 concentrations were reduced by 5% – 12%, and the overestimated 95th percentile was abated by 8% – 10%.

This work is the first to combine VOC field measurements with CTM modeling studies in the PRD region. The results demonstrate that top-down constraints based on observation can be used to update the VOC emission profiles, which further help to reduce biases in the simulations of VOCs and O_3 that the CTMs are suffering from. The improved simulations of VOCs were favorable for further studying atmospheric chemistry, especially O_3 photochemistry. More importantly, our observational constraint is flexible to reflect the emission variations in a specific region during a short-term period, in particular, the emission changes due to human interference. For example, the Covid-19 lockdowns, as well as the emission controls in China during the 2008 Summer Olympics in Beijing and the 2016 G20 Summit in Hangzhou. The constrained VOC emissions would better represent the emission characteristics during these periods and assist in air quality studies, providing useful information for air pollution control policies.

Chapter 7 Conclusions and Suggestions for Future Study

7.1 Conclusions

This thesis investigates warm-season O_3 pollution in China by integrating global perspectives, regional impacts, and local emissions. Using extensive observational data and advanced numerical modeling, the study: (1) assesses the current status and emerging challenges of O_3 pollution control in China and worldwide; (2) deciphers the physical and chemical processes driving summer O_3 accumulation in South China, with a quantitative assessment of transboundary transport from Southeast Asia; and (3) develops an observationally constrained approach to refine local VOC emission estimates and evaluates its impacts on model simulations of VOCs and O_3. The main findings of this thesis are summarized as follows:

1.1 During 2014 – 2019, China experienced the most severe warm-season O_3 pollution worldwide, characterized by the highest peak concentrations and the fastest rate of increase. This rapid escalation underscores the necessity for coordinated control of both NO_x and VOCs, alongside $PM_{2.5}$.

1.2 As traditional combustion-related emissions of O_3 precursors have declined substantially, previously overlooked emission sources have emerged as critical contributors to O_3 precursor levels. Consequently, targeted investigations and effective control strategies for these emerging sources are urgently required.

1.3 An enhanced climate penalty on O_3 has been observed worldwide under warming and drying conditions, posing significant challenges for O_3 air quality management. Therefore, integrated strategies that address both O_3 pollution and climate change are essential to effectively confront this growing global threat.

2.1 Summer O_3 pollution in South China has intensified over the past decade (2013 – 2022), with more frequent high O_3 episodes and elevated peak concentrations.

2.2 Widespread O_3 episodes across South China occurred under strong monsoon conditions, as regional sources from upwind Southeast Asia and shipping emissions transported O_3 and its precursors into South China, contributing an additional 4 ppbv to local O_3 levels.

2.3 The Beibu Gulf functioned as an O_3 reservoir, where O_3 and its precursors from upwind regions and ship emissions underwent chemical processing and accumulation. This sustained high O_3 concentrations and supplied O_3 to South China through prevailing southwesterly winds.

2.4 The summer monsoon plays a dual role in South China's O_3 pollution, both alleviating local pollution and facilitating the transboundary transport of air pollutants. Therefore, effectively mitigating regional O_3 pollution requires a multifaceted strategy that combines local emission reductions in China with strengthened international cooperation.

3.1 Observation-constrained VOC emissions revealed distinct diurnal variations and corrected the spatially concentrated emissions found in the prior inventory. Peak emissions in central PRD cities were reduced by 15% – 36%, while emissions in other cities, previously underestimated, were elevated.

3.2 Incorporating these constrained emissions, the model accurately reproduced the spatiotemporal variations of VOCs, reducing biases from -55% – 85% to -13% – 13%. As a result, simulations of O_3, especially peak levels, were significantly improved, with biases reduced by 5% – 12%.

3.3 This observational constraint method is adaptive for refining and updating VOC emission inventories. It is particularly valuable for studying the impacts of local, short-term emission

changes on O_3 pollution through model simulations, thereby aiding in the development of targeted emission control policies.

7.2 Suggestions for future study

This thesis has made significant progress in understanding the worsening O_3 pollution in China, providing a solid foundation for future research. However, some limitations remain. To comprehensively address O_3 pollution in China, the following suggestions for future studies are proposed:

1. Ongoing efforts to reduce fossil fuel combustion for air quality management and climate change mitigation have shifted the sources of O_3 precursors. Non-combustion-related sources have emerged and gained prominence as significant contributors to reactive organic compounds, primarily VOCs, in urban environments. These emerging sources include solvent evaporation from the widespread use of volatile chemical products (e.*g.*, personal care products, cleaning agents, pesticides, and paints) (McDonald et al., 2018; Coggon et al., 2021), biogenic emissions from both natural reserves and urban green spaces (Emmerson et al., 2018), non-exhaust emissions from road traffic (such as wear on brakes, tires, and road surfaces) (Khare et al., 2020; Harrison et al., 2021), and emissions from indoor activities (*e.g.*, cooking and the use of chemical products) (Abbatt & Wang, 2020). Notably, some of these sources, such as biogenic emissions and emissions from volatile chemical products (Qin et al., 2025), are highly sensitive to temperature and humidity, making them climate-dependent. Therefore, future research should focus on characterizing the emissions, speciation, chemical processing, and climate response of these emerging sources to accurately quantify their contributions to O_3

pollution and to develop targeted pollution control strategies in the context of a changing climate.

2. This study (Chapter 5) identified shipping emissions as an important contributor to O_3 pollution across South China. Globally, emissions from marine vessels are known to affect O_3 air quality in coastal regions and port cities due to their substantial release of NO_x and VOCs (Isakson et al., 2001; Viana et al., 2009; Fan et al., 2016). In response to air pollution concerns, a new global fuel oil sulfur limit was implemented in 2020 (IMO, 2019). While these regulations primarily target reductions in sulfur dioxide (SO_2) and particulate matter (PM), recent studies have reported notable increases in NO_x and VOC emissions following fuel switching (Luo et al., 2024). Pilot studies further indicate that shifts in fuel types have led to significant variations in both the abundance and composition of VOC species in shipping emissions, which are also influenced by ship type and operating mode (Wu et al., 2020; Zhang et al., 2024a). With seven of the world's top 10 ports located in China, shipping emissions in offshore and port areas are particularly substantial. Therefore, future research should investigate the impacts of shipping emissions on O_3 pollution not only in coastal cities but also across the entire country.

3. Although this study developed and successfully applied an observational constraint approach to refine anthropogenic VOC emission estimates (Chapter 6), its application was limited to one representative sampling site per city, despite concurrent measurements at ten sites. To extend the observational constraint and incorporate new measurement technologies, future studies could apply this approach to a broader and denser network of sampling locations, employing continuous, multi-year monitoring with online GC-MS, proton-transfer-reaction time-of-flight mass spectrometry (PTR-ToF-MS), and similar techniques. In addition, integrating ground-based measurements with satellite products and airborne observations

would combine the strengths of diverse observational data sources, thereby delivering extended spatial coverage, higher temporal resolution, a wider range of pollutant species, improved vertical profiling, and other enhancements. Furthermore, efforts are needed to improve traditional bottom-up emission estimates and to establish more accurate emission inventories for VOCs, as well as NO_x, OVOCs, and particulate matter. These improvements will benefit air pollution modeling and are essential for conducting long-term analyses of emission trends and for evaluating control policies. In particular, advanced chemical analysis techniques are crucial for measuring emission factors and rates across a wide range of air pollutants and with high temporal resolution. By leveraging big data from various sectors, the estimation of emission activity levels and their spatiotemporal variations could be enhanced.

REFERENCES

Abatzoglou, J. T., & Williams, A. P. (2016). Impact of anthropogenic climate change on wildfire across western US forests. *Proceedings of the National Academy of Sciences, 113*(42), 11770-11775. doi:10.1073/pnas.1607171113

Abbatt, J. P. D., & Wang, C. (2020). The atmospheric chemistry of indoor environments. *Environmental Science: Processes & Impacts, 22*(1), 25-48. 10.1039/C9EM00386J

Akimoto, H., Mori, Y., Sasaki, K., Nakanishi, H., Ohizumi, T., & Itano, Y. (2015). Analysis of monitoring data of ground-level ozone in Japan for long-term trend during 1990–2010: Causes of temporal and spatial variation. *Atmospheric Environment, 102*, 302-310.

An, J., Huang, Y., Huang, C., Wang, X., Yan, R., Wang, Q., et al. (2021). Emission inventory of air pollutants and chemical speciation for specific anthropogenic sources based on local measurements in the Yangtze River Delta region, China. *Atmospheric Chemistry and Physics, 21*(3), 2003-2025. 10.5194/acp-21-2003-2021

An, J., Zhu, B., Wang, H., Li, Y., Lin, X., & Yang, H. (2014). Characteristics and source apportionment of VOCs measured in an industrial area of Nanjing, Yangtze River Delta, China. *Atmospheric Environment, 97*, 206-214. https://doi.org/10.1016/j.atmosenv.2014.08.021

Andersson, C., Alpfjord, H., Robertson, L., Karlsson, P. E., & Engardt, M. (2017). Reanalysis of and attribution to near-surface ozone concentrations in Sweden during 1990–2013. *Atmospheric Chemistry and Physics, 17*(22), 13869-13890. 10.5194/acp-17-13869-2017

Anenberg, S. C., Henze, D. K., Tinney, V., Kinney, P. L., Raich, W., Fann, N., et al. (2018). Estimates of the Global Burden of Ambient PM2.5, Ozone, and NO2 on Asthma Incidence and Emergency Room Visits. *Environmental Health Perspectives, 126*(10), 107004. doi:10.1289/EHP3766

Ang, A. H.-S., & Tang, W. H. (1984). *Probability concepts in engineering planning and design, vol. 2: Decision, risk, and reliability*. New York: John Wiley & Sons Inc.

Askari, A., & Chan, A. W. H. (2024). Organic Emissions of Volatile Chemical Products in Canada: Emission Inventories, Indoor-to-Outdoor Transfer, and Regional Impacts. *Environmental science & technology, 58*(25), 11074-11083. 10.1021/acs.est.3c10753

Atkinson, R. (1986). Kinetics and mechanisms of the gas-phase reactions of the hydroxyl radical with organic compounds under atmospheric conditions. *Chemical Reviews, 86*(1), 69-201. 10.1021/cr00071a004

Atkinson, R. (1997). Gas-Phase Tropospheric Chemistry of Volatile Organic Compounds: 1. Alkanes and Alkenes. *Journal of Physical and Chemical Reference Data, 26*(2), 215-290. 10.1063/1.556012

Atkinson, R. (2000). Atmospheric chemistry of VOCs and NOx. *Atmospheric Environment, 34*(12), 2063-2101. https://doi.org/10.1016/S1352-2310(99)00460-4

Atkinson, R., & Arey, J. (2003). Gas-phase tropospheric chemistry of biogenic volatile organic compounds: a review. *Atmospheric Environment, 37*, 197-219. https://doi.org/10.1016/S1352-2310(03)00391-1

Bai, X., Liu, W., Wu, B., Liu, S., Liu, X., Hao, Y., et al. (2023). Emission characteristics and inventory of volatile organic compounds from the Chinese cement industry based on field measurements. *Environmental Pollution, 316*, 120600. https://doi.org/10.1016/j.envpol.2022.120600

Barletta, B., Meinardi, S., Sherwood Rowland, F., Chan, C.-Y., Wang, X., Zou, S., et al. (2005). Volatile organic compounds in 43 Chinese cities. *Atmospheric Environment, 39*(32), 5979-5990. https://doi.org/10.1016/j.atmosenv.2005.06.029

Bash, J. O., Baker, K. R., & Beaver, M. R. (2016). Evaluation of improved land use and canopy representation in BEIS v3.61 with biogenic VOC measurements in California. *Geoscientific Model Development, 9*(6), 2191-2207. 10.5194/gmd-9-2191-2016

Bian, Y., Huang, Z., Ou, J., Zhong, Z., Xu, Y., Zhang, Z., et al. (2019). Evolution of anthropogenic air pollutant emissions in Guangdong Province, China, from 2006 to 2015. *Atmospheric Chemistry and Physics, 19*(18), 11701-11719. https://doi.org/10.5194/acp-19-11701-2019

Binkowski, F. S., & Roselle, S. J. (2003). Models-3 Community Multiscale Air Quality (CMAQ) model aerosol component 1. Model description. *Journal of Geophysical Research: Atmospheres, 108*(D6). https://doi.org/10.1029/2001JD001409

Blake, N. J., Blake, D. R., Simpson, I. J., Meinardi, S., Swanson, A. L., Lopez, J. P., et al. (2003). NMHCs and halocarbons in Asian continental outflow during the Transport and Chemical Evolution over the Pacific (TRACE-P) Field Campaign: Comparison With PEM-West B. *Journal of Geophysical Research: Atmospheres, 108*(D20). https://doi.org/10.1029/2002JD003367

Bojkov, R. D. (1986). Surface Ozone During the Second Half of the Nineteenth Century. *Journal of Applied Meteorology and Climatology, 25*(3), 343-352. https://doi.org/10.1175/1520-0450(1986)025<0343:SODTSH>2.0.CO;2

Borbon, A., Gilman, J. B., Kuster, W. C., Grand, N., Chevaillier, S., Colomb, A., et al. (2013). Emission ratios of anthropogenic volatile organic compounds in northern mid-latitude megacities: Observations versus emission inventories in Los Angeles and Paris. *Journal of Geophysical Research: Atmospheres, 118*(4), 2041-2057. https://doi.org/10.1002/jgrd.50059

Bouarar, I., Brasseur, G., Petersen, K., Granier, C., Fan, Q., Wang, X., et al. (2019). Influence of anthropogenic emission inventories on simulations of air quality in China during winter and summer 2010. *Atmospheric Environment, 198*, 236-256. https://doi.org/10.1016/j.atmosenv.2018.10.043

Brauer, M., Freedman, G., Frostad, J., van Donkelaar, A., Martin, R. V., Dentener, F., et al. (2016). Ambient Air Pollution Exposure Estimation for the Global Burden of Disease 2013. *Environmental science & technology, 50*(1), 79-88. 10.1021/acs.est.5b03709

Brown, S. S., Dubé, W. P., Peischl, J., Ryerson, T. B., Atlas, E., Warneke, C., et al. (2011). Budgets for nocturnal VOC oxidation by nitrate radicals aloft during the 2006 Texas Air Quality Study. *Journal of Geophysical Research: Atmospheres, 116*(D24305). https://doi.org/10.1029/2011JD016544

Brown, S. S., & Stutz, J. (2012). Nighttime radical observations and chemistry. *Chemical Society Reviews, 41*(19), 6405-6447. 10.1039/C2CS35181A

Cao, H., Fu, T. M., Zhang, L., Henze, D. K., Miller, C. C., Lerot, C., et al. (2018). Adjoint inversion of Chinese non-methane volatile organic compound emissions using space-based observations of formaldehyde and glyoxal. *Atmospheric Chemistry and Physics, 18*(20), 15017-15046. https://doi.org/10.5194/acp-18-15017-2018

Cardelino, C. A., & Chameides, W. L. (1995). An Observation-Based Model for Analyzing Ozone Precursor Relationships in the Urban Atmosphere. *Journal of the Air & Waste Management Association, 45*(3), 161-180. 10.1080/10473289.1995.10467356

Carlton, A. G., Bhave, P. V., Napelenok, S. L., Edney, E. O., Sarwar, G., Pinder, R. W., et al. (2010). Model representation of secondary organic aerosol in CMAQv4.7. *Environmental science & technology, 44*(22), 8553-8560. https://doi.org/10.1021/es100636q

Carvalho, D., Rocha, A., Gómez-Gesteira, M., & Santos, C. (2012). A sensitivity study of the WRF model in wind simulation for an area of high wind energy. *Environmental Modelling & Software, 33*, 23-34. https://doi.org/10.1016/j.envsoft.2012.01.019

Chaliyakunnel, S., Millet, D. B., & Chen, X. (2019). Constraining emissions of volatile organic compounds over the Indian Subcontinent using space-based formaldehyde measurements. *Journal of Geophysical Research: Atmospheres, 124*(19), 10525-10545. https://doi.org/10.1029/2019JD031262

Chameides, W., & Walker, J. C. (1973). A photochemical theory of tropospheric ozone. *Journal of Geophysical Research, 78*(36), 8751-8760.

Chan, C. Y., & Chan, L. Y. (2000). Effect of meteorology and air pollutant transport on ozone episodes at a subtropical coastal Asian city, Hong Kong. *Journal of Geophysical Research: Atmospheres, 105*(D16), 20707-20724. 10.1029/2000jd900140

Chan, C. Y., Y., C. L., & and Harris, J. M. (2003). Urban and Background Ozone Trend in 1984-1999 at Subtropical Hong Kong, South China. *Ozone: Science & Engineering, 25*(6), 513-522. 10.1080/01919510390481829

Chan, L. Y., Chan, C. Y., & Qin, Y. (1998). Surface Ozone Pattern in Hong Kong. *Journal of Applied Meteorology, 37*(10), 1153-1165. 10.1175/1520-0450(1998)037<1153:Sopihk>2.0.Co;2

Chang, K. L., McDonald, B. C., Harkins, C., & Cooper, O. R. (2025). Surface ozone trend variability across the United States and the impact of heat waves (1990–2023). *Atmospheric Chemistry and Physics, 25*(10), 5101-5132. 10.5194/acp-25-5101-2025

Chen, D., Li, Q., Stutz, J., Mao, Y., Zhang, L., Pikelnaya, O., et al. (2013). WRF-Chem simulation of NOx and O3 in the L.A. basin during CalNex-2010. *Atmospheric Environment, 81*, 421-432. https://doi.org/10.1016/j.atmosenv.2013.08.064

Chen, H., Huang, Y., Shen, H., Chen, Y., Ru, M., Chen, Y., et al. (2016). Modeling temporal variations in global residential energy consumption and pollutant emissions. *Applied Energy, 184*, 820-829. https://doi.org/10.1016/j.apenergy.2015.10.185

Chen, S.-P., Liu, T.-H., Chen, T.-F., Yang, C.-F. O., Wang, J.-L., & Chang, J. S. (2010). Diagnostic modeling of PAMS VOC observation. *Environmental science & technology, 44*(12), 4635-4644. https://doi.org/10.1021/es903361r

Chen, X., & Mauzerall, D. L. (2021). The Expanding Coal Power Fleet in Southeast Asia: Implications for Future CO2 Emissions and Electricity Generation. *Earth's Future, 9*(12), e2021EF002257. https://doi.org/10.1029/2021EF002257

Chen, X., Wang, N., Wang, G., Wang, Z., Chen, H., Cheng, C., et al. (2022). The Influence of Synoptic Weather Patterns on Spatiotemporal Characteristics of Ozone Pollution Across Pearl River Delta of Southern China. *Journal of Geophysical Research: Atmospheres, 127*(21), e2022JD037121. https://doi.org/10.1029/2022JD037121

Chen, Y., Zhou, D., Tang, X., & Tang, Y. (1985). Changes in ozone concentrations in Xigu during summer: Measurement using portable ozone meter. *Research of Environmental Sciences (In Chinese)*(5), 39-43.

Cheng, L., Ye, Z., Wei, W., Wang, K., Wang, R., Yang, L., et al. (2024). Study on the establishment of air pollutant and carbon emission inventory and collaborative emission reduction potential of China's coking industry from 2012 to 2022. *Science of The Total Environment, 951*, 175183. https://doi.org/10.1016/j.scitotenv.2024.175183

Cheung, V. T. F., & Wang, T. (2001). Observational study of ozone pollution at a rural site in the Yangtze Delta of China. *Atmospheric Environment, 35*(29), 4947-4958. https://doi.org/10.1016/S1352-2310(01)00351-X

Chock, D. P., & Heuss, J. M. (1987). Urban ozone and its precursors. *Environmental science & technology, 21*(12), 1146-1153. 10.1021/es00165a001

Chutia, L., Ojha, N., Girach, I. A., Sahu, L. K., Alvarado, L. M. A., Burrows, J. P., et al. (2019). Distribution of volatile organic compounds over Indian subcontinent during winter: WRF-chem simulation versus observations. *Environmental Pollution, 252*(Pt A), 256-269. https://doi.org/10.1016/j.envpol.2019.05.097

CNEMC. (2013). *China Technical specifications for installation and acceptance of ambient air quality continuous automated monitoring system for SO2, NO2, O3 and CO*. China National Environmental Protection Standard, China Environmental Science Press, http://english.mee.gov.cn/Resources/standards/Air_Environment/air_method/201308/t20130816_257560.shtml

Coggon, M. M., Gkatzelis, G. I., McDonald, B. C., Gilman, J. B., Schwantes, R. H., Abuhassan, N., et al. (2021). Volatile chemical product emissions enhance ozone and modulate urban chemistry. *Proceedings of the National Academy of Sciences, 118*(32), e2026653118. doi:10.1073/pnas.2026653118

Colette, A., Andersson, C., Baklanov, A., Bessagnet, B., Brandt, J., Christensen, J. H., et al. (2015). Is the ozone climate penalty robust in Europe? *Environmental Research Letters, 10*(8), 084015. 10.1088/1748-9326/10/8/084015

Cooper, O. R., Parrish, D. D., Ziemke, J., Balashov, N. V., Cupeiro, M., Galbally, I. E., et al. (2014). Global distribution and trends of tropospheric ozone: An observation-based review. *Elementa: Science of the Anthropocene, 2*. 10.12952/journal.elementa.000029

Cooper, O. R., Schultz, M. G., Schröder, S., Chang, K.-L., Gaudel, A., Benítez, G. C., et al. (2020). Multi-decadal surface ozone trends at globally distributed remote locations. *Elementa: Science of the Anthropocene, 8*. 10.1525/elementa.420

Crippa, M., Guizzardi, D., Butler, T., Keating, T., Wu, R., Kaminski, J., et al. (2023). The HTAP_v3 emission mosaic: merging regional and global monthly emissions (2000–2018) to support air quality modelling and policies. *Earth System Science Data, 15*(6), 2667-2694. 10.5194/essd-15-2667-2023

Crooks, J. L., Licker, R., Hollis, A. L., & Ekwurzel, B. (2022). The ozone climate penalty, NAAQS attainment, and health equity along the Colorado Front Range. *Journal of Exposure Science & Environmental Epidemiology, 32*(4), 545-553. 10.1038/s41370-021-00375-9

CSC. (2013). *Notice of the General Office of the State Council on Issuing the Air Pollution Prevention and Control Action Plan*. State Council of the People's Republic of China, https://www.gov.cn/jrzg/2013-09/12/content_2486918.htm.

CSC. (2018). *Notice of the General Office of the State Council on Issuing the Three-Year Action Plan for Winning the Blue Sky Defense Battle*. State Council of the People's Republic of China, http://www.gov.cn/zhengce/content/2018-07/03/content_5303158.htm.

Cuchiara, G. C., Li, X., Carvalho, J., & Rappenglück, B. (2014). Intercomparison of planetary boundary layer parameterization and its impacts on surface ozone concentration in the WRF/Chem model for a case study in Houston/Texas. *Atmospheric Environment, 96*, 175-185. https://doi.org/10.1016/j.atmosenv.2014.07.013

Cui, C., Guan, D., Wang, D., Meng, J., Chemutai, V., Brenton, P., et al. (2022). Global mitigation efforts cannot neglect emerging emitters. *National Science Review, 9*(12). 10.1093/nsr/nwac223

de Gouw, J. A., Gilman, J. B., Kim, S.-W., Lerner, B. M., Isaacman-VanWertz, G., McDonald, B. C., et al. (2017). Chemistry of volatile organic compounds in the Los Angeles basin: Nighttime removal of alkenes and determination of emission ratios. *Journal of Geophysical Research: Atmospheres, 122*(21), 11,843-811,861. https://doi.org/10.1002/2017JD027459

Di Carlo, P., Brune, W. H., Martinez, M., Harder, H., Lesher, R., Ren, X., et al. (2004). Missing OH Reactivity in a Forest: Evidence for Unknown Reactive Biogenic VOCs. *Science, 304*(5671), 722-725. doi:10.1126/science.1094392

Ding, A., Wang, T., Zhao, M., Wang, T., & Li, Z. (2004). Simulation of sea-land breezes and a discussion of their implications on the transport of air pollution during a multi-day ozone episode in the Pearl River Delta of China. *Atmospheric Environment, 38*(39), 6737-6750. https://doi.org/10.1016/j.atmosenv.2004.09.017

EEA. (2023). *EMEP/EEA air pollutant emission inventory guidebook 2023* (EEA Report 06/2023). European Environment Agency, 10.2800/795737. https://www.eea.europa.eu/en/analysis/publications/emep-eea-guidebook-2023

EEA. (2024a). *Emissions of air pollutants from transport in Europe*. European Environment Agency, https://www.eea.europa.eu/en/analysis/indicators/emissions-of-air-pollutants-from

EEA. (2024b). *European Union emission inventory report 1990-2022 — Under the UNECE Convention on Long-range Transboundary Air Pollution (Air Convention)*. European Environment Agency, EEA Report 08/2024. doi: 10.2800/2893. https://www.eea.europa.eu/en/analysis/publications/european-union-emissions-inventory-report-1990-2022

EEA. (2024c). *Sustainability of Europe's mobility systems - Air pollution*. European Environment Agency, EEA Web report no. 01/2024. 10.2800/8560026. https://www.eea.europa.eu/en/analysis/publications/sustainability-of-europes-mobility-systems/air-pollution

Emberson, L. (2020). Effects of ozone on agriculture, forests and grasslands. *Philosophical Transactions of the Royal Society A: Mathematical, Physical and Engineering Sciences, 378*(2183), 20190327. doi:10.1098/rsta.2019.0327

Emery, C., Liu, Z., Russell, A. G., Odman, M. T., Yarwood, G., & Kumar, N. (2017). Recommendations on statistics and benchmarks to assess photochemical model performance. *Journal of the Air & Waste Management Association, 67*(5), 582-598. https://doi.org/10.1080/10962247.2016.1265027

Emery, C., Tai, E., & Yarwood, G. (2001). *Enhanced meteorological modeling and performance evaluation for two Texas ozone episodes*. Final Report Submitted to Texas Natural Resources Conservation Commission, Prepared by ENVIRON, International Corp., Novato.,

Emmerson, K. M., Cope, M. E., Galbally, I. E., Lee, S., & Nelson, P. F. (2018). Isoprene and monoterpene emissions in south-east Australia: comparison of a multi-layer canopy model with MEGAN and with atmospheric observations. *Atmospheric Chemistry and Physics, 18*(10), 7539-7556. 10.5194/acp-18-7539-2018

Enami, S., Hoffmann, M. R., & Colussi, A. J. (2008). Acidity enhances the formation of a persistent ozonide at aqueous ascorbate/ozone gas interfaces. *Proceedings of the National Academy of Sciences, 105*(21), 7365-7369. doi:10.1073/pnas.0710791105

Fan, Q., Zhang, Y., Ma, W., Ma, H., Feng, J., Yu, Q., et al. (2016). Spatial and Seasonal Dynamics of Ship Emissions over the Yangtze River Delta and East China Sea and Their Potential Environmental Influence. *Environmental science & technology, 50*(3), 1322-1329. 10.1021/acs.est.5b03965

Fang, X., Shao, M., Stohl, A., Zhang, Q., Zheng, J., Guo, H., et al. (2016). Top-down estimates of benzene and toluene emissions in the Pearl River Delta and Hong Kong, China. *Atmospheric Chemistry and Physics, 16*(5), 3369-3382. https://doi.org/10.5194/acp-16-3369-2016

Feister, U., & Warmbt, W. (1987). Long-term measurements of surface ozone in the German Democratic Republic. *Journal of Atmospheric Chemistry, 5*(1), 1-21. 10.1007/BF00192500

Ferrarese, C., Franzetti, J., Selleri, T., & Suarez-Bertoa, R. (2024). VOC emissions from Euro 6 vehicles. *Environmental Sciences Europe, 36*(1), 27. 10.1186/s12302-024-00854-4

Fishman, G. (2013). *Monte Carlo: Concepts, algorithms, and applications* (illustrated ed.). New York: Springer Science & Business Media.

Fishman, J., & Crutzen, P. J. (1978). The origin of ozone in the troposphere. *Nature, 274*(5674), 855-858.

Fleming, Z. L., Doherty, R. M., von Schneidemesser, E., Malley, C. S., Cooper, O. R., Pinto, J. P., et al. (2018). Tropospheric Ozone Assessment Report: Present-day ozone distribution and trends relevant to human health. *Elementa: Science of the Anthropocene, 6*. 10.1525/elementa.273

Friedl, M., & Sulla-Menashe, D. (2015). *MCD12C1 MODIS/Terra+Aqua Land Cover Type Yearly L3 Global 0.05Deg CMG V006*. NASA Land Processes Distributed Active Archive Center, https://doi.org/10.5067/MODIS/MCD12C1.006. Date Accessed: 2025-08-05

Friedl, M., & Sulla-Menashe, D. (2022). *MODIS/Terra+Aqua Land Cover Type Yearly L3 Global 0.05Deg CMG V061*. NASA Land Processes Distributed Active Archive Center, https://doi.org/10.5067/MODIS/MCD12C1.061. Date Accessed: 2025-08-05

Friedrich, R., & Obermeier, A. (1999). Chapter 1 - Anthropogenic Emissions of Volatile Organic Compounds. In C. N. Hewitt (Ed.), *Reactive Hydrocarbons in the Atmosphere* (pp. 1-39). San Diego: Academic Press.

Fu, T.-M., Jacob, D. J., Palmer, P. I., Chance, K., Wang, Y. X., Barletta, B., et al. (2007). Space-based formaldehyde measurements as constraints on volatile organic compound emissions in east and south Asia and implications for ozone. *Journal of Geophysical Research: Atmospheres, 112*(D6). https://doi.org/10.1029/2006JD007853

Fu, J. S., Hsu, N. C., Gao, Y., Huang, K., Li, C., Lin, N. H., & Tsay, S. C. (2012). Evaluating the influences of biomass burning during 2006 BASE-ASIA: a regional chemical transport modeling. *Atmospheric Chemistry and Physics*, 12(9), 3837-3855. 10.5194/acp-12-3837-2012

Fuhrer, J., & Booker, F. (2003). Ecological issues related to ozone: agricultural issues. *Environment International, 29*(2), 141-154. https://doi.org/10.1016/S0160-4120(02)00157-5

Gao, M., Wang, F., Ding, Y., Wu, Z., Xu, Y., Lu, X., et al. (2023). Large-scale climate patterns offer preseasonal hints on the co-occurrence of heat wave and O_3 pollution in China. *Proceedings of the National Academy of Sciences, 120*(26), e2218274120. doi:10.1073/pnas.2218274120

Gaudel, A., Cooper, O. R., Ancellet, G., Barret, B., Boynard, A., Burrows, J. P., et al. (2018). Tropospheric Ozone Assessment Report: Present-day distribution and trends of tropospheric ozone relevant to climate and global atmospheric chemistry model evaluation. *Elementa: Science of the Anthropocene, 6*. 10.1525/elementa.291

Gaudel, A., Cooper, O. R., Chang, K.-L., Bourgeois, I., Ziemke, J. R., Strode, S. A., et al. (2020). Aircraft observations since the 1990s reveal increases of tropospheric ozone at multiple locations across the Northern Hemisphere. *Science Advances, 6*(34), eaba8272. doi:10.1126/sciadv.aba8272

Geng, G., Liu, Y., Liu, Y., Liu, S., Cheng, J., Yan, L., et al. (2024). Efficacy of China's clean air actions to tackle PM2.5 pollution between 2013 and 2020. *Nature Geoscience, 17*(10), 987-994. 10.1038/s41561-024-01540-z

Geng, G., Zhang, Q., Martin, R. V., Lin, J., Huo, H., Zheng, B., et al. (2017). Impact of spatial proxies on the representation of bottom-up emission inventories: A satellite-based analysis. *Atmospheric Chemistry and Physics, 17*(6), 4131-4145. 10.5194/acp-17-4131-2017

Ghude, S. D., Pfister, G. G., Jena, C., van der A, R. J., Emmons, L. K., & Kumar, R. (2013). Satellite constraints of nitrogen oxide (NOx) emissions from India based on OMI observations and WRF-Chem simulations. *Geophysical Research Letters, 40*(2), 423-428. https://doi.org/10.1002/grl.50065

Gkatzelis, G. I., Coggon, M. M., McDonald, B. C., Peischl, J., Gilman, J. B., Aikin, K. C., et al. (2021). Observations Confirm that Volatile Chemical Products Are a Major Source of Petrochemical Emissions in U.S. Cities. *Environmental science & technology, 55*(8), 4332-4343. 10.1021/acs.est.0c05471

Gkatzelis, G. I., Coggon, M. M., Stockwell, C. E., Hornbrook, R. S., Allen, H., Apel, E. C., et al. (2024). Parameterizations of US wildfire and prescribed fire emission ratios and emission factors based on FIREX-AQ aircraft measurements. *Atmospheric Chemistry and Physics, 24*(2), 929-956. 10.5194/acp-24-929-2024

Goldstein, A. H., & Galbally, I. E. (2007). Known and unexplored organic constituents in the Earth's atmosphere. *Environmental science & technology, 41*(5), 1514-1521. https://doi.org/10.1021/es072476p

Gu, S., Guenther, A., & Faiola, C. (2021). Effects of Anthropogenic and Biogenic Volatile Organic Compounds on Los Angeles Air Quality. *Environmental science & technology, 55*(18), 12191-12201. 10.1021/acs.est.1c01481

Gu, X., Li, B., Sun, C., Liao, H., Zhao, Y., & Yang, Y. (2022). An improved hourly-resolved NOx emission inventory for power plants based on continuous emission monitoring system (CEMS) database: A case in Jiangsu, China. *Journal of Cleaner Production, 369*, 133176. https://doi.org/10.1016/j.jclepro.2022.133176

Guan, D., Liu, Z., Geng, Y., Lindner, S., & Hubacek, K. (2012). The gigatonne gap in China's carbon dioxide inventories. *Nature Climate Change, 2*(9), 672-675. 10.1038/nclimate1560

Guenther, A., Hewitt, C. N., Erickson, D., Fall, R., Geron, C., Graedel, T., et al. (1995). A global model of natural volatile organic compound emissions. *Journal of Geophysical Research: Atmospheres, 100*(D5), 8873-8892. https://doi.org/10.1029/94JD02950

Guenther, A., Karl, T., Harley, P., Wiedinmyer, C., Palmer, P. I., & Geron, C. (2006). Estimates of global terrestrial isoprene emissions using MEGAN (Model of Emissions of Gases and Aerosols from Nature). *Atmospheric Chemistry and Physics, 6*(11), 3181-3210. 10.5194/acp-6-3181-2006

Guenther, A. B., Jiang, X., Heald, C. L., Sakulyanontvittaya, T., Duhl, T., Emmons, L. K., & Wang, X. (2012). The Model of Emissions of Gases and Aerosols from Nature version 2.1 (MEGAN2.1): an extended and updated framework for modeling biogenic emissions. *Geoscientific Model Development, 5*(6), 1471-1492. 10.5194/gmd-5-1471-2012

Guo, H., Chen, K., Wang, P., Hu, J., Ying, Q., Gao, A., & Zhang, H. (2019). Simulation of summer ozone and its sensitivity to emission changes in China. *Atmospheric Pollution Research, 10*(5), 1543-1552. https://doi.org/10.1016/j.apr.2019.05.003

Guo, H., Cheng, H. R., Ling, Z. H., Louie, P. K., & Ayoko, G. A. (2011). Which emission sources are responsible for the volatile organic compounds in the atmosphere of Pearl River Delta? *Journal of Hazardous Materials, 188*(1-3), 116-124. https://doi.org/10.1016/j.jhazmat.2011.01.081

Guo, H., Ling, Z. H., Cheng, H. R., Simpson, I. J., Lyu, X. P., Wang, X. M., et al. (2017). Tropospheric volatile organic compounds in China. *Science of The Total Environment, 574*, 1021-1043. https://doi.org/10.1016/j.scitotenv.2016.09.116

Guo, H., Ling, Z. H., Cheung, K., Jiang, F., Wang, D. W., Simpson, I. J., et al. (2013). Characterization of photochemical pollution at different elevations in mountainous areas in Hong Kong. *Atmospheric Chemistry and Physics, 13*(8), 3881-3898. 10.5194/acp-13-3881-2013

Guo, H., So, K. L., Simpson, I. J., Barletta, B., Meinardi, S., & Blake, D. R. (2007). C1–C8 volatile organic compounds in the atmosphere of Hong Kong: Overview of atmospheric processing and source apportionment. *Atmospheric Environment, 41*(7), 1456-1472. https://doi.org/10.1016/j.atmosenv.2006.10.011

Guo, H., Wang, T., Blake, D. R., Simpson, I. J., Kwok, Y. H., & Li, Y. S. (2006). Regional and local contributions to ambient non-methane volatile organic compounds at a polluted rural/coastal site in Pearl River Delta, China. *Atmospheric Environment, 40*(13), 2345-2359. https://doi.org/10.1016/j.atmosenv.2005.12.011

Guo, J., Miao, Y., Zhang, Y., Liu, H., Li, Z., Zhang, W., et al. (2016). The climatology of planetary boundary layer height in China derived from radiosonde and reanalysis data. *Atmospheric Chemistry and Physics, 16*(20), 13309-13319. https://doi.org/10.5194/acp-16-13309-2016

Guttikunda, S. K., Tang, Y., Carmichael, G. R., Kurata, G., Pan, L., Streets, D. G., et al. (2005). Impacts of Asian megacity emissions on regional air quality during spring 2001. *Journal of Geophysical Research: Atmospheres, 110*(D20). https://doi.org/10.1029/2004JD004921

Haagen-Smit, A. J. (1952). Chemistry and Physiology of Los Angeles Smog. *Industrial & Engineering Chemistry, 44*(6), 1342-1346. 10.1021/ie50510a045

Haagen-Smit, A. J., Bradley, C. E., & Fox, M. M. (1953). Ozone Formation in Photochemical Oxidation of Organic Substances. *Industrial & Engineering Chemistry, 45*(9), 2086-2089. 10.1021/ie50525a044

Hammer, M.-U., Vogel, B., & Vogel, H. (2002). Findings on H2O2/HNO3 as an indicator of ozone sensitivity in Baden-Württemberg, Berlin-Brandenburg, and the Po valley based on numerical simulations. *Journal of Geophysical Research: Atmospheres, 107*(D22), LOP 3-1-LOP 3-18. https://doi.org/10.1029/2000JD000211

Harrison, R. M., Allan, J., Carruthers, D., Heal, M. R., Lewis, A. C., Marner, B., et al. (2021). Non-exhaust vehicle emissions of particulate matter and VOC from road traffic: A review. *Atmospheric Environment, 262*, 118592. https://doi.org/10.1016/j.atmosenv.2021.118592

He, H., Liang, X. Z., Sun, C., Tao, Z., & Tong, D. Q. (2020). The long-term trend and production sensitivity change in the US ozone pollution from observations and model simulations. *Atmospheric Chemistry and Physics, 20*(5), 3191-3208. 10.5194/acp-20-3191-2020

He, Y. J., Uno, I., Wang, Z. F., Pochanart, P., Li, J., & Akimoto, H. (2008). Significant impact of the East Asia monsoon on ozone seasonal behavior in the boundary layer of Eastern China and the west Pacific region. *Atmospheric Chemistry and Physics, 8*(24), 7543-7555. 10.5194/acp-8-7543-2008

He, Z., Wang, X., Ling, Z., Zhao, J., Guo, H., Shao, M., & Wang, Z. (2019). Contributions of different anthropogenic volatile organic compound sources to ozone formation at a receptor site in the Pearl River Delta region and its policy implications. *Atmospheric Chemistry and Physics, 19*(13), 8801-8816. https://doi.org/10.5194/acp-19-8801-2019

HEI. (2020). *State of Global Air 2020. Special Report*. Health Effects Institute (HEI), https://www.stateofglobalair.org/

Helton, J. C. (1994). Treatment of uncertainty in performance assessments for complex systems. *Risk Analysis, 14*(4), 483-511. https://doi.org/10.1111/j.1539-6924.1994.tb00266.x

Henneman, L. R. F., Shen, H., Hogrefe, C., Russell, A. G., & Zigler, C. M. (2021). Four Decades of United States Mobile Source Pollutants: Spatial–Temporal Trends Assessed by Ground-Based Monitors, Air Quality Models, and Satellites. *Environmental science & technology, 55*(2), 882-892. 10.1021/acs.est.0c07128

Hersbach, H., Bell, B., Berrisford, P., Biavati, G., Horányi, A., Muñoz Sabater, J., et al. (2023). *ERA5 hourly data on single levels from 1940 to present*. C. C. C. S. C. S. C. D. S. (CDS) 10.24381/cds.adbb2d47. https://cds.climate.copernicus.eu/datasets/reanalysis-era5-single-levels?tab=overview. Date Accessed:

Heuss, J. M., Kahlbaum, D. F., & Wolff, G. T. (2003). Weekday/Weekend Ozone Differences: What Can We Learn from Them? *Journal of the Air & Waste Management Association, 53*(7), 772-788. 10.1080/10473289.2003.10466227

Higuera, P. E., Shuman, B. N., & Wolf, K. D. (2021). Rocky Mountain subalpine forests now burning more than any time in recent millennia. *Proceedings of the National Academy of Sciences, 118*(25), e2103135118. doi:10.1073/pnas.2103135118

Hofzumahaus, A., Rohrer, F., Lu, K., Bohn, B., Brauers, T., Chang, C. C., et al. (2009). Amplified trace gas removal in the troposphere. *Science, 324*(5935), 1702-1704. https://doi.org/10.1126/science.1164566

Holzworth, G. C. (1967). Mixing depths, wind speeds and air pollution potential for selected locations in the United States. *Journal of Applied Meteorology and Climatology, 6*(6), 1039-1044. https://doi.org/10.1175/1520-0450(1967)006%3C1039:MDWSAA%3E2.0.CO;2

Hong, C., Zhang, Q., He, K., Guan, D., Li, M., Liu, F., & Zheng, B. (2017). Variations of China's emission estimates: response to uncertainties in energy statistics. *Atmospheric Chemistry and Physics, 17*(2), 1227-1239. 10.5194/acp-17-1227-2017

Hong, S.-Y., Dudhia, J., & Chen, S.-H. (2004). A revised approach to ice microphysical processes for the bulk parameterization of clouds and precipitation. *Monthly Weather Review, 132*(1), 103-120. https://doi.org/10.1175/1520-0493(2004)132%3C0103:ARATIM%3E2.0.CO;2

Hong, S.-Y., Noh, Y., & Dudhia, J. (2006). A new vertical diffusion package with an explicit treatment of entrainment processes. *Monthly Weather Review, 134*(9), 2318-2341. https://doi.org/10.1175/mwr3199.1

Hsu, Y.-K., VanCuren, T., Park, S., Jakober, C., Herner, J., FitzGibbon, M., et al. (2010). Methane emissions inventory verification in southern California. *Atmospheric Environment, 44*(1), 1-7. https://doi.org/10.1016/j.atmosenv.2009.10.002

Hu, J., Chen, J., Ying, Q., & Zhang, H. (2016). One-year simulation of ozone and particulate matter in China using WRF/CMAQ modeling system. *Atmospheric Chemistry and Physics*, 16(16), 10333-10350. 10.5194/acp-16-10333-2016

Hu, X.-M., Klein, P. M., & Xue, M. (2013). Evaluation of the updated YSU planetary boundary layer scheme within WRF for wind resource and air quality assessments. *Journal of*

Geophysical Research: Atmospheres, 118(18), 10,490-410,505. https://doi.org/10.1002/jgrd.50823

Huang, J.-P., Fung, J. C. H., & Lau, A. K. H. (2006). Integrated processes analysis and systematic meteorological classification of ozone episodes in Hong Kong. *Journal of Geophysical Research: Atmospheres, 111*(D20). https://doi.org/10.1029/2005JD007012

Huang, J.-P., Fung, J. C. H., Lau, A. K. H., & Qin, Y. (2005). Numerical simulation and process analysis of typhoon-related ozone episodes in Hong Kong. *Journal of Geophysical Research: Atmospheres, 110*(D5). https://doi.org/10.1029/2004JD004914

Huang, L., Zhang, X., Emery, C., Mu, Q., Yarwood, G., Zhai, H., et al. (2025). Recommendations on benchmarks for numerical air quality model applications in China – Part 2: Ozone and uncertainty analysis. *Atmospheric Chemistry and Physics, 25*(7), 4233-4249. 10.5194/acp-25-4233-2025

Huang, Y., Lu, X., Fung, J. C. H., Wong, D. C., Li, Z., Chen, Y., & Chen, W. (2023). Investigating Southeast Asian biomass burning by the WRF-CMAQ two-way coupled model: Emission and direct aerosol radiative effects. *Atmospheric Environment, 294*, 119521. https://doi.org/10.1016/j.atmosenv.2022.119521

Huang, Z., Zhong, Z., Sha, Q., Xu, Y., Zhang, Z., Wu, L., et al. (2021). An updated model-ready emission inventory for Guangdong Province by incorporating big data and mapping onto multiple chemical mechanisms. *Science of The Total Environment, 769*, 144535. https://doi.org/10.1016/j.scitotenv.2020.144535

IMO. (2019). *IMO 2020: Consistent implementation of MARPOL Annex VI* (ISBN 978-92-801-17189). International Maritime Organization, https://wwwcdn.imo.org/localresources/en/publications/Documents/Flyers/Flyers/I666E.pdf

IPCC. (2021). *Climate Change 2021: The Physical Science Basis. Contribution of Working Group I to the Sixth Assessment Report of the Intergovernmental Panel on Climate Change (IPCC)* (Vol. In Press). Cambridge, United Kingdom and New York, NY, USA: Cambridge University Press.

Isakson, J., Persson, T. A., & Selin Lindgren, E. (2001). Identification and assessment of ship emissions and their effects in the harbour of Göteborg, Sweden. *Atmospheric Environment, 35*(21), 3659-3666. https://doi.org/10.1016/S1352-2310(00)00528-8

Jacob, D. J. (1999). *Introduction to Atmospheric Chemistry*: Princeton University Press.

Jacob, D. J., Horowitz, L. W., Munger, J. W., Heikes, B. G., Dickerson, R. R., Artz, R. S., & Keene, W. C. (1995). Seasonal transition from NOx- to hydrocarbon-limited conditions for ozone production over the eastern United States in September. *Journal of Geophysical Research: Atmospheres, 100*(D5), 9315-9324. https://doi.org/10.1029/94JD03125

Jaffe, D. A., & Wigder, N. L. (2012). Ozone production from wildfires: A critical review. *Atmospheric Environment, 51*, 1-10. https://doi.org/10.1016/j.atmosenv.2011.11.063

Jenkin, M. E., & Clemitshaw, K. C. (2000). Ozone and other secondary photochemical pollutants: chemical processes governing their formation in the planetary boundary layer. *Atmospheric Environment, 34*(16), 2499-2527. https://doi.org/10.1016/S1352-2310(99)00478-1

Jenkin, M. E., Davies, T. J., & Stedman, J. R. (2002). The origin and day-of-week dependence of photochemical ozone episodes in the UK. *Atmospheric Environment, 36*(6), 999-1012. https://doi.org/10.1016/S1352-2310(01)00360-0

Jiang, F., Guo, H., Wang, T. J., Cheng, H. R., Wang, X. M., Simpson, I. J., et al. (2010). An ozone episode in the Pearl River Delta: Field observation and model simulation. *Journal of Geophysical Research: Atmospheres, 115*(D22). https://doi.org/10.1029/2009jd013583

Jiang, Y., Song, G., Zhang, Z., Zhai, Z., & Yu, L. (2021). Estimation of Hourly Traffic Flows from Floating Car Data for Vehicle Emission Estimation. *Journal of Advanced Transportation, 2021*(1), 6628335. https://doi.org/10.1155/2021/6628335

Jiang, Y. C., Zhao, T. L., Liu, J., Xu, X. D., Tan, C. H., Cheng, X. H., et al. (2015). Why does surface ozone peak before a typhoon landing in southeast China? *Atmospheric Chemistry and Physics, 15*(23), 13331-13338. 10.5194/acp-15-13331-2015

Jiang, Z., McDonald, B. C., Worden, H., Worden, J. R., Miyazaki, K., Qu, Z., et al. (2018). Unexpected slowdown of US pollutant emission reduction in the past decade. *Proceedings of the National Academy of Sciences, 115*(20), 5099-5104. doi:10.1073/pnas.1801191115

Jiang, Z., Zhu, R., Miyazaki, K., McDonald, B. C., Klimont, Z., Zheng, B., et al. (2022). Decadal Variabilities in Tropospheric Nitrogen Oxides Over United States, Europe, and China. *Journal of Geophysical Research: Atmospheres, 127*(3), e2021JD035872. https://doi.org/10.1029/2021JD035872

Jiménez, P. A., Dudhia, J., González-Rouco, J. F., Navarro, J., Montávez, J. P., & García-Bustamante, E. (2012). A revised scheme for the WRF surface layer formulation. *Monthly Weather Review, 140*(3), 898-918. https://doi.org/10.1175/mwr-d-11-00056.1

Jiménez, P. A., González-Rouco, J. F., García-Bustamante, E., Navarro, J., Montávez, J. P., de Arellano, J. V.-G., et al. (2010). Surface Wind Regionalization over Complex Terrain: Evaluation and Analysis of a High-Resolution WRF Simulation. *Journal of Applied Meteorology and Climatology, 49*(2), 268-287. 10.1175/2009jamc2175.1

Jin, X., Fiore, A., Boersma, K. F., Smedt, I. D., & Valin, L. (2020). Inferring Changes in Summertime Surface Ozone–NOx–VOC Chemistry over U.S. Urban Areas from Two Decades of Satellite and Ground-Based Observations. *Environmental science & technology, 54*(11), 6518-6529. 10.1021/acs.est.9b07785

Jin, X., Fiore, A. M., & Cohen, R. C. (2023). Space-Based Observations of Ozone Precursors within California Wildfire Plumes and the Impacts on Ozone-NOx-VOC Chemistry. *Environmental science & technology, 57*(39), 14648-14660. 10.1021/acs.est.3c04411

Jin, X., Fiore, A. M., Murray, L. T., Valin, L. C., Lamsal, L. N., Duncan, B., et al. (2017). Evaluating a Space-Based Indicator of Surface Ozone-NOx-VOC Sensitivity Over Midlatitude Source Regions and Application to Decadal Trends. *Journal of Geophysical Research: Atmospheres, 122*(19), 10,439-410,461. https://doi.org/10.1002/2017JD026720

Jin, X., & Holloway, T. (2015). Spatial and temporal variability of ozone sensitivity over China observed from the Ozone Monitoring Instrument. *Journal of Geophysical Research: Atmospheres, 120*(14), 7229-7246. https://doi.org/10.1002/2015JD023250

Johnson, M. S., Philip, S., Meech, S., Kumar, R., Sorek-Hamer, M., Shiga, Y. P., & Jung, J. (2024). Insights into the long-term (2005–2021) spatiotemporal evolution of summer ozone production sensitivity in the Northern Hemisphere derived with the Ozone Monitoring Instrument (OMI). *Atmospheric Chemistry and Physics, 24*(18), 10363-10384. 10.5194/acp-24-10363-2024

Kain, J. S. (2004). The Kain–Fritsch convective parameterization: An update. *Journal of Applied Meteorology, 43*(1), 170-181. https://doi.org/10.1175/1520-0450(2004)043%3C0170:TKCPAU%3E2.0.CO;2

Karl, T., Guenther, A., Yokelson, R. J., Greenberg, J., Potosnak, M., Blake, D. R., & Artaxo, P. (2007). The tropical forest and fire emissions experiment: Emission, chemistry, and transport of biogenic volatile organic compounds in the lower atmosphere over Amazonia. *Journal of Geophysical Research: Atmospheres, 112*(D18). https://doi.org/10.1029/2007JD008539

Karl, T., Harley, P., Emmons, L., Thornton, B., Guenther, A., Basu, C., et al. (2010). Efficient atmospheric cleansing of oxidized organic trace gases by vegetation. *Science, 330*(6005), 816-819. https://doi.org/10.1126/science.1192534

Karnosky, D. F., Skelly, J. M., Percy, K. E., & Chappelka, A. H. (2007). Perspectives regarding 50years of research on effects of tropospheric ozone air pollution on US forests. *Environmental Pollution, 147*(3), 489-506. https://doi.org/10.1016/j.envpol.2006.08.043

Khare, P., Machesky, J., Soto, R., He, M., Presto, A. A., & Gentner, D. R. (2020). Asphalt-related emissions are a major missing nontraditional source of secondary organic aerosol precursors. *Science Advances, 6*(36), eabb9785. doi:10.1126/sciadv.abb9785

Kim, S. W., McKeen, S. A., Frost, G. J., Lee, S. H., Trainer, M., Richter, A., et al. (2011). Evaluations of NOx and highly reactive VOC emission inventories in Texas and their implications for ozone plume simulations during the Texas Air Quality Study 2006. *Atmospheric Chemistry and Physics, 11*(22), 11361-11386. 10.5194/acp-11-11361-2011

Kleinman, L., Lee, Y.-N., Springston, S. R., Nunnermacker, L., Zhou, X., Brown, R., et al. (1994). Ozone formation at a rural site in the southeastern United States. *Journal of Geophysical Research: Atmospheres, 99*(D2), 3469-3482. https://doi.org/10.1029/93JD02991

Kleinman, L. I., Daum, P. H., Lee, Y.-N., Nunnermacker, L. J., Springston, S. R., Weinstein-Lloyd, J., & Rudolph, J. (2005). A comparative study of ozone production in five U.S. metropolitan areas. *Journal of Geophysical Research: Atmospheres, 110*(D2). https://doi.org/10.1029/2004JD005096

Kok, G. L., Lind, J. A., & Fang, M. (1997). An airborne study of air quality around the Hong Kong Territory. *Journal of Geophysical Research: Atmospheres, 102*(D15), 19043-19057. https://doi.org/10.1029/97JD01306

Kong, H., Zhang, Q., Du, Y., & Zhang, F. (2020). Characteristics of Coastal Low-Level Jets Over Beibu Gulf, China, During the Early Warm Season. *Journal of Geophysical Research: Atmospheres, 125*(14), e2019JD031918. https://doi.org/10.1029/2019JD031918

Koplitz, S., Simon, H., Henderson, B., Liljegren, J., Tonnesen, G., Whitehill, A., & Wells, B. (2022). Changes in Ozone Chemical Sensitivity in the United States from 2007 to 2016. *ACS Environmental Au, 2*(3), 206-222. 10.1021/acsenvironau.1c00029

Kumar, R., Naja, M., Pfister, G. G., Barth, M. C., Wiedinmyer, C., & Brasseur, G. P. (2012). Simulations over South Asia using the Weather Research and Forecasting model with Chemistry (WRF-Chem): chemistry evaluation and initial results. *Geoscientific Model Development, 5*(3), 619-648. https://doi.org/10.5194/gmd-5-619-2012

Kumar, S., Mondal, A. N., Gaikwad, S. A., Devotta, S., & Singh, R. N. (2004). Qualitative assessment of methane emission inventory from municipal solid waste disposal sites: a case study. *Atmospheric Environment, 38*(29), 4921-4929. https://doi.org/10.1016/j.atmosenv.2004.05.052

Kurokawa, J., Ohara, T., Morikawa, T., Hanayama, S., Janssens-Maenhout, G., Fukui, T., et al. (2013). Emissions of air pollutants and greenhouse gases over Asian regions during 2000–2008: Regional Emission inventory in ASia (REAS) version 2. *Atmospheric Chemistry and Physics, 13*(21), 11019-11058. 10.5194/acp-13-11019-2013

Kwok, R. H. F., Baker, K. R., Napelenok, S. L., & Tonnesen, G. S. (2015). Photochemical grid model implementation and application of VOC, NOx, and O3 source apportionment. *Geoscientific Model Development, 8*(1), 99-114. 10.5194/gmd-8-99-2015

Lan, R., Eastham, S. D., Liu, T., Norford, L. K., & Barrett, S. R. H. (2022). Air quality impacts of crop residue burning in India and mitigation alternatives. *Nature Communications, 13*(1), 6537. 10.1038/s41467-022-34093-z

Lang, J., Cheng, S., Zhou, Y., Zhang, Y., & Wang, G. (2014). Air pollutant emissions from on-road vehicles in China, 1999–2011. *Science of The Total Environment, 496*, 1-10. https://doi.org/10.1016/j.scitotenv.2014.07.021

Lary, D. J., & Shallcross, D. E. (2000). Central role of carbonyl compounds in atmospheric chemistry. *Journal of Geophysical Research: Atmospheres*, 105(D15), 19771-19778. https://doi.org/10.1029/1999JD901184

Laughner, J. L., Neu, J. L., Schimel, D., Wennberg, P. O., Barsanti, K., Bowman, K. W., et al. (2021). Societal shifts due to COVID-19 reveal large-scale complexities and feedbacks between atmospheric chemistry and climate change. *Proceedings of the National Academy of Sciences, 118*(46), e2109481118. doi:10.1073/pnas.2109481118

Lefohn, A. S., Malley, C. S., Smith, L., Wells, B., Hazucha, M., Simon, H., et al. (2018). Tropospheric ozone assessment report: Global ozone metrics for climate change, human health, and crop/ecosystem research. *Elementa: Science of the Anthropocene, 6*. 10.1525/elementa.279

Lefohn, A. S., Shadwick, D., & Oltmans, S. J. (2008). Characterizing long-term changes in surface ozone levels in the United States (1980–2005). *Atmospheric Environment, 42*(35), 8252-8262.

Lefohn, A. S., Shadwick, D., & Oltmans, S. J. (2010). Characterizing changes in surface ozone levels in metropolitan and rural areas in the United States for 1980–2008 and 1994–2008. *Atmospheric Environment, 44*(39), 5199-5210. https://doi.org/10.1016/j.atmosenv.2010.08.049

Lei, Y., Yue, X., Liao, H., Zhang, L., Zhou, H., Tian, C., et al. (2022). Global Perspective of Drought Impacts on Ozone Pollution Episodes. *Environmental science & technology, 56*(7), 3932-3940. 10.1021/acs.est.1c07260

Leue, C., Wenig, M., Wagner, T., Klimm, O., Platt, U., & Jähne, B. (2001). Quantitative analysis of NO x emissions from Global Ozone Monitoring Experiment satellite image sequences.

Journal of Geophysical Research: Atmospheres, 106(D6), 5493-5505. https://doi.org/10.1029/2000JD900572

Lewis, A. C., Hopkins, J. R., Carslaw, D. C., Hamilton, J. F., Nelson, B. S., Stewart, G., et al. (2020). An increasing role for solvent emissions and implications for future measurements of volatile organic compounds. *Philosophical Transactions of the Royal Society A: Mathematical, Physical and Engineering Sciences, 378*(2183), 20190328. doi:10.1098/rsta.2019.0328

Li, B., Ho, S. S. H., Li, X., Guo, L., Chen, A., Hu, L., et al. (2021a). A comprehensive review on anthropogenic volatile organic compounds (VOCs) emission estimates in China: Comparison and outlook. *Environment International, 156*, 106710. https://doi.org/10.1016/j.envint.2021.106710

Li, G., Bei, N., Cao, J., Wu, J., Long, X., Feng, T., et al. (2017a). Widespread and persistent ozone pollution in eastern China during the non-winter season of 2015: observations and source attributions. *Atmospheric Chemistry and Physics*, *17*(4), 2759-2774. 10.5194/acp-17-2759-2017

Li, H., Zheng, B., Lei, Y., Hauglustaine, D., Chen, C., Lin, X., et al. (2024). Trends and drivers of anthropogenic NOx emissions in China since 2020. *Environmental Science and Ecotechnology, 21*, 100425. https://doi.org/10.1016/j.ese.2024.100425

Li, K., Jacob, D. J., Liao, H., Shen, L., Zhang, Q., & Bates, K. H. (2019a). Anthropogenic drivers of 2013–2017 trends in summer surface ozone in China. *Proceedings of the National Academy of Sciences, 116*(2), 422-427. doi:10.1073/pnas.1812168116

Li, K., Jacob, D. J., Shen, L., Lu, X., De Smedt, I., & Liao, H. (2020). Increases in surface ozone pollution in China from 2013 to 2019: anthropogenic and meteorological influences. *Atmospheric Chemistry and Physics, 20*(19), 11423-11433. 10.5194/acp-20-11423-2020

Li, K., Li, J., Tong, S., Wang, W., Huang, R. J., & Ge, M. (2019b). Characteristics of wintertime VOCs in suburban and urban Beijing: concentrations, emission ratios, and festival effects. *Atmospheric Chemistry and Physics, 19*(12), 8021-8036. https://doi.org/10.5194/acp-19-8021-2019

Li, M., Liu, H., Geng, G., Hong, C., Liu, F., Song, Y., et al. (2017b). Anthropogenic emission inventories in China: a review. *National Science Review*, *4*(6), 834-866. 10.1093/nsr/nwx150

Li, M., Song, Y., Mao, Z., Liu, M., & Huang, X. (2016). Impacts of thermal circulations induced by urbanization on ozone formation in the Pearl River Delta region, China. *Atmospheric Environment*, *127*, 382-392. https://doi.org/10.1016/j.atmosenv.2015.10.075

Li, M., Zeng, W., Yang, Z., Luo, Y., Zhu, Q., Wang, L., et al. (2023). Multiple sources emission inventory closely integrated with atmospheric environment management: A case study of Guangdong, China. *Atmospheric Pollution Research, 14*(8), 101825. https://doi.org/10.1016/j.apr.2023.101825

Li, M., Zhang, Q., Kurokawa, J.-i., Woo, J.-H., He, K., Lu, Z., et al. (2017c). MIX: a mosaic Asian anthropogenic emission inventory under the international collaboration framework of the MICS-Asia and HTAP. *Atmospheric Chemistry and Physics, 17*(2), 935-963. https://doi.org/10.5194/acp-17-935-2017

Li, M., Zhang, Q., Streets, D. G., He, K. B., Cheng, Y. F., Emmons, L. K., et al. (2014). Mapping Asian anthropogenic emissions of non-methane volatile organic compounds to multiple chemical mechanisms. *Atmospheric Chemistry and Physics, 14*(11), 5617-5638. https://doi.org/10.5194/acp-14-5617-2014

Li, M., Zhang, Q., Zheng, B., Tong, D., Lei, Y., Liu, F., et al. (2019c). Persistent growth of anthropogenic non-methane volatile organic compound (NMVOC) emissions in China during 1990–2017: drivers, speciation and ozone formation potential. *Atmospheric Chemistry and Physics, 19*(13), 8897-8913. 10.5194/acp-19-8897-2019

Li, R., Xu, M., Li, M., Chen, Z., Zhao, N., Gao, B., & Yao, Q. (2021b). Identifying the spatiotemporal variations in ozone formation regimes across China from 2005 to 2019 based on polynomial simulation and causality analysis. *Atmospheric Chemistry and Physics, 21*(20), 15631-15646. 10.5194/acp-21-15631-2021

Li, S., Liu, W., Xie, P., Qin, M., & Yang, Y. (2012). Observation of nitrate radical in the nocturnal boundary layer during a summer field campaign in Pearl River Delta, China. *Terrestrial, Atmospheric and Oceanic Sciences, 23*(1), 39-48. https://doi.org/10.3319/TAO.2011.07.26.01(A)

Liang, X., Sun, X., Xu, J., & Ye, D. (2020). Improved emissions inventory and VOCs speciation for industrial OFP estimation in China. *Science of The Total Environment, 745*, 140838. https://doi.org/10.1016/j.scitotenv.2020.140838

Liao, Z., Ling, Z., Gao, M., Sun, J., Zhao, W., Ma, P., et al. (2021). Tropospheric Ozone Variability Over Hong Kong Based on Recent 20 years (2000–2019) Ozonesonde Observation. *Journal of Geophysical Research: Atmospheres*, 126(3), e2020JD033054. https://doi.org/10.1029/2020JD033054

Lin, M., Fiore, A. M., Horowitz, L. W., Langford, A. O., Oltmans, S. J., Tarasick, D., & Rieder, H. E. (2015). Climate variability modulates western US ozone air quality in spring via deep stratospheric intrusions. *Nature Communications, 6*(1), 7105. 10.1038/ncomms8105

Lin, M., Horowitz, L. W., Oltmans, S. J., Fiore, A. M., & Fan, S. (2014). Tropospheric ozone trends at Mauna Loa Observatory tied to decadal climate variability. *Nature Geoscience, 7*(2), 136-143. 10.1038/ngeo2066

Lin, M., Horowitz, L. W., Payton, R., Fiore, A. M., & Tonnesen, G. (2017). US surface ozone trends and extremes from 1980 to 2014: quantifying the roles of rising Asian emissions, domestic controls, wildfires, and climate. *Atmospheric Chemistry and Physics, 17*(4), 2943-2970. 10.5194/acp-17-2943-2017

Lin, M., Horowitz, L. W., Xie, Y., Paulot, F., Malyshev, S., Shevliakova, E., et al. (2020). Vegetation feedbacks during drought exacerbate ozone air pollution extremes in Europe. *Nature Climate Change, 10*(5), 444-451. 10.1038/s41558-020-0743-y

Ling, Z. H., Guo, H., Zheng, J. Y., Louie, P. K. K., Cheng, H. R., Jiang, F., et al. (2013). Establishing a conceptual model for photochemical ozone pollution in subtropical Hong Kong. *Atmospheric Environment, 76*, 208-220. https://doi.org/10.1016/j.atmosenv.2012.09.051

Lippmann, M. (1989). HEALTH EFFECTS OF OZONE A Critical Review. *Journal of the Air & Waste Management Association, 39*(5), 672-695. 10.1080/08940630.1989.10466554

Lippmann, M. (1991). Health effects of tropospheric ozone. *Environmental science & technology, 25*(12), 1954-1962. 10.1021/es00024a001

Liu, F., Beirle, S., Zhang, Q., van der A, R. J., Zheng, B., Tong, D., & He, K. (2017a). NOx emission trends over Chinese cities estimated from OMI observations during 2005 to 2015. *Atmospheric Chemistry and Physics, 17*(15), 9261-9275. 10.5194/acp-17-9261-2017

Liu, F., Zhang, Q., Tong, D., Zheng, B., Li, M., Huo, H., & He, K. B. (2015). High-resolution inventory of technologies, activities, and emissions of coal-fired power plants in China from 1990 to 2010. *Atmospheric Chemistry and Physics, 15*(23), 13299-13317. 10.5194/acp-15-13299-2015

Liu, F., Zhang, Q., van der A, R. J., Zheng, B., Tong, D., Yan, L., et al. (2016a). Recent reduction in NOx emissions over China: synthesis of satellite observations and emission inventories. *Environmental Research Letters, 11*(11), 114002. 10.1088/1748-9326/11/11/114002

Liu, H., Fu, M., Jin, X., Shang, Y., Shindell, D., Faluvegi, G., et al. (2016b). Health and climate impacts of ocean-going vessels in East Asia. *Nature Climate Change, 6*(11), 1037-1041. 10.1038/nclimate3083

Liu, H., He, K., & Barth, M. (2011). Traffic and emission simulation in China based on statistical methodology. *Atmospheric Environment, 45*(5), 1154-1161. https://doi.org/10.1016/j.atmosenv.2010.10.051

Liu, H., Man, H., Cui, H., Wang, Y., Deng, F., Wang, Y., et al. (2017b). An updated emission inventory of vehicular VOCs and IVOCs in China. *Atmospheric Chemistry and Physics, 17*(20), 12709-12724. 10.5194/acp-17-12709-2017

Liu, S., Trainer, M., Fehsenfeld, F., Parrish, D., Williams, E., Fahey, D. W., et al. (1987a). Ozone production in the rural troposphere and the implications for regional and global ozone distributions. *Journal of Geophysical Research: Atmospheres, 92*(D4), 4191-4207.

Liu, S. C., Trainer, M., Fehsenfeld, F. C., Parrish, D. D., Williams, E. J., Fahey, D. W., et al. (1987b). Ozone production in the rural troposphere and the implications for regional and global ozone distributions. *Journal of Geophysical Research: Atmospheres, 92*(D4), 4191-4207. https://doi.org/10.1029/JD092iD04p04191

Liu, X.-H., Zhang, Y., Xing, J., Zhang, Q., Wang, K., Streets, D. G., et al. (2010). Understanding of regional air pollution over China using CMAQ, part II. Process analysis and sensitivity of ozone and particulate matter to precursor emissions. *Atmospheric Environment, 44*(30), 3719-3727. https://doi.org/10.1016/j.atmosenv.2010.03.036

Liu, X., Lyu, X., Wang, Y., Jiang, F., & Guo, H. (2019). Intercomparison of O3 formation and radical chemistry in the past decade at a suburban site in Hong Kong. *Atmospheric Chemistry and Physics, 19*(7), 5127-5145. 10.5194/acp-19-5127-2019

Liu, X., Wang, N., Lyu, X., Zeren, Y., Jiang, F., Wang, X., et al. (2021). Photochemistry of ozone pollution in autumn in Pearl River Estuary, South China. *Science of The Total Environment, 754*, 141812. https://doi.org/10.1016/j.scitotenv.2020.141812

Liu, Y.-H., Ma, J.-L., Li, L., Lin, X.-F., Xu, W.-J., & Ding, H. (2018). A high temporal-spatial vehicle emission inventory based on detailed hourly traffic data in a medium-sized city of China. *Environmental Pollution, 236*, 324-333. https://doi.org/10.1016/j.envpol.2018.01.068

Liu, Y., Geng, G., Cheng, J., Liu, Y., Xiao, Q., Liu, L., et al. (2023). Drivers of Increasing Ozone during the Two Phases of Clean Air Actions in China 2013–2020. *Environmental science & technology, 57*(24), 8954-8964. 10.1021/acs.est.3c00054

Liu, Y., Han, F., Liu, W., Cui, X., Luan, X., & Cui, Z. (2020). Process-based volatile organic compound emission inventory establishment method for the petroleum refining industry. *Journal of Cleaner Production, 263*, 121609. https://doi.org/10.1016/j.jclepro.2020.121609

Liu, Y., Shao, M., Lu, S., Chang, C.-C., Wang, J.-L., & Fu, L. (2008). Source apportionment of ambient volatile organic compounds in the Pearl River Delta, China: Part II. *Atmospheric Environment, 42*(25), 6261-6274. https://doi.org/10.1016/j.atmosenv.2008.02.027

Liu, Y., & Wang, T. (2020a). Worsening urban ozone pollution in China from 2013 to 2017 – Part 1: The complex and varying roles of meteorology. *Atmospheric Chemistry and Physics, 20*(11), 6305-6321. https://doi.org/10.5194/acp-20-6305-2020

Liu, Y., & Wang, T. (2020b). Worsening urban ozone pollution in China from 2013 to 2017 – Part 2: The effects of emission changes and implications for multi-pollutant control. *Atmospheric Chemistry and Physics, 20*(11), 6323-6337. 10.5194/acp-20-6323-2020

Liu, Z., Wang, Y., Vrekoussis, M., Richter, A., Wittrock, F., Burrows, J. P., et al. (2012). Exploring the missing source of glyoxal (CHOCHO) over China. *Geophysical Research Letters, 39*(10). https://doi.org/10.1029/2012GL051645

Logan, J., Staehelin, J., Megretskaia, I., Cammas, J. P., Thouret, V., Claude, H., et al. (2012). Changes in ozone over Europe: Analysis of ozone measurements from sondes, regular aircraft (MOZAIC) and alpine surface sites. *Journal of Geophysical Research: Atmospheres, 117*(D9).

Logan, J. A. (1985). Tropospheric ozone: Seasonal behavior, trends, and anthropogenic influence. *Journal of Geophysical Research: Atmospheres, 90*(D6), 10463-10482. https://doi.org/10.1029/JD090iD06p10463

Louie, P. K. K., Ho, J. W. K., Tsang, R. C. W., Blake, D. R., Lau, A. K. H., Yu, J. Z., et al. (2013). VOCs and OVOCs distribution and control policy implications in Pearl River Delta region, China. *Atmospheric Environment, 76*, 125-135. https://doi.org/10.1016/j.atmosenv.2012.08.058

Low, P. S., Davies, T. D., Kelly, P. M., & Farmer, G. (1990). Trends in surface ozone at Hohenpeissenberg and Arkona. *Journal of Geophysical Research: Atmospheres, 95*(D13), 22441-22453. https://doi.org/10.1029/JD095iD13p22441

Lu, H., Lyu, X., Cheng, H., Ling, Z., & Guo, H. (2019a). Overview on the spatial–temporal characteristics of the ozone formation regime in China. *Environmental Science: Processes & Impacts, 21*(6), 916-929. https://doi.org/10.1039/C9EM00098D

Lu, K., Guo, S., Tan, Z., Wang, H., Shang, D., Liu, Y., et al. (2018a). Exploring atmospheric free-radical chemistry in China: the self-cleansing capacity and the formation of secondary air pollution. *National Science Review, 6*(3), 579-594. https://doi.org/10.1093/nsr/nwy073

Lu, K. D., Rohrer, F., Holland, F., Fuchs, H., Bohn, B., Brauers, T., et al. (2012). Observation and modelling of OH and HO2 concentrations in the Pearl River Delta 2006: a missing OH source in a VOC rich atmosphere. *Atmospheric Chemistry and Physics, 12*(3), 1541-1569. https://doi.org/10.5194/acp-12-1541-2012

Lu, Q., Zheng, J., Ye, S., Shen, X., Yuan, Z., & Yin, S. (2013). Emission trends and source characteristics of SO2, NOx, PM10 and VOCs in the Pearl River Delta region from 2000 to 2009. *Atmospheric Environment, 76*, 11-20. https://doi.org/10.1016/j.atmosenv.2012.10.062

Lu, X., Hong, J., Zhang, L., Cooper, O. R., Schultz, M. G., Xu, X., et al. (2018b). Severe Surface Ozone Pollution in China: A Global Perspective. *Environmental Science & Technology Letters, 5*(8), 487-494. 10.1021/acs.estlett.8b00366

Lu, X., Liu, Y., Su, J., Weng, X., Ansari, T., Zhang, Y., et al. (2025). Tropospheric ozone trends and attributions over East and Southeast Asia in 1995–2019: an integrated assessment using statistical methods, machine learning models, and multiple chemical transport models. *Atmospheric Chemistry and Physics, 25*(14), 7991-8028. 10.5194/acp-25-7991-2025

Lu, X., Ye, X., Zhou, M., Zhao, Y., Weng, H., Kong, H., et al. (2021). The underappreciated role of agricultural soil nitrogen oxide emissions in ozone pollution regulation in North China. *Nature Communications, 12*(1), 5021. 10.1038/s41467-021-25147-9

Lu, X., Zhang, L., Wang, X., Gao, M., Li, K., Zhang, Y., et al. (2020). Rapid Increases in Warm-Season Surface Ozone and Resulting Health Impact in China Since 2013. *Environmental Science & Technology Letters, 7*(4), 240-247. 10.1021/acs.estlett.0c00171

Lu, X., Zhang, L., Zhao, Y., Jacob, D. J., Hu, Y., Hu, L., et al. (2019b). Surface and tropospheric ozone trends in the Southern Hemisphere since 1990: possible linkages to poleward expansion of the Hadley circulation. *Science Bulletin, 64*(6), 400-409. https://doi.org/10.1016/j.scib.2018.12.021

Luo, C., St. John, J. C., Xiuji, Z., Lam, K. S., Wang, T., & Chameides, W. L. (2000). A nonurban ozone air pollution episode over eastern China: Observations and model simulations. *Journal of Geophysical Research: Atmospheres, 105*(D2), 1889-1908. https://doi.org/10.1029/1999JD900970

Luo, Z., Lv, Z., Zhao, J., Sun, H., He, T., Yi, W., et al. (2024). Shipping-related pollution decreased but mortality increased in Chinese port cities. *Nature Cities, 1*(4), 295-304. 10.1038/s44284-024-00050-8

Lyu, X., Li, K., Guo, H., Morawska, L., Zhou, B., Zeren, Y., et al. (2023). A synergistic ozone-climate control to address emerging ozone pollution challenges. *One Earth, 6*(8), 964-977. https://doi.org/10.1016/j.oneear.2023.07.004

Ma, Z., Xu, J., Quan, W., Zhang, Z., Lin, W., & Xu, X. (2016). Significant increase of surface ozone at a rural site, north of eastern China. *Atmospheric Chemistry and Physics, 16*(6), 3969-3977. 10.5194/acp-16-3969-2016

Maison, A., Lugon, L., Park, S. J., Baudic, A., Cantrell, C., Couvidat, F., et al. (2024). Significant impact of urban tree biogenic emissions on air quality estimated by a bottom-up inventory and chemistry transport modeling. *Atmospheric Chemistry and Physics, 24*(10), 6011-6046. 10.5194/acp-24-6011-2024

Mar, K. A., Ojha, N., Pozzer, A., & Butler, T. M. (2016). Ozone air quality simulations with WRF-Chem (v3.5.1) over Europe: model evaluation and chemical mechanism comparison. *Geoscientific Model Development, 9*(10), 3699-3728. 10.5194/gmd-9-3699-2016

Marr, L. C., Noblet, G. S., & Harley, R. A. (2002). Formation of photochemical air pollution in central California 2. Impact of revised emissions on Eulerian model predictions. *Journal of Geophysical Research: Atmospheres, 107*(D6), ACH 6-1-ACH 6-11. https://doi.org/10.1029/2001JD000690

Martin, R. V., Fiore, A. M., & Van Donkelaar, A. (2004). Space-based diagnosis of surface ozone sensitivity to anthropogenic emissions. *Geophysical Research Letters, 31*(6). https://doi.org/10.1029/2004GL019416

Martinez, J., Maxwell, C., Javitz, H., & Bawol, R. (1983). *Evaluation of The Empirical Kinetic Modeling Approach (EKMA)*. U.S. Environmental Protection Agency, https://nepis.epa.gov/Exe/ZyPURL.cgi?Dockey=940054V3.txt.

Marvin, M. R., Palmer, P. I., Yao, F., Latif, M. T., & Khan, M. F. (2024). Uncertainties from biomass burning aerosols in air quality models obscure public health impacts in Southeast Asia. *Atmospheric Chemistry and Physics, 24*(6), 3699-3715. 10.5194/acp-24-3699-2024

Matsui, H., Koike, M., Kondo, Y., Takegawa, N., Kita, K., Miyazaki, Y., et al. (2009). Spatial and temporal variations of aerosols around Beijing in summer 2006: Model evaluation and source apportionment. *Journal of Geophysical Research: Atmospheres, 114*(D2). https://doi.org/10.1029/2008JD010906

McClure, C. D., & Jaffe, D. A. (2018). Investigation of high ozone events due to wildfire smoke in an urban area. *Atmospheric Environment, 194*, 146-157. https://doi.org/10.1016/j.atmosenv.2018.09.021

McDonald, B. C., de Gouw, J. A., Gilman, J. B., Jathar, S. H., Akherati, A., Cappa, C. D., et al. (2018). Volatile chemical products emerging as largest petrochemical source of urban organic emissions. *Science, 359*(6377), 760-764. doi:10.1126/science.aaq0524

MEE. (2024). *Technical Guidelines for the Compilation of Atmospheric Volatile Organic Compounds Emission Inventory* (000014672/2024-00045). Ministry of Ecology and Environment of the People's Republic of China, https://www.mee.gov.cn/xxgk2018/xxgk/xxgk06/202401/W020240130539574113045.pdf

Meng, Y., Song, J., Zeng, L., Zhang, Y., Zhao, Y., Liu, X., et al. (2022). Ambient volatile organic compounds at a receptor site in the Pearl River Delta region: Variations, source apportionment and effects on ozone formation. *Journal of Environmental Sciences, 111*, 104-117. https://doi.org/10.1016/j.jes.2021.02.024

Mills, G., Pleijel, H., Malley, C. S., Sinha, B., Cooper, O. R., Schultz, M. G., et al. (2018). Tropospheric Ozone Assessment Report: Present-day tropospheric ozone distribution and trends relevant to vegetation. *Elementa: Science of the Anthropocene, 6*. 10.1525/elementa.302

Mlawer, E. J., Taubman, S. J., Brown, P. D., Iacono, M. J., & Clough, S. A. (1997). Radiative transfer for inhomogeneous atmospheres: RRTM, a validated correlated-k model for the longwave. *Journal of Geophysical Research: Atmospheres, 102*(D14), 16663-16682. https://doi.org/10.1029/97JD00237

Mo, Z., Cui, R., Yuan, B., Cai, H., McDonald, B. C., Li, M., et al. (2021). A mass-balance-based emission inventory of non-methane volatile organic compounds (NMVOCs) for solvent use in China. *Atmospheric Chemistry and Physics, 21*(17), 13655-13666. 10.5194/acp-21-13655-2021

Mo, Z., Huang, S., Yuan, B., Pei, C., Song, Q., Qi, J., et al. (2020). Deriving emission fluxes of volatile organic compounds from tower observation in the Pearl River Delta, China. *Science of The Total Environment, 741*, 139763. https://doi.org/10.1016/j.scitotenv.2020.139763

Mo, Z., Shao, M., & Lu, S. (2016). Compilation of a source profile database for hydrocarbon and OVOC emissions in China. *Atmospheric Environment, 143*, 209-217. https://doi.org/10.1016/j.atmosenv.2016.08.025

Monks, P. S., Archibald, A. T., Colette, A., Cooper, O., Coyle, M., Derwent, R., et al. (2015). Tropospheric ozone and its precursors from the urban to the global scale from air quality to short-lived climate forcer. *Atmospheric Chemistry and Physics, 15*(15), 8889-8973. 10.5194/acp-15-8889-2015

Murray, C. J. L., Aravkin, A. Y., Zheng, P., Abbafati, C., Abbas, K. M., Abbasi-Kangevari, M., et al. (2020). Global burden of 87 risk factors in 204 countries and territories, 1990–2019: a systematic analysis for the Global Burden of Disease Study 2019. *The Lancet, 396*(10258), 1223-1249. 10.1016/S0140-6736(20)30752-2

Myhre, G., Shindell, D., Bréon, F.-M., Collins, W., Fuglestvedt, J., Huang, J., et al. (2013). Anthropogenic and Natural Radiative Forcing, in: Climate Change 2013: The Physical Science Basis. Contribution of Working Group I to the Fifth Assessment Report of the Intergovernmental Panel on Climate Change. In T. F. Stocker, D. Qin, G.-K. Plattner, M. Tignor, S. K. Allen, J. Boschung, A. Nauels, Y. Xia, V. Bex and P. M. Midgley (Eds.), (pp. 659–740). Cambridge, United Kingdom and New York, NY, USA: Cambridge University Press.

Nault, B. A., Laughner, J. L., Wooldridge, P. J., Crounse, J. D., Dibb, J., Diskin, G., et al. (2017). Lightning NOx Emissions: Reconciling Measured and Modeled Estimates With Updated NOx Chemistry. *Geophysical Research Letters, 44*(18), 9479-9488. https://doi.org/10.1002/2017GL074436

NCEP. (2000). NCEP FNL Operational Model Global Tropospheric Analyses, continuing from July 1999 (Updated daily). In. Boulder, CO: Research Data Archive at the National Center for Atmospheric Research, Computational and Information Systems Laboratory.

Nguyen, T. B., Crounse, J. D., Teng, A. P., St. Clair, J. M., Paulot, F., Wolfe, G. M., & Wennberg, P. O. (2015). Rapid deposition of oxidized biogenic compounds to a temperate forest. *Proceedings of the National Academy of Sciences, 112*(5), E392-E401. https://doi.org/10.1073/pnas.1418702112

NIFC. (2024). *Wildland Fire Summary and Statistics Annual Report 2024*. U.S. National Interagency Coordination Center, https://www.nifc.gov/fire-information/statistics

Oikawa, P. Y., Ge, C., Wang, J., Eberwein, J. R., Liang, L. L., Allsman, L. A., et al. (2015). Unusually high soil nitrogen oxide emissions influence air quality in a high-temperature agricultural region. *Nature Communications, 6*(1), 8753. 10.1038/ncomms9753

Olszyna, K. J., Bailey, E. M., Simonaitis, R., & Meagher, J. F. (1994). O3 and NO y relationships at a rural site. *Journal of Geophysical Research: Atmospheres, 99*(D7), 14557-14563. https://doi.org/10.1029/94JD00739

Oltmans, S. J., Johnson, B. J., Harris, J. M., Thompson, A. M., Liu, H. Y., Chan, C. Y., et al. (2004). Tropospheric ozone over the North Pacific from ozonesonde observations. *Journal of Geophysical Research: Atmospheres, 109*(D15). https://doi.org/10.1029/2003JD003466

Oltmans, S. J., Lefohn, A. S., Shadwick, D., Harris, J. M., Scheel, H. E., Galbally, I., et al. (2013). Recent tropospheric ozone changes – A pattern dominated by slow or no growth. *Atmospheric Environment, 67*, 331-351. https://doi.org/10.1016/j.atmosenv.2012.10.057

Ouyang, S., Deng, T., Liu, R., Chen, J., He, G., Leung, J. C. H., et al. (2022). Impact of a subtropical high and a typhoon on a severe ozone pollution episode in the Pearl River Delta, China. *Atmospheric Chemistry and Physics, 22*(16), 10751-10767. 10.5194/acp-22-10751-2022

Parrish, D. D., & Ennis, C. A. (2019). Estimating background contributions and US anthropogenic enhancements to maximum ozone concentrations in the northern US. *Atmospheric Chemistry and Physics, 19*(19), 12587-12605. 10.5194/acp-19-12587-2019

Parrish, D. D., Lamarque, J.-F., Naik, V., Horowitz, L., Shindell, D. T., Staehelin, J., et al. (2014). Long-term changes in lower tropospheric baseline ozone concentrations: Comparing chemistry-climate models and observations at northern midlatitudes. *Journal of Geophysical Research: Atmospheres, 119*(9), 5719-5736. https://doi.org/10.1002/2013JD021435

Parrish, D. D., Stohl, A., Forster, C., Atlas, E. L., Blake, D. R., Goldan, P. D., et al. (2007). Effects of mixing on evolution of hydrocarbon ratios in the troposphere. *Journal of Geophysical Research: Atmospheres, 112*(D10). https://doi.org/10.1029/2006JD007583

Permar, W., Wang, Q., Selimovic, V., Wielgasz, C., Yokelson, R. J., Hornbrook, R. S., et al. (2021). Emissions of Trace Organic Gases From Western U.S. Wildfires Based on WE-CAN Aircraft Measurements. *Journal of Geophysical Research: Atmospheres, 126*(11), e2020JD033838. https://doi.org/10.1029/2020JD033838

Pfannerstill, E. Y., Arata, C., Zhu, Q., Schulze, B. C., Ward, R., Woods, R., et al. (2024). Temperature-dependent emissions dominate aerosol and ozone formation in Los Angeles. *Science, 384*(6702), 1324-1329. doi:10.1126/science.adg8204

Pope, R. J., Kerridge, B. J., Chipperfield, M. P., Siddans, R., Latter, B. G., Ventress, L. J., et al. (2023). Investigation of the summer 2018 European ozone air pollution episodes using novel satellite data and modelling. *Atmospheric Chemistry and Physics, 23*(20), 13235-13253. 10.5194/acp-23-13235-2023

Qi, J., Mo, Z., Yuan, B., Huang, S., Huangfu, Y., Wang, Z., et al. (2021). An observation approach in evaluation of ozone production to precursor changes during the COVID-19 lockdown. *Atmospheric Environment, 262*, 118618. https://doi.org/10.1016/j.atmosenv.2021.118618

Qin, M., Murphy, B. N., Isaacs, K. K., McDonald, B. C., Lu, Q., McKeen, S. A., et al. (2021). Criteria pollutant impacts of volatile chemical products informed by near-field modelling. *Nature Sustainability, 4*(2), 129-137. 10.1038/s41893-020-00614-1

Qin, M., She, Y., Wang, M., Wang, H., Chang, Y., Tan, Z., et al. (2025). Increased urban ozone in heatwaves due to temperature-induced emissions of anthropogenic volatile organic compounds. *Nature Geoscience, 18*(1), 50-56. 10.1038/s41561-024-01608-w

Qin, Y., Wang, H., Wang, Y., Lu, X., Tang, H., Zhang, J., et al. (2024). Wildfires in Southeast Asia pollute the atmosphere in the northern South China Sea. *Science Bulletin, 69*(8), 1011-1015. https://doi.org/10.1016/j.scib.2024.02.026

Qu, H., Wang, Y., Zhang, R., & Li, J. (2020). Extending Ozone-Precursor Relationships in China From Peak Concentration to Peak Time. *Journal of Geophysical Research: Atmospheres, 125*(22), e2020JD033670. https://doi.org/10.1029/2020JD033670

Qu, K., Wang, X., Yan, Y., Shen, J., Xiao, T., Dong, H., et al. (2021). A comparative study to reveal the influence of typhoons on the transport, production and accumulation of O3 in the Pearl River Delta, China. *Atmospheric Chemistry and Physics, 21*(15), 11593-11612. 10.5194/acp-21-11593-2021

Rasmussen, D. J., Hu, J., Mahmud, A., & Kleeman, M. J. (2013). The Ozone–Climate Penalty: Past, Present, and Future. *Environmental science & technology, 47*(24), 14258-14266. 10.1021/es403446m

Ren, J., Guo, F., & Xie, S. (2022). Diagnosing ozone–NOx–VOC sensitivity and revealing causes of ozone increases in China based on 2013–2021 satellite retrievals. *Atmospheric Chemistry and Physics, 22*(22), 15035-15047. 10.5194/acp-22-15035-2022

Ryan, R. G., Silver, J. D., & Schofield, R. (2021). Air quality and health impact of 2019–20 Black Summer megafires and COVID-19 lockdown in Melbourne and Sydney, Australia. *Environmental Pollution, 274*, 116498. https://doi.org/10.1016/j.envpol.2021.116498

Saikawa, E., Kim, H., Zhong, M., Avramov, A., Zhao, Y., Janssens-Maenhout, G., et al. (2017). Comparison of emissions inventories of anthropogenic air pollutants and greenhouse gases in China. *Atmospheric Chemistry and Physics, 17*(10), 6393-6421. 10.5194/acp-17-6393-2017

Sarwar, G., Luecken, D., Yarwood, G., Whitten, G. Z., & Carter, W. P. L. (2008). Impact of an Updated Carbon Bond Mechanism on Predictions from the CMAQ Modeling System: Preliminary Assessment. *Journal of Applied Meteorology and Climatology*, 47(1), 3-14. https://doi.org/10.1175/2007JAMC1393.1

Schnell, J. L., Prather, M. J., Josse, B., Naik, V., Horowitz, L. W., Zeng, G., et al. (2016). Effect of climate change on surface ozone over North America, Europe, and East Asia. *Geophysical Research Letters, 43*(7), 3509-3518. https://doi.org/10.1002/2016GL068060

Seinfeld, J. H., & Pandis, S. N. (2006). *Atmospheric Chemistry and Physics: From Air Pollution to Climate Change* (2nd Edition ed.). Hoboken, NJ: John Wiley & Sons, Inc.

Seltzer, K. M., Murphy, B. N., Pennington, E. A., Allen, C., Talgo, K., & Pye, H. O. T. (2022). Volatile Chemical Product Enhancements to Criteria Pollutants in the United States. *Environmental science & technology, 56*(11), 6905-6913. 10.1021/acs.est.1c04298

Shao, M., Wang, W., Yuan, B., Parrish, D. D., Li, X., Lu, K., et al. (2021). Quantifying the role of PM2.5 dropping in variations of ground-level ozone: Inter-comparison between Beijing and Los Angeles. *Science of The Total Environment, 788*, 147712. https://doi.org/10.1016/j.scitotenv.2021.147712

Shen, L., Jacob, D. J., Zhu, L., Zhang, Q., Zheng, B., Sulprizio, M. P., et al. (2019). The 2005–2016 trends of formaldehyde columns over China observed by satellites: Increasing anthropogenic emissions of volatile organic compounds and decreasing agricultural fire emissions. *Geophysical Research Letters, 46*(8), 4468-4475. https://doi.org/10.1029/2019gl082172

Shindell, D., Faluvegi, G., Lacis, A., Hansen, J., Ruedy, R., & Aguilar, E. (2006). Role of tropospheric ozone increases in 20th-century climate change. *Journal of Geophysical Research: Atmospheres, 111*(D8). https://doi.org/10.1029/2005JD006348

Sicard, P., Agathokleous, E., De Marco, A., Paoletti, E., & Calatayud, V. (2021a). Urban population exposure to air pollution in Europe over the last decades. *Environmental Sciences Europe, 33*(1), 28. 10.1186/s12302-020-00450-2

Sicard, P., Crippa, P., De Marco, A., Castruccio, S., Giani, P., Cuesta, J., et al. (2021b). High spatial resolution WRF-Chem model over Asia: Physics and chemistry evaluation. *Atmospheric Environment, 244*, 118004. https://doi.org/10.1016/j.atmosenv.2020.118004

Sillman, S. (1995). The use of NOy , H2O2, and HNO3 as indicators for ozone-NOx-hydrocarbon sensitivity in urban locations. *Journal of Geophysical Research: Atmospheres, 100*(D7), 14175-14188. https://doi.org/10.1029/94JD02953

Sillman, S. (1999). The relation between ozone, NOx and hydrocarbons in urban and polluted rural environments. *Atmospheric Environment, 33*(12), 1821-1845. https://doi.org/10.1016/S1352-2310(98)00345-8

Sillman, S., He, D., Cardelino, C., & Imhoff, R. E. (1997). The Use of Photochemical Indicators to Evaluate Ozone-NOx-Hydrocarbon Sensitivity: Case Studies from Atlanta, New York, and Los Angeles. *Journal of the Air & Waste Management Association, 47*(10), 1030-1040. 10.1080/10962247.1997.11877500

Sillman, S., Vautard, R., Menut, L., & Kley, D. (2003). O3-NOx-VOC sensitivity and NOx-VOC indicators in Paris: Results from models and Atmospheric Pollution Over the Paris Area (ESQUIF) measurements. *Journal of Geophysical Research: Atmospheres, 108*(D17). https://doi.org/10.1029/2002JD001561

Silver, B., Reddington, C. L., Arnold, S. R., & Spracklen, D. V. (2018). Substantial changes in air pollution across China during 2015–2017. *Environmental Research Letters, 13*(11), 114012. 10.1088/1748-9326/aae718

Simayi, M., Hao, Y., Li, J., Wu, R., Shi, Y., Xi, Z., et al. (2019). Establishment of county-level emission inventory for industrial NMVOCs in China and spatial-temporal characteristics for 2010–2016. *Atmospheric Environment, 211*, 194-203. https://doi.org/10.1016/j.atmosenv.2019.04.064

Simon, H., Reff, A., Wells, B., Xing, J., & Frank, N. (2015). Ozone Trends Across the United States over a Period of Decreasing NOx and VOC Emissions. *Environmental science & technology, 49*(1), 186-195. 10.1021/es504514z

Simpson, I. J., Akagi, S. K., Barletta, B., Blake, N. J., Choi, Y., Diskin, G. S., et al. (2011). Boreal forest fire emissions in fresh Canadian smoke plumes: C1-C10 volatile organic compounds (VOCs), CO2, CO, NO2, NO, HCN and CH3CN. *Atmospheric Chemistry and Physics, 11*(13), 6445-6463. 10.5194/acp-11-6445-2011

Simpson, I. J., Blake, N. J., Barletta, B., Diskin, G. S., Fuelberg, H. E., Gorham, K., et al. (2010). Characterization of trace gases measured over Alberta oil sands mining operations: 76 speciated C2–C10 volatile organic compounds (VOCs), CO2, CH4, CO, NO, NO2, NOy, O3 and SO2. *Atmospheric Chemistry and Physics, 10*(23), 11931-11954. https://doi.org/10.5194/acp-10-11931-2010

Skamarock, W. C., Klemp, J. B., Dudhia, J., Gill, D. O., Liu, Z., Berner, J., et al. (2019). *A Description of the Advanced Research WRF Model Version 4* (NCAR/TN-556+STR). National Center for Atmospheric Research https://www2.mmm.ucar.edu/wrf/users/docs/technote/v4_technote.pdf

Smith, A., Lott, N., & Vose, R. (2011). The Integrated Surface Database: Recent Developments and Partnerships. *Bulletin of the American Meteorological Society, 92*(6), 704-708. https://doi.org/10.1175/2011BAMS3015.1

Spirig, C., Neftel, A., Kleinman, L. I., & Hjorth, J. (2002). NOx versus VOC limitation of O3 production in the Po valley: Local and integrated view based on observations. *Journal of Geophysical Research: Atmospheres, 107*(D22), LOP 4-1-LOP 4-19. https://doi.org/10.1029/2001JD000561

Staehelin, J., Thudium, J., Buehler, R., Volz-Thomas, A., & Graber, W. (1994). Trends in surface ozone concentrations at Arosa (Switzerland). *Atmospheric Environment, 28*(1), 75-87.

Stasiuk Jr, W. N., & Coffey, P. E. (1974). Rural and Urban Ozone Relationships In New York State. *Journal of the Air Pollution Control Association, 24*(6), 564-568. 10.1080/00022470.1974.10469941

Stavrakou, T., Müller, J. F., Bauwens, M., De Smedt, I., Van Roozendael, M., De Mazière, M., et al. (2015). How consistent are top-down hydrocarbon emissions based on formaldehyde observations from GOME-2 and OMI? *Atmospheric Chemistry and Physics, 15*(20), 11861-11884. https://doi.org/10.5194/acp-15-11861-2015

Stohl, A., Bonasoni, P., Cristofanelli, P., Collins, W., Feichter, J., Frank, A., et al. (2003). Stratosphere-troposphere exchange: A review, and what we have learned from STACCATO. *Journal of Geophysical Research: Atmospheres, 108*(D12). https://doi.org/10.1029/2002JD002490

Sun, L., Xue, L., Wang, T., Gao, J., Ding, A., Cooper, O. R., et al. (2016). Significant increase of summertime ozone at Mount Tai in Central Eastern China. *Atmospheric Chemistry and Physics, 16*(16), 10637-10650. 10.5194/acp-16-10637-2016

Sun, W., Shao, M., Granier, C., Liu, Y., Ye, C. S., & Zheng, J. Y. (2018a). Long-Term Trends of Anthropogenic SO2, NOx, CO, and NMVOCs Emissions in China. *Earth's Future, 6*(8), 1112-1133. https://doi.org/10.1029/2018EF000822

Sun, Y., Liu, C., Palm, M., Vigouroux, C., Notholt, J., Hu, Q., et al. (2018b). Ozone seasonal evolution and photochemical production regime in the polluted troposphere in eastern China derived from high-resolution Fourier transform spectrometry (FTS) observations. *Atmospheric Chemistry and Physics, 18*(19), 14569-14583. 10.5194/acp-18-14569-2018

Taccone, R. A., Moreno, A., Colmenar, I., Salgado, S., Martín, M. P., & Cabañas, B. (2016). Kinetic study of the OH, NO3 radicals and Cl atom initiated atmospheric photo-oxidation of iso-propenyl methyl ether. *Atmospheric Environment, 127*, 80-89. https://doi.org/10.1016/j.atmosenv.2015.12.033

Tan, Z., Lu, K., Hofzumahaus, A., Fuchs, H., Bohn, B., Holland, F., et al. (2019). Experimental budgets of OH, HO2, and RO2 radicals and implications for ozone formation in the Pearl River Delta in China 2014. *Atmospheric Chemistry and Physics, 19*(10), 7129-7150. https://doi.org/10.5194/acp-19-7129-2019

Tanaka, P. L., Allen, D. T., McDonald-Buller, E. C., Chang, S., Kimura, Y., Mullins, C. B., et al. (2003). Development of a chlorine mechanism for use in the carbon bond IV chemistry model. *Journal of Geophysical Research: Atmospheres, 108*(D4). https://doi.org/10.1029/2002JD002432

Tang, J.-H., Chan, L.-Y., Chan, C.-Y., Li, Y.-S., Chang, C.-C., Liu, S.-C., & Li, Y.-D. (2007a). Nonmethane hydrocarbons in the transported and local air masses at a clean remote site on Hainan Island, south China. *Journal of Geophysical Research: Atmospheres, 112*(D14). https://doi.org/10.1029/2006JD007796

Tang, J. H., Chan, L. Y., Chan, C. Y., Li, Y. S., Chang, C. C., Liu, S. C., et al. (2007b). Characteristics and diurnal variations of NMHCs at urban, suburban, and rural sites in the Pearl River Delta and a remote site in South China. *Atmospheric Environment, 41*(38), 8620-8632. https://doi.org/10.1016/j.atmosenv.2007.07.029

Tang, L., Xue, X., Qu, J., Mi, Z., Bo, X., Chang, X., et al. (2020). Air pollution emissions from Chinese power plants based on the continuous emission monitoring systems network. *Scientific Data, 7*(1), 325. 10.1038/s41597-020-00665-1

Tang, W., Zhao, C., Geng, F., Peng, L., Zhou, G., Gao, W., et al. (2008). Study of ozone "weekend effect" in Shanghai. *Science in China Series D: Earth Sciences, 51*(9), 1354-1360. 10.1007/s11430-008-0088-2

Tarasick, D., Galbally, I. E., Cooper, O. R., Schultz, M. G., Ancellet, G., Leblanc, T., et al. (2019). Tropospheric Ozone Assessment Report: Tropospheric ozone from 1877 to 2016, observed levels, trends and uncertainties. *Elementa: Science of the Anthropocene, 7*. 10.1525/elementa.376

Tewari, M., Chen, F., Wang, W., Dudhia, J., LeMone, M., Mitchell, K., et al. (2004). *Implementation and verification of the unified NOAH land surface model in the WRF model.* Paper presented at the 20th conference on weather analysis and forecasting/16th conference on numerical weather prediction.

Thompson, A. M. (1992). The Oxidizing Capacity of the Earth's Atmosphere: Probable Past and Future Changes. *Science, 256*(5060), 1157-1165. doi:10.1126/science.256.5060.1157

Tie, X., Zhang, R., Brasseur, G., & Lei, W. (2002). Global NOx Production by Lightning. *Journal of Atmospheric Chemistry, 43*(1), 61-74. 10.1023/A:1016145719608

Tong, D., Zhang, Q., Liu, F., Geng, G., Zheng, Y., Xue, T., et al. (2018). Current Emissions and Future Mitigation Pathways of Coal-Fired Power Plants in China from 2010 to 2030. *Environmental science & technology, 52*(21), 12905-12914. 10.1021/acs.est.8b02919

Torres-Vazquez, A., Pleim, J., Gilliam, R., & Pouliot, G. (2022). Performance Evaluation of the Meteorology and Air Quality Conditions From Multiscale WRF-CMAQ Simulations for the Long Island Sound Tropospheric Ozone Study (LISTOS). *Journal of Geophysical Research: Atmospheres,* 127(5), e2021JD035890. https://doi.org/10.1029/2021JD035890

Tuccella, P., Curci, G., Visconti, G., Bessagnet, B., Menut, L., & Park, R. J. (2012). Modeling of gas and aerosol with WRF/Chem over Europe: Evaluation and sensitivity study. *Journal of Geophysical Research: Atmospheres, 117*(D3). https://doi.org/10.1029/2011jd016302

UNECE. (1988). *Protocol to the 1979 Convention on Long-Range Transboundary Air Pollution Concerning the Control of Emissions of Nitrogen Oxides and Their Transboundary Fluxes* (ECE/EB.AIR/21). United Nations Economic Commission for Europe, https://unece.org/sites/default/files/2021-10/1988.NOX_.e.pdf

UNECE. (1991). *Protocol to the 1979 Convention on Long-Range Transboundary Air Pollution Concerning the Control of Emissions of Volatile Organic Compounds or Their Transboundary Fluxes* (ECE/EB.AIR/30). United Nations Economic Commission for Europe, https://unece.org/sites/default/files/2021-10/1991.VOC_.e.pdf

Unger, N., Zheng, Y., Yue, X., & Harper, K. L. (2020). Mitigation of ozone damage to the world's land ecosystems by source sector. *Nature Climate Change*, *10*(2), 134-137. 10.1038/s41558-019-0678-3

Urbanski, S. P., Hao, W. M., & Baker, S. (2008). Chapter 4 Chemical Composition of Wildland Fire Emissions. In A. Bytnerowicz, M. J. Arbaugh, A. R. Riebau and C. Andersen (Eds.), *Developments in Environmental Science* (Vol. 8, pp. 79-107): Elsevier.

USEPA. (1998a). *Final Update to NOx SIP Call Regulations* (84 FR 8422). U.S. Environmental Protection Agency, https://www.epa.gov/power-sector/final-update-nox-sip-call-regulations

USEPA. (1998b). *Guideline on Data Handling Conventions for the 8-Hour Ozone NAAQS* (EPA-454/R-98-017). U.S. Environmental Protection Agency, https://www3.epa.gov/ttn/naaqs/aqmguide/collection/cp2_old/19981201_oaqps_epa-454_r-99-017.pdf

USEPA. (1999). *Compendium of Methods for the Determination of Toxic Organic Compounds in Ambient Air - Second Edition*. Compendium Method TO-15: Determination Of Volatile Organic Compounds (VOCs) In Air Collected In Specially-Prepared Canisters And Analyzed By Gas Chromatography/Mass Spectrometry (GC/MS) U.S. Environmental Protection Agency, EPA/625/R-96/010b. https://www.epa.gov/sites/default/files/2019-11/documents/to-15r.pdf

USEPA. (2017). *Quality Assurance Project Plan for the Standard Reference Photometer Program*. U.S. Environmental Protection Agency, https://www.epa.gov/sites/default/files/2020-09/documents/srp_qapp.pdf

USEPA. (2023). *2020 National Emissions Inventory Technical Support Document: Biogenics – Vegetation and Soil* (EPA-454/R-23-001h). U.S. Environmental Protection Agency, https://www.epa.gov/system/files/documents/2023-03/NEI2020_TSD_Section8_Biogenics_0.pdf

USEPA. (2024a). *Managing Air Quality - Emissions Inventories*. U.S. Environmental Protection Agency, https://www.epa.gov/air-quality-management-process/managing-air-quality-emissions-inventories

USEPA. (2024b). *Progress Report - Emission Controls and Monitoring*. U.S. Environmental Protection Agency, https://www.epa.gov/power-sector/progress-report-emission-controls-and-monitoring#noxannual

USEPA. (2025a). *Air Pollutant Emissions Trends Data — Criteria Pollutants National Tier 1 Trends for 1970 - 2024*. U.S. Environmental Protection Agency, https://www.epa.gov/air-emissions-inventories/air-pollutant-emissions-trends-data

USEPA. (2025b). *All EPA Emission Standards*. U.S. Environmental Protection Agency, https://www.epa.gov/emission-standards-reference-guide/all-epa-emission-standards

USEPA. (2025c). *AP-42: Compilation of Air Emissions Factors from Stationary Sources*. U.S. Environmental Protection Agency, https://www.epa.gov/air-emissions-factors-and-quantification/ap-42-compilation-air-emissions-factors-stationary-sources

van der Werf, G. R., Randerson, J. T., Giglio, L., van Leeuwen, T. T., Chen, Y., Rogers, B. M., et al. (2017). Global fire emissions estimates during 1997–2016. *Earth System Science Data, 9*(2), 697-720. 10.5194/essd-9-697-2017

Vellingiri, K., Kim, K.-H., Jeon, J. Y., Brown, R. J. C., & Jung, M.-C. (2015). Changes in NOx and O3 concentrations over a decade at a central urban area of Seoul, Korea. *Atmospheric Environment, 112*, 116-125. https://doi.org/10.1016/j.atmosenv.2015.04.032

Viana, M., Amato, F., Alastuey, A., Querol, X., Moreno, T., García Dos Santos, S., et al. (2009). Chemical Tracers of Particulate Emissions from Commercial Shipping. *Environmental science & technology, 43*(19), 7472-7477. 10.1021/es901558t

Visser, A. J., Boersma, K. F., Ganzeveld, L. N., & Krol, M. C. (2019). European NOx emissions in WRF-Chem derived from OMI: impacts on summertime surface ozone. *Atmospheric Chemistry and Physics, 19*(18), 11821-11841. 10.5194/acp-19-11821-2019

Volz, A., & Kley, D. (1988). Evaluation of the Montsouris series of ozone measurements made in the nineteenth century. *Nature, 332*(6161), 240-242. 10.1038/332240a0

Wang, A., Yuan, Z., Liu, X., Wang, M., Yang, J., Sha, Q. e., & Zheng, J. (2022a). Measurement-based intermediate volatility organic compound emission inventory from on-road vehicle exhaust in China. *Environmental Pollution, 310*, 119887. https://doi.org/10.1016/j.envpol.2022.119887

Wang, C., Duan, W., Cheng, S., & Zhang, J. (2023). Multi-component emission characteristics and high-resolution emission inventory of non-road construction equipment (NRCE) in China. *Science of The Total Environment, 877*, 162914. https://doi.org/10.1016/j.scitotenv.2023.162914

Wang, H., Chen, J., & Lu, K. (2015a). Measurement of NO3 and N2O5 in the troposphere. *Progress in Chemistry, 27*(7), 963. https://doi.org/10.7536/PC141230

Wang, H., Liu, X., Wu, C., & Lin, G. (2024a). Regional to global distributions, trends, and drivers of biogenic volatile organic compound emission from 2001 to 2020. *Atmospheric Chemistry and Physics, 24*(5), 3309-3328. 10.5194/acp-24-3309-2024

Wang, H., Lu, K., Guo, S., Wu, Z., Shang, D., Tan, Z., et al. (2018a). Efficient N2O5 uptake and NO3 oxidation in the outflow of urban Beijing. *Atmospheric Chemistry and Physics, 18*(13), 9705-9721. https://doi.org/10.5194/acp-18-9705-2018

Wang, H., Lu, X., Palmer, P. I., Zhang, L., Lu, K., Li, K., et al. (2024b). Deciphering decadal urban ozone trends from historical records since 1980. *National Science Review, 11*(11). 10.1093/nsr/nwae369

Wang, H., Lyu, X., Guo, H., Wang, Y., Zou, S., Ling, Z., et al. (2018b). Ozone pollution around a coastal region of South China Sea: interaction between marine and continental air. *Atmospheric Chemistry and Physics, 18*(6), 4277-4295. 10.5194/acp-18-4277-2018

Wang, H., Yan, R., Xu, T., Wang, Y., Wang, Q., Zhang, T., et al. (2020). Observation Constrained Aromatic Emissions in Shanghai, China. *Journal of Geophysical Research: Atmospheres, 125*(6), e2019JD031815. https://doi.org/10.1029/2019JD031815

Wang, N., Guo, H., Jiang, F., Ling, Z. H., & Wang, T. (2015b). Simulation of ozone formation at different elevations in mountainous area of Hong Kong using WRF-CMAQ model. *Science of The Total Environment, 505*, 939-951. https://doi.org/10.1016/j.scitotenv.2014.10.070

Wang, N., Huang, X., Xu, J., Wang, T., Tan, Z.-m., & Ding, A. (2022b). Typhoon-boosted biogenic emission aggravates cross-regional ozone pollution in China. *Science Advances, 8*(2), eabl6166. doi:10.1126/sciadv.abl6166

Wang, N., Lyu, X., Deng, X., Huang, X., Jiang, F., & Ding, A. (2019a). Aggravating O3 pollution due to NOx emission control in eastern China. *Science of The Total Environment, 677*, 732-744. https://doi.org/10.1016/j.scitotenv.2019.04.388

Wang, N., Lyu, X. P., Deng, X. J., Guo, H., Deng, T., Li, Y., et al. (2016). Assessment of regional air quality resulting from emission control in the Pearl River Delta region, southern China. *Science of The Total Environment, 573*, 1554-1565. 10.1016/j.scitotenv.2016.09.013

Wang, S., Zheng, J., Fu, F., Yin, S., & Zhong, L. (2011). Development of an emission processing system for the Pearl River Delta Regional air quality modeling using the SMOKE model: Methodology and evaluation. *Atmospheric Environment, 45*(29), 5079-5089. https://doi.org/10.1016/j.atmosenv.2011.06.037

Wang, T., Dai, J., Lam, K. S., Nan Poon, C., & Brasseur, G. P. (2019b). Twenty-Five Years of Lower Tropospheric Ozone Observations in Tropical East Asia: The Influence of Emissions and Weather Patterns. *Geophysical Research Letters, 46*(20), 11463-11470. https://doi.org/10.1029/2019GL084459

Wang, T., Lam, K. S., Lee, A. S. Y., Pang, S. W., & Tsui, W. S. (1998). Meteorological and Chemical Characteristics of the Photochemical Ozone Episodes Observed at Cape D'Aguilar in Hong Kong. *Journal of Applied Meteorology, 37*(10), 1167-1178. https://doi.org/10.1175/1520-0450(1998)037<1167:MACCOT>2.0.CO;2

Wang, T., Wei, X. L., Ding, A. J., Poon, C. N., Lam, K. S., Li, Y. S., et al. (2009). Increasing surface ozone concentrations in the background atmosphere of Southern China, 1994–2007. *Atmospheric Chemistry and Physics, 9*(16), 6217-6227. 10.5194/acp-9-6217-2009

Wang, T., Xue, L., Brimblecombe, P., Lam, Y. F., Li, L., & Zhang, L. (2017a). Ozone pollution in China: A review of concentrations, meteorological influences, chemical precursors, and effects. *Science of The Total Environment, 575*, 1582-1596. https://doi.org/10.1016/j.scitotenv.2016.10.081

Wang, W., Parrish, D. D., Wang, S., Bao, F., Ni, R., Li, X., et al. (2022c). Long-term trend of ozone pollution in China during 2014–2020: distinct seasonal and spatial characteristics and ozone sensitivity. *Atmospheric Chemistry and Physics, 22*(13), 8935-8949. 10.5194/acp-22-8935-2022

Wang, X., Fu, T.-M., Zhang, L., Lu, X., Liu, X., Amnuaylojaroen, T., et al. (2022d). Rapidly Changing Emissions Drove Substantial Surface and Tropospheric Ozone Increases Over Southeast Asia. *Geophysical Research Letters, 49*(19), e2022GL100223. https://doi.org/10.1029/2022GL100223

Wang, X., Liang, X.-Z., Jiang, W., Tao, Z., Wang, J. X. L., Liu, H., et al. (2010). WRF-Chem simulation of East Asian air quality: Sensitivity to temporal and vertical emissions distributions. *Atmospheric Environment, 44*(5), 660-669. https://doi.org/10.1016/j.atmosenv.2009.11.011

Wang, X., Yi, W., Lv, Z., Deng, F., Zheng, S., Xu, H., et al. (2021). Ship emissions around China under gradually promoted control policies from 2016 to 2019. *Atmospheric Chemistry and Physics*, 21(18), 13835-13853. 10.5194/acp-21-13835-2021

Wang, Y., Guo, H., Lyu, X., Zhang, L., Zeren, Y., Zou, S., & Ling, Z. (2019c). Photochemical evolution of continental air masses and their influence on ozone formation over the South China Sea. *Science of The Total Environment, 673*, 424-434. 10.1016/j.scitotenv.2019.04.075

Wang, Y., Guo, H., Zou, S., Lyu, X., Ling, Z., Cheng, H., & Zeren, Y. (2018c). Surface O3 photochemistry over the South China Sea: Application of a near-explicit chemical mechanism box model. *Environmental Pollution, 234*, 155-166. https://doi.org/10.1016/j.envpol.2017.11.001

Wang, Y., Huang, J., Zhao, B., Du, Y., Huang, L., Lai, D., et al. (2024c). Full-Volatility Reactive Organic Carbon Emissions from Volatile Chemical Products in Mainland China. *ACS ES&T Air, 1*(12), 1541-1553. 10.1021/acsestair.4c00116

Wang, Y., Wang, H., Guo, H., Lyu, X., Cheng, H., Ling, Z., et al. (2017b). Long-term O3–precursor relationships in Hong Kong: field observation and model simulation. *Atmospheric Chemistry and Physics, 17*(18), 10919-10935. 10.5194/acp-17-10919-2017

Warneke, C., de Gouw, J. A., Goldan, P. D., Kuster, W. C., Williams, E. J., Lerner, B. M., et al. (2004). Comparison of daytime and nighttime oxidation of biogenic and anthropogenic VOCs along the New England coast in summer during New England Air Quality Study 2002. *Journal of Geophysical Research: Atmospheres, 109*(D10). https://doi.org/10.1029/2003JD004424

Wayne, R. P., Barnes, I., Biggs, P., Burrows, J. P., Canosa-Mas, C. E., Hjorth, J., et al. (1991). The nitrate radical: Physics, chemistry, and the atmosphere. *Atmospheric Environment. Part A. General Topics, 25*(1), 1-203. https://doi.org/10.1016/0960-1686(91)90192-A

Wei, W., Li, Y., Wang, Y., Cheng, S., & Wang, L. (2018). Characteristics of VOCs during haze and non-haze days in Beijing, China: Concentration, chemical degradation and regional transport impact. *Atmospheric Environment, 194*, 134-145. https://doi.org/10.1016/j.atmosenv.2018.09.037

Wei, W., Wang, S., Chatani, S., Klimont, Z., Cofala, J., & Hao, J. (2008). Emission and speciation of non-methane volatile organic compounds from anthropogenic sources in China. *Atmospheric Environment, 42*(20), 4976-4988. https://doi.org/10.1016/j.atmosenv.2008.02.044

Wei, X., Lam, K.-s., Cao, C., Li, H., & He, J. (2016). Dynamics of the Typhoon Haitang Related High Ozone Episode over Hong Kong. *Advances in Meteorology, 2016*, 1-12. 10.1155/2016/6089154

Wentworth, G. R., Aklilu, Y.-a., Landis, M. S., & Hsu, Y.-M. (2018). Impacts of a large boreal wildfire on ground level atmospheric concentrations of PAHs, VOCs and ozone. *Atmospheric Environment, 178*, 19-30. https://doi.org/10.1016/j.atmosenv.2018.01.013

Wesely, M. L. (1989). Parameterization of surface resistances to gaseous dry deposition in regional-scale numerical models. *Atmospheric Environment, 23*(6), 1293-1304. https://doi.org/10.1016/0004-6981(89)90153-4

Whitten, G. Z., Heo, G., Kimura, Y., McDonald-Buller, E., Allen, D. T., Carter, W. P. L., & Yarwood, G. (2010). A new condensed toluene mechanism for Carbon Bond: CB05-TU. *Atmospheric Environment, 44*(40), 5346-5355. https://doi.org/10.1016/j.atmosenv.2009.12.029

WHO. (2013). Review of evidence on health aspects of air pollution: REVIHAAP project: technical report. In. Copenhagen, Danmark: World Health Organization Regional Office for Europe.

Wiedinmyer, C., Akagi, S. K., Yokelson, R. J., Emmons, L. K., Al-Saadi, J. A., Orlando, J. J., & Soja, A. J. (2011). The Fire INventory from NCAR (FINN): a high resolution global model to estimate the emissions from open burning. *Geoscientific Model Development, 4*(3), 625-641. 10.5194/gmd-4-625-2011

Wiedinmyer, C., Kimura, Y., McDonald-Buller, E. C., Emmons, L. K., Buchholz, R. R., Tang, W., et al. (2023). The Fire Inventory from NCAR version 2.5: an updated global fire emissions model for climate and chemistry applications. *Geoscientific Model Development, 16*(13), 3873-3891. 10.5194/gmd-16-3873-2023

Wolff, G. T., & Korsog, P. E. (1992). Ozone Control Strategies Based on the Ratio of Volatile Organic Compounds to Nitrogen Oxides. *Journal of the Air & Waste Management Association, 42*(9), 1173-1177. 10.1080/10473289.1992.10467064

Wu, J., Bei, N., Li, X., Wang, R., Liu, S., Jiang, Q., et al. (2022). Impacts of Transboundary Transport on Coastal Air Quality of South China. *Journal of Geophysical Research: Atmospheres, 127*(8), e2021JD036213. https://doi.org/10.1029/2021JD036213

Wu, M., Wu, D., Fan, Q., Wang, B. M., Li, H. W., & Fan, S. J. (2013). Observational studies of the meteorological characteristics associated with poor air quality over the Pearl River Delta in China. *Atmospheric Chemistry and Physics, 13*(21), 10755-10766. 10.5194/acp-13-10755-2013

Wu, N., Geng, G., Xu, R., Liu, S., Liu, X., Shi, Q., et al. (2024). Development of a high-resolution integrated emission inventory of air pollutants for China. *Earth System Science Data, 16*(6), 2893-2915. 10.5194/essd-16-2893-2024

Wu, N., Geng, G., Yan, L., Bi, J., Li, Y., Tong, D., et al. (2021a). Improved spatial representation of a highly resolved emission inventory in China: evidence from TROPOMI measurements. *Environmental Research Letters, 16*(8), 084056. 10.1088/1748-9326/ac175f

Wu, R., Bo, Y., Li, J., Li, L., Li, Y., & Xie, S. (2016a). Method to establish the emission inventory of anthropogenic volatile organic compounds in China and its application in the period 2008–2012. *Atmospheric Environment, 127*, 244-254. https://doi.org/10.1016/j.atmosenv.2015.12.015

Wu, X., Wu, Y., Zhang, S., Liu, H., Fu, L., & Hao, J. (2016b). Assessment of vehicle emission programs in China during 1998–2013: Achievement, challenges and implications. *Environmental Pollution, 214*, 556-567. https://doi.org/10.1016/j.envpol.2016.04.042

Wu, Y., Zhang, S., Hao, J., Liu, H., Wu, X., Hu, J., et al. (2017). On-road vehicle emissions and their control in China: A review and outlook. *Science of The Total Environment, 574*, 332-349. https://doi.org/10.1016/j.scitotenv.2016.09.040

Wu, Z., Zhang, L., Walker, J. T., Makar, P. A., Perlinger, J. A., & Wang, X. (2021b). Extension of a gaseous dry deposition algorithm to oxidized volatile organic compounds and hydrogen cyanide for application in chemistry transport models. *Geoscientific Model Development, 14*(8), 5093-5105. 10.5194/gmd-14-5093-2021

Wu, Z., Zhang, Y., He, J., Chen, H., Huang, X., Wang, Y., et al. (2020). Dramatic increase in reactive volatile organic compound (VOC) emissions from ships at berth after implementing the fuel switch policy in the Pearl River Delta Emission Control Area. *Atmospheric Chemistry and Physics, 20*(4), 1887-1900. 10.5194/acp-20-1887-2020

Xiao, Q., Geng, G., Xue, T., Liu, S., Cai, C., He, K., & Zhang, Q. (2022). Tracking PM2.5 and O3 Pollution and the Related Health Burden in China 2013–2020. *Environmental science & technology, 56*(11), 6922-6932. 10.1021/acs.est.1c04548

Xie, Q., Tham, Y. J., Yu, X., Wang, Z., Ling, Z., Wang, X., et al. (2023). Seasonal variations of O3 formation mechanism and atmospheric photochemical reactivity during severe high O3 pollution episodes in the Pearl River Delta region. *Atmospheric Environment, 309*, 119918. https://doi.org/10.1016/j.atmosenv.2023.119918

Xing, J., Mathur, R., Pleim, J., Hogrefe, C., Gan, C. M., Wong, D. C., et al. (2015). Observations and modeling of air quality trends over 1990–2010 across the Northern Hemisphere: China, the United States and Europe. *Atmospheric Chemistry and Physics, 15*(5), 2723-2747. 10.5194/acp-15-2723-2015

Xing, L., Bei, N., Guo, J., Wang, Q., Liu, S., Han, Y., et al. (2021). Impacts of Biomass Burning in Peninsular Southeast Asia on PM2.5 Concentration and Ozone Formation in Southern China During Springtime—A Case Study. *Journal of Geophysical Research: Atmospheres, 126*(22), e2021JD034908. https://doi.org/10.1029/2021JD034908

Xu, L., Crounse, J. D., Vasquez, K. T., Allen, H., Wennberg, P. O., Bourgeois, I., et al. (2021). Ozone chemistry in western U.S. wildfire plumes. *Science Advances, 7*(50), eabl3648. doi:10.1126/sciadv.abl3648

Xu, X., Lin, W., Wang, T., Yan, P., Tang, J., Meng, Z., & Wang, Y. (2008). Long-term trend of surface ozone at a regional background station in eastern China 1991-2006: enhanced variability. *Atmospheric Chemistry and Physics, 8*(10), 2595-2607. 10.5194/acp-8-2595-2008

Xue, L., Gu, R., Wang, T., Wang, X., Saunders, S., Blake, D., et al. (2016). Oxidative capacity and radical chemistry in the polluted atmosphere of Hong Kong and Pearl River Delta region: analysis of a severe photochemical smog episode. *Atmospheric Chemistry and Physics, 16*(15), 9891-9903. 10.5194/acp-16-9891-2016

Yan, C., Tham, Y. J., Zha, Q., Wang, X., Xue, L., Dai, J., et al. (2019). Fast heterogeneous loss of N2O5 leads to significant nighttime NOx removal and nitrate aerosol formation at a coastal background environment of southern China. *Science of The Total Environment, 677*, 637-647. https://doi.org/10.1016/j.scitotenv.2019.04.389

Yan, Y., Pozzer, A., Ojha, N., Lin, J., & Lelieveld, J. (2018). Analysis of European ozone trends in the period 1995–2014. *Atmospheric Chemistry and Physics, 18*(8), 5589-5605. 10.5194/acp-18-5589-2018

Yang, L., Zhang, Q., Zhang, Y., Lv, Z., Wang, Y., Wu, L., et al. (2021a). An AIS-based emission inventory and the impact on air quality in Tianjin port based on localized emission factors. *Science of The Total Environment, 783*, 146869. https://doi.org/10.1016/j.scitotenv.2021.146869

Yang, X., Lu, K., Ma, X., Gao, Y., Tan, Z., Wang, H., et al. (2022). Radical chemistry in the Pearl River Delta: observations and modeling of OH and HO2 radicals in Shenzhen in 2018. *Atmospheric Chemistry and Physics, 22*(18), 12525-12542. https://doi.org/10.5194/acp-22-12525-2022

Yang, Y., Zhao, Y., Zhang, L., Zhang, J., Huang, X., Zhao, X., et al. (2021b). Improvement of the satellite-derived NOx emissions on air quality modeling and its effect on ozone and secondary inorganic aerosol formation in the Yangtze River Delta, China. *Atmospheric Chemistry and Physics, 21*(2), 1191-1209. 10.5194/acp-21-1191-2021

Yarwood, G., Rao, S., Yocke, M., & Whitten, G. (2005). *Updates to the Carbon Bond Chemical Mechanism: CB05*. Final Report to the US EPA, Rep. RT-04-00675.

Young, P. J., Archibald, A. T., Bowman, K. W., Lamarque, J. F., Naik, V., Stevenson, D. S., et al. (2013). Pre-industrial to end 21st century projections of tropospheric ozone from the Atmospheric Chemistry and Climate Model Intercomparison Project (ACCMIP). *Atmospheric Chemistry and Physics, 13*(4), 2063-2090. 10.5194/acp-13-2063-2013

Yuan, B., Chen, W., Shao, M., Wang, M., Lu, S., Wang, B., et al. (2012). Measurements of ambient hydrocarbons and carbonyls in the Pearl River Delta (PRD), China. *Atmospheric Research, 116*, 93-104. https://doi.org/10.1016/j.atmosres.2012.03.006

Yuan, B., Kaser, L., Karl, T., Graus, M., Peischl, J., Campos, T. L., et al. (2015). Airborne flux measurements of methane and volatile organic compounds over the Haynesville and Marcellus shale gas production regions. *Journal of Geophysical Research: Atmospheres, 120*(12), 6271-6289. https://doi.org/10.1002/2015JD023242

Zanis, P., Akritidis, D., Turnock, S., Naik, V., Szopa, S., Georgoulias, A. K., et al. (2022). Climate change penalty and benefit on surface ozone: a global perspective based on CMIP6 earth system models. *Environmental Research Letters, 17*(2), 024014. 10.1088/1748-9326/ac4a34

Zeren, Y., Guo, H., Lyu, X., Jiang, F., Wang, Y., Liu, X., et al. (2019). An Ozone "Pool" in South China: Investigations on Atmospheric Dynamics and Photochemical Processes Over the Pearl River Estuary. *Journal of Geophysical Research: Atmospheres, 124*(22), 12340-12355. https://doi.org/10.1029/2019JD030833

Zeren, Y., Guo, H., Lyu, X., Zhou, B., Liu, X., Yang, L., et al. (2022a). Remarkable spring increase overwhelmed hard-earned autumn decrease in ozone pollution from 2005 to 2017 at a suburban site in Hong Kong, South China. *Science of The Total Environment, 831*, 154788. https://doi.org/10.1016/j.scitotenv.2022.154788

Zeren, Y., Zhou, B., Zheng, Y., Jiang, F., Lyu, X., Xue, L., et al. (2022b). Does Ozone Pollution Share the Same Formation Mechanisms in the Bay Areas of China? *Environmental science & technology, 56*(20), 14326-14337. 10.1021/acs.est.2c05126

Zhang, F., Xiao, B., Liu, Z., Zhang, Y., Tian, C., Li, R., et al. (2024a). Real-world emission characteristics of VOCs from typical cargo ships and their potential contributions to secondary organic aerosol and O3 under low-sulfur fuel policies. *Atmospheric Chemistry and Physics, 24*(16), 8999-9017. 10.5194/acp-24-8999-2024

Zhang, L., Brook, J. R., & Vet, R. (2002). On ozone dry deposition—with emphasis on non-stomatal uptake and wet canopies. *Atmospheric Environment, 36*(30), 4787-4799. https://doi.org/10.1016/S1352-2310(02)00567-8

Zhang, L., Brook, J. R., & Vet, R. (2003). A revised parameterization for gaseous dry deposition in air-quality models. *Atmospheric Chemistry and Physics, 3*(6), 2067-2082. https://doi.org/10.5194/acp-3-2067-2003

Zhang, L., He, Z., Wu, Z., Macdonald, A. M., Brook, J. R., & Kharol, S. (2023). A database of modeled gridded dry deposition velocities for 45 gaseous species and three particle size ranges across North America. *Journal of Environmental Sciences, 127*, 264-272. https://doi.org/10.1016/j.jes.2022.05.030

Zhang, Q., Streets, D. G., Carmichael, G. R., He, K. B., Huo, H., Kannari, A., et al. (2009a). Asian emissions in 2006 for the NASA INTEX-B mission. *Atmospheric Chemistry and Physics, 9*(14), 5131-5153. 10.5194/acp-9-5131-2009

Zhang, Q., Zheng, Y., Tong, D., Shao, M., Wang, S., Zhang, Y., et al. (2019). Drivers of improved PM2.5 air quality in China from 2013 to 2017. *Proceedings of the National Academy of Sciences, 116*(49), 24463-24469. doi:10.1073/pnas.1907956116

Zhang, R., Wang, Y., He, Q., Chen, L., Zhang, Y., Qu, H., et al. (2017). Enhanced trans-Himalaya pollution transport to the Tibetan Plateau by cut-off low systems. *Atmospheric Chemistry and Physics, 17*(4), 3083-3095. https://doi.org/10.5194/acp-17-3083-2017

Zhang, X., Lu, X., Wang, F., Zhou, W., Wang, P., & Gao, M. (2024b). Enhanced Late Spring Ozone in Southern China by Early Onset of the South China Sea Summer Monsoon. *Journal of Geophysical Research: Atmospheres, 129*(4), e2023JD039029. https://doi.org/10.1029/2023JD039029

Zhang, Y., Sartelet, K., Wu, S. Y., & Seigneur, C. (2013). Application of WRF/Chem-MADRID and WRF/Polyphemus in Europe – Part 1: Model description, evaluation of meteorological predictions, and aerosol–meteorology interactions. *Atmospheric Chemistry and Physics, 13*(14), 6807-6843. 10.5194/acp-13-6807-2013

Zhang, Y., Shao, K., & Tang, X. (1998). The study of urban photochemical smog pollution in China. *Acta Scientiarum Naturalium-Universitatis Pekinensis, 34*, 392-400.

Zhang, Y., & Wang, Y. (2016). Climate-driven ground-level ozone extreme in the fall over the Southeast United States. *Proceedings of the National Academy of Sciences, 113*(36), 10025-10030. doi:10.1073/pnas.1602563113

Zhang, Y., Wen, X.-Y., Wang, K., Vijayaraghavan, K., & Jacobson, M. Z. (2009b). Probing into regional O3 and particulate matter pollution in the United States: 2. An examination of formation mechanisms through a process analysis technique and sensitivity study. *Journal of Geophysical Research: Atmospheres, 114*(D22). https://doi.org/10.1029/2009JD011900

Zhao, B., Wang, S. X., Liu, H., Xu, J. Y., Fu, K., Klimont, Z., et al. (2013). NOx emissions in China: historical trends and future perspectives. *Atmospheric Chemistry and Physics, 13*(19), 9869-9897. 10.5194/acp-13-9869-2013

Zhao, C., Wang, Y., Yang, Q., Fu, R., Cunnold, D., & Choi, Y. (2010). Impact of East Asian summer monsoon on the air quality over China: View from space. *Journal of Geophysical Research: Atmospheres, 115*(D9). https://doi.org/10.1029/2009JD012745

Zhao, Y., Nielsen, C. P., Lei, Y., McElroy, M. B., & Hao, J. (2011). Quantifying the uncertainties of a bottom-up emission inventory of anthropogenic atmospheric pollutants in China. *Atmospheric Chemistry and Physics, 11*(5), 2295-2308. https://doi.org/10.5194/acp-11-2295-2011

Zheng, B., Cheng, J., Geng, G., Wang, X., Li, M., Shi, Q., et al. (2021a). Mapping anthropogenic emissions in China at 1 km spatial resolution and its application in air quality modeling. *Science Bulletin, 66*(6), 612-620. https://doi.org/10.1016/j.scib.2020.12.008

Zheng, B., Huo, H., Zhang, Q., Yao, Z. L., Wang, X. T., Yang, X. F., et al. (2014). High-resolution mapping of vehicle emissions in China in 2008. *Atmospheric Chemistry and Physics, 14*(18), 9787-9805. 10.5194/acp-14-9787-2014

Zheng, B., Tong, D., Li, M., Liu, F., Hong, C., Geng, G., et al. (2018). Trends in China's anthropogenic emissions since 2010 as the consequence of clean air actions. *Atmospheric Chemistry and Physics, 18*(19), 14095-14111. 10.5194/acp-18-14095-2018

Zheng, B., Zhang, Q., Tong, D., Chen, C., Hong, C., Li, M., et al. (2017). Resolution dependence of uncertainties in gridded emission inventories: a case study in Hebei, China. *Atmospheric Chemistry and Physics, 17*(2), 921-933. 10.5194/acp-17-921-2017

Zheng, J., Shao, M., Che, W., Zhang, L., Zhong, L., Zhang, Y., & Streets, D. (2009a). Speciated VOC emission inventory and spatial patterns of ozone formation potential in the Pearl River Delta, China. *Environmental science & technology, 43*(22), 8580-8586. https://doi.org/10.1021/es901688e

Zheng, J., Zhang, L., Che, W., Zheng, Z., & Yin, S. (2009b). A highly resolved temporal and spatial air pollutant emission inventory for the Pearl River Delta region, China and its uncertainty assessment. *Atmospheric Environment, 43*(32), 5112-5122. https://doi.org/10.1016/j.atmosenv.2009.04.060

Zheng, J., Zhong, L., Wang, T., Louie, P. K. K., & Li, Z. (2010). Ground-level ozone in the Pearl River Delta region: Analysis of data from a recently established regional air quality monitoring network. *Atmospheric Environment, 44*(6), 814-823. https://doi.org/10.1016/j.atmosenv.2009.11.032

Zheng, S., Jiang, F., Feng, S., Liu, H., Wang, X., Tian, X., et al. (2024). Impact of Marine Shipping Emissions on Ozone Pollution During the Warm Seasons in China. *Journal of Geophysical Research: Atmospheres, 129*(14), e2024JD040864. https://doi.org/10.1029/2024JD040864

Zheng, Y., Jiang, F., Feng, S., Cai, Z., Shen, Y., Ying, C., et al. (2021b). Long-range transport of ozone across the eastern China seas: A case study in coastal cities in southeastern China. *Science of The Total Environment, 768*, 144520. https://doi.org/10.1016/j.scitotenv.2020.144520

Zhong, Z., Zheng, J., Zhu, M., Huang, Z., Zhang, Z., Jia, G., et al. (2018). Recent developments of anthropogenic air pollutant emission inventories in Guangdong province, China. *Science of The Total Environment, 627*, 1080-1092. https://doi.org/10.1016/j.scitotenv.2018.01.268

Zhou, Y., Yang, Y., Wang, H., Wang, J., Li, M., Li, H., et al. (2022). Summer ozone pollution in China affected by the intensity of Asian monsoon systems. *Science of The Total Environment, 849*, 157785. https://doi.org/10.1016/j.scitotenv.2022.157785

Zhou, Y., Zhao, Y., Mao, P., Zhang, Q., Zhang, J., Qiu, L., & Yang, Y. (2017). Development of a high-resolution emission inventory and its evaluation and application through air quality modeling for Jiangsu Province, China. *Atmospheric Chemistry and Physics, 17*(1), 211-233. 10.5194/acp-17-211-2017

Zhu, S., Ma, J., Wang, S., Sun, S., Wang, P., & Zhang, H. (2023). Shifts of Formation Regimes and Increases of Atmospheric Oxidation Led to Ozone Increase in North China Plain and Yangtze River Delta From 2016 to 2019. *Journal of Geophysical Research: Atmospheres, 128*(13), e2022JD038373. https://doi.org/10.1029/2022JD038373

Zhuang, Y., Fu, R., Santer, B. D., Dickinson, R. E., & Hall, A. (2021). Quantifying contributions of natural variability and anthropogenic forcings on increased fire weather risk over the western United States. *Proceedings of the National Academy of Sciences, 118*(45), e2111875118. doi:10.1073/pnas.2111875118

Zou, Y., Deng, X. J., Zhu, D., Gong, D. C., Wang, H., Li, F., et al. (2015). Characteristics of 1 year of observational data of VOCs, NOx and O3 at a suburban site in Guangzhou, China. *Atmospheric Chemistry and Physics, 15*(12), 6625-6636. https://doi.org/10.5194/acp-15-6625-2015